NASA/CR—1998–208803

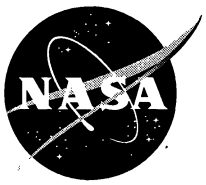

Research Reports—1997 NASA/ASEE Summer Faculty Fellowship Program

G.R. Karr, Editor
The University of Alabama, Huntsville, Alabama

J. Dowdy, Editor
Marshall Space Flight Center, Marshall Space Flight Center, Alabama

L.M. Freeman, Editor
The University of Alabama, Tuscaloosa, Alabama

Contract NGT8–52836
Prepared for Marshall Space Flight Center

September 1998

The NASA STI Program Office...in Profile

Since its founding, NASA has been dedicated to the advancement of aeronautics and space science. The NASA Scientific and Technical Information (STI) Program Office plays a key part in helping NASA maintain this important role.

The NASA STI Program Office is operated by Langley Research Center, the lead center for NASA's scientific and technical information. The NASA STI Program Office provides access to the NASA STI Database, the largest collection of aeronautical and space science STI in the world. The Program Office is also NASA's institutional mechanism for disseminating the results of its research and development activities. These results are published by NASA in the NASA STI Report Series, which includes the following report types:

- TECHNICAL PUBLICATION. Reports of completed research or a major significant phase of research that present the results of NASA programs and include extensive data or theoretical analysis. Includes compilations of significant scientific and technical data and information deemed to be of continuing reference value. NASA's counterpart of peer-reviewed formal professional papers but has less stringent limitations on manuscript length and extent of graphic presentations.

- TECHNICAL MEMORANDUM. Scientific and technical findings that are preliminary or of specialized interest, e.g., quick release reports, working papers, and bibliographies that contain minimal annotation. Does not contain extensive analysis.

- CONTRACTOR REPORT. Scientific and technical findings by NASA-sponsored contractors and grantees.

- CONFERENCE PUBLICATION. Collected papers from scientific and technical conferences, symposia, seminars, or other meetings sponsored or cosponsored by NASA.

- SPECIAL PUBLICATION. Scientific, technical, or historical information from NASA programs, projects, and mission, often concerned with subjects having substantial public interest.

- TECHNICAL TRANSLATION. English-language translations of foreign scientific and technical material pertinent to NASA's mission.

Specialized services that complement the STI Program Office's diverse offerings include creating custom thesauri, building customized databases, organizing and publishing research results...even providing videos.

For more information about the NASA STI Program Office, see the following:

- Access the NASA STI Program Home Page at ***http://www.sti.nasa.gov***

- E-mail your question via the Internet to help@sti.nasa.gov

- Fax your question to the NASA Access Help Desk at (301) 621–0134

- Telephone the NASA Access Help Desk at (301) 621–0390

- Write to:
  NASA Access Help Desk
  NASA Center for AeroSpace Information
  800 Elkridge Landing Road
  Linthicum Heights, MD 21090–2934

NASA/CR—1998–208803

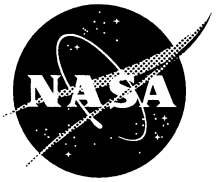

Research Reports—1997 NASA/ASEE Summer Faculty Fellowship Program

G.R. Karr, Editor
The University of Alabama, Huntsville, Alabama

J. Dowdy, Editor
Marshall Space Flight Center, Marshall Space Flight Center, Alabama

L.M. Freeman, Editor
The University of Alabama, Tuscaloosa, Alabama

Prepared under Contract NGT8–52836

National Aeronautics and
Space Administration

Marshall Space Flight Center

September 1998

Available from:

NASA Center for AeroSpace Information
800 Elkridge Landing Road
Linthicum Heights, MD 21090–2934
(301) 621–0390

National Technical Information Service
5285 Port Royal Road
Springfield, VA 22161
(703) 487–4650

TABLE OF CONTENTS

I. Adams, Glynn
University of Arkansas
Loading considerations for implementing friction stir welding for large diameter tank fabrication

II. Ahmed, Ardsher
University of Massachusetts, Dartmouth
Optimization of Super Conductor use on EADS II System

III. Boulet, Joseph
University of Tennessee
Structural modeling of the next generation space telescope's primary mirror

IV. Bradley, William
Western New England College
Data compression techniques for advanced space transportation systems

V. Brewer, William
Jackson State University
Rocket Propellant ducts: First cut approximations and design guidance

VI. Brush, Lucien
University of Washington
Solidification of Drops in the MSFC Drop Tube

VII. Chu, Tsuchin
Southern Illinois University at Carbondale
Finite Element Modeling of transient thermography inspection of composite materials

VIII. Dean, John
Park College
Virtual Reality at the PC level

IX. Dumas, Joseph
University of Tennessee at Chattanooga
Virtual Environment User Interfaces to support RLV and space station simulations in the ANVIL Virtual Reality Lab

X. Emerson, Charles
Southwest Missouri State University
Multi-Scale Fractal Analysis of image texture and pattern

XI. Fragomeni, James
The University of Alabama
Potential for EMU fabric damage by electron beam and molten metal during space welding for the International Space Welding experiment

XII. Geerts, Bart
Embry-Riddle Aeronautical University
Characterization of Mesoscale convective systems by means of composite radar reflectivity data

XIII. George, Lynnane
U.S. Air Force Academy
Mar Mission Design Handbook (2009-2024 Opportunities)

XIV. Hampton, Roy
McNeese State University
Optimal Controller design for the Microgravity Isolation Mount (MIM)

XV. Han, Samuel
Tennessee Technology University
1-D Numerical analysis of RBCC engine performance

XVI. Heard, Pamala
Langston University
EDCATS: An Evaluation Tool

XVII. Helmer, Wayne
Southern Illinois University at Carbondale
The effect of jetting parameters on the performance of droplet formation for ink-jet rapid prototyping

XVIII. Hopkins, Randall
The University of Alabama
Uncertainty in calibration, detection, and estimation of Metal concentration in Engine Plumes using Opad

XIX. Hung, John
Auburn University
Dynamic Models of Instruments using rotating unbalanced masses

XX. Javan, Hank
North Carolina A&T State University
Application of Fresnel Zone to cross talk

XXI. Jones, Peter
Auburn University
Flammability of Heterogeneously combusting metals

XXII. Jordan, William
Louisiana Tech University
Modeling the Mechanical behavior of Ceramic matrix composite materials

XXIII. Katsinis, Constantine
The University of Alabama in Huntsville
Spectrum preprocessing in the OPAD system

XXIV. Kennedy, Alvin
North Carolina A&T State University
Investigation of solution polymerization in microgravity and 1G

XXV. Larson, Jr., David
State University of New York at Stony Brook
Orbital processing of Eutectic rod-like arrays

XXVI. Lebo, George
University of Florida
Development of an outreach program for NASA: "NASA Ambassadors"

XXVII. Lindsey, Patricia
East Carolina University
Object creation and human factors evaluation for virtual environments

XXVIII. Lowry, James
East Central University
Remote sensing in archeology: classifying Bajors of the Peten, Guatemala

XXIX. Lundberg, John
Auburn University
Evaluation of GPS coverage for the X-33 Michael-6 trajectory

XXX. Lunsford, Myrtis
Alabama A&M University
Virtual Environment computer simulations to support human factors Engineering and operations analysis for the RLV program.

XXXI. Mastrangelo, Christina
University of Virginia
Development of Technology transfer economic growth metrics

XXXII. McDonald, Malcolm
Berry College
NASA Ambassadors: A speaker outreach program

XXXIII. McGuire, Timothy
West Texas A&M University
Performance of a bounce-averaged global model of super-thermal electron transport in the Earth's magnetic field

XXXIV. Munroe, Jr., Ray
University of Mobile
A Geant study of the Scintillating optical fiber (SOFCAL) cosmic ray detector

XXXV. Navaz, Homayun
GMI Engineering & Management Institution
Current and Future critical issues in rocket propulsion systems

XXXVI. Ray, Paul
The University of Alabama
Program risk planning with risk as a resource

XXXVII. Ritter, Timothy
University of North Carolina at Pembroke
Low temperature Photoluminescence characterization of orbitally growth CdZnTe

XXXVIII. Romine, Peter
Alabama A&M University
Friction Stir Welding development

XXXIX. Schall, Constance
University of Tulsa
The Effects of Impurities on Protein Crystal Growth and Nucleation: A Preliminary Study

XL. Schinstock, Dale
The University of Alabama
Controller Design for EMA in TVC Incorporating Force Feedback

XLI. Sherif, S.A.
University of Florida
Modeling of a two-phase jet pump with phase change, shocks and temperature dependent properties

XLII. Sherrod, Jerry
Pellissippi State Tech. C. C.
Software products for temperature data reduction of platinum resistance thermometers (PRT)

XLIII. Shtessel, Yuri
The University of Alabama in Huntsville
X-33 Reusable launch vehicle control on sliding modes: concepts for a control system development

XLIV. Smalley, Larry
The University of Alabama in Huntsville
Application of Parametrized Post-Newtonian methods to the gravitational is of satellite energy exchange data

XLV. Smith , Montgomery
University of Tennessee Space Institute
Design of the experimental exposure conditions to simulate ionizing radiation effects on candidate replacement materials for the Hubble Space Telescope

XLVI. Stewart, Michael
University of Arkansas
Mechanistic Models of Friction Stir Welding

XLVII. Taylor, Charles
Western Oregon University
Imaging extra-solar planets with an ultra-large space telescope

XLVIII. Taylor, Jaime
Austin Peay State University
Development of a sunspot tracking system

XLIX. Trivoli, George
Jacksonville State University
Technology transfer activities of NASA/MSFC: Enhancing the Southeast region's production capabilities

L. Wang, Lingjun
University of Tennessee at Chattanooga
Characterization of PVT grown ZnSe by low temperature photoluminescence

LI. Zeiler, Thomas
The University of Alabama
Including Aeroelastic effects in the calculation of X-33 loads and control characteristics

1997

NASA/ASEE SUMMER FACULTY FELLOWSHIP PROGRAM

MARSHALL SPACE FLIGHT CENTER

THE UNIVERSITY OF ALABAMA IN HUNTSVILLE

LOADING CONSIDERATIONS FOR IMPLEMENTING FRICTION STIR WELDING FOR LARGE DIAMETER TANK FABRICATION

Prepared by:	Glynn Adams
Academic Rank:	Assistant Professor
Institution and Department:	University of Arkansas Mechanical Engineering Department
NASA/MSFC:	
Branch:	Metallurgical Research and Development
Division:	Metallic Materials and Processes
Laboratory:	Materials and Processing
MSFC Colleagues:	Robert J. Ding Clyde Jones

Introduction

The main objectives of the research presented here are to determine the reaction loads associated with friction stir welding (FSW) and to determine the suitability of an existing welding fixture for implementing this welding process in the fabrication of large diameter tanks. Friction stir welding is a relatively new process which is being investigated as a method for joining aluminum alloys. The aluminum-lithium alloy, Al-Li 2195, which is being used to fabricate the super-light-weight shuttle external tank has proven difficult to join using fusion techniques. Therefore, FSW and its potential applicability to joining Al-Li 2195 are of particular interest to NASA.

A schematic of the process as applied to welding an Al-Li 2195 butt joint is shown in Figure 1. The process will be described in reference to this type of weld. The main components required to conduct the friction stir weld include the pin tool, the anvil (backing bar) and the plates to be welded. The pin tool consists of a hardened steel tool with a large diameter shoulder and a smaller diameter threaded probe. The anvil is a flat, rigid steel plate. The aluminum plates which are to be joined are rigidly clamped to the anvil to prevent lateral movement and deflections relative to the anvil. The pin tool is rotated at approximately 300-400rpm and tilted at a lead angle of approximately 2.5 degrees to the plates. When the FSW process is initiated, the pin tool is not in contact with the plates. The pin tool is then plunged into the plates such that the trailing edge of the shoulder is approximately 0.006 inches below the top surface of the plates. The dimensions of the pin tool are such that in this position, the probe of the pin tool is approximately 0.002 inches above the top surface of the anvil. The friction stir weld is completed by traversing the weld seam at a travel speed of approximately 4 inches per minute.

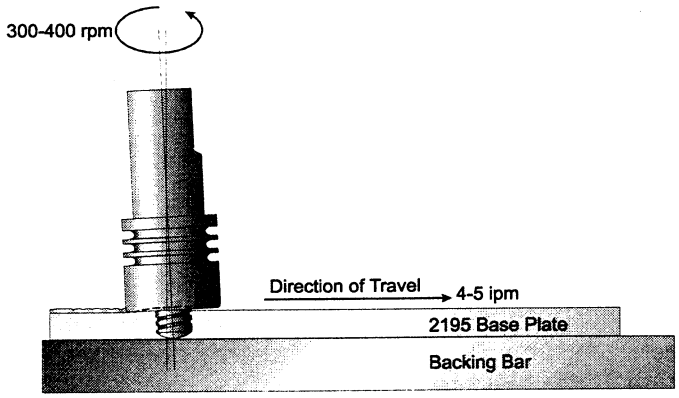

Figure 1 Schematic of friction stir welding process.

The exact mechanisms which define the friction stir welding process are not completely understood. However, FSW is best described in conventional processing terms as a combination of extrusion and forging. The threaded probe shears and plasticizes the material in the region near the probe. This plasticized material is extruded around the circumference of the probe and between the probe tip and the top surface of the anvil. This extruded material is then forged between the shoulder and the anvil as it reaches the heel of the shoulder.

There are several advantages of FSW as compared to fusion welds when applied to joining many aluminum alloys. The most significant of these is that FSW appears to be a solid state process. Although the material temperature increases to the point where the aluminum becomes plastic, it does not reach the melting point. The phase change which occurs with fusion welds of Al-Li 2195 cause problems in the resulting microstructure and tend to reduce the overall joint efficiency. Since FSW is a solid state process, some of these problems can be avoided. Other advantages of FSW are the limited number of process parameters which must be controlled, and the relatively minor amount of weld preparation which is required. However, there are also several disadvantages to the FSW process. These disadvantages include the key-hole which remains at the end of the weld when the pin tool is extracted, the reduced travel speed as compared to typical fusion welds, the tolerances with which the pin tool, weld material and anvil must be located relative to one another, and the tooling and fixtures required to react the forces produced during friction stir welding. The reaction loads and associated tooling requirements are addressed here. In a typical fusion weld, the welding head is not in direct contact with the workpiece and produces no reaction loads between the weld head and the workpiece. Therefore, the fixture for a fusion weld is required only to maintain the workpiece in its proper position and provide the needed movement of the weld head. However, the magnitude of the reaction loads between the weld head and the workpiece are significant in a FSW. These reaction loads cause deflections in the fixture which must be accommodated in the process control in order to maintain accurate location of the pin tool.

Reaction Load Measurement

A laboratory set-up was used to measure the reaction loads in a typical FSW butt joint. A 5-axis horizontal boring mill is the foundation for the set-up. An anvil was fabricated and fixed to the mill bed. The anvil is used to rigidly clamp plates configured in a butt weld position. The pin tool is held and rotated by the spindle while one of the mill axes is used to obtain the desired lead angle between the pin tool and the material. Two methods were used to determine the reaction loads during the welding process. An indirect measurement was established using measurements of the motor current for each axis of the mill. Load cells were used to establish calibration curves for converting current to force. The motor currents were measured during the weld process and converted to forces using the calibration curves. More recently, a rotating dynamometer was used to directly measure the reaction loads during the welds. The dynamometer serves as a tool holder and interfaces the pin tool with the spindle. The dynamometer is capable of directly measuring 4 separate loads, forces in the x,y,z directions and torque on the z axis. The z coordinate is collinear with the rotating axis of the dynamometer and measures the thrust load on the pin tool. The x and y coordinates provide a rotating reference plane whose normal is the z axis and are used to measure the transverse force in the direction of the weld seam. A typical set of measurements is shown in Figure 2. The absolute magnitude of the forces is not shown due to confidentiality agreements. However, the forces are accurately represented in a qualitative sense.

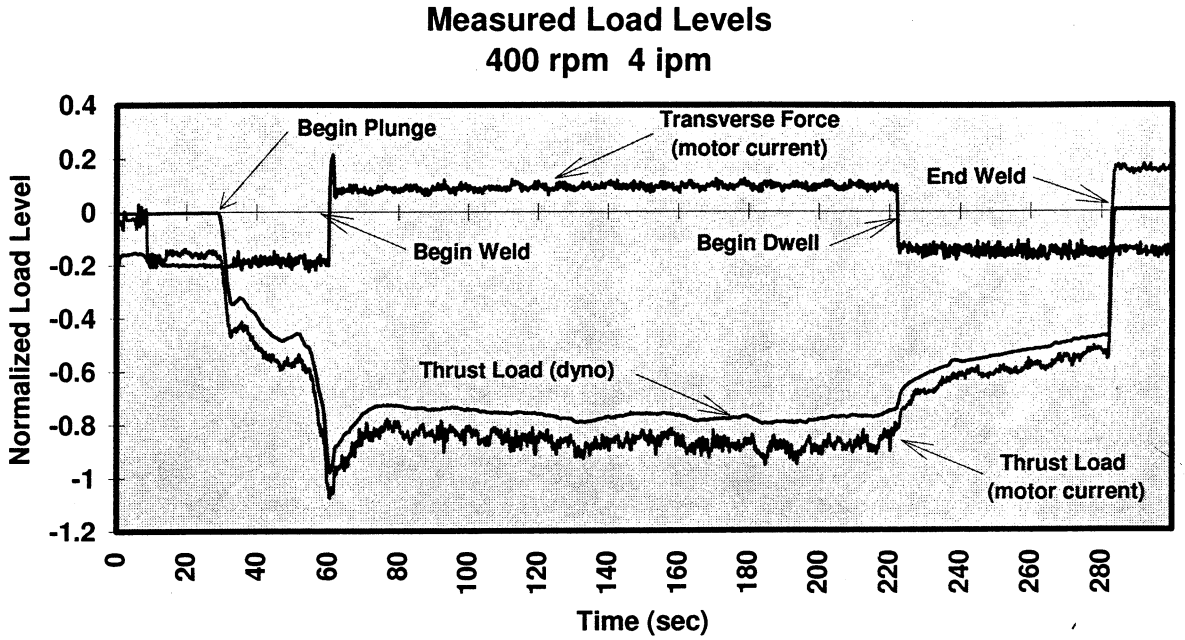

Good agreement was obtained between the indirect measurements using the motor currents and the direct measurements using the rotating dynamometer. This is significant in that it allows future analysis of motor current data which was acquired before the dynamometer measurements were available. The weld data plotted in Figure 2 begins with the pin tool initially at some offset distance from the material. At approximately 30 seconds the pin tool begins to plunge into the material. The magnitude of the thrust load reaches a maximum at the end of the plunge. The magnitudes of the transverse force along the weld seam and the thrust load on the pin tool remain essentially constant during the weld. At the completion of the weld, the pin tool is allowed to dwell for 60 seconds without traveling along the weld seam before it is extracted. This is not typical but was done in order to acquire data for development of models of the welding process.

The torque, not shown here, also remains essentially constant during the weld and decreases during the dwell period at the end of the weld. Depending upon the weld parameters, plots of the torque have demonstrated a combination of high frequency components superimposed on low frequency components. The source of these components is not currently understood.

Deflection Measurements

In order to implement the friction stir welding process for fabricating large diameter tanks, the effect of the reaction loads on fixtures and tooling must be determined. The current investigation involves modification of a vertical weld tool (VWT). The VWT is designed for

conducting longitudinal fusion welds of tanks ranging from approximately 8 feet to 14 feet in diameter and approximately 16 feet in height. This fixture was designed to support the articles being welded. It must be determined if the VWT can support the reaction loads associated with friction stir welding. The main load of interest is the axial thrust load directed along the pin tool axis. In order to successfully implement friction stir welding on the VWT, the fixture must be rigid enough to maintain the accurate positioning of the pin tool, weld material and anvil. Using the load measurements discussed above, design loads for implementing FSW were determined. Deflection measurements of the VWT were made using these design loads. The measurement technique and results are discussed here.

The VWT consists of several stanchions designed to locate and hold barrel sections of a tank for welding. A cylinder is fabricated by completing a succession of welds to join barrel sections. Four columns are located at the position where the barrel sections are joined. These four columns are designed to accurately locate the barrel sections while a fusion weld is conducted. The cross section of each column is the same and they are located symmetrically about the centerline of the weld. A plan view of the four columns, Figure 3, includes an observer tower located near the columns and a schematic of the loading arrangement used to obtain deflection measurements.

The implementation of FSW on the VWT requires a welding head to be mounted on a carriage which travels vertically on rails along the length of the two columns located on the south side. The carriage motion will be accomplished via two rails attached to the two columns on the south side. An anvil will be located across the two columns on the north side and will extend the length of the columns. The material to be welded will be located between the anvil and the welding head. A loading device was designed to simulate the reactions associated with this FSW implementation. A beam was attached across the two south columns, with the attachment points located at the proposed position for the FSW carriage rails. A load cell extends from this beam to an anvil attached to the two north columns. This load cell consists of a hydraulic actuator with pressure regulation capabilities. With this loading arrangement it is possible to simulate the thrust loads associated with the planned FSW implementation. The loading device was located at 5 separate positions vertically along the length of the fixture. At each position the fixture was loaded to 25%, 50%, 75% and 100% of the design load.

The main objectives of the measurements were to determine the relative deflection between the north and south columns at the weld seam and to determine the absolute deflection of the south columns near the proposed location of the carriage rails. Measurements of the relative deflections are important for determining the amount of position compensation which will be required by the weld head / carriage arrangement to successfully conduct FSW over the length of the fixture. The absolute measurements are important to determine if the columns are rigid enough to prevent the carriage drive mechanism from binding as it travels the length of the weld. In Figure 3, the circles indicate relative deflection measurement locations and the diamonds indicate absolute deflection measurement locations. All measurements were made with digital dial indicators accurate to within ± 0.00005 inches. The relative measurements were obtained by measuring the deflections between the north and south columns at the locations shown. The absolute deflections were obtained using the observer tower as a reference since it was unaffected by the loading.

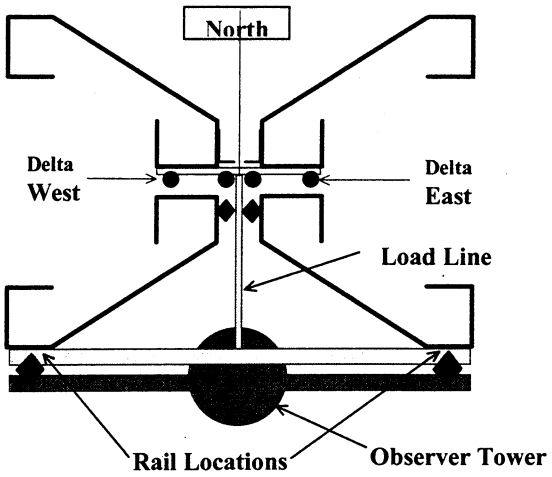

Figure 3 Plan view of the VWT weld station columns

The maximum absolute deflections of the south columns measured at the rail locations was 0.030 inches. In addition, the absolute deflections of the column located in the south west quadrant and the column located in the south east quadrant differed by less than 0.010 inches. The maximum relative deflection measured near the weld centerline was 0.047 inches. However, the relative deflection of the columns on the west side and the relative deflection of the columns located on the east side differed by as much as 0.030 inches. This difference may be difficult to accommodate during a friction stir weld. This difference in deflections is believed to be due to the fact that the top of the columns are joined by a bolted connection. A more rigidly designed connection may need to be designed to replace the existing bolted connection. With this modification, the measurements indicate that the fixture is adequate for conducting FSW.

Conclusions

The FSW process seems to have many advantages over typical fusion processes for joining aluminum alloys. However, the reaction loads associated with FSW must not be overlooked. The quality of the weld produced by FSW is directly dependent upon the accuracy with which the pin tool, material and anvil are positioned relative to one another. Small deflections in fixtures can have adverse affects on weld quality. Fixtures designed for fusion welds should be tested to determine their rigidity when modifications are planned for FSW implementation.

Acknowledgments

The following people contributed to the work presented here and deserve to be acknowledged: R. Jeff Ding, NASA, Marc Verhage, NASA, Richard Venable, LHMC, Pete Oelgoetz, Boeing, Pete Romine, Univ. of Alabama, A&M.

1997

NASA/ASEE SUMMER FACULTY FELLOWSHIP PROGRAM

MARSHAL SPACE FLIGHT CENTER

THE UNIVERSITY OF ALABAMA IN HUNTSVILLE

OPTIMIZATION OF SUPERCOMPUTER USE ON EADS II SYSTEM

Prepared By: Ardsher Ahmed
Academic Rank: Assistant Professor
Institution: University of Massachusetts Dartmouth
Department: Electrical and Computer Engineering

NASA/MSFC:
Office: AI41
Division: Information Systems

MSFC Colleagues: Amy S. Epps
Debby Bowerman

Introduction

The main objective of this research was to optimize supercomputer use to achieve better throughput and utilization of supercomputers. And to help facilitate the move non-supercomputing (inappropriate for supercomputer) codes to mid-range systems for better use of Government resources at Marshal Space Flight Center (MSFC). This work involved the survey of architectures available on EADS II and monitoring customer (user) applications running on CRAY T90 system.

The overall EADS II system is designed in a hierarchical fashion, with each higher level of the hierarchy designed to provide increased computing power or special computational facilities not economically justifiable at the desktop. As more speed, memory, and compute power is required, the user moves up the hierarchy.

EADS II Hardware configurations

a. **VMCS** - Virtual Memory Compute System
   SGI Power Challenge XL (8 processors, 1 GB memory, 87 GB RMDS)
   QIC 150 tape drive, 4mm DAT tape drive, 8mm DAT tape drive

b. **VPCS** - Vector Processor Compute System
   Cray T916/4-256 (4 processors, 256 MW memory,
   512 MW SSD, 170 GB RMDS)

c. **EDFS** - EADS DMF File Server
   Cray J916 (12 processors, 512 MW memory)
   510 GB disk
   8 STK tape drives

Performance Monitoring Tools on CRAY T90 & J90

All the CRAY platforms are loaded with hardware that can allow a user to monitor the performance of CRAY supercomputer while executing the code. The Cray Research Inc.'s publication "Guide to Parallel Vector Applications [1], includes a good number of decent performance monitoring and code tuning tools. Some of these useful tools are: HPM (Hardware Performance Monitor), ATExpert, flowview, jumpview, perfview, and perftrace, which are highly recommended for supercomputing.

Performance Monitoring on SGI Power Challenge XL

There is no performance monitoring tool available on the SGI platform. One can only obtain the elapsed, run, and system times of executables. There is no direct way to determine the throughput of the system in terms of Megaflops or MIPS.

Benchmark to compare the three systems

The matrix-multiplication algorithms was designed as a benchmark to compare system performance of CRAY T90, CRAY J90, and SGI. One of the objective was to achieve the "advertised" peak performance and other was to see the affects of migrating the code from high-end supercomputers (CRAYs) to mid-range supercomputer (SGI Power Challenge XL).

Scalar Algorithm:

```
do i=1,n
 do j=1,n
  do k=1,n
    C(i,j) = C(i,j) + A(i,k)*B(k,j);
 end do
 end do
end do
```

Vector Algorithm:

```
do i=1,n
 do j=1,n
   C(:,j) = C(:,j) + A(:,i)*B(i,j);
 end do
end do
```

Brief Results of Benchmark

On SGI, the Split-C algorithm (designed specially to handle stack size problems) gave the best run time for n=256 and up, followed by vector code. The reason for vector code not producing the best run time is due to the fact that SGI Power Challenge XL is not equipped with a vector-processor facility. The run times (in seconds) are:

n=256; real=1.1 , user=.73 , sys=.08 (split)
n=256; real=2.94, user=2.89, sys=0.03 (scalar)
n=256; real=2.56, user=2.47, sys=0.03 (vector)
n=512; real=2.7 , user=5.83 , sys=.21 (split)
n=512; real=32.85 , user=32.33 , sys=.14 (scalar)
n=512; real=21.46 , user=20.96 , sys=.15 (vector)
n=1024; real=28.07 , user=1:16.71 , sys=1.95 (split)
n=1024; real=27:30, user=21:53.04, sys=1.9 (scalar)
n=1024; real=3:24.25 , user=3:21.06 , sys=0.89 (Vector)
n=2*1024; eal=10:09.61 , user=9:59.78 , sys=2.36 (split)
n=2*1024; real 2:58:58.07, user 2:55:33.53,sys=12.40 (scalar)
n=2*1024; real=33:26 , user=1620 , sys=1.9 (vector)
n=3*1024; real=30:15.46, user=29:34.93 , sys=9.87 (split)
n=3*1024; real=10:03:22.77 ,user=9:59:55.13 ,sys=42.52 (scalar)
n=3*1024; real=1:39.50.04 , user=1:37:10.76 ,sys=19.61(vector)
n=4*1024; real=1:00:44.45 , user=1:53:32.11 ,sys=1:25.53(split)
n=4*1024; real=23:37:20.49,user=23:31:00.65 ,sys=1:34.23(scalar)
n=4*1024; real=3:38:57.95 , user=3:37:20.6 ,sys=42.85 (vector)

Run Times Statistics for Matrix-Mult Benchmark on CRAY J90

n=64; Mega Flops = 49 MFlops, Exec.Time = 1.3 mSec
n=128; Mega Flops = 135.7 MFlops, Exec.Time = 8.5 mSec
n=256; Mega Flops = 181.5 MFlops, Exec.Time = 45.75 mSec
n=512; Mega Flops = 191.99 MFlops, Exec.Time = 345.88 mSec
n=1024; Mega Flops = 193.93 MFlops, Exec.Time = 2.78 Sec
n=2048; Mega Flops = 194.73 MFlops, Exec.Time = 22 Sec
n=3072; Mega Flops = 195.04 MFlops, Exec.Time = 74.28 Sec

Statistics show that peak performance 195 Mega Flops (as opposed to peak advertised rating of 200 Mega Flops) is achieved which is saturated from the n=512 and up. The run times are from 1.3 ms to 74.28 seconds. These fast times are due to pipelining and vectorization on J90 (not available on SGI).

Run Times Statistics for Matrix-Mult Benchmark on CRAY T90

n=4096; 1.637 GFLOPS, VL = 127.97, t = 22.24 s
n=3072; 1.64 GFLOPS, VL = 127.97, t = 8.83 s
n=2048; 1.628 GFLOPS, VL = 127.95, t = 2.89 s
n=1024; 1.633 GFLOPS, VL = 127.89, t = 0.33 s
n=512; 1.607 GFLOPS VL=127.76, t = 46 ms
n=256; 1.475 GFLOPS VL=127.25, t = 12.63 ms
n=128; 1.011 GFLOPS VL=124.56, t = 2.67 ms
n=64; 0.267 GFLOPS VL=60.91, t = 0.22 ms

Statistics show that peak performance 1.64 Giga Flops (as opposed to peak advertised rating of 1.8 Giga Flops) is achieved which is saturated from the n=1024 and up. The run times are from 0.22 ms to 22.24 seconds. The T90 has achieved the speed up of up to 8 on this problem compared to J90 system. The Vector Lengths (VL) achieved are nearly ideal (peak VL=128). This shows that code is highly vectorized.

Customer Code Performance Analysis

Various application packages and user codes were analyzed on CRAY T90 during this research. Due to 5 page space limitation of this report it is not possible to include the performance statistics except for the MSC-NASTRAN which is a widely used application at MSFC. A benchmark was run at Johnson Space Center to compare J90 and SGI platforms. We extended this study by running same model on T90 machine. Following tables indicate the performance, vector lengths, run times, and analysis/comments.

TABLE 1
MSC-NASTRAN Performance Measurements on CRAY T90

Test case	Mflops	Vector Length	S/V Ratio	Elapsed Time (sec)	User CPU Time (sec)	Sys. CPU Time (sec)	Comment
test0	110.52	63.79	4:1	8448	1598.37	384.66	scalar code
	1.18	14.61	143:1	72	32.47	3.27	scalar code
test2b	1.03	14.67	49:1	20	5.62	0.68	scalar code
test2c	0.49	26.36	25:1	9	1.39	0.37	scalar code
test2d	0.37	32.95	23:1	8	1.2	0.39	scalar code
test2e	0.99	14.5	37:1	13	3.56	0.51	scalar code
test2f	1.02	14.06	38:1	14	3.97	0.52	scalar code

TABLE 2
Summary of Run Times for "test0" on 3 platforms

Time in (hr:min:sec)	SGI Power Challenge	CRAY T90	CRAY J90
Elapsed	1:43:11.72	2:20:48	5:46:1.46
User	1:23:42.39	26:29.37	1:57:50.92
System	12:44.47	6.24.66	11:19.27

Source: SGI Power Challenge and CRAY J90 data from report by Kevin Partins at JSC
CRAY T90 data compiled by running same model by A. Ahmed and Ric Moore (7/18/97).

Analysis of MSC-NASTRAN software

- The elapsed time is the most essential of all times as it is the turn-around time for the job. The SGI Power Challenge is faster than both CRAY systems!! SGI is 37 minutes faster than T90, and 4 hr 3 minutes faster than J90.

- The user time is best on T90 system due to fast I/O and memory banks but is overshadowed by T90's huge elapsed time. This may be due to the load on the T90 but depicts the realistic situation as the standalone CRAY T90 is almost impossible to find.

- The system times are pretty comparable from 6 to 12 minutes across all the three platforms.

- The vector lengths utilized and the scalar/vector (hold issue) ratios indicate that MSC-NASTRAN is predominantly a scalar code. It must be noted that the fortran90 compiler provides the best code vectorization capability and is strongly recommended for future releases.

- Based on this analysis, it is strongly recommendation that either:

  MSC-NASTRAN be rewritten and optimized in vector form to take full advantage of vector facility on CRAY platforms, or

  MSC-NASTRAN be migrated to the SGI Power Challenge system in its current version.

Conclusions and Recommendations

Most of the MSFC computing community is relying on the software developed by a third party code developer, to which they have no control over to modify or optimize. And most of this licensed software is written in FORTRAN 77 or FORTRAN IV without any vectorization or performance tuning for supercomputers. Basically it is "dusty-deck" software and no matter how powerful the supercomputer is it cannot speed up the code beyond a factor of 2, which can be attributed to a faster clock rate on CRAY T90. In order to attain the performance close to the peak one has to rewrite the code. Following are some of the recommendations for code developers and supercomputer users

- Just running a program on a supercomputer does not guarantee "supercomputing" performance
- Use best algorithm for solving a problem
- Optimize the code by hand (dependence analysis)
- Use compiler optimization flags
- Know the details of your Supercomputer hardware and limitations
- Use FORTRAN90 or HPF
- Use performance monitoring tools to tune the code for supercomputing

Acknowledgments: I would like to thank Dr. Jerry Karr, and my MSFC colleagues Ms. Debby Bowerman, Ms. Eppy Epps, Jerry Gray, Mike Knowels, Tom Brister, Ed Reske, Ric Moore, Ms. Vertayn Spencer, Ms. Vu, Ms. Patty Montgomery, who all contributed to my work and made my experience at MSFC an enjoyable one.

Reference:

[1] Guide to Parallel Vector Applications, SG-2182 2.0, Cray Research Inc. publication.

1997 NASA SUMMER FACULTY FELLOWSHIP PROGRAM

MARSHALL SPACE FLIGHT CENTER
THE UNIVERSITY OF ALABAMA IN HUNTSVILLE

STRUCTURAL MODELING OF THE NEXT GENERATION SPACE TELESCOPE'S PRIMARY MIRROR

Prepared by:

J. A. M. Boulet, Ph. D.
Associate Professor
Department of Mechanical and Aerospace Engineering and Engineering Science
University of Tennessee, Knoxville

MSFC Colleagues:

Max Nein(PS02)
Larry Craig (ED25)
Dave Jacobson (EJ31)

STRUCTURAL MODELING OF THE NGST

Introduction

In recent years, astronomical observations made with space telescopes have dramatically increased our understanding of the history of the universe. In particular, the cosmic Background Explorer (COBE) and the Hubble Space Telescope (HST) have yielded observations that cannot be achieved at ground-based observatories. We now have views of the universe before galaxies existed (from COBE) and views of young galaxies (from HST). But none of the existing observatories can provide views of the period in which the galaxies were born, about 100 million to one billion years after the "big bang." NASA expects the Next Generation Space Telescope (NGST) to fill this gap.

Although several preliminary designs have been proposed for the NGST, the current focus of NASA's effort is the design proposed in 1996 by a NASA team with members at Goddard Space Flight Center (GSFC), the Jet Propulsion Laboratory (JPL), and Marshall Space Flight Center (MSFC). This design is depicted in Figure 1. The salient features of the design are the inflatable sunshade (to keep the mirror's temperature at about 40 K), the large segmented primary mirror, the central mast supporting the secondary mirror, and the remaining optics and other instruments placed between the primary mirror and the sunshade. The primary and secondary mirrors, together with their supporting structures, are referred to as the optical telescope assembly (OTA).

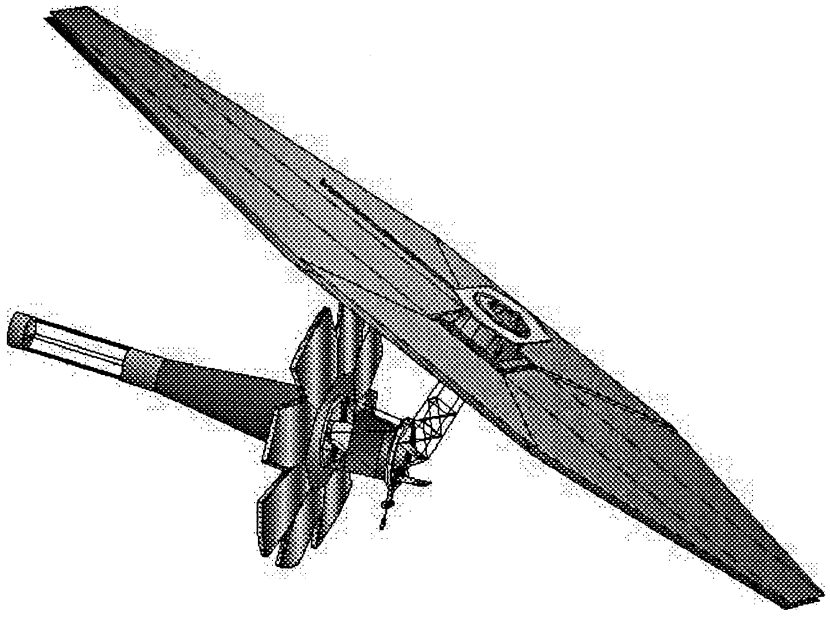

Figure 1. NASA (GSFC, JPL, MSFC) Preliminary design for the NGST.

Because the primary mirror, which is eight meters in diameter, is to be launched by an existing vehicle, the mirror cannot be made in one piece. In the current design, the mirror is made of nine segments. These include a central octagon, itself containing a central circular hole, and eight movable petals. For launch, four of the petals fold toward the front of the mirror and the other four fold toward the back, as shown in Figure 2. On orbit, the petals are opened and the mast holding the secondary mirror is extended, as seen in Figure 3. Each petal is supported by its own reaction structure, depicted in Figures 2 and 3 as a second layer of material in each petal.

Various materials have been proposed for the primary mirror, including beryllium, nickel, silicon carbide, and glass. The first three of these are sufficiently stiff so that the mirror portion of each petal need be supported only at three points. But a glass mirror would be so flexible as to require support at about 150 points per petal. In what follows, we discuss the ability of current modeling techniques to predict the behavior of a glass primary mirror.

Current structural models of the NGST primary mirror are based on the finite element method (FEM) and incorporate triangular, flat-plate elements. Models are analyzed with standard computer codes such as NASTRAN and EAL. The discussion below is focused on two specific aspects of what could be called, in general, validation of the models used in these codes. Are the models sufficiently accurate for the current design of the glass primary mirror? For what aspects of the glass design have the codes been validated? If the codes converge to some "best" analysis as the finite element mesh is refined, how accurate are the results of that "best" analysis?

The launch of any space telescope would be preceded by a program of testing, which would be used to validate (or invalidate) modeling. But successful validation through testing requires that the tests include measurements that can be used to assess the accuracy of all aspects of the modeling that have not been otherwise validated. Answers to the questions posed above are needed to insure that testing programs measure only that which needs to be measured.

Structural models of the NGST's primary mirror should accurately predict both stress and deformation. Accurate stress prediction is needed to prevent the loss of structural integrity. Accurate deformation prediction is needed to insure acceptable optical performance, which is characterized by waveform error. Optical modeling techniques predict this error using detailed predictions of the mirror's deformation. If the structural models do not accurately predict the deformation, the optical models may not accurately predict the optical performance. In that case, despite maintaining its structural integrity, a space telescope could be a failure. It follows that validation of the modeling, through testing or otherwise, should include validation of both stress and deformation predictions.

Two assumptions currently used in structural modeling of the NGST's primary mirror are (a) that shear deformation is negligible and (b) that deformation

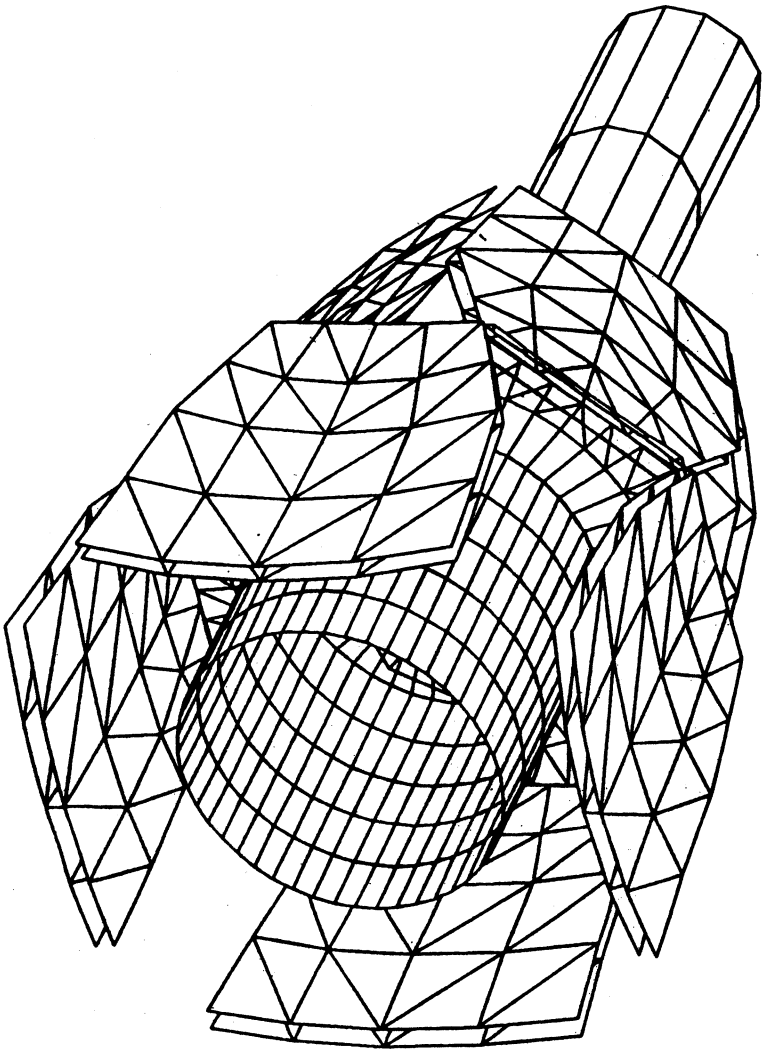

Figure 2. Launch configuration for the NGST's optical telescope assembly.

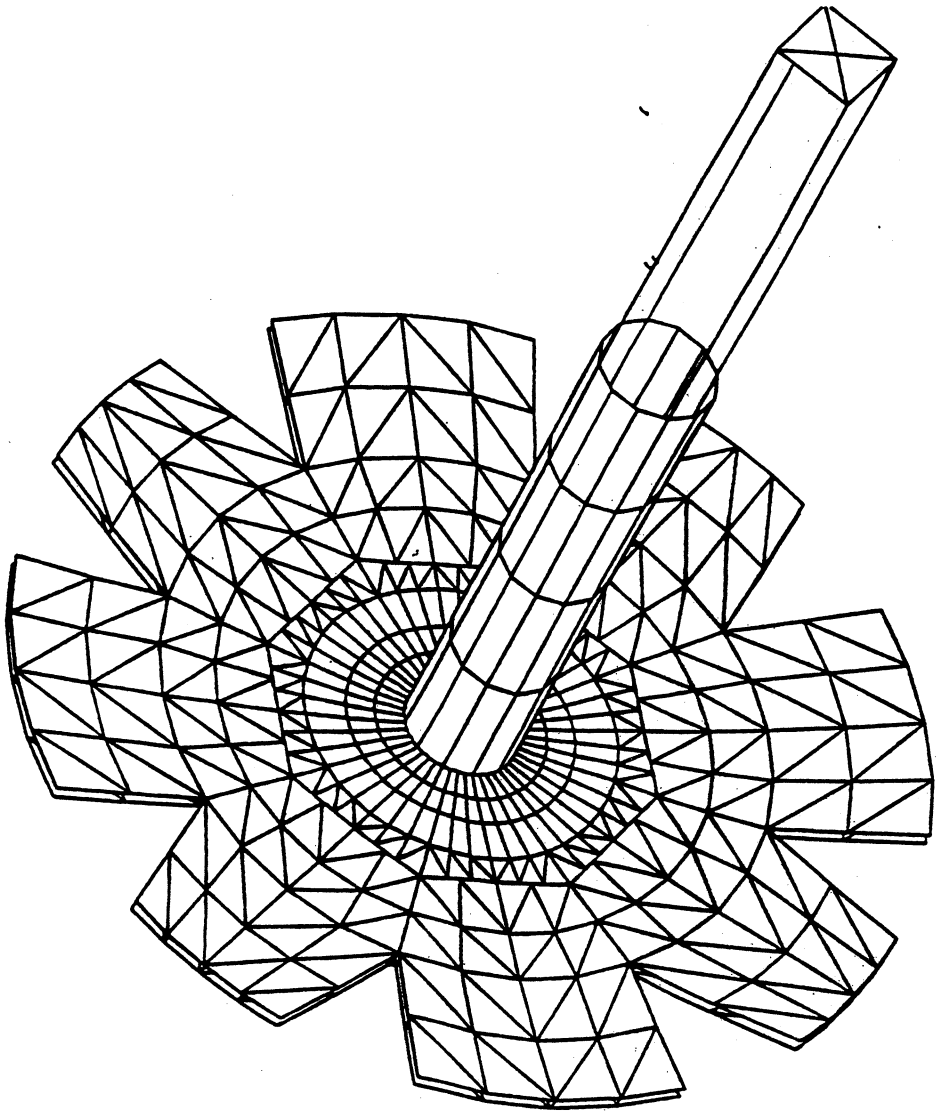

Figure 3. Deployed (on-orbit) configuration for the NGST's optical telescope assembly.

varies slowly with position over the surface of any petal. The validity of both these assumptions was investigated during the period covered by this report. The investigation began with a brief literature search, which revealed little documented work that would apply to these issues as manifested in the NGST mirror. This literature search continues.

Methodology

Lacking applicable previous work, we conducted a preliminary investigation of the two assumptions listed above by analyzing the simple models depicted in Figures 4 through 7. Each model is an infinite beam with equally spaced support loads. The support loads represent those that a mirror petal would experience on orbit.

In Figures 4 and 5, the support loads are developed in reaction to a uniformly distributed load applied to the beam. On orbit, such a load would not be present. Rather, the predominant loading experienced by the supports would be created by the mirror's tendency to deform in response to temperature gradients. If such gradients were small, the support loads would vary slowly over the surface of the petal. In that case, the deformation between the supports would be approximately the same as that for the model shown in Figures 4 and 5.

In Figures 6 and 7, the support loads are assumed to be developed in response to rapidly varying deformation of the mirror. For convenience, the support loads are taken to be equal in magnitude and alternating in direction. This could only occur in response to large temperature gradients.

Results

Elementary beam theory (no shear deformation) leads to deformation patterns illustrated in Figure 8. From the figure it is apparent that the peak-to-peak deformation expected for the model depicted in Figure 6 is about fifteen times larger than that expected for the model depicted in Figure 4. This indicates that the assumption of small temperature gradients is critical. If it is significantly in error, performance of the mirror may not be as expected.

When elementary beam theory is combined with well-known analysis of shear deformation, the deformation patterns for the two beam models are as shown in Figures 9 and 10. These figures indicate that shear deformation will not be significant provided the mirror thickness remains less than about one-tenth the spacing of the support loads. For the current glass design, this ratio is about 0.025. Hence, it is unlikely that shear deformation will be significant in the NGST's primary mirror.

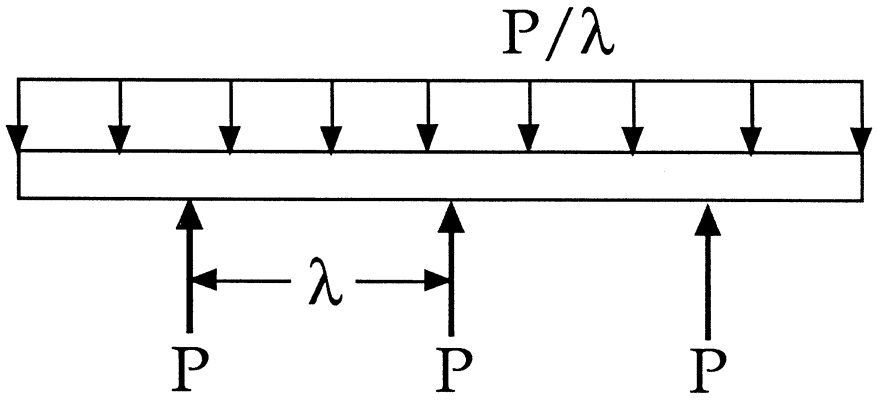

Figure 4. Infinite beam with uniformly distributed applied load and equally spaced supports.

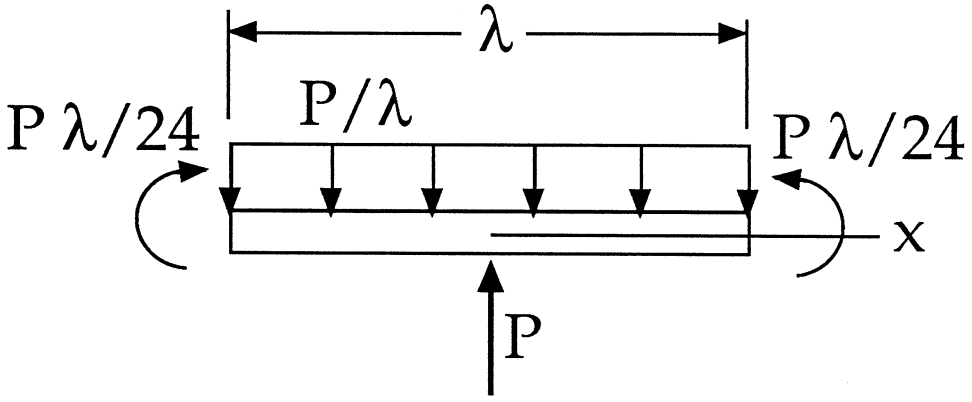

Figure 5. Free-body diagram of one wavelength of the beam depicted in Figure 4.

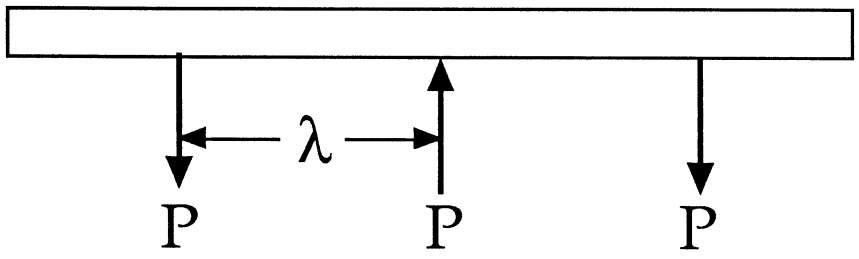

Figure 6. Infinite beam with no applied load and equally spaced, self-equilibrating support loads.

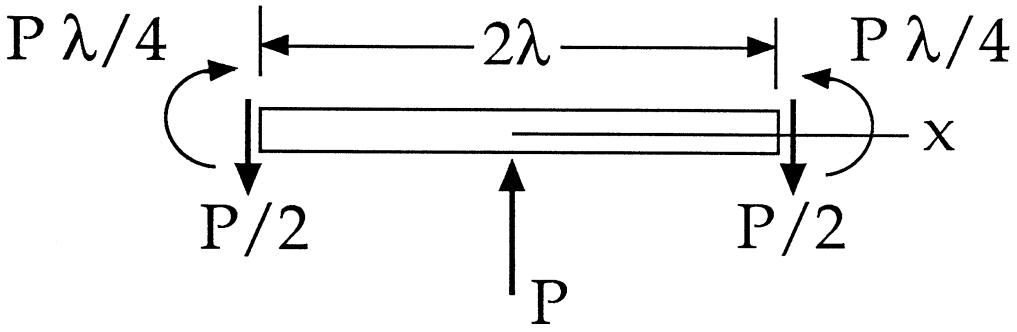

Figure 7. Free-body diagram of one wavelength of the beam depicted in Figure 6.

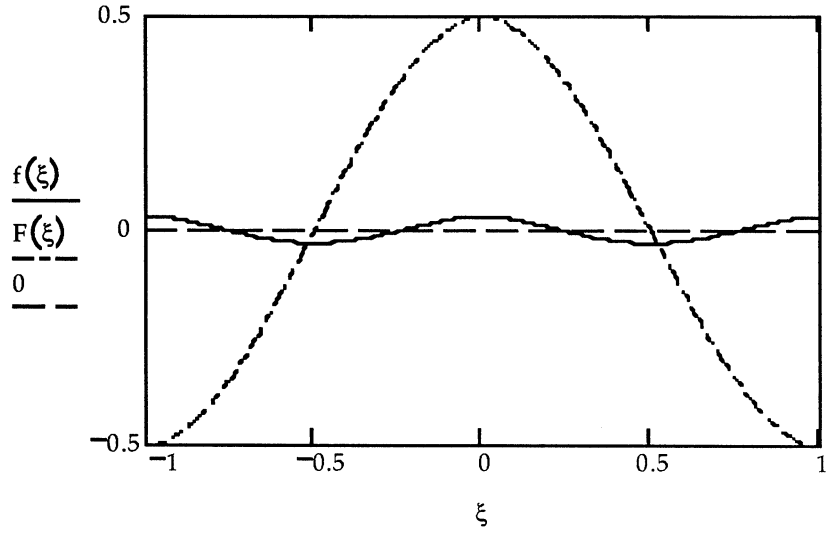

Figure 8. Normalized deflections of beams depicted in Figure 4 (solid line) and Figure 5 (nonuniformly dashed line), without shear deformation.

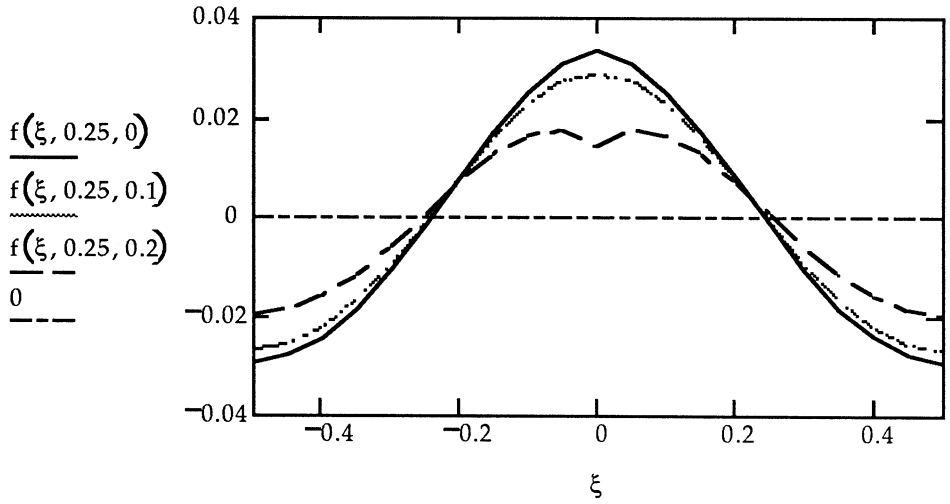

Figure 9. Effect of shear deformation on beam depicted in Figure 4. Poisson's ratio is 0.25. The ratio of the beam thickness to the spacing between the supports varies from zero (no shear deformation) to 0.2

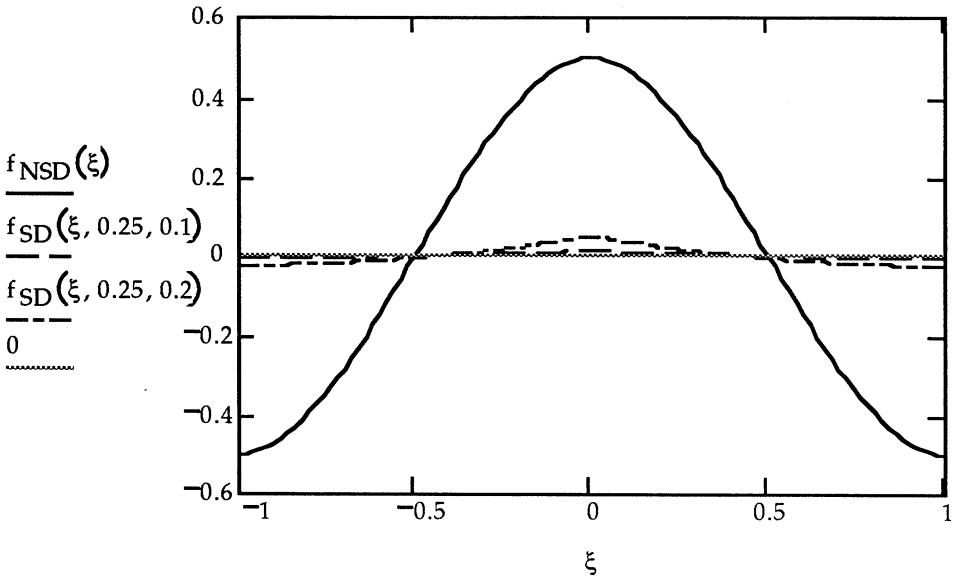

Figure 10. Effect of shear deformation on beam depicted in Figure 6. Poisson's ratio is 0.25. When the beam thickness is zero (solid line), there is no shear deformation. The dashed lines show the deformation that would be added to the solid line due to shear deformation when the beam thickness is 0.1 or 0.2 times the spacing of the support loads.

Conclusions

Although shear deformations is not likely to be significant in the NGST's primary mirror, the assumption of small temperature gradients is critical. If its validity cannot be verified, the current design should be pursued under the assumption that large temperature gradients may exist.

Acknowledgement

The author would like to acknowledge the kind assistance and cordiality of Max Nein (PS02), Larry Craig (ED 25), Dave Jacobson (EJ31), the entire ED25 branch, and the staff of the Summer Faculty Fellowship Program. Without their help, this work would not have been possible.

1997

NASA/ASEE SUMMER FACULTY FELLOWSHIP PROGRAM

MARSHALL SPACE FLIGHT CENTER
THE UNIVERSITY OF ALABAMA IN HUNTSVILLE

DATA COMPRESSION TECHNIQUES FOR ADVANCED SPACE TRANSPORTATION SYSTEMS

Prepared by: William G. Bradley, Ph.D.

Academic Rank: Professor of Electrical Engineering

Institution and Department: Western New England College
Department of Electrical Engineering

NASA/MSFC

Office: Astrionics Laboratory
Division: Computers and Data Systems

MSFC Colleague: Leann Thomas

Introduction

Advanced space transportation systems, including vehicle state of health systems, will produce large amounts of data which must be stored on board the vehicle and or transmitted to the ground and stored. The cost of storage or transmission of the data could be reduced if the number of bits required to represent the data is reduced by the use of data compression techniques. Most of the work done in this study was rather generic and could apply to many data compression systems, but the first application area to be considered was launch vehicle state of health telemetry systems.

A very large amount of information on data compression is available in journals, in books and on the Internet. The book Introduction to Data Compression (Sayood 1996) was used as an introduction to the broad field.

Both lossless and lossy compression techniques were considered in this study. Lossless data compression guarantees that no information is lost. This means that the original signal can be reconstructed from the compressed signal with no distortion. Lossy compression may introduce some distortion when the signal is reconstructed from the compressed version, but has the potential of much higher compression ratios (The ratio of the number of bits before compression to the number of bits after compression) than lossless compression when a small amount of distortion can be tolerated. "Lossless compression is generally used with "discrete" data such as text, computer generated data, and some kinds of image and video information" (Sayood 1996, p. 3) Lossy compression must be used very carefully, if at all, on signals where post processing techniques may be used to enhance the data. The post processing may "enhance" small differences between the original signal and the reconstructed signal (Sayood 1996, pp. 4-5). However, there are many applications where small differences between the original and reconstructed signals are acceptable. For example, in video and image processing small distortions are acceptable if they are not seen by the human eye, and lossy compression is usually used. Sensor data often starts as an analog signal, and the digitized signal is an approximation of the analog signal. Also, in many cases, the signal contains a significant amount of noise. The lossy reconstruction of a noisy signal may be better than the original if noise is removed.

Lossless Data Compression

Lossless Data compression techniques are subdivided into dictionary codes and entropy codes. There are several types of **dictionary codes**, but they all work by looking for repeating patterns or words in the data and assigning them special codes. Some applications that use dictionary codes include; 1) ZIP and PKZIP that are used to compress PC files and were tested on telemetry data as part of this study, 2) UNIX Compress algorithm, 3) GIF used to compress graphics images, and 4) V.42 used in modems. **Entropy codes** work by assigning short code words to the most common letters (or bit patterns in binary data), and longer code words to less common letters. The most common entropy code is the Huffman code. It gives optimum results if the statistics of the data are known is advance. Unfortunately the statistics of scientific data are seldom known in advance. There are adaptive Huffman codes that adapt to the statistics of the data, but the code trees get very cumbersome if the alphabet is large. Arithmetic coding is

another type of entropy coding that has become increasingly popular recently (Sayood 1996, Ch. 4). The entropy code that was given the most attention is this study is the Rice algorithm.

Rice Algorithm

The Rice algorithm was initially developed by Robert Rice at JPL (Rice et el. 1971, 1991). A research group at Goddard Space Flight Center, including Pen-Shu Yeh, refined the algorithm, and called it "Universal Source Encoding for Space" (Yeh and Miller Dec. 1993). It was shown to produce optimum code for the special case of Laplacian distributed data (Yeh et al. Oct. 1993). The Rice Algorithm has been adopted as a standard for space data systems (Consultative 1995). It is highly adaptive and suitable for real time high speed applications. The algorithm has been implemented in a chip called USES (Universal Source Encoding for Science Data) that is available from the Microelectronics Research Center at the University of New Mexico (MRC 1997). This chip has been used on several space missions.

Software called 'szip' that simulates the USES chip can be downloaded from the Microelectronics Research Center web site (MRC 1997). It was downloaded along with some sample test data. When szip was used to compress the sample test data, the results were identical to those given on the web site. The only discrepancy was that it was observed that the seismic data had been zero padded with about ten thousand zeros, and when the zeros were removed the compression ratio dropped from 1.97:1 to 1.68:1.

The Rice algorithm consists of a predictor, a mapper, and an entropy coder. Any prediction algorithm could be used with the Rice Algorithm, but the USES chip and the szip software use a simple nearest neighbor predictor. The mapper maps the output of the predictor into the standard format required by the entropy coder. The standard format requires that the data must be all positive integers with zero the most probable integer and the probability of occurrence of other integers must decrease with their magnitude. If adjacent samples of the data are correlated, use of the predictor improves the compression ratio. However, if adjacent samples are uncorrelated, use of the predictor decreases the compression ratio, and better results are obtained by bypassing the predictor. If the predictor is by passed, the user must provide his own algorithm to map the data into the standard format required by the entropy coder. The data is divided into blocks and each block is coded with up to 8 different coding options. The option that yields the highest compression ratio is chosen for that block of data. The default block size is 16, but other block sizes may yield higher compression ratios for some types of data.

Lossy Compression with Wavelets

The wavelet transform is an invertable transform (Rioul and Vetterli 1991, Strang and Nguyen 1996) However, losses may occur due to computational accuracy and quantization of the wavelet coefficients. Wavelet compression is possible because of the relative scarceness of the wavelet domain representation of the signal. This allows compression of the wavelet coefficients because the original signal can be approximated by a small number of approximation coefficients at an appropriate level and some of the detail coefficients with the rest of the detail coefficients set to zero (Misti et al. 1996 p. 6-86).

The wavelet computations in this sturdy used the MATLAB Wavelet Tool Box and the 1-D Graphical Tool. (Misti et al. 1996). Use of the Graphical Tool made it possible to try many different wavelets at different levels in a short time. However, implementation of wavelet compression will require work with the details that MATLAB performs automatically.

Engine Data Test Results

The first test of the compression algorithms was on state of health telemetry data from the DC-XA that was recorded by Lisa Blue. Of the many variables recorded, a rocket engine vibration trace was chosen for initial testing. This trace was chosen because its sampling rate of 12,000 samples per second was the highest of the available data, and it appeared to be 'noise like' data and was thought to be the hardest to compress. Unfortunately, after most of the testing was done, it was determined that the trace contained only every third sample of the original data. This means that it was the engine vibration data used was effectively sampled at 4000 samples per second. It is believed that the compression ratios would have been somewhat higher if all of the samples had been available. A subset of 32,768 samples from the test was used to obtain the results shown in table 1. When using the Rice Algorithm with the predictor, 128 was added to all samples to make the data positive integers as required by the szip software. When the Rice Algorithm was used without the predictor, a program was needed to map the data into the standard format required by the entropy coder. A MATLAB m-file was written and used as the mapper. When using the Rice Algorithm, the block size is a variable. The default block size is 16, but for some cases, block sizes of 8 and 4 were tried. When using wavelets, the wavelet coefficients were quantized to 8 bits and coded with the Rice Algorithm and PKZIP. The coefficients were then thresholded at two different levels and then coded with the Rice Algorithm and PKZIP. Space limitations do not permit including the original and reconstructed waveforms, but they are in a Power Point presentation that is available from the author at wbradley@wnec.edu. Wavelet Packet Analysis was also tried on this data. However, the considerable extra complexity of the Wavelet Packet Analysis does not appear to be justified by the very small increases in the compression ratio that were obtained.

	Original Data	**Wavelet Coef**	**Thresholded Coef 90.1% Retain En 80.1% Zeros**	**Thresholded Coef 85.1% Retain En 85.1% Zeros**
Rice With Predictor	**1.21**	**1.24**	**-**	**2.91**
Rice (WO pred) Block Size 16	**1.22**	**1.40**	**2.88**	**3.24**
Rice (WO pred) Block Size 8	**-**	**1.37**	**2.89**	**3.38**
Rice (WO pred) Block Size 4	**-**	**-**	**2.93**	**3.48**
PKZIP	**1.22**	**1.34**	**3.92**	**5.02**

Table 1 Compression Ratios for Engine Data

The compression ratios in table 1 are relatively modest. However, this is believed to be a worst case example, and the compression ratios should be higher for most other data. The fact that PKZIP did significantly better that the Rice Algorithm when coding the wavelet coefficients indicates that there probably are better lossless algorithms than the Rice Algorithm for coding the wavelet coefficients.

Other Data from DC-XA

In addition to the engine vibration data, one temperature, one pressure and one strain trace from the DC-XA test were obtained. Not much time was available for analyzing this data, but a few results were obtained. The 8 bit pressure data was compressed with the Rice Algorithm resulting in a compression ratio of 1.26:1 and with PKZIP resulting in a compression ratio of 1.31:1. When a 1024 byte subset of the pressure data was analyzed with the MATLAB 1-D Compression Tool, 97.52% of the coefficients were zeroed. However, not enough is known about the actual pressure to tell whether the high frequency fluctuations that were removed by the wavelet compression are noise or actual pressure fluctuations.

AR&C Data Test Results

Data from an AR&C (Automatic Rendezvous and Capture) system simulation and some unfiltered sensor data was obtained from Richard Dabney. The data was state of health information from an automatic docking system. This was relatively slowly varying data that was sampled at 20 samples per second and stored as floating point numbers. The Rice algorithm was not used on this data because it would require that the data be scaled and converted to integer form. However, the MATLAB Wavelet Tool Box was used to analyze the data.

Three separate signals were analyzed. Each signal contained 7,989 data points. Several different wavelets and different levels of decomposition were tried on each signal. The exact wavelet used and level of decomposition was not very critical, but it was found that the Daubechies 3 or 5 wavelets at levels 7 or 9 worked as well as any that were tried. The first two traces were from a simulation and contained little noise.

- The first signal was a relative distance measurement. When compressed using the Daubechies 5 wavelet at level 7, 99.04% of the coefficients were zeroed while retaining 99.06% of the signal energy. The second was a differential distance measurement. When compressed with the Daubechies 5 wavelet at level 9, 99.5% of the coefficients were zeroed while retaining 99.49% of the signal energy. In both cases the reconstructed signal appeared to be an excellent approximation to the original signal.
- The third signal to be analyzed was very interesting because it was unfiltered altitude sensor data that contained a significant amount of noise. When compressed with the Daubechies 3 wavelet at level 7, 98.87% of the coefficients were zeroed while retaining 98.7% of the signal energy. **When the signal was reconstructed, almost all of the noise was removed.**

It is believed that a code other than the Rice algorithm should be used to code the wavelet coefficients when most of the coefficients have been zeroed. Perhaps an identifier tag could be added to the coefficients that are retained, and the zeros not transmitted.

Conclusions

1) Lossless compression with the Rice Algorithm gives modest compression ratios.
   - Compression ratios of only about 1.2:1 to1.3:1 were obtained with the Rice Algorithm on the data tested. Somewhat higher compression ratios would be possible if the data had more correlation between samples.
   - It is not clear whether or not the relatively small amount of compression is enough to justify the extra complexity that would be required to handle the varying word length, and possible error propagation due to the lossless coding.
   - PKZIP did as well or a little better than the Rice Algorithm.
2) Wavelet compression should be considered for higher compression ratio.
   - Compression Ratios of 3:1 to 5:1 were obtained on the engine vibration data with 85% of the coefficients zeroed.
   - 98.9 to 99.5% of the coefficients were zeroed with the AR&C (autodock) data.
   - Most of the noise was removed from a noisy AR&C signal.
   - Two dimensional wavelet analysis could be tried as has been used successfully with seismic data (Aware 1997)
   - Much additional study of wavelet compression is needed including more testing and better methods of coding wavelet coefficients.

References

Aware Inc. (1997), SeisPact Wavelet based Seismic Data Compression, http://www.aware.com/

Consultative Committee for Space Data Systems (1995), Universal Source Coding for Data Compression, CCSDS 121.0-R-1 RED BOOK, Nov. 1995.

Rice, R. F., and Plaunt, J. R. (1971), "Adaptive Variable Length Coding for Efficient Compression of Spacecraft Television Data", IEEE Transactions on Communication Technology, vol.COM-19 part 1, Dec. 1971, pp. 889-897

Rice, R. F., Yeh, P. S. and Miller, W. (1991), Algorithms for a Very High Speed Universal Noiseless Coding Module, JPL Publication 91-1, 1991.

Rioul, O. and Vetterli, M. (1991), "Wavelets and Signal Processing", IEEE Signal Processing Magazine, Oct. 1991, pp. 14-38.

Sayood, K. (1996), Introduction to Data Compression, Morgan Kaufmann Publishers, Inc., San Francisco CA

Strang, G. and Nguyen, T. (1996), Wavelets and Filter Banks, Wellesley-Cambridge Press, Wellesley MA.

Microelectronics Research Center (MRC, 1997), Web Site 'http://www.mrc.unm.edu'

Misti, M., Misti, Y., Oppenheim, G. and Poggi, m. (1996), Wavelet Tool Box for use with MATLAB, The Math Works, Inc., Natic MA

Yeh, P. S., Rice, R. F. and Miller, W. H.(Oct. 1993), On the Optimality of Code Options for a Universal Noiseless Coder, revised version, JPL Publication 91-2, 1991, a shortened version in Proceedings of the AIAA computing in Aerospace 9 Conference, San Diego, CA, Oct. 19-21, 1993.

Yeh, P. S. and Miller, W. H. (Dec. 1993), Application Guide of Universal Source Encoding for Space, NASA Technical Paper 3441, Dec. 1993.

1997

NASA/ASEE SUMMER FACULTY FELLOWSHIP PROGRAM

MARSHALL SPACE FLIGHT CENTER
UNIVERSITY OF ALABAMA
IN HUNTSVILLE

ROCKET PROPELLANT DUCTS :
(cryogenic fuel lines)
FIRST CUT APPROXIMATIONS AND DESIGN GUIDANCE

Prepared by: William V. Brewer, Ph.D.

Academic Rank: Professor

Institution and Department: Jackson State University, School of Science & Technology, Technology

NASA/MSFC:

Office: Propulsion Laboratory
Division: Propulsion and Mechanical Systems
Branch: Mechanical Systems Design

MSFC Colleagues: Lance Moore, Tim Ezell

INTRODUCTION

Problem: The design team has to set parameters before analysis can take place. Analysis is customarily a thorough and time consuming process which can take weeks or even months. Only when analysis is complete can the designer obtain feedback. If margins are negative, the process must be repeated to a greater or lessor degree until satisfactory results are achieved. Reduction of the number of iterations thru this loop would beneficially conserve time and resources.

Task: Develop relatively simple, easy to use, guidelines and analytic tools that allow the designer to evaluate what effect various alternatives may have on performance as the design progresses. Easy to use is taken to mean closed form approximations and the use of graphic methods. Simple implies that 2-d and quasi 3-d approximations be exploited to whatever degree is useful before more resource intensive methods are applied. The objective is to avoid the grosser violation of performance margins at the outset.

Initial efforts are focused on thermal expansion/contraction and rigid body kinematics as they relate to propellent duct displacements in the gimbal plane loop (GPL). Purpose of the loop is to place two flexible joints on the same two orthogonal intersecting axes as those of the rocket motor gimbals. This supposes the ducting will flex predictably with independent rotations corresponding to those of the motor gimbal actions. It can be shown that if GPL joint axes do not coincide with motor gimbal axes, displacement incompatibilities result in less predictable movement of the ducts.

OBSERVATION

Pierced Ear Principle: Violation of this principle guarantees that for combined rotations of the motor about both gimbal axes, joint and gimbal axes will not coincide thus defeating the purpose of the GPL. This principle has been used in the past [1] but is not generally recognized in the design community. The principle may be stated as follows:

The axis of the GPL joint attached to the motor must be coincident with the axis piercing the ears of the gimbal conjugate that attaches to the motor.

The axis of the GPL joint closest to the vehicle must be coincident with the axis piercing the ears of the gimbal conjugate that attaches to the vehicle.

In the absence of compelling reasons to the contrary this principle is a reasonable candidate for a design guideline (or rule of thumb).

That GPL performance does not always conform to expectations has been noted by practitioners with the result that a third joint in a line perpendicular to the gimbal plane is usually included to allow for thermal expansion and manufacturing imprecision. If the "as-built" GPL configuration succeeds in achieving coincident joint and gimbal axes, this will not be the case over the entire operating temperature range. Rocket motors experience temperatures in negative hundreds of degrees F. in their cryogenic propellant conduits contrasting with combustion chamber temperatures in thousands of degrees F.

APPROXIMATION MODELS

Sample calculations and coordinate system used in the following discussion are for the PT AI 60K Engine [2]. The x-y plane passes thru the gimbal axes and is the plane intended for the GPL.

To explore thermal effects on the GPL configuration, the 3 joints mentioned above are examined 2 at a time in planes parallel to the 3 coordinate planes (Figure 1). This was done graphically with the assistance of an AutoCad package. Results thus achieved are superposed as a measure of dimensional incompatibility that must be resolved by the 3-d, 3 joint space linkage. MathCad software was used for this purpose and gimbal rotations were included in addition to the thermal expansion estimate. Results of sample calculations (Figure 2) are superposed for the extreme articulations of the motor gimbals (+/- 5 degrees). Where estimates in 2 planes are based on thermal expansion of the same pipe lengths the results are averaged; where based on different lengths they are simply added. Results for this example indicated that thermal expansion has a relatively greater impact than does gimbal rotation thru a small angle. Thermal effects were, in this case, based on gross aggregations of temperature distribution. Larger rotations can be explored using the model. Extent and source of problems may be estimated on a comparative basis with experience of the user.

A 4th 2-d plane passing thru the three joints may also be of value (Figure 3). Assume 3 ball joints where the terminal joints #1 and #3 have a conjugate attached respectively: joint #1 to the motor; and joint #3 to the vehicle frame. Then the locations of these joints are known. The other conjugates of Joints #1 and #3 are attached to the 2 links which span the distance between them. The links are connected by the middle joint, #2. If the middle joint were broken then the free end of each link could move on a spherical surface the radius of which is the length of the link. The circle representing the intersection of the 2 spheres is the domain of possible locations of the middle joint. The circle also may be visualized as the intersection of 2 cones whose elements are the length of the links. A plane passed thru the 3 joints sees the intersecting cones as triangles. As thermal expansion and/or gimbal rotation changes, the center locations and radii of the spheres change with a corresponding change in the triangular intersections. Comparing these changes with the as-built images gives a measure of the accommodation necessary from the linkage in 3-d.

RESULTS

In the example where these methods were applied to the PT AI 60K engine GPL, results indicate relatively small perturbations coming from the +/-5degree gimbal rotations compared with those caused by thermal expansion.

CONCLUSIONS

Where as in the example thermal effects dominated the results, other designs in which larger gimbal rotations are used may produce a significantly different result which may be quantified with the methods outlined here.

Thermal effects amplify distortions caused by gimbal rotation by moving joints in the Gimbal Plane Loop away from the gimbal plane.

Pierce Ear Principle is generally a very inexpensive precaution that should be observed by the design community in practice, absent any compelling need to the contrary.

ACKNOWLEDGEMENTS

I would like to thank my mentors for all the assistance rendered, especially in providing appropriate background literature and making comfortable and convenient work space available with all the required utilities.

REFERENCES

[1] **Liquid Rocket Lines, Bellows, Flexible Hoses, and Filters**, NASA Space Vehicle Design Criteria (Chemical Propulsion), NASA SP-8123, April 1977, p.83, Figure 41.

[2] "PT AI 60K Engine Interface Control Drawing", No. 96M30760, Code 14981, MSFC/NASA Huntsville AL, 6/97.

SUMMARY OF RESULTS

COMBINATIONS of THERMAL EXPANSIONS and EXTREME GIMBAL ROTATIONS in 3 COORDINATE PLANES

NOTE : Multiple estimates of a quantity based on a thermal expansion of the same length of pipe are averaged. Multiple estimates of a quantity based on a thermal expansion of different lengths of pipe are added.

NOTE : 1st index identifies x - rotation ; 2nd index identifies y - rotation.
+ indicated by 1 ; - indicated by 2 .

positive x-rotation positive y-rotation	positive x-rotation negative y-rotation	negative x-rotation positive y-rotation	negative x-rotation negative y-rotation
$\Delta Xa_{11} = 0.363$	$\Delta Xa_{12} = 0.363$	$\Delta Xa_{21} = 0.517$	$\Delta Xa_{22} = 0.517$
$\Delta Ya_{11} = 0.412$	$\Delta Ya_{12} = 0.441$	$\Delta Ya_{21} = 0.453$	$\Delta Ya_{22} = 0.482$
$\Delta Za_{11} = 0.097$	$\Delta Za_{12} = 0.111$	$\Delta Za_{21} = 0.108$	$\Delta Za_{22} = 0.122$
Vector Sum of Displacement Incompatibilities :			
$\Delta Ra_{11} = 0.558$	$\Delta Ra_{12} = 0.582$	$\Delta Ra_{21} = 0.696$	$\Delta Ra_{22} = 0.718$

Figure 2: Example Results for 2-D Approximations of Dimensional Incompatibility

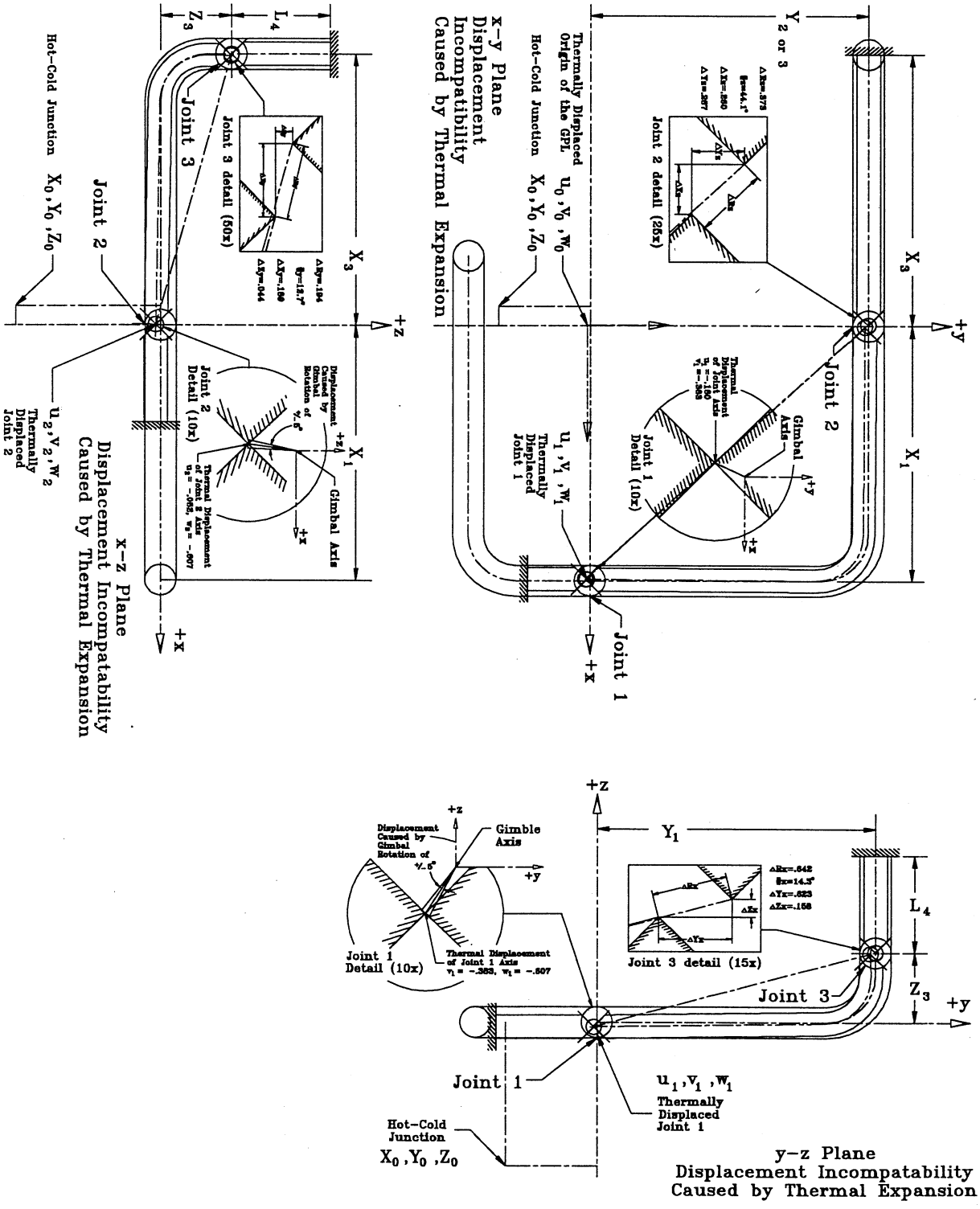

Figure 1:

Displacement Incompatibility Caused by Thermal Expansion

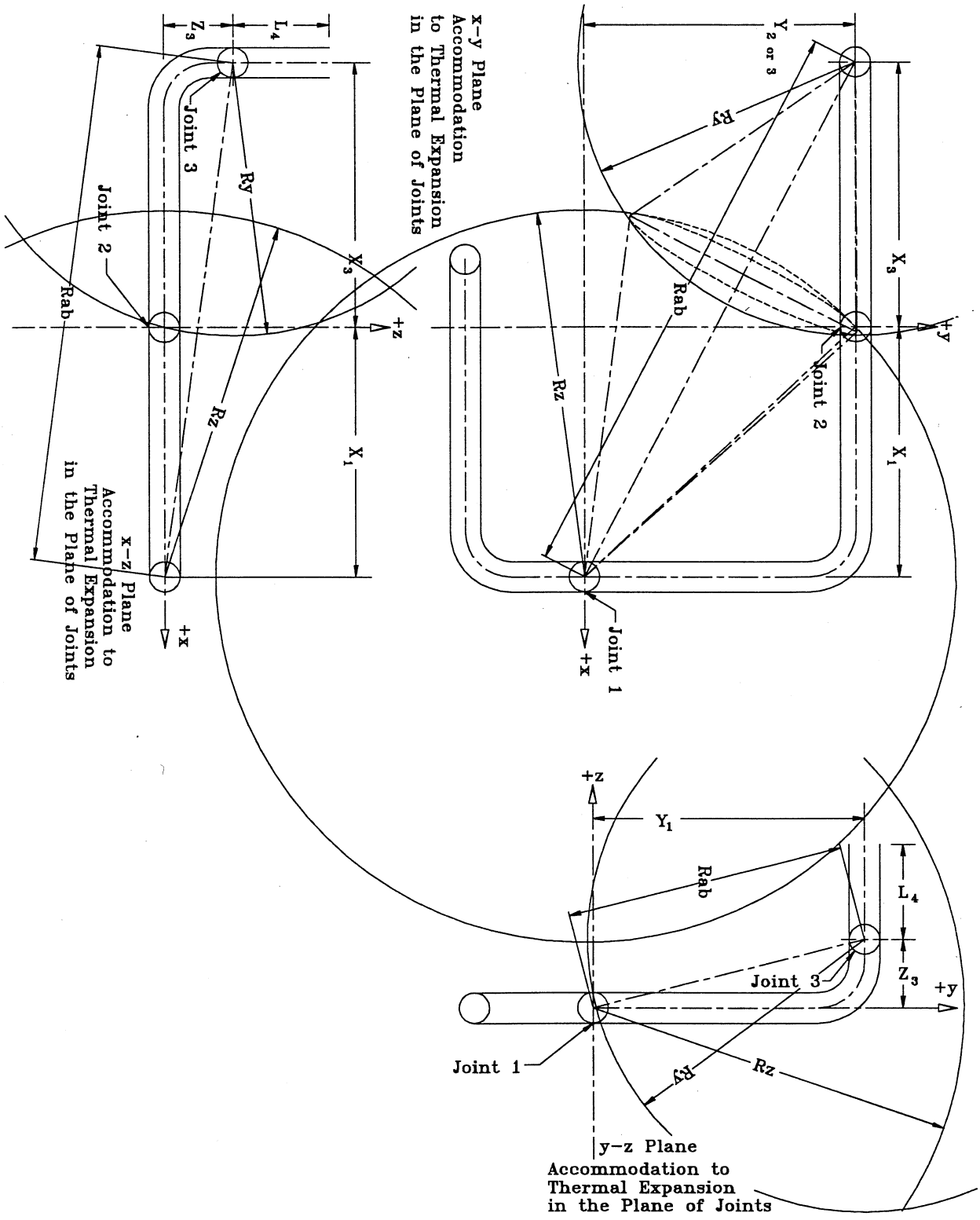

Figure 3:
Accommodation to Thermal Expansion in the Plane of Joints

1997

NASA/ASEE SUMMER FACULTY FELLOWSHIP PROGRAM

MARSHALL SPACE FLIGHT CENTER
THE UNIVERSITY OF ALABAMA IN HUNTSVILLE

SOLIDIFICATION OF DROPS

IN THE MSFC DROP TUBE

Prepared by:	Lucien N. Brush
Academic Rank:	Associate Professor
Institution and Department:	University of Washington Department of Materials Science and Engineering
MSFC Colleague:	Peter Curruri

Solidification of Drops in the MSFC Drop Tube

Professor Lucien N. Brush
Department of Materials Science and Engineering
University of Washington
325 Roberts Hall, Box 352120
Seattle, WA 98195

I. Abstract

Silver drops (99.9%, 7 mm diameter) were levitated, melted, and released to fall through the Marshall Space Flight Center's 105m drop tube in an He-6%H atmosphere at 170 degrees superheat. The extent of solidification during the ~4.6s of free fall time prior to impact was measured experimentally and computed numerically using a newly developed solidification heat transfer model. Comparison of the experimental observation of the fraction of liquid transformed with the numerical solutions showed reasonable agreement. Possible modifications of the model, in an attempt to close the gap between the experiment and the model comparison are discussed.

II. Introduction

The intent of this work is to investigate solidification behavior in "bulk" spheres, i.e. those having diameters greater than 1mm. An experimental study of drop solidification necessitates the sample to be free of a container. This constraint can be relaxed by levitating the sample in an electromagnetic field or, as utilized here, by letting it free fall a significant length through a controlled environment, i.e. a drop tube. Many studies have utilized drop tubes to investigate various aspects of solidification phenomena and processing. (See [1-3] and references therein.)

Szekeley and Fischer [4] among others [5,6] have numerically studied a simple model of the solidification behavior of pure materials with radiation as the transport mechanism for heat outward through the surface of the solidifying shell. McCoy et al. [7,8] simultaneously solved the dynamical equations for drop position and velocity in order to provide an approximate value of the heat transfer coefficient at the surface of an isothermal drop as a function of the drop time, or distance covered, during free fall. Their results showed that the amount of microgravity time the drop actually experienced was very short. In addition, allowance was made for the influence of heat transfer on solidification.

The goal of this work is to present experimental observation showing the extent of solidification of a liquid Ag sphere of diameter 7mm and 170 degrees (K) superheat, and to correlate this finding with the solution to a model of droplet solidification during free fall. The details of the heat flow and the dynamics of the interface motion within the sphere, as well as the external environmental influence on the convective heat transfer adjacent to the sphere surface, are explicitly included in the numerical procedure. By comparing the experimental results with theory, insight into the

important physical parameters affecting the solidification microstructure of drops can be illuminated.

III. Experimental Procedure

Ag shot (99.9% purity) was weighed with the intent of producing a 7mm diameter spherical drop [1-3]. The shot was placed in a graphite crucible and melted with the aid of an hydrogen torch. The subsequent sample was generally shiny and oblately spherical in appearance. The sample was placed in a pedestal in the bell jar atop Marshall Space Flight Center's 105 meter drop. After a mixed He - 6% atmosphere was established within the tube, at an overall pressure of ~690 torr, the individual sample was raised within the coil of an electromagnetic levitator (EM). A two color pyrometer continually recorded the temperature of the levitating sample. The thermal arrest which was observed during melting of the Ag (T_M = 1233.8K) sample served as a calibration reference. After melting, the sample oscillated slightly and proceeded to heat at a rate of ~60K/s. Once a preset superheat temperature was reached power to the coil was automatically cut and the sample fell the length of the tube; the dropped sample was retrieved after the run. Review of the temperature versus time plot shows the release temperature to be within ±5K of that stated. Finally as indicated by the purity of the Ag used, no attempt was made to promote undercooling during free fall, and no recalescence was observed. The physical state of the 7mm drop was found by an examination chunks of solid pieces retrieved after impact. The sample dropped with little if any supercooling in the liquid prior to solidification.

IV. Model Development

A numerical procedure is developed to solve equations governing heat transfer within the drop, heat transfer from the drop to the surrounding medium and the kinetics of solidification within the drop. After release of the molten drop, it is assumed the sample remains a sphere of radius R_{out} throughout free fall. During this time, heat may be expelled into the surrounding medium by a combination of convection and radiation.

After the drop is released and sufficient heat has been transported to the surrounding medium, such that the outer surface temperature reaches the bulk melting point, solidification begins uniformly along the outer surface. Within the solid or liquid material, radially symmetric heat flow is the governed by the heat equations, each phase having unique but constant values of thermal diffusivity. At the solid-liquid interface, the standard conservation of heat condition balances the latent heat released to the jump in heat fluxes at the solid-liquid interface. In this work, the interfacial temperature is assumed to remain at the bulk melting point. Solidification continues until impact (~4.6s) at the drop tube bottom. More details are provided in references [1-3].

The heat conducted to the outer radius from within the sphere is transported to the environment by convection and/or radiation using a standard mixed boundary condition. The value of the heat transfer coefficient is assumed to depend on the Prandtl and Reynold's numbers for the free falling drops. Since Re and Pr depend upon

the free fall velocity of the drop the dynamical equations for the drop position and velocity must be solved simultaneously with the temperatures throughout the sphere as a function of time. The expressions for the drop speed and acceleration are as in references [7-9]. The internal solid-liquid interface position is determined when solidification is occurring and used to compute fraction transformed.

V. Results

For a given Ag drop of diameter, 7mm in an He - 6%H atmosphere the calculation were was carried out for the superheat of 170K. In Figure 1, results for the 7mm drop are shown. During the first 2.78 seconds of free fall the drop has lost its 170K superheat and established a nearly uniform temperature profile. In the remaining time before impact (2.78s-4.62s), the solid-liquid interface propagates from the outer surface of the drop inward. Comparison of the shell thickness computed numerically and measured experimentally agree to within 50 percent, with the numerical results underestimating the fraction transformed.

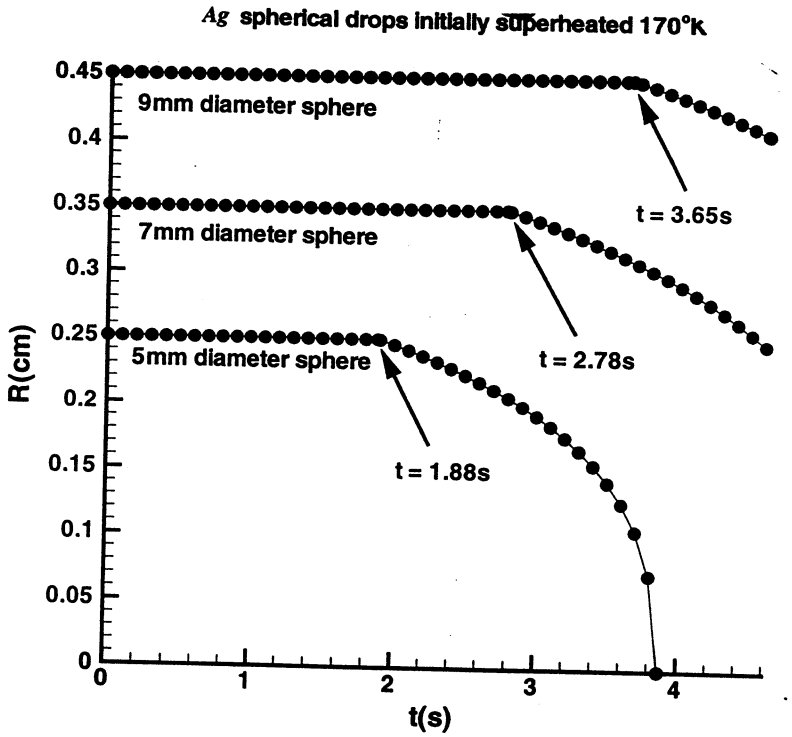

Figure 1: The radius of the liquid interior to the sphere as a function of time measured from the time of release of the drop. Radii are plotted for a 7mm diameter sphere. The time indicated on the plot corresponds to the time at which solidification commenced at R_{out}. The initial temperature of the drop was 170K above the melting point.

VI. Conclusions

Liquid silver spheres having diameter 7mm were released into free fall in a gaseous atmosphere of He - 6%H at 170 degrees superheating. Observations of and measurements of the retrieved sample remnants were compared to the results of a fully transient, spherically symmetric model of the cooling and solidification which occurs during free fall. The model accounts for the variation in the gas properties and explicitly tracks the solid-liquid interface as it progresses through the liquid during the solidification phase.

The results compared favorably. Differences in the observed solidification structure with the results of the calculations indicate additional factors need future consideration in modeling efforts to provide a more quantitative comparison. During solidification the temperature in the interior liquid was seen to remain constant, whereas a nearly linear temperature gradient developed in the solid shell. This has implications related to the morphological instability and the subsequent development of dendritic microstructures which may develop in alloy drops.

VII. Acknowledgments

The author expresses his sincere gratitude to NASA and ASEE for the opportunity to participate in the Summer Faculty Program. In addition, the author wishes to convey sincere gratitude to Dr. Richard Grugel, Collaborator from USRA and Dr. Peter Curreri, NASA Summer faculty mentor. In addition Mr. Thomas J. Rathz and the MSFC drop tube team for their effort in facilitating this work. NASA, USRA and the University Of Alabama in Huntsville are also acknowledged for support and facilities.

VIII. References

1. R.N. Grugel and L.N. Brush, Accepted for publication in the Proceedings of the 8th International Symposium on Experimental Methods for Microgravity Materials Science, March, 1996.
2. R.N. Grugel and L.N. Brush, SPIE Proceedings, Space Processing of Materials, N. Ramachandran, ed., SPIE Vol. 2809, 4-5 August, 1996, p. 258-262.
3. L.N. Brush , R.N. Grugel , and T.J. Rathz: Paper # AIAA 97-0452, 35th Aerospace Sciences Meeting & Exhibit, 6-10 January 1997, Reno, NV.
4. J. Szekeley and R. Fischer: *Metall. Trans. A*, 1970, Vol. 11A, p. 1480.
5. J.M. Forgac, T.P. Schur and J.C. Angus: *J. Appl. Mech.*, 1979, vol. 46, pp. 83-89.
6. J.M. Forgac and J.C. Angus: *Met. Trans. B*, 1981, vol. 12B, pp. 413-416.
7. J.K. McCoy, A.J. Markworth, R.S. Brodkey and E.W. Collings: *Mat. Res. Soc. Sym. Proc.*, 1987, vol. 87 pp. 163-172.
8. J.K. McCoy, A.J. Markworth, E.W. Collings and R.S. Brodkey: *J. Mat. Sci.*, 1992, vol. 27, pp. 761- 766.

9. R. Clift, J.R. Grace and M.E. Weber: in Bubbles, Drops and Particles, Academic Press, Inc., (1978), p. 112.
10. J. Crank: The Mathematics of Diffusion, Oxford, Clarendon Press, London, (1956) p. 85-86
11. N.B. Vargaftik: in Tables on the Thermophysical Properties of Liquids and Gases, Ed. Y.S. Touloukian, 1975, 2nd Edition, Wiley Pub., New York.
12. Handbook of Chemistry and Physics, 57th edition, 1976, Ed. R.C. Weast, CRC Press, Cleveland, OH.

1997

NASA/ASEE SUMMER FACULTY FELLOSHIP PROGRAM

MARSHALL SPACE FLIGHT CENTER
THE UNIVERSITY OF ALABAMA IN HUNTSVILLE

FINITE ELEMENT MODELING OF TRANSIENT THERMOGRAPHY INSPECTION OF COMPOSITE MATERIALS

Prepared By:	Tsuchin Philip Chu, Ph.D.
Academic Rank:	Associate Professor
Institution and Department:	Southern Illinois Universaity at Carbondale Department of Mechanical Engineering and Energy Processes
NASA/MSFC:	
Office:	Material and Processes Laboratory
Division:	Engineering Physics Division
MSFC Colleagues:	Samuel S. Russell, Ph.D., PE

Introduction

The objective of this project was to model the transient thermal behavior of composite materials with defects for thermographic inspection. Thermography is one of the key techniques available today for non-destructive evaluation (NDE) of materials or performing quality assurance for manufacturing process. It is non-invasive and non-contacting. A relatively large area can be inspected at one shot. Furthermore, the data can be easily stored as digital thermal images for further analysis and retrieval. To inspect materials for defects and imperfection in ambient temperature, a very short burst of heat can be introduced to one of the surfaces or slow heating of the side opposite to the side being observed. Due to the interruption of the heat flow through the defects, the thermal images will reveal the defective area by contrasting against the surrounding good materials. This technique is called transient thermography, pulse video thermography, or thermal wave imaging. A schematic diagram of a typical transient thermography inspection system is shown in Figure 1.

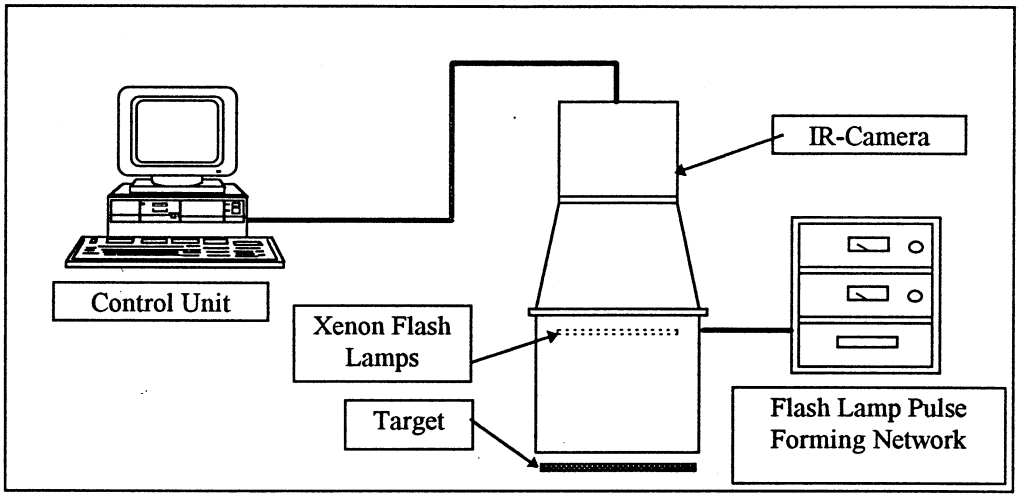

Figure 1. A Typical Transient Thermography System

Thermography is being used to inspect void, debond, impact damage, and porosity in composite materials at NASA Marshall Space Flight Center and is the standard inspection method for the ET Composite Nose Cone. It has been shown that most of the defects and imperfection can be detected. However, the current method of inspection using thermography technique is more of an art than a practical scientific and engineering approach. The success rate of determining the defect location and defect type is largely depend on the experience of the person who operates thermography system and performs the inspection. The operator has to try different type of heat source, different duration of its application time, as well as experimenting with the thermal image acquisition time and interval during the inspection process. Furthermore, the complexity of the lay-up and structure of composites makes it more difficult to determine the optimal operating condition for revealing the defects.

In order to develop an optimal thermography inspection procedure, we must understand the thermal behavior inside the material subjected to transient heat in order to interpret the thermal images correctly. Fabrication of finite element models of characteristic defects in

composite materials subjected to transient heat will enable the development of appropriate procedure for thermography inspection. Design of phantom defects could be modeled and behavior characterized prior to physically building these test parts. Since production of phantom test parts can be very time consuming and laborious, it is important to design good representative defects. Phantom defects frequently will not function as expected. Additionally, methods of thermography could be modeled and compared based upon the FEA modeling without performing the test.

Finite Element Modeling

Finite element method is a very powerful numerical tool that is widely used in the industry for stress, dynamic, and thermal analyses of structure and materials including composites. The finite element models constructed include composites with square and circular debond and void in various depths. Finite element modeling and analysis were performed on Pentium type computers using the COSMOS/M FEA package. This FEA software contains static, dynamic, and thermal modules that allow both linear and nonlinear analyses. The results of the finite element analysis showed that the models of composite panels with void or debond can effectively reveal the temperature distribution at any time step.

All finite element models were generated for a composite panel with a $[\pm 0/90]_s$ laminate geometry. The thickness of the panel is 0.61 mm. The area of the panel under consideration for all models is 38x 38 mm. Quarter symmetry was considered in modeling the panel. The element used is the 8-node isoparametric solid element (brick element). Each ply is one element thick. The duration of the time under investigation is 0.1 seconds. The time step used is 0.001 sec. The heat flux applied to the top surface of the model is 2800 kw/m^2 for the first 0.004 seconds with a total energy of 11.2 kJ/m^2. The coefficient of natural convection applied to the bottom surface is 58.9 w/m^2-°C. The initial temperature is 24 °C. The composite panel used for constructing the model has a density of 1.492 g/cc and a specific heat of 1.269 J/kg-°C. The thermal conductivity is calculated to be 2.272 along the fiber direction and 0.194 w/m-°C in the directions perpendicular to the fiber and through the thickness.

Figure 2 shows the result from the finite elment analysis of the panel with a square debond between the 2nd and the 3rd plies. The size of the debond is 12.7 x 12.7 mm. This figure shows the temperature distribution at time step of 25 which is corresponding to 25 msec after firing the flash lamps. As can be seen from the temperature distribution in the figure, more heat is transferred along fiber direction in the top ply. The maximum temperature difference at the top surface is about 3.3 °C. The temperature on the top reaches equilibrium after about 40 msec. Two more FE models with square debond were built. One has a 5 x 5 element disbond (quarter symetry) between the 1st and the 2nd layers, another has a disbond between the 3rd and the 4th layers. Prior to building these two models, a study of the effect of the size and mesh density of the model on the resulting temperature distribution has been conducted. It has been determined that a 15 x 15 element model with convection defined only on one surface would produce similar results to a 30 x 30 element model or a 15 x 15 element model with convection defined on the top and bottom surfaces.

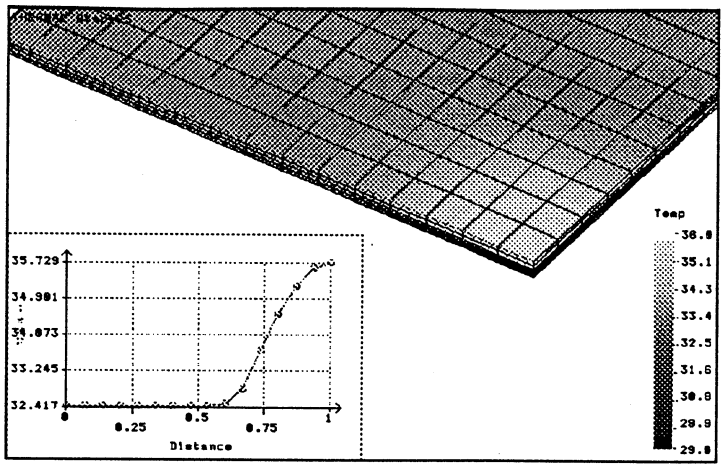

Figure 2. Plot of the FEA results of the panel with a square debond in the mid-plane

The effect of heat flux modeling has also been studied. A model of two heat flux curves has been created in Excel. The first curve, a square curve, was used to model the first series of finite element models. The second curve were created to generate the next series of finite element models. Figure 3 shows the two heat flux time curves. The goal in creating these heat flux curves was to more accurately model the flash lamp while keeping a similar area under the modified curve to the square curve. The results show that the effect of different time curve is minimal.

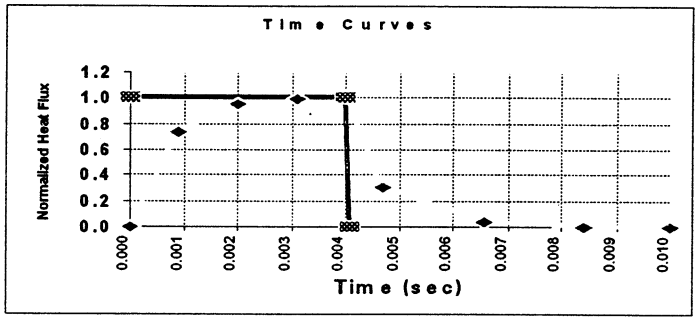

Figure 3. Heat flux time curves

A new model of a composite panel with a square defect at the mid-plane was constructed in SI units. The results from finite element analysis was compared to that from the thermogrphy inspection. The 305 mm square panel has three 12.7 mm square phantom defects fabricated at the mid-plane. The materials used are Teflon tape, backing film, and vacuum bag paper. The temperature profiles at several time steps were compared to the thermal images of the phantom defects. The ranges of temperature are very similar. Since the timing and profile of the heat pulse from the xenon lamps are still unknown, exact comparison is not possible. More information is needed to model the heat flux in order to determine the optimal environment for transient thermography inspection. The thermal images of the panel is shown in Figure 4.

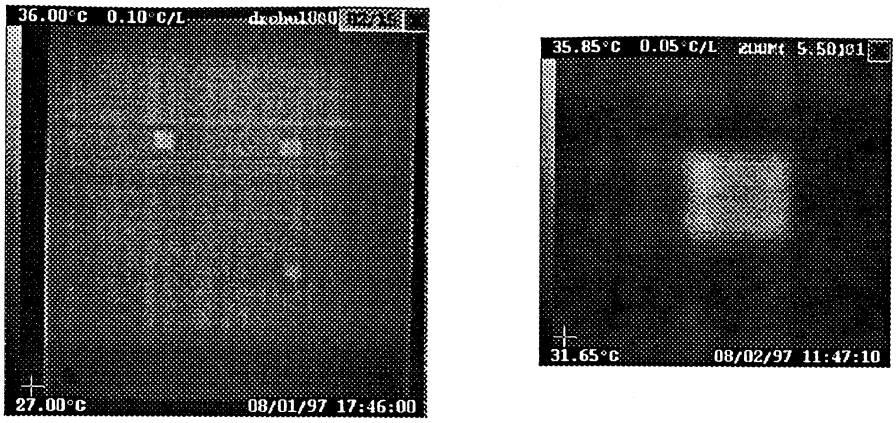

Figure 4. Thermal images of the panel

Conclusions

Several finite element models of defects such as debond and void have been developed for composite panels subjected to transient thermography inspection. Since the exact nature of the heat generated from the flash lamps is unknown, direct comparison between FEA and experimental results is not possible. However, some similarity of the results has been observed. The shape of the time curve that simulates the heat flux from the flash lamps has minimal effect on the temperature profiles. Double the number of flash lamps could increase the contrast of thermal image and define the shape of defect better.

Heat flux from the flash lamps need to be measured. Build database of thermal properties for composites. Model composite structures. Establish proper procedure that could provide the optimal thermal inspection environment by analyzing the FEA results. Model impact damage and porosity.

1997

NASA/ASEE SUMMER FACULTY FELLOWSHIP PROGRAM

MARSHALL SPACE FLIGHT CENTER
PARK COLLEGE

VIRTUAL REALITY AT THE PC LEVEL

Prepared By:	John Dean, M.S.
Academic Rank:	Assistant Professor
Institution and Department:	Park College Department of Computer Science
NASA/MSFC:	
Office:	Advanced Concepts
Division:	Advanced Systems and Technology
MSFC Colleagues:	Daniel O'Neil

Introduction

The main objective of my research has been to incorporate virtual reality at the desktop level; i.e., create virtual reality software that can be run fairly inexpensively on standard PC's.

The standard language used for virtual reality on PC's is VRML (Virtual Reality Modeling Language). It is a new language so it is still undergoing a lot of changes. VRML 1.0 came out only a couple years ago and VRML 2.0 came out around last September. VRML is an interpreted language that is run by a web browser plug-in. It is fairly flexible in terms of allowing you to create different shapes and animations. Before this summer, I knew very little about virtual reality and I did not know VRML at all. I learned the VRML language by reading two books and experimenting on a PC.

CAD to VRML

My first task was to translate existing NASA CAD drawings to VRML code. This would allow different NASA sites to create different components of a project using different CAD packages. The CAD files could then be converted to VRML and combined into one VRML document. Users could then view the objects using a free VRML browser. Users would then have the ability to easily check for compatibility between the different components.

In the next couple years, most of the CAD packages will probably be able to directly export to VRML format. Currently, most CAD packages require the use of a translator software package to convert their drawings to VRML. We were able to convert Intergraph's EMS and SolidEdge CAD drawings to VRML 2.0 by using the 3D/EYE's Trispectives translator. The Trispectives translator costs $299 for the standard edition and $999 for the professional edition. Support costs an additional $500 per year. There are many other translators, such as Okino's PolyTrans, but I did not fully investigate them because that would have been too time-consuming and expensive. The new version of Parametric's ProEngineer CAD tool does have the capability to directly export to VRML 1.0. Most VRML browsers are able to handle both VRML 1.0 and VRML 2.0 files.

VRML 1.0 to VRML 2.0

CAD packages and VRML 1.0 files allow you to create shapes, and the viewer can then choose to spin the objects, zoom in/out, etc. VRML 2.0 allows the designer to add programmable, interactive animation to the scene. That leads to a more appealing viewing experience and it can allow for more information to be disseminated. If you have an existing VRML 1.0 file, and you want to add animation to it, you need to convert the VRML 1.0 file to VRML 2.0 first, and then add VRML 2.0 animation commands. I found a free VRML 1.0 to 2.0 converter from SONY and checked it into the VRC library.

VRML Authoring Tools

In addition to creating VRML files through the use of CAD packages, you can create VRML files by 1) directly entering VRML code into an ASCII text editor or 2) using a VRML authoring tool. It is very time-consuming and tedious to create an elaborate VRML world by directly entering VRML code into an ASCII text editor. Therefore, I recommend using a VRML authoring tool for elaborate VRML worlds. After using several trial version authoring tools, we purchased the VRealm Builder VRML authoring tool for $495. It allows you to create rather complex VRML worlds fairly quickly.

I feel that is best to create elaborate shapes using the VRealm Builder tool, but it is best to create animation using native VRML code entered into an ASCII text editor. The VRealm Builder does provide the ability to add animation to VRML worlds, but it is rather cumbersome. Even if you use VRealm Builder to create the animation, you usually end up having to fine-tune and debug the resulting VRML code using an ASCII text editor. However, I expect that the animation capabilities of VRML authoring tools will improve in the future. VRealm provides one year of free technical support for any VRML questions.

VRML Browsers

VRML browsers enable VRML worlds to be viewed. There are many VRML browsers. The two most popular ones are free – SGI's (Silicon Graphics's) Cosmo Player and InterVista's WorldView. They are both installed as plug-ins to the user's web browser. They both operate on Windows, UNIX, and MAC platforms, and with Netscape Navigator and Internet Explorer web browsers. They both render worlds fairly well, but they are not perfect. For example, if a "ViewPoint node" (a VRML object that describes where the viewer is positioned) is too close to another object, then the object is invisible to the viewer/user. Also, sphere and cylinder shapes do not appear smooth if the viewer is close to their edges. EMD's GlView appears to be a slightly better VRML browser than Cosmo Player or WorldView, but it is not free – it costs $69. GlView includes a minimal VRML authoring tool. I primarily used Cosmo Player because I wanted to use what the VRC's customers would most likely be using. Cosmo Player is the most popular VRML browser because it is free and because Netscape has promoted and integrated it as its standard VRML browser. According to SGI, Cosmo Player version 2.0 is scheduled to "preview soon." I expect Cosmo Player and other VRML browsers to improve in the future. With the new browsers, VRML worlds will probably be able to load faster and render with greater clarity and smoother animation.

VRML Embedded within HTML

VRML worlds can be embedded in HTML pages by using HTML page frames. Embedding VRML worlds in HTML pages can lead to more interesting and informative web pages. VRML and HTML frames can interact. Hyperlinks in either a VRML frame or an HTML frame can cause specified VRML or HTML files to be loaded into specified frames. The hyperlinks can also cause viewpoints to be changed within a VRML frame.

Finding Virtual Reality Applications

I feel that one good way to find applications for virtual reality technology is to let people know about the technology so that it might spark ideas for its use in their current or future projects. The VRC may want to send e-mail out to NASA employees asking them to view the VRML models in the VRC library and the VRML models on the Mars PathFinder web pages. If they have questions or virtual reality project possibilities, then they could fill out an appropriate electronic form in the VRC. The VRC could periodically respond to the user requests.

AXAF Project

The project that I have spent the most time on is the creation of VRML code in order to display the AXAF telescope's view during its orbit. The idea for using VRML for the AXAF project came about due to NASA contractor Billy Wilson hearing about VRML's capabilities, and realizing that it would be a good fit for the AXAF project. Previously, AXAF project group members would visualize AXAF's orbit around the earth by looking at two stereoscopic images of the AXAF orbit and then crossing their eyes. This was a difficult task since the viewer's eyes need to be focused at a precise position behind the stereoscopic images.

The stereoscopic images were generated by an APL program written by Billy Wilson. In order to generate VRML images, Billy's program generates 3D coordinate points for the perimeters of the earth's land masses and for the AXAF orbit. The 3D coordinate points are passed into dll's (dynamic link libraries) that generate the corresponding VRML code. I wrote the dll's using C. Thus, the APL program generates a VRML file that contains the basic shapes needed for a 3D representation of the AXAF's orbit around the earth. I then added VRML animation code to the VRML file - the earth rotates and the user can press a button to start a virtual tour on the AXAF orbit. The tour changes the user's viewpoint so that the user sees what the AXAF telescope would see during its tour of the earth. Apparently, this is very helpful to the AXAF project members.

The AXAF VRML models were very favorably received by the AXAF project group leader, Leonard Howell. Leonard asked whether certain other features could be added to the VRML model. He asked 1) could we precisely coordinate the rotation of the earth with the revolutions of the AXAF orbit?, 2) could we add translucent radiation clouds above the earth? (the AXAF charter includes environmental issues such as radiation clouds), 3) could we turn off the user's headlight (by default, the current viewpoint emanates a forward directional light source called a headlight) and, instead, use light sources from the actual sun and moon positions? The answer to all these questions is yes (VRML is a powerful language!)

VRML Generator Program

In addition to writing the C dll's as mentioned above, I wrote a complete program in C that generates VRML code for basic shapes. The program allows the user to create a new VRML file or append to an existing VRML file. It allows the user to create one or more of the following types of nodes – IndexedFaceSet, IndexedLineSet, ElevationGrid. I chose to handle these three node types because they are very useful building blocks for complex VRML worlds and because their syntax in native VRML code is not very user friendly. An IndexedFaceSet is a group of planar surfaces in 3D space such as the triangular surfaces that were used to form the earth's land mass shapes. An IndexedLineSet is a group of points in 3D space such as the ones used to form the AXAF's orbit line. An ElevationGrid is a contour map where heights (= y values) are specified at each intersecting x, z point. For the below grid, sixteen heights must be specified in left to right, top to bottom order:

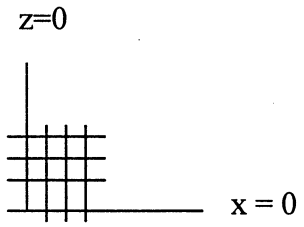

Currently, the ElevationGrid function in the VRML generator program requires this very specific (and therefore limiting) input format. The ElevationGrid function can and should be enhanced so that it can handle any 3D coordinates entered in any order. The function should also be modified so that it automatically displays different heights with different colors (like a standard contour map).

The ElevationGrid function of my VRML generator program could be used to generate VRML representations of 3D spreadsheet applications. The ElevationGrid function could also be used to generate 3D displays for other applications that generate 3D coordinate values. NASA employee Carl Holden is working on a simulation of the thermal enclosure of protein crystal growth. He would like to be able to display his simulation output using 3D coordinates values. After talking to Billy Wilson about VRML, it occurred to Carl that he might be able to better represent his output values by taking advantage of VRML's capabilities. The VRML generator program could be used to create a VRML file for his output values.

Web Communities

A web community consists of a group of users who regularly meet at a web site to discuss topics of common interest. A recent Business Week study found that the average visitation time for a standard web site is seven minutes, and the average visitation time for a web community site is thirty minutes. Thus, a web site's chances of making an impact on customers would tend to be greater if a web community is in place. 3D community web sites have been somewhat popular for the past several years. 3D communities allow each user to choose an avatar to represent himself/herself so that others may see him/her within the community world. Messages typically appear as cartoon bubbles appearing next to the speaker's avatar. The mouse and keypad arrows

are used to navigate within the world. The point of introducing 3D to web sites is to make the web site more appealing. However, 3D community companies have had limited success due to the cumbersome nature of moving around and communicating within the 3D worlds. The main problem appears to be that a user's limited forward viewpoint makes it difficult to quickly see the surroundings. 3D community companies such as WorldsInc and Oz have folded and others such as Blaxxun have scaled back their products considerably.

In searching for 3D web communities, I found ThePalace, a 2D web community product. ThePalace server software is much less expensive and much more popular than the 3D community server software. With ThePalace, it is very easy to move around and communicate within the worlds. ThePalace's most appealing feature is its auditorium capability. One or more speakers at various sites are able to speak while listeners at various sites are able to hear the speakers in real-time. Speakers can set up a slide show presentation and have the slides displayed in one of the auditorium web page's frames. Listeners are able to enter questions during a presentation. The questions are read by an auditorium moderator who decides which questions should be addressed by the speaker(s). I would expect the auditorium to be a valuable resource at NASA for conducting distance presentations and speeches.

On August 5, a representative from ThePalace visited the VRC and provided a demonstration of ThePalace product. We were favorably impressed. Their server software costs approximately $2400 and their client software costs approximately $600.

Future Plans

I recommend that the VRC continues its pursuit of promoting and developing virtual reality at the PC level. ThePalace should be purchased and a server needs to be set up for it (ThePalace agreed to provide free telephone support to help set up the server). A developer should continue to work on the AXAF project. A more complete VRML AXAF world would be a good advertisement for attracting other virtual reality projects. Also, a more complete VRML AXAF world would be of great benefit to the AXAF project group. A developer should continue to work on the VRML generator program as it could be a useful utility for many VRML projects. The VRC might want to consider more advertising for its virtual reality tools so that NASA employees might contact the VRC with more project ideas. Without any advertising, we have already had several unsolicited suggestions for virtual reality projects, so there does appear to be a real practical need for virtual reality technology.

1997

NASA/ASEE SUMMER FACULTY FELLOWSHIP PROGRAM

MARSHALL SPACE FLIGHT CENTER
THE UNIVERSITY OF ALABAMA IN HUNTSVILLE

VIRTUAL ENVIRONMENT USER INTERFACES TO SUPPORT RLV AND SPACE STATION SIMULATIONS IN THE ANVIL VIRTUAL REALITY LAB

Prepared By:	Joseph D. Dumas II, Ph.D.
Academic Rank:	Assistant Professor
Institution and Department:	University of Tennessee at Chattanooga Department of Computer Science and Electrical Engineering
NASA/MSFC:	
Laboratory:	Mission Operations Laboratory
Division:	Training and Crew Systems Division
Branch:	Systems Branch
MSFC Colleague:	Joseph Hale

Introduction

The Army/NASA Virtual Innovations Laboratory (ANVIL) has been established at Marshall Space Flight Center to conduct investigations into the application of Virtual Reality (VR) technology. This new laboratory combines the resources of MSFC's former CAVE (Computer Applications and Virtual Environments) lab facility with those of the former Army Missile Command virtual reality program. As a result of this collaboration, the new ANVIL laboratory possesses a variety of hardware and software resources, including several Silicon Graphics computer systems and two software packages designed for developing and running VR applications. These packages, WorldToolKit (by Sense8 Corporation) and dVISE (by Division, Inc.), support a number of standard peripheral I/O devices which are used to allow a user to interact with the virtual environment. For example, both dVISE and WorldToolKit support magnetic trackers such as the Polhemus Fastrak which are used to track the movements of the user's head, hands, and/or other body parts, as well as other devices such as the mouse and Spacetec Spaceball which may be used to navigate in the virtual world. Both packages also provide support for display devices, such as the CrystalEyes stereographic viewing glasses (by StereoGraphics Corporation) as well as a number of head-mounted displays (HMDs), which allow the user to view his/her virtual surroundings.

Some of the peripheral devices in the ANVIL laboratory, for one reason or another, are not supported by one or both of the VR packages. This requires that custom hardware interfaces and/or software drivers be defined and put in place to allow data generated by the user's interaction with these devices to specify his/her interaction with the simulation and to allow the user to view the virtual world. As part of his Summer Faculty Fellowship, the author was tasked with developing and verifying as many of these peripheral interfaces as possible in order to support Reusable Launch Vehicle (RLV) design analyses and other ANVIL projects. The ultimate goal is to develop the capability and expertise required to produce VR simulations using any or all of the I/O devices with either of the software packages in support of any project assigned to ANVIL. In addition, some time and effort were expended to complete the integration of a networked simulation of the Space Shuttle Remote Manipulator System (RMS) being used for a Space Station assembly task, which was begun during the previous summer's Fellowship period.

Development of Peripheral I/O Interfaces and Drivers

The peripheral I/O devices that we desired to integrate with the virtual reality software packages discussed above fall, in general, into one of two categories: input devices, which are used to track user motions or accept navigational input for moving through the virtual environment, and visual output devices, which provide the user a view of his/her surroundings in the virtual environment. Some of these I/O devices, such as the VPL DataGlove, are not supported by Division or Sense8 because the manufacturer has gone out of business and/or the device is considered obsolete (even though functional devices exist at MSFC and many other sites). Other devices, such as the Fakespace FS^2, are so new, and installed in so few locations, that software support is not yet available. Finally, some peripherals, such as the Space Shuttle RMS hand controllers (present in the laboratory as part of the RMS simulation

discussed below) are nonstandard devices unique to NASA and of course are not supported by commercial software packages.

The hardware interface for the RMS hand controllers was designed and implemented during the summer of 1996 as part of the development of the Space Station module docking simulation described more fully below. This interface consists of a 486-based PC with a data acquisition card which reads analog data from the controllers, converts the data to digital form, and transmits the data over an Ethernet-based local network to a Silicon Graphics Indigo^2 which runs the WorldToolKit-based simulation. At that time, it was decided to configure the hand controllers so that they can be used either to control the RMS and its payload (their intended purpose) or, by sliding a switch, to "fly" the viewpoint (move the user within in the virtual world). This proved to be a judicious choice, as it was discovered that the RMS hand controllers work very well as a general-purpose navigational input device for virtual reality simulations. This prompted the author's development of driver code that can be compiled with any WorldToolKit simulation to allow the use of the hand controllers as a "sensor" device. A sensor can be "attached" to the user's viewpoint or to any object in the virtual universe in order to generate movement. The original version of this driver allows navigation in three dimensions (six degrees of freedom: x, y, and z translation and roll, pitch, and yaw orientation). At the request of one of the NASA personnel in the laboratory, an alternate version was developed that constrains the user to two-dimensional (three degree of freedom) movements in the x-y plane. The RMS hand controllers are now fully functional as a sensor device in WorldToolKit simulations.

The dVISE software that was acquired in early 1997 is a more full-featured development package than WorldToolKit. It is also more object-oriented and uses a Graphical User Interface (GUI) to make it easier for the end user to create VR applications. One of the first projects undertaken by the author this summer was to develop a driver that would allow the RMS hand controllers to be used with dVISE. This was complicated somewhat by the fact that dVISE applications are not constructed in C program code as in WorldToolKit, but rather can only access code which has been pre-compiled and linked into a specific shared library format which is not well documented in Division's on-line manuals. However, with some technical assistance from Division support personnel, the author was able to develop a hand controller device driver which creates a sensor that can be attached to any part of the user's virtual body. For example, the hand controllers can be coupled to the virtual head (in order to move the viewpoint) or to the virtual hand (in order to point, etc.). An enhancement to this basic capability uses the dVISE Virtual Keyboard (VKB) feature to generate "button presses" which activate events in the virtual world, in particular "picking" or grasping a virtual object. Finally, an enhanced hand controller driver was developed which mimics the action of two separate sensors (the gray button on top of the right hand controller acts as a toggle switch for selection of a sensor) so that two virtual body parts can be controlled. This allows the user to travel to a desired location in the virtual world by "flying" the head, then toggle to controlling the virtual hand so that a nearby object can be touched and, if desired, picked up and moved. This feature is very useful for interacting with many types of simulated environments.

Another input device which is very useful for picking up objects in the virtual world, and can be used even more intuitively than the hand controllers, is the DataGlove. This device senses the amount of light transmitted through optical fibers to characterize the bending of the wearer's fingers, allowing him/her to touch or grasp virtual objects or make gestures which have meaning in the virtual world. The ANVIL laboratory has two VPL devices, a "Glovebox" which controls a single DataGlove, and a Data Acquisition/ Transmission Unit (DATU) which allows the use of up to four DataGloves simultaneously. These devices were made by VPL Research, Inc., a firm which has been out of business for some time; thus, Division and most other software developers do not support the DataGlove. The author was able to find some old VPL example code for reference and, after some work, was able to establish data communications to and from the Glovebox via its RS-232 serial interface to allow calibration of the glove to a user's hand and retrieval of the finger bend data. Efforts to make use of the DATU were thwarted by the lack of documentation and insufficient time to "reverse-engineer" the special, nonstandard interface used by the device. The author's dVISE dataglove driver allows a user to grasp and release a virtual object by bending and straightening the forefinger. The bending of the forefinger generates button press events that cause an object to be picked up if it is being touched by the virtual hand. The object can then be moved by moving the hand, which is tracked by a Polhemus Fastrak sensor (for which Division does provide support), and released by straightening the forefinger. At present, the finger bend data are not used to articulate the virtual hand; however, dVISE provides the ability to do this and the finger bend data are available if this level of realism becomes necessary for a particular application. No WorldToolKit driver was developed for the DataGlove since that package does not render a representation of the user's body and thus there is no virtual hand with which to grasp objects.

Another device which is new to the ANVIL lab is the Fakespace FS^2 (also known as the LeBaron since the first unit was sold to Chrysler for use in designing that automobile). The FS^2 is a new product (MSFC's unit is the eighth installed worldwide) which is both an input and output device. It consists of a mechanical-linkage head motion tracker (which provides reduced tracking latency compared to magnetic trackers) coupled to a high-resolution stereographic HMD used to view the virtual environment. Since there are so few of these devices installed, there is as yet no software support from Division or Sense8. Fakespace did provide the source code for a generic test program that is used for all their products; this illustrated the use of some of their library functions which can be used to initialize the tracker and access the data for the user's head position and orientation. Using these library calls, the author was able to create drivers for dVISE and WorldToolKit which allow the head data to control the user's viewpoint in the virtual world. User presses of the two buttons on the HMD are also detected by the code and can be used to perform virtual actions as allowed by each software package.

With drivers for several input devices in place, some attention was given to configuring the dVISE software for use with various visual output devices. Division's package allows one to configure displays without writing any program code, but rather by making entries in a "registry" file which specifies the configuration details. In addition, some display devices require the issuance of operating system commands in order to alter display characteristics at the hardware level. At the start of the author's Fellowship period, the only

display devices usable with dVISE were the "mono" (flat system monitor screen) and CrystalEyes displays. With considerable experimentation, successful configuration of the Fakespace FS^2 and Virtual Research EyeGen3 displays was accomplished, giving the ANVIL lab the capability for true "immersive" virtual environment simulations.

Completion of Shuttle RMS Simulation

During the summer of 1996, the author helped develop a real-time, immersive simulation of the task of docking a pair of Space Station modules using the Shuttle RMS. This simulation was conceived not only with the idea of simulating space operations on earth but with the intent of demonstrating the feasibility of using high-resolution range sensors in combination with an immersive virtual environment as a superior alternative to video camera observation for on-orbit operations. For the purpose of demonstrating the concept, the range sensor (which would provide the relative offset and orientation of the modules being docked) was replaced with a high-fidelity, real-time simulation of the RMS and payload dynamics. This code runs on an Alliant FX-8 supercomputer in the Robotic Simulation Lab at MSFC. The integration of the virtual docking simulation thus required the networking of three computer systems (a personal computer used for hand controller data acquisition, the Alliant, and the Silicon Graphics host which renders the virtual environment). All hardware interfacing, data communications, and graphics programming necessary for integration of the simulation were accomplished during the author's 1996 Fellowship period; however, problems with integrating the RMS dynamics model prevented the successful demonstration of closed-loop operation. This summer, in cooperation with personnel from the Robotic Simulation Lab, the author was able to complete the integration of the simulation by successfully extracting the RMS joint angles, offset coordinates, and Euler angles from the dynamics model, applying the appropriate transformations, and coupling the data to the graphical representation of the RMS and payload in the WorldToolKit simulation. The simulation is now fully integrated and can be viewed either on the "mono" display or immersively by using the EyeGen3 HMD.

Summary and Conclusions

Several virtual reality I/O peripherals were successfully configured and integrated as part of the author's 1997 Summer Faculty Fellowship work. These devices, which were not supported by the developers of VR software packages, use new software drivers and configuration files developed by the author to allow them to be used with simulations developed using those software packages. The successful integration of these devices has added significant capability to the ANVIL lab at MSFC. In addition, the author was able to complete the integration of a networked virtual reality simulation of the Space Shuttle Remote Manipulator System docking Space Station modules which was begun as part of his 1996 Fellowship. The successful integration of this simulation demonstrates the feasibility of using VR technology for ground-based training as well as on-orbit operations.

1997

NASA/ASEE SUMMER FACULTY FELLOWSHIP PROGRAM

MARSHALL SPACE FLIGHT CENTER
THE UNIVERSITY OF ALABAMA IN HUNTSVILLE

MULTI-SCALE FRACTAL ANALYSIS OF IMAGE TEXTURE AND PATTERN

Prepared By:	Charles W. Emerson, Ph.D.
Academic Rank:	Assistant Professor
Institution and Department:	Southwest Missouri State University Department of Geography, Geology, and Planning
NASA/MSFC:	
Office:	Global Hydrology and Climate Center
Division:	Earth System Science Division
MSFC Colleagues:	Dale A. Quattrochi, Ph.D. Jeffrey C. Luvall, Ph.D.

Introduction

Fractals embody important ideas of self-similarity, in which the spatial behavior or appearance of a system is largely independent of scale (5). Self-similarity is defined as a property of curves or surfaces where each part is indistinguishable from the whole, or where the form of the curve or surface is invariant with respect to scale. An ideal fractal (or monofractal) curve or surface has a constant dimension over all scales, although it may not be an integer value. This is in contrast to Euclidean or topological dimensions, where discrete one, two, and three dimensions describe curves, planes, and volumes. Theoretically, if the digital numbers of a remotely sensed image resemble an ideal fractal surface, then due to the self-similarity property, the fractal dimension of the image will not vary with scale and resolution. However, most geographical phenomena are not strictly self-similar at all scales, but they can often be modeled by a stochastic fractal in which the scaling and self-similarity properties of the fractal have inexact patterns that can be described by statistics. Stochastic fractal sets relax the monofractal self-similarity assumption and measure many scales and resolutions in order to represent the varying form of a phenomenon as a function of local variables across space.

In image interpretation, pattern is defined as the overall spatial form of related features, and the repetition of certain forms is a characteristic pattern found in many cultural objects and some natural features. Texture is the visual impression of coarseness or smoothness caused by the variability or uniformity of image tone or color. A potential use of fractals concerns the analysis of image texture. In these situations it is commonly observed that the degree of roughness or inexactness in an image or surface is a function of scale and not of experimental technique. The fractal dimension of remote sensing data could yield quantitative insight on the spatial complexity and information content contained within these data (2). A software package known as the Image Characterization and Modeling System (ICAMS) (6) was used to explore how fractal dimension is related to surface texture and pattern. The ICAMS software was verified using simulated images of ideal fractal surfaces with specified dimensions. The fractal dimension for areas of homogeneous land cover in the vicinity of Huntsville, Alabama was measured to investigate the relationship between texture and resolution for different land covers.

Methodology

The isarithm or line-divider method (3) for calculating fractal dimension was used in this analysis due to its robustness, accuracy, and its relative lack of sensitivity to input parameters. In this method, the fractal dimension of a curve (in a two-dimensional case) is measured using different step sizes that represent the segments necessary to traverse a curve. For an irregular curve, as the step sizes become smaller, the complexity and length of the stepped representation of the curve increases. For surface representations (such as remotely sensed images), the isarithm method uses contours of equal z values as the objects of measurement whose fractal dimensions are estimated. The contours or isarithms are generated by dividing the range of pixel values into a number of equally spaced intervals. For each resulting isarithm line, the image is divided into two regions--areas above and below the isarithmic value. Each isarithm's length (as represented by the number of edges in a grid representation of a surface) is then measured at step sizes up to a user specified maximum. The logarithm of the number of edges is

regressed against the log of the step sizes and the slope of the regression is used to calculate the fractal dimension, resulting in a unique value of *D* for each isarithm. The fractal dimension of the entire image is calculated by averaging the fractal dimensions of each isarithm.

Huntsville Texture Analysis

High resolution imagery of the Huntsville, Alabama area was used to evaluate the differences in fractal dimension that occur among textures associated with differing land covers. Mission M424 conducted by the Lockheed Engineering and Science Company collected 10 meter resolution data using the Advanced Thermal and Land Applications (ATLAS) sensor system mounted in a NASA Learjet, (4). The collection date was 7 September, 1994, a clear day with less than 5 percent cloud cover. ATLAS is a 15 channel imaging system which incorporates the bandwidths of the Landsat Thematic Mapper with additional bands in the middle reflective infrared and thermal infrared range . 384 x 384 pixel images containing homogeneous land uses were obtained from the 10 meter ATLAS data set. Three land uses were analyzed: 1) an agricultural area located north of Huntsville; 2) a forested area located in the mountains to the southeast of town; and 3) an urban area containing the central business district and adjacent commercial/residential areas. The agricultural area contains large cotton fields and pastures devoted to grazing, with a sparse road network oriented generally along the cardinal directions. The image of the forested area is fairly uniform, since the 10 meter resolution is insufficient to resolve individual trees. Topographical features such as the valley extending from the northwest corner to the south central part of the image are the main distinguishing features. The urban image is highly complex, with individual streets and buildings clearly visible.

The Normalized Difference Vegetation Index (NDVI) was computed for the agricultural, forest, and urban images at 10 meter resolution (384 x 384 pixels) and for resampled images at 20, 40, and 80 m resolution using an image pyramid approach (1). NDVI was computed from resampled images in ATLAS channels 6 (near infrared) and 4 (red) using the following formula:

$$[1] \qquad NDVI = (ch6 - ch4) / (ch6 + ch4)$$

NDVI varies from -1 to +1, and provides a good indication of the amount of photosynthetically active biomass in the image. Snow, water, clouds, moist soil, and highly reflective non-vegetated surfaces generally have NDVI values less than zero, rock and dry soils have values close to zero, and highly vegetated surfaces have indices close to +1.0. NDVI varies across spatial extents in a complex fashion due to influences of the varying domains of topography, slope, availability of solar radiation, and other factors (7). The NDVI values were rescaled to an 8 bit format to facilitate comparisons between the three land cover textures. The image size and the range of resolutions analyzed was limited at the upper end by the need to get a homogeneous land cover (thus limiting the maximum size of the image) and at the lower end by the minimum image size (48 x 48 pixels) necessary to use five steps in the isarithm method of computing fractal dimension.

Increasing the pixel size from 10 to 80 meters affected the non-spatial variance of the three land covers in different ways (Table 1). Variance dropped by a moderate amount for the

agricultural image and by a greater amount in the forested image, but it changed very little for the urban image. Moran's *I* spatial statistic dropped as resolution decreased from 10 to 80 meter pixels in the agricultural and urban images (indicating decreasing spatial autocorrelation), and *I* increased then declined in the forested image. These measures provide indications that the resampling process (and by extension, imaging at different resolutions) affects both the non-spatial distribution of the values in an image as well as the relationships between features in the image.

Table 1. Descriptive Statistics--Huntsville NDVI Texture Analysis

Land Cover	Resolution	D	Mean	Median	Std. Dev.	Moran's I
Agricultural	10	2.6101	127.10	137	42.18	0.9023
	20	2.6640	127.13	137	42.10	0.8763
	40	2.7893	127.15	136	41.97	0.8217
	80	2.9371	127.22	134.5	41.79	0.7369
Forest	10	2.8667	127.73	132	38.68	0.7557
	20	2.8229	127.86	132	38.19	0.7830
	40	2.8159	127.89	131	37.73	0.8073
	80	2.7419	128.02	131	37.53	0.7932
Urban	10	2.7417	127.01	137	42.50	0.7587
	20	2.7471	127.00	133	42.50	0.7595
	40	2.7734	126.99	132	42.50	0.7063
	80	2.7829	127.00	133	42.51	0.6726

The ICAMS isarithm method with step size of five and contour interval of 10 was used to compute fractal dimension for the three land uses. Unlike the ideal fractal surfaces, real world images are rarely self-similar, so one would expect fractal dimension to vary with the resolution of the sensor. The slope of the changes in *D* with changes in resolution for the three land uses indicates how agricultural, urban, and forested areas compare over the range of pixel sizes considered. Figure 1 shows that over the 10 to 80 meter range of resolutions, the agricultural image *D* increases from just over 2.6 to more than 2.9. The forest image shows a general decline in *D* with decreasing resolution, and resampling the 10 meter resolution image has only a small negative effect on the computed *D* value. The forested scene behaves as one would expect—larger pixel sizes decrease the complexity of the image as individual clumps of trees are averaged into larger blocks. It is likely that the complexity of the forested image (as indicated by a higher *D* value) would increase if the sensor were able to resolve individual trees within the scene. A linear regression on the three land cover responses leads to the conclusion that the urban image behaves most like an ideal fractal surface and can be said to be self-similar over the range of pixel sizes analyzed, since one cannot reject the hypothesis that the slope of the pixel size-fractal dimension relationship is equal to zero. The 95 percent confidence interval for the regression slope overlaps zero (although just barely at the low end). It should be noted, however, that these regressions are based on only one image and four pixel sizes in a limited range for each land

cover type. Although the R^2 values for the agriculture and forest images is 0.94 or higher, the regression of the urban resolution-*D* relationship is 0.87 which is not as strongly linear.

The increased complexity of the agricultural image with increasing pixel size results from the loss of homogeneous groups of pixels in the large fields to mixed pixels composed of varying combinations of NDVI values that correspond to roads and vegetation. As resolution decreases in the agricultural image, the roads tend to appear wider and the fields are smaller, until eventually the image appears very complex, with few homogeneous areas. This is also reflected in the changes in Moran's I statistic in Table 1. The I statistic for the agricultural area drops from near + 1.0 (indicating a high level of spatial autocorrelation) to 0.74, indicating a more dispersed spatial arrangement of values in the image as resolution grows more coarse. The same process occurs in the urban image to some extent, but the lack of large, homogeneous areas in the high resolution NDVI image means the initially high *D* value is maintained as pixel size increases.

Figure 1. Fractal Dimension of Huntsville NDVI Images

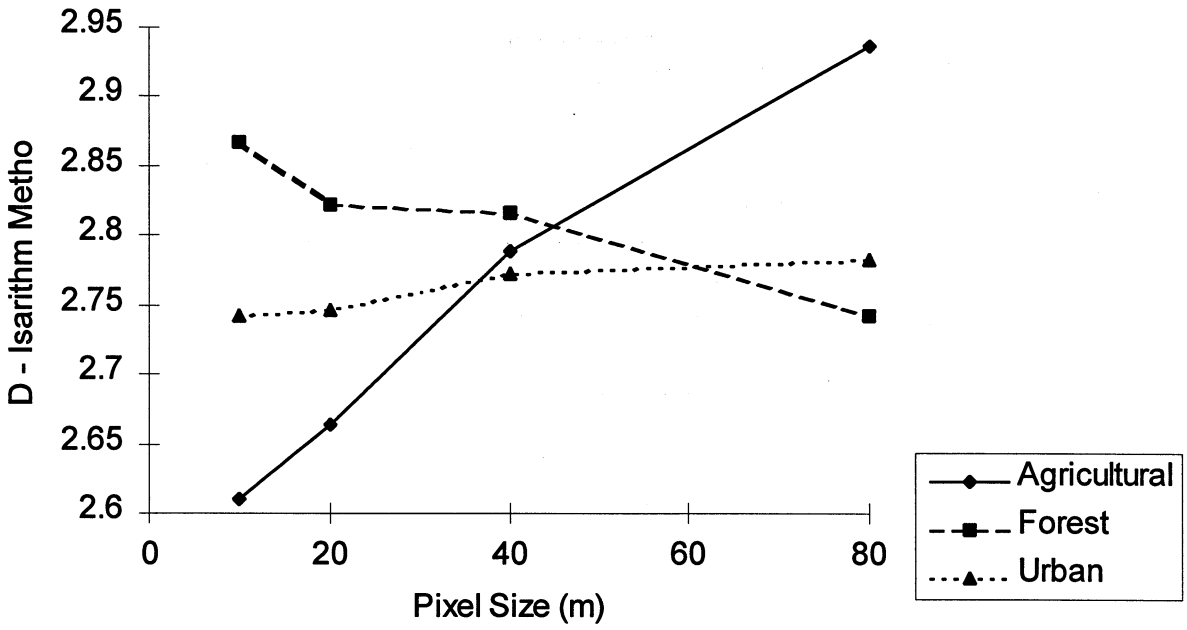

Conclusions

In the example presented here, the complexity of NDVI images of agriculture, forest, and urban areas responds differently to aggregation. The image of the agricultural area grew more complex as the pixel size increased from 10 to 80 meters, while the forested area grew slightly smoother and the complexity of the urban area remained approximately the same. In examining the changes in fractal dimensions with changing pixel size, an obvious question to ask is whether it is best to use a fine resolution for analyzing complex scenes with heterogeneous land uses, or is it best to select a resolution where the complexity of each land cover is approximately the same

(around 40 meters resolution). If one is wishing to distinguish between the different land covers, then the resolution at which the greatest differences in complexity occur may provide the maximum discrimination between land covers. If the question is concerned with determining lumped characteristics of a heterogeneous scene, then the resolution with the least differences in fractal dimension between land covers will likely provide more unbiased estimates of the scene taken as a whole.

More research is needed to examine how the complexity of a geographical process having a known spatial domain is depicted in remotely sensed images. This process domain benchmark would allow significance testing of the fractal dimension's response to changes in resolution. Processes that are more scale independent (closer to the monofractal ideal) require fewer data (i.e., lower resolutions) than other processes that are highly scale dependent. No one resolution is optimal for all research questions, so further investigation is needed to determine how the fractal dimension can be used to provide indications of the tradeoffs involved in selecting the scale, resolution, and spatial extent of the input imagery.

References

(1) De Cola, L., 1997, "Multiresolution Covariation among Landsat and AVHRR Vegetation Indices," *in* Scale in Remote Sensing and GIS (Quattrochi, D.A. and Goodchild, M.F. eds.), Boca Raton, FL: CRC Press, pp. 73-92.

(2) Lam, N.S.N., 1990, "Description and Measurement of Landsat TM Images Using Fractals," Photogrammetric Engineering and Remote Sensing, Vol. 56, No. 2, pp. 187-195.

(3) Lam, N.S.N. and De Cola, L., 1993 "Fractal Measurement," *in* Fractals in Geography (N.S.N. Lam and L. De Cola, eds.), Englewood Cliffs, NJ: Prentice Hall, pp. 23-55.

(4) Lo, C.P., Quattrochi, D.A., and Luvall, J.C., 1997, "Application of High-resolution Thermal Infrared Remote Sensing and GIS to Assess the Urban Heat Island Effect," International Journal of Remote Sensing, Vol. 18, No. 2, pp. 287-304.

(5) Mandelbrot, B.B., 1983, The Fractal Geometry of Nature, New York: W.H. Freeman and Co., 468 pp.

(6) Quattrochi, D.A., Lam, N.S.N., Qiu, H., and Zhao, Wei, 1997, "Image Characterization and Modeling System (ICAMS): A Geographic Information System for the Characterization and Modeling of Multiscale Remote Sensing Data," *in* Scale in Remote Sensing and GIS (Quattrochi, D.A. and Goodchild, M.F. eds.), Boca Raton, FL: CRC Press, pp. 295-308.

(7) Walsh, S.J., Moody, A., Allen, T.R., and Brown, D.G., 1997, "Scale Dependence of NDVI and its Relationship to Mountainous Terrain," *in* Scale in Remote Sensing and GIS (Quattrochi, D.A. and Goodchild, M.F. eds.), Boca Raton, FL: CRC Press, pp. 27-56.

1997

NASA/ASEE SUMMER FACULTY FELLOWSHIP PROGRAM

MARSHALL SPACE FLIGHT CENTER
THE UNIVERSITY OF ALABAMA

POTENTIAL FOR EMU FABRIC DAMAGE BY ELECTRON BEAM AND MOLTEN METAL DURING SPACE WELDING FOR THE INTERNATIONAL SPACE WELDING EXPERIMENT

Prepared By:	James M. Fragomeni, Ph.D.
Academic Rank:	Assistant Professor
Institution and Department:	The University of Alabama Department of Aerospace Engineering & Mechanics
NASA/MSFC:	
Laboratory:	Materials and Processes
Division:	Metallic Materials and Processes
Branch:	Metallurgical Research & Development
MSFC Colleague:	Arthur C. Nunes, Jr., Ph.D.

Introduction

As a consequence of preparations concerning the International Space Welding Experiment (ISWE) studies were performed to better understand the effect of molten metal contact and electron beam impingement with various fabrics for space suit applications. The question arose as to what would occur if the electron beam from the Ukrainian Universal Hand Tool (UHT) designed for welding in space were to impinge upon a piece of Nextel AF-62 ceramic cloth designed to withstand temperatures up to 1427 °C. The expectation was that the electron beam would lay down a static charge pattern with no damage to the ceramic fabric. The electron beam is capable of spraying the fabric with enough negative charge to repel further electrons from the fabric before significant heating occurs. The static charge pattern would deflect any further charge accumulation except for a small initial amount of leakage to the grounded surface of the welder. However, when studies were made of the effect of the electron beam on the insulating ceramic fabric it was surprisingly found that the electron beam did indeed burn through the ceramic fabric. It was also found that the shorter electron beam standoff distances had longer burnthrough times than did some greater electron beam standoff distances. A possible explanation for the longer burnthrough times for the small electron beam standoff distance would be outgassing of the fabric which caused the electron beam hand-tool to cycle on and off to provide some protection for the cathodes. The electron beam hand tool was observed to cycle off at the short standoff distance of two inches likely due to vapors being outgassed.

During the electron beam welding process there is an electron leakage, or current leakage, flow from the fabric. A static charge pattern is initially laid down by the electron beam current flow. The static charge makes up the current leakage flow which initially slightly heats up the fabric. The initially laid down surface charge leaks a small amount of current. The rate at which the current charge leaks from the fabric controls how fast the fabric heats up. As the ceramic fabric is heated it begins to outgass primarily from contamination/impurities atoms or molecules on and below the fabric surface. The contaminant gases ionize to create extra charge carriers and multiply a current of electrons. The emitted gas which ionized in the electron leakage flow promotes further leakage. Thus, the small leakage of charge from the fabric surface is enhanced by outgassing. When the electron beam current makes up the lost current, the incoming electrons heat the fabric and further enhance the outgassing. The additional leakage promotes additional heating up of the ceramic fabric. The electrons bound to the ceramic fabric surface leak off more and more as the surface gets hotter promoting even greater leakage. The additional electrons that result also gain energy in the field and produce further electrons. Eventually the process becomes unstable and accelerates to the point where a hole is burned through the fabric.

Low Pressure Gas Effects

When modeling the penetration effect of the electron beam impingement on the surface of the ceramic cloth, various assumptions can be made to simplify the modeling. It can be assumed that the heat of the fabric i.e., the heat that goes into the fabric comes from placement of beam current with the leakage current. If the cloth is heated an amount due to the beam power iε then the change in temperature over the corresponding change in time is given by:

$$dT/dt = -(i\varepsilon - q_L)/\rho a \omega C_p \qquad [1]$$

where q_L is the conduction heat loss per unit volume per unit time, i is the current, ε is the voltage, a is the cross-sectional area of the cloth that is impinged by the electron beam, ω is the width of the ceramic fabric, ρ is the density of the ceramic fabric, and C_p is the specific heat of the ceramic fiber. Nextel AF-62 ceramic fiber cloth has a specific heat C_p' of 1000 J/kg/°K and a density ρ' of 820 kg/m^3, and is able to withstand temperatures up to 1427°C (2600°F). The current i in equation [1] can be determined by the expression

$$i = enav \qquad [2]$$

where e is the charge of an electron, and v is the mean velocity of the electrons. The electron velocity can be approximated from a consideration of the electron charge and the voltage. The kinetic energy of an electron can be equated to voltage potential times the charge of the electron such that

$$0.5m_e v^2 = eV \qquad [3]$$

Thus, the velocity of the electron(s) can be determined from the above expression as

$$v = (2eV/m_e)^{0.5} \qquad [4]$$

where m_e is the mass of an electron (9.11E10^{-31} kg), e is the charge of the electron (1.602E10^{-19} Coulombs), V is the voltage of the electron gun (8000 Volts), and v is the velocity of the electron. The velocity of the electrons coming out of the gun for 8000 volts potential would be approximately 53E10^6 m/sec.

The passage of electrons from the orifice of the UHT electron beam gun at high velocities (see equation 4) through a vacuum chamber at low partial pressures approaching 10^{-4} Torr results in electron collisions with the gas atoms/molecules dispersed throughout the vacuum chamber that are in the line of path of the electron beam. The number of electron collisions with the gas molecules/atom (say oxygen or nitrogen) will depend in part on the vacuum pressure since number density of the molecules/atoms in vacuum is proportional to the pressure. So as the vacuum pressure decreases the number of electron collisions with the gas molecules also decreases and as the vacuum pressure increases the frequency of electron collisions with the gas molecules also increases. The vacuum pressure inside the chamber is also inversely proportional the mean free path λ of the gas atoms/molecules dispersed throughout the chamber. As the vacuum pressure increases the free mean path of the gas molecules will decrease and as the pressure decreases the free mean path increases. The gas in the chamber is assumed to be monatomic oxygen and nitrogen. Thus as the vacuum pressure decreases in the chamber more electrons are able to reach the target because the free mean space between the molecules increases and the thus the number of electron collisions with the gas molecules decreases. The mean free distance between the gas molecules in the chamber can be determined in terms of the number of gas molecules per cubic volume and the collision cross section. The collision cross section σ of electrons colliding with gas monatomic molecules is given by the expression

$$\sigma = \pi r^2 \qquad [5]$$

where r is the radius of the molecule that has been hit by an electron. Thus the collision cross section for electrons colliding with gas containing monatomic oxygen ($r = 1.8E10^{-10}$ m) would be equal to $1.02E10^{-19}$ m^2. The collision cross section for electrons colliding with monatomic nitrogen ($r = 2.13E10^{-10}$) would be equal to $1.43E10^{-19}$ m^2. If there are n molecules per unit volume, the number of collisions per unit time, or the collision frequency z, is

$$z = \sigma n v \qquad [6]$$

where v is the average speed of the gas molecules. The mean free path between collisions i.e., the average distance between collisions, is equal to the total distance covered in some interval time divided by the number of collisions in that time and would thus be equal to

$$\lambda = 1/\sigma n \qquad [7]$$

The number of gas molecules at standard pressure and temperature can calculated from the ideal gas equation as

$$n = p/kT \qquad [8]$$

where k is Boltzman's constant ($1.38E10^{-23}$ J/K), p is the pressure, and T is the temperature. Thus if p is 1 atm. and T is 273 K, then n is approximately $2.7E10^{+25}$ molecules/m^3. Thus, the number of oxygen molecules at a vacuum chamber pressure of 10^{-5} Torr can be determined from the expression

$$n_2 = (p_2/p_1)n_1 \qquad [9]$$

Therefore, if p_1 is 1 atm, and p_2 is 10^{-4} Torr, and n_1 is $2.7E10^{+25}$ molecules/m^3, then n_2 would be equal to $3.553E10^{+18}$ molecules/m^3 of oxygen molecules. The free mean path of gas in the vacuum chamber can thus be calculated from equation (2.8) for monatomic oxygen as $\lambda = 2.759$ m (or 9.053 ft.), and for monatomic nitrogen as 1.968 m (or 6.458 ft.). If the gas pressure in the vacuum chamber was decreased to say 10^{-5} Torr then the free mean path would be $\lambda = 27.59$ m (or 90.53 ft.) for monatomic oxygen and would be $\lambda = 19.68$ m (or 64.58 ft) for monatomic nitrogen. However, if gas pressure in the vacuum chamber was increased to say 10^{-3} Torr, then the free mean path would be $\lambda = 0.2759$ m (or 0.9053 ft.) for monatomic oxygen and would be $\lambda = 0.1968$ m (or 0.6458 ft) for monatomic nitrogen. Thus, changes in the partial pressure can have indeed a large effect on the free mean path distance.

The electron beam directed through the randomly dispersed gas in the vacuum chamber will interact with the gas molecules and scatter some of the molecules. The probability that the electron beam will scatter an atom or molecule will be σ/A, and the volume of the electron beam directed through the vacuum at a distance λ would be given by λA. The total number of electrons scattered by the beam would be $\lambda A n_{gas}$. The probability that the entire electron beam would be scattered would be

$$(\lambda A n_{gas})(\sigma/A) = 1 \qquad [10]$$

The free mean path can thus be determined from the above equation as

$$\lambda = 1/n_{gas}\sigma_{gas} \quad [11]$$

If an electron beam of current i_o starts out across the vacuum chamber, in distance interval dx an attenuation di occurs of the local current i proportional to the ratio of the distance interval dx to the mean free path. The drop in current di can be expressed in terms of the travel interval distance dx of the total length of the beam as

$$di = -i(dx/\lambda) \quad [12]$$

or

$$di = -i\, n_{gas}\sigma_{gas}\, dx \quad [13]$$

If equation [13] is integrated, the results is given by

$$i = i_o \exp\{-x/\lambda\} \quad [14]$$

Thus the ratio of the beam current to the leakage current can be expressed as

$$i/i_o = \exp(-x/\lambda) \quad [15]$$

where the ratio of the beam current to the leakage current represents the percent of residual power in the beam. Table 1. shows some calculations comparing different standoff distances to the percent residual power to the beam for different vacuum chamber pressures, pressures starting from within the normal UHT operating range below 10^{-5} Torr (depending upon the capability of the vacuum chamber) and rising to 10^{-3} Torr.

Table 1 Percent Residual Power to the Beam for various electron beam gun standoff distances for three different vacuum chamber pressures for monatomic nitrogen.

x, standoff distance, in.	percent residual power to the beam, % (10^{-3}Torr)	percent residual power to the beam, % (10^{-4}Torr)	percent residual power to the beam, % (10^{-5}Torr)
2	77	97	100
6	46	93	99
12	21	86	98
24	5	73	97
48	0	54	94

Table 1 demonstrates that the attenuation of the electron beam causes the beam to lose it potency at long standoff distances. For example with a vacuum pressure of 10^{-4} Torr and a standoff distance of 48 inches roughly only half of the beam current power reaches the target. However, the above analysis suggests that the electron beam may not lose its potency for lower vacuum chamber pressures.

The translational kinetic energy associated with a molecule of mass m and velocity v_m is 0.5m v_m^2. If the mean translational kinetic energy of a molecule is equated to the available kinetic energy 1.5kT for three translational degrees of freedom then the approximate speed of a molecule at some temperature heated above room temperature would be

$$v_m = (3kT/m)^{0.5} \qquad [16]$$

where k is Boltzman's constant ($1.38E10^{-23}$ J/°K), and T is the absolute temperature for a surface heated above room temperature. If nitrogen gas in the vacuum chamber is considered, then v_m can be determined based on the Atomic Mass Units (AMU) of the gas, which for a nitrogen gas molecule would be 28. Thus, $v_m=\{[3(1.38E10^{-23}$ J/°K)(600°K)]/[(28AMU)$(1.673E10^{-27}$Kg/AMU)(1Jsec^2/m^2/Kg)]$\}^{0.5}$=728 m/sec. It is hard to know for sure what gas(s) is emerging from the cloth, but if water or oxygen were emerging then the appropriate AMU should be used (AMU = 18 for water, AMU = 21 for oxygen). Correspondingly for water v_m = 908 m/sec, and for oxygen v_m = 841 m/sec. Thus, the velocity of gas molecules at 600°K in the vacuum chamber would be in the range of about 700-900 m/sec for a gas mixture consisting of oxygen, nitrogen, and water molecules.

Fabric Damage From Molten Metal Detachment

Observations were made of the interaction of 2219 aluminum droplets on 10 oz./yd^2 Teflon fabric in a vacuum chamber at pressures of 10^{-4} to 10^{-5} Torr. The metal drops were obtained from impact ejection from a horizontal weld pool onto a teflon cloth spread over the floor of the vacuum chamber. An 8000 volt electron beam, produced by a Ukrainian "Universal Hand Tool" (UHT) designed for welding in the space environment, was the source of heat for generating the weld pool. After the drops had solidified on the cloth, they were collected and measurements were made of the drop sizes and the amount of fabric damage they caused while cooling. It was experimentally observed for molten droplets of 2219 aluminum metal on the 10 oz./yd^2 Teflon fabric (0.23mm thick) that up to about 4.8 mm metal drop diameter no holes were developed in the fabric. At drop sizes of about 5 mm penetration of the fabric occurred and rapidly increased to about the diameter of the drop. However, at drop diameters less than 5 mm, the fabric was charred (both front side char and back side char), and the front side char was very roughly about half the size of the molten metal 2219 Al droplet and the back side char was very roughly about two-thirds the size of the front side char. These results appear to indicate that for a 2219 Al drop on 10 oz./yd^2 Teflon fabric a hole will burn through when the molten metal droplet size is twice the thickness of the Teflon fabric.

Depending on the chemistry involved, the process of the decomposition of the fabric is complex. The chemistry of the interaction between the molten metal and ceramic fabric is an important consideration in determining the possible amount of fabric damage. Contaminants from

the surface of the fabric can outgass while the molten metal is resting on the fabric surface which can alter the conduction transfer of heat from the metal to fabric. In addition, the chemistry of the burning of the ceramic fabric, can affect the amount of potential damage to the fabric. The 10 oz./yd^2 Teflon fabric chars in the range of 300-500 °C and ablates in the range of 600 to 700 °C until nothing is left according to Differential Thermal Analysis and Thermogravimetric Analysis. However, even though the details of fabric decomposition are complex, one may evaluate in a very basic, semiquantitative manner the general features of metal and fabric interaction that control the damage process. A simple expression can be derived to relate several parameters such as the weight, pressure, force, surface tension etc. to the surface area that will first char on the fabric surface from the molten metal drop. Assuming that a spherical molten metal drop is sitting on the fabric surface and that the drop remains spherical, the weight of the metal drop can be approximated as

$$W = \rho\, g\, V = \rho\, g\, (4\, \pi\, r^3/3) \qquad [17]$$

The contact area that will first be charred from the metal drop which sits flat on the fabric surface can be expressed as

$$A_c = W/p \qquad [18]$$

where p is the internal pressure which holds the drop together, and A_c is the cross-section area of fabric which the drop sits upon i.e., the contact area. Substituting equation [17] into [18] gives the contact area as

$$A_c = \rho\, g\, (4\, \pi\, r^3/3)/p \qquad [19]$$

Equating the force the drop applies on the fabric surface with the surface tension force of the metal drop

$$p\pi r^2 = 2\pi r\gamma \qquad [20]$$

thus the pressure can be expressed as

$$p = 2\gamma/r \qquad [21]$$

Thus substituting equation [21] into [19] gives the contact area as

$$A_c = (2\pi/3)(\rho g/\gamma) r^4 \qquad [22]$$

where γ is the interfacial surface tension of the molten metal droplet. If the contact area A_c is a circular surface contact area ($\pi D^2/4$) of diameter D then the above expression can be written in terms of the contact diameter and drop diameter as

$$D = d^2(\rho g/6\gamma)^{0.5} \qquad [23]$$

Thus, for the various drop sizes of the 2219 Al alloy, the contact diameters can be computed using the above expression.

Fabric Damage Model from Molten Metal Detachment

A simple model will now be presented to describe the amount of damage done to a ceramic fabric cloth from a molten metal droplet in terms of specific material parameters and variables. In order for the metal drop to burn through the fabric to a certain volume of fabric ΔV the metal drop must provide a certain amount of energy to the fabric. The amount of energy that the metal drop must supply to burn a volume ΔV of fabric through charring and ablation would be given as

$$\rho' C_p' \Delta V\{(T_{ablat}-T_a)\}+ \rho' \Delta V(L_{char}+L_{ablat}) = \rho' \Delta V\{C_p'(T_{ablat}-T_a) + L_{char}+L_{ablat}\} \quad [24]$$

where ρ' is the density of the fabric, C_p' is the specific heat of the fabric, T_{ablat} is the ablation temperature of the fabric, T_a is the ambient temperature, ΔV is the volume of the fabric that has been charred and ablated, L_{char} is the latent heat of charring, and L_{ablat} is the latent heat of ablation . However, the energy that is available from the drop is

$$m C_p \Delta T = \rho H_d C_p \Delta T = \rho (4 \pi r^3/3) C_p(T_{do} - T_{df}) \quad [25]$$

where $H_d = 4\pi r^3/3$ is the volume of the drop sitting on the fabric surface, ρ is the molten metal density, C_p is the specific heat of the metal droplet, T_{do} is the initial temperature of the drop, and T_{df} is the final temperature of the fabric. Thus, equating the energy that is available from the metal drop to the energy the drop must supply for ablation and charring yields

$$\rho' \Delta V\{C_p'(T_{ablat}-T_a) + L_{char}+L_{ablat}\} = \rho (4 \pi r^3/3) C_p(T_{do} - T_{df}) \quad [26]$$

where r is the radius of the metal drop. The volume of fabric that has been charred and ablated can be determined from the geometry of the damage done to the ceramic fabric. For a given thickness of fabric, w, and assuming a partial hemispherical geometric burnthrough of fabric from the molten metal drop which sits on the surface, the volume of fabric that has been damaged can be evaluated in terms of the hole radius that has been burned in the fabric. Thus, the damage volume can be determined as

$$\Delta V = \pi R^3(W/R - W^3/(3R^3)) = \pi R^2 W(1 - W^2/(3R^2)) \quad [27]$$

where R is the radius of the hole burned in the cloth and W is the thickness of the cloth (0.254 mm for Teflon). Thus, when R=W, the volume is that of a half sphere $\Delta V=2\pi R^3/3$

However, if the fabric is only charred and no ablation takes place then the amount of energy that the metal drop must supply to char a volume $\Delta V'$ of fabric would be given as

$$\rho' C_p' \Delta V'(T_{charr}-T_a) + \rho' \Delta V'(L_{charr} + L_{htloss}) = \rho' \Delta V'\{C_p'(T_{charr}-T_a) + L_{char} + L_{htloss}\} \quad [28]$$

where L_{htloss} is the latent heat lost by conduction of the metal drop with the metal floor of the vacuum chamber after the metal drop has burned a hole through the teflon fabric, and T_{charr} is the

charring temperature of the teflon fabric. However, the energy that is available from the metal drop would be

$$m\, C_p \Delta T = \rho\, (4\, \pi\, r^3/3) C_p (T_{ablat} - T_{charr}) \qquad [29]$$

Thus, equating the energy that is available from the metal drop to the energy the drop must supply for charring yields

$$\rho' \Delta V' \{ C_p' (T_{charr} - T_a) + L_{char} + L_{htloss} \} = \rho\, (4\pi r^3/3) C_p (T_{ablat} - T_{charr}) \qquad [30]$$

The charring temperature is roughly 350°C and the ablation temperature is roughly 570°C. The volume of material that has been charred $\Delta V'$ can be determined from the total volume that has been both charred and ablated as well as the char radius and is given by the expression

$$\Delta V' = \pi\, R_c^2 W [1 - 0.33 (W/R_c)^2] - \Delta V \qquad [31]$$

or

$$\Delta V' = \pi W \{ R_c^2 [1 - 0.33 (W/R_c)^2] - R^2 (1 - W^2/(3R^2)) \} \qquad [32]$$

where R_c is the radius from charring and W is the fabric cloth thickness. Table 2 gives the calculated values for ΔV and $\Delta V'$ based on different metal drop and hole dimensions.

Table 2. Fabric Damage for 2219 Aluminum Drops on 10 oz/yd^2 Teflon Fabric

Drop Size Diameter (mm)	Char Radius (mm)	Fabric Thickness (mm)	Hole Radius (mm)	ΔV Char/Ablate (mm^3)	$\Delta V'$ Char (mm^3)
3.47	0.75	0.25	0.0	0.0	0.425
4.80	1.75	0.25	0.0	0.0	2.394
4.96	1.75	0.25	0.25	0.033	2.394
5.13	3.50	0.25	2.75	6.017	3.741

A sample calculation can be done for determining the latent heats for a given metal alloy acting on the surface the specific ceramic fabric surface namely Teflon (10 oz. Per yard) which is 0.0254 cm (0.01 in.) thick. Teflon ceramic cloth has a specific heat C_p' of roughly 1046 J/kg/°K (0.25 cal/gram/°C) and a density ρ' of roughly 1.33 g/cm^3 (1330 kg/m^3 or 0.048 lb/in^3=82.9 lb/ft^3). The ambient outside temperature T_a can be taken as roughly 23°C (room temp.), the ablation temperature of teflon fabric is 570°C, the charring temperature T_c is approximately 350°C, and the effective initial drop temperature T_{do} approximated as 640°C, and the effective final drop temperature T_{df} can be approximated as 570°C. Thus, an estimated value for $L_{char}+L_{ablat}$ can be determined using the given values for the temperatures and constants. Thus, using a metal drop size of 5.13 mm diameter and drop volume ΔV of 6.017 mm^3 and from using equation [27], $L_{char}+L_{ablat}$ = 7,416,169. J/Kg (1.8 Kcal/gram). Also from using equation [31] with a drop size of

5.13 mm diameter and drop volume ΔV' of 3.741 mm^3 an estimated value for L_{char}+ L_{htloss} can be determined as 39,858,963. J/Kg (9.5 Kcal/gram). The latent heat loss L_{htloss} takes into account the heat lost through conduction of the metal drop with the metal plate floor of the vacuum chamber once a hole has been burned through the teflon fabric.

Summary and Conclusions

The effective power or potency of the electron beam was limited to about four feet under the given vacuum conditions due to electron collisions with gas molecules in the vacuum chamber.

Lower vacuum pressures result in increased electronic free mean path; thus potentially greater electron beam damage to the ceramic fabric.

The outgassing of contaminates from the ceramic fabric enhanced the fabric potency to electron beam damage.

The outgassing of the ceramic fabric which resulted in the electron beam gun cycling off at the two inch standoff distance i.e., the intermittent operation of the UHT, resulted in considerably longer burnthrough times as compared with the longer standoff distances of 6, 12, 24, & 48 inches. However, at intermediate to longer standoff distances, a tendency to outgas makes a ceramic fabric subject to electron beam damage; and just a small tendency seems adequate.

From experiments carried out concerning the molten metal detachments on the teflon fabric some additional variables were determined important and necessary to control such as the impact velocity of the drop on the fabric cloth, heat lost through the chamber floor as drop sits on the fabric surface, and the rolling motion of the metal drop on the fabric surface.

Recommendations for Future Work

Investigate electron beam damage range at lower vacuum pressures ($<10^{-5}$ Torr).

Measure/monitor the local dynamic pressure at/near the fabric surface.

Perform damage studies based on the controlled exposure of the fabric to an anvil heated to different temperatures, at different lengths of time, and different sizes of fabric contact surface area.

ACKOWLEDGEMENTS

Carolyn Russell for invaluable help with the experimental aspects of this work. Also the Ukrainians for their assistance with the experimental work in the enclosed vacuum chamber.

1997
NASA/ASEE SUMMER FACULTY FELLOWSHIP PROGRAM

MARSHALL SPACE FLIGHT CENTER
THE UNIVERSITY OF ALABAMA IN HUNTSVILLE

CHARACTERIZATION OF MESOSCALE CONVECTIVE SYSTEMS BY MEANS OF COMPOSITE RADAR REFLECTIVITY DATA

Prepared By:	Dr. Bart Geerts
Academic Rank:	Assistant Professor
Department:	Department of Aeronautical Sciences
University:	Embry-Riddle University
Location of Fellowship	Global Hydrology and Climate Center (NASA/MSFC and UAH)
MSFC colleague	Dr. Steven Goodman
UAH colleague	Dr. Kevin Knupp

CHARACTERIZATION OF MESOSCALE CONVECTIVE SYSTEMS BY MEANS OF COMPOSITE RADAR REFLECTIVITY DATA

Bart Geerts

1. Introduction

A mesoscale convective system (MCS) is broadly defined (as in Houze 1993), i.e. a cloud and precipitation system of mesoscale dimensions (often too large for most aircraft to circumnavigate) with deep-convective activity concentrated in at least part of the MCS, or present during part of its evolution. A large areal fraction of MCSs is stratiform in nature, yet estimates from MCSs over the Great Plains (Biggerstaff and Houze 1991), the Southeast (Knupp et al 1997), and tropical waters (Houze an Cheng 1977; Mapes and Houze 1993) indicate that at least half of the precipitation is of convective origin. The presence of localized convection is important, because within convective towers cloud particles and hydrometeors are carried upward towards the cloud top. Ice crystals then move over more stratiform regions, either laterally, or through in situ settling over decaying and spreading convection. These ice crystals then grow to precipitation-size particles in mid- to upper tropospheric mesoscale updrafts. The convective portion of a MCS is often a more or less continuous line of thunderstorms, and may be either short-lived or long-lived.

Geerts (1997) presents a preliminary climatology of MCSs in the southeastern USA, using just one year of composite digital radar reflectivity data (the same data as used for this project, see Section 2). In this study MCSs are identified and characterized by means of visual inspection of animated images. A total of 398 MCSs were identified. In the warm season MCSs were found to be about twice as frequent as in the cold season. The average lifetime and maximum length of MCSs are 9 hours, and 350 km, respectively, but some MCSs are much larger and more persistent. In the summer months small and short-lived MCSs are relatively more common, whereas in winter larger and longer-lived systems occur more frequently. MCSs occur more commonly in the afternoon, in phase with thunderstorm activity, but the amplitude of the diurnal cycle is small compared to that of observed thunderstorms. It is estimated that in the Southeast more than half of all precipitation and severe weather results from MCSs.

2. The data

We are using the composite digital radar reflectivity data available at a resolution of 2x2 km and 15 minutes, archived at the NASA Marshall Space Flight Center (MSFC). There are 16 possible values of radar reflectivity, ranging from 2.5 dB (level 0) to 75.5 dB (level 15), in 5 dB increments. For instance, level 4 data have a radar reflectivity ranging between 20 and 25 dBZ. The recorded reflectivity is the maximum value within a 2x2 km box at any vertical level, recorded by any radar in the network. Most but not all of these radars are WSR-88D NEXRAD.

Since some NEXRAD radars came online after 1994, because radar down-times have been reduced lately, and because the algorithms to remove ground clutter and other anomalies have improved in recent years, it is likely that the more recent data are of superior quality. The best coverage is east of the Rockies, because topographic blockage is minimal and the density of radars in the network is slightly higher. Therefore, the data is excellently suited to study precipitation characteristics in the Mississippi drainage basin (Goodman and Raghavan 1997).

For the dataset examined by Geerts (1997), ie the southeastern quadrant from 5/'94 to 4/'95, about 3% (or a cumulative period of 11 days) of the data were missing from the archive. Usually the gaps were found to be fairly long (up to 2 days), sometimes they are very short (one single 15 min interval). Occasionally a considerable number of radars is not included in the composite image. In this case large gaps can be seen, as well as concentric rainfall boundaries around those radars that are in operation.

The actual grid size is 2 km or less. The zonal (east-west) dimension of the grid drops from 2 km at the southern border (20N) to 1.28 km at the northern border (53N). Rows and columns in the data set are aligned with meridians and latitude circles, so there is some distortion. In some regions (furthest away from radars, in the northern states), the grid spacing actually smaller than the radar beamwidth/gate_spacing, so some interpolation occurs in the cartesian transformation.

3. The algorithm that identifies mesoscale precipitating systems

Currently we are processing the 2x2 km composite radar reflectivity data archived at NASA MSFC, to extract the spatial characteristics of all precipitating systems (PS). A PS is defined more broadly as a continuous area of precipitation (at least 20 dB, ie level 4) of mesoscale dimensions (at least 500 km^2). For every gridpoint within a PS, the reflectivity value is retained, as well as a stratiform/convective qualifier, based on the algorithm by Steiner et al (1995), and used by Steiner and Houze (1997). We used the 'medium' size domain of influence of a local convective dB maximum, as defined in Steiner et al (1995).

We define the reflectivity-weighted centerpoint of any PS, as well as the basic PS spatial pattern. The centerpoint is used to allow easier tracking of PSs (see Section 5), and also to plot geographical distributions of PSs. The reflectivity weighting is justified is follows: the area of highest reflectivity is the area of strongest vertical and also horizontal storm-scale motions, and dynamically it is area of highest energy conversions, so it is the 'center of activity'. Also, from the perspective of storm tracking, we believe that the weighted centerpoint is more stable than the un-weighted centerpoint, considering the occasional appearance of false low-dB echoes, and the rapid expansion and decay of stratiform regions.

The spatial pattern is described simply as the ellipsoid that most closely approximates the PS. The orientation of the long axis is found, and its length is defined as four standard deviations (2 SDs from the centerpoint). The length of the short axis, then, is +/- 2 SDs in the direction normal to the long axis. SDs are calculated as the distance of any PS gridpoint from the centerpoint, again weighted by reflectivity (in dB units). The ratio of the respective lengths of the axes is a measure of how linear the PS is.

A PS is considered to be a *potential MCS* if it satisfies the following criteria: the long axis has to be at least 100 km long; and the peak reflectivity needs to be at least 40 dB (level 8). We say potential MCS because a complete definition of a MCS also includes a time dependency (see Section 5). Rather than thresholding the data arbitrarily, we are examining the entire spectrum of PSs, not just the potential MCSs, as discussed in the next section.

4. Survey of the mesoscale organization of precipitating systems

For the month of June '95, we identified and characterized all PSs. Note that time continuity is not checked, and the number of PSs reflects both the number of precipitation systems, and the number of times that they are sampled (at a 15 min interval) during their lifetime. We do not attempt to define a lifetime here, because we are not tracking a PSs. Rather, the total number of PSs, divided by the number of samples (2544, that is 88.3% of all possible samples for the month of June), gives an average number of precipitation systems that occurred at any time somewhere in the continental USA during June '95. The information we collected is as follows:

- the size distribution (in area units, km^2) of all PSs, for various threshold Z levels; the default is level 4 (20 dB); alternative cut-offs are levels 3 (15dB) and 5 (25 dB);
- a histogram of the convective fraction within all PSs, as well as the fraction of convective rainfall;
- the average dBZ (calculated in units of mm^6/m^3, ie linear Z) as well as the relectivity distribution;
- using the default threshold of level 4, display the following, for small, medium, and large size PSs:
    - diurnal variation

- geographical distribution
- spatial patterns (length, linearity, and orientation)

We define a small PS as 500 km^2 < A < 4,000 km^2, a medium-size PS is 4,000 km^2 < A < 32,000 km^2, and a large PS has an area exceeding 32,000 km^2. Some of the large-size PSs will qualify as mesoscale convective complexes (MCC), which are defined by means of satellite IR imagery. For an MCS to qualify as a MCC, its anvil (T<220K) needs to be at least 50,000km^2 (Maddox 1980).

The number of PSs drops off exponentially both with increasing PS size and increasing convective fraction. The scale factor in the exponential approximation was found to be 2,000 km^2 and 5%, respectively (ie the probability of encountering a PS of 2,000 km^2 is 2.7 times less than that of a PS of 500 km^2 , and the odds of finding a PS with 4-6% convection is 2.7 times less than that of a PS in which 0-2% of the pixels are convective). This argument provides an inductive, rather than ad-hoc definition of a MCS. Mesoscale convective systems are defined as those PSs that are of mesoscale dimensions (at least 2,000 km^2) and contain some convective activity (at least 5% of the pixels are convective).

We found that for June 1995, 22% of the PSs qualified as MCSs, yet these MCSs produced an estimated 84% of the overall rainfall. A clear diurnal oscillation occurs. For the entire contiguous USA, the number of PSs, and their convective fraction, peak at about 3pm local time, and they reach their minimum around 7 am. The amplitude of the diurnal cycle is 30-50% of the mean, both in terms of frequency and convective fraction. MCSs peak at a slightly later time, 4-5pm local time, and they are more common in the first half of the night. On a pixel-by-pixel basis, we find that the higher the radar reflectivity, the more intense the diurnal modulation. A slight phase shift is observed from the most intense echoes, which are most common around 4pm, to stratiform precipitation, which is most common at 6pm.

Some characteristic spatial patterns of PSs emerged. For instance we found that by far the most common orientation is SW-NE (some 60% of the PCs have a northeast limb between 30° and 70° from north), and that 80% of the PCs had an aspect ratio (length-to-width) between 3 and 8. MCSs tend to be more elongated than PSs in general. The mean length of MCSs and PSs is about 230 km and 120 km, respectively.

We also contrasted MCS/PC behavior in various geographical regions, in particular, the Great Plains region (with a focus on the Arkansas/Red River Basin), the Southeast, and Florida.

5. Conclusions

The methodology of MCS identification, and subsequent analysis of the US-wide composite radar reflectivity data for June '95, can be summarized as follows.

- A *precipitating system* (PS) is defined as an area (exceeding 500 km^2 in size) of spatially continuous reflectivities exceeding a certain threshold value.
- The higher this threshold reflectivity, the less noise, yet a reflectivity threshold over 20 dB will remove most large systems.
- The frequency of PSs drops off exponentially with increasing PS size.
- Mesoscale convective systems (MCSs) can be defined in various ways, as long as the definition includes a mesoscale dimension and a condition on convective activity. We propose that MCSs are those PSs that are at least 2,000 km^2 in size and have at least 5% convective pixels. This definition excludes 78% of all PSs.
- The fraction of PSs that qualify as MCSs increases with increasing system size. This suggests that the large systems are convectively driven. This result comes as a surprise; we expected that smaller systems would exhibit a larger convective fraction, on average.
- A clear diurnal cycle exists: in the afternoon there are more PSs and MCSs, and they both smaller and more intense.

- Small systems are most active in the early afternoon, while large systems are most active around sunset.
- Geographical differences are present, but they are not outstanding. For instance, PSs in Florida tend to be smaller and those in the Great Plains are larger and are more common towards sunset, but the differences are small.

6. Future work

A first extension of the work done during the summer faculty fellowship will be to repeat the same process for a longer time period, ideally as long as 4 years, ie the entire data set. This would make the results more significant in terms of a typical summer pattern. Also, we could analyse the entire seasonal cycle, and even examine interannual variability.

A complete definition of a MCS also includes a time dependency. Geerts (1997) suggested that a MCS should be recognized (according to the above spatial definitions) for at least 4 consecutive hours. This implies that the movement and evolution of PSs needs to be tracked in time. Visual inspection using time lapse movies easily allows assessment of the continuity of echo patterns, and readily identifies birth or decay, movement or expansion, merger or splitting. On computer this is more difficult, especially the merger and splitting of PSs constitutes a problem and demands complicated tracking software. We have defined the centerpoint to allow easier tracking of PSs.

The tracking of PSs and the description of their evolution (lifetime, convective vs stratiform phase, direction and speed of movement, evolution of size and reflectivity properies ...) is a second extension of this work.

Finally, it has been suggested that a similar analysis would be done on lightning data, which are available at the same time/space resolution. Lightning data are primarily an indicator of convective activity. The lightning data can be compared to reflectivity-estimated convective activity, and the two data sets can be combined to obtain a more comprehensive description of MCSs.

5. References

Biggerstaff, M.I. and R.A. Houze, Jr., 1991: Kinematic and precipitation structure of the 10-11 June 1985 squall line. *Mon. Wea Rev.*, **119**, 3035-3065.

Geerts B., 1997: Mesoscale convective systems in the Southeast: A survey. *Wea. and Forecasting*, accepted for publication.

Goodman S.J. and R. Raghavan, 1997: Multi-year characterization of rainfall over the Mississippi River Basin. Proposal in response to NRA-97-MTPE-GCIP.

Houze, R.A.,Jr., 1993: *Cloud Dynamics.* Academic Press, 573 pp.

Houze, R.A.,Jr. And C.P. Cheng, 1977: Radar characteristics of tropical convection observed during GATE: mean properties and trends over the summer season. *Mon. Wea. Rev.*, **105**, 964-980.

Knupp K.R., B. Geerts and S. Goodman, 1997: Structure of a small, vigorous mesoscale convective system. Part I: Formation, echo morphology and lightning behavior. **Mon. Wea Rev.**, in press.

Maddox, R.A. 1980: Mesoscale Convective Complexes. *Bull. Amer. Meteor. Soc.*, **61**, 1372-1387.

Mapes, B.E. and R.A. Houze, Jr., 1993: An integrated view of the 1987 Australian monsoon and its mesoscale convective systems. Part II: Vertical structure. *Quart. J. Royal Meteor. Soc.*, **119**, 733-754.

Steiner, M., R.A. Houze Jr., and S.E. Yuter, 1995: Climatological characterization of three-dimensional storm structure from operational radar and rain gauge data. *J. Appl. Meteor.*, **34**, 1978-2007.

Steiner, M. and R.A. Houze Jr., 1997: Sensitivity of estimated monthly convective rain fraction to the choice of Z-R relation. *J. Appl. Meteor.*, **36**, 452-462.

Summer Faculty Final Presentation:

Mars Mission Design Handbook

2009 – 2024 Opportunities

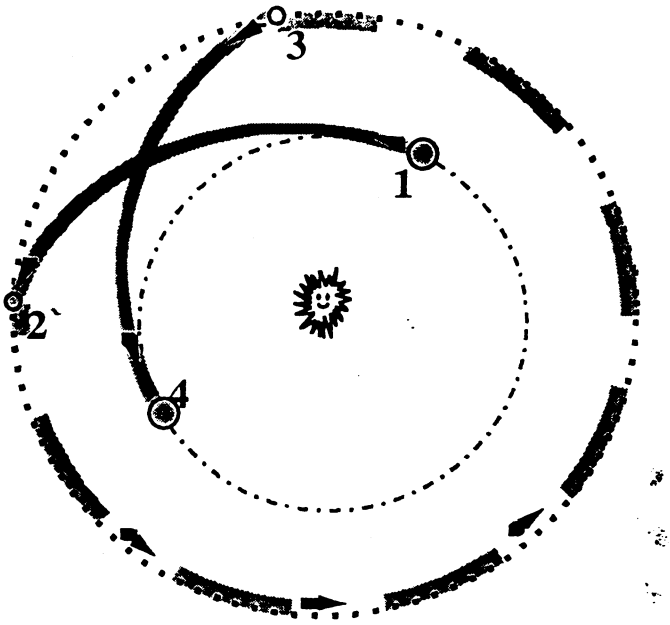

Capt. Lynnane George

Air Force Academy Faculty Instructor
Astronautical Engineering Dept.
NASA Summer Faculty / PD32

Wednesday
July 30th, 1997
2:30 – 3:20

CR 329

INTRODUCTION/OVERVIEW

Purpose: To provide a mission design handbook specifically designed for a Human Mars mission

2009-2024

ASSUMPTIONS

- Used general ground-rules for HMM study
- Split mission (2 cargo/1 piloted)
- Earth departure:
  - Launch from LEO (400 km circular)
  - Nuclear thermal propulsion (LH_2)
    - Isp = 931 secs, three 15,000 lb thrust engines
  - 2 perigee burns at departure

Human Mars Mission Architecture

Design Reference Mission: 2011 Opportunity

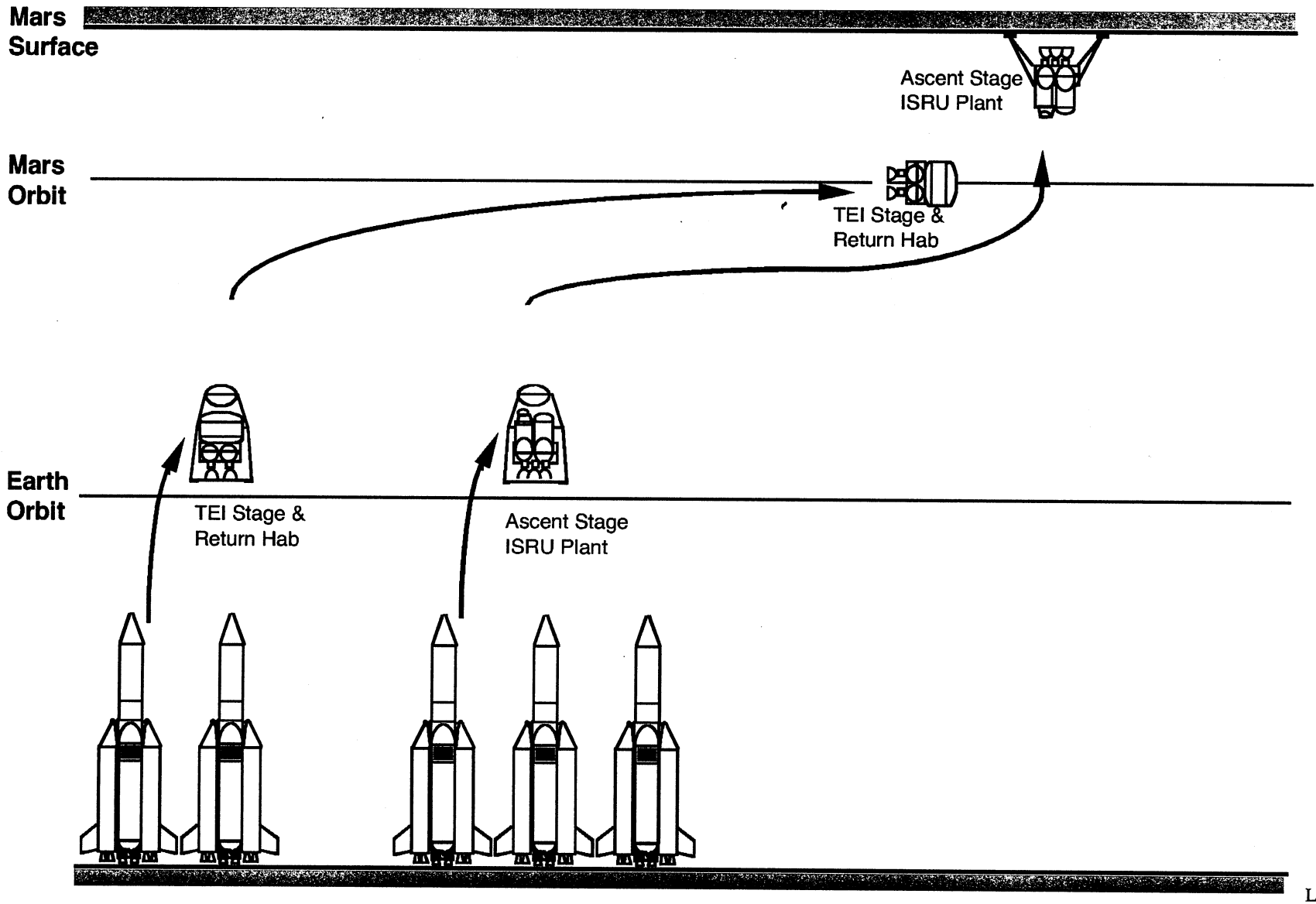

Four – Five 80 mt LV Launches

Larry Kos
MSFC / PD32
7/10/97

Human Mars Mission Architecture

Design Reference Mission: 2014 Opportunity

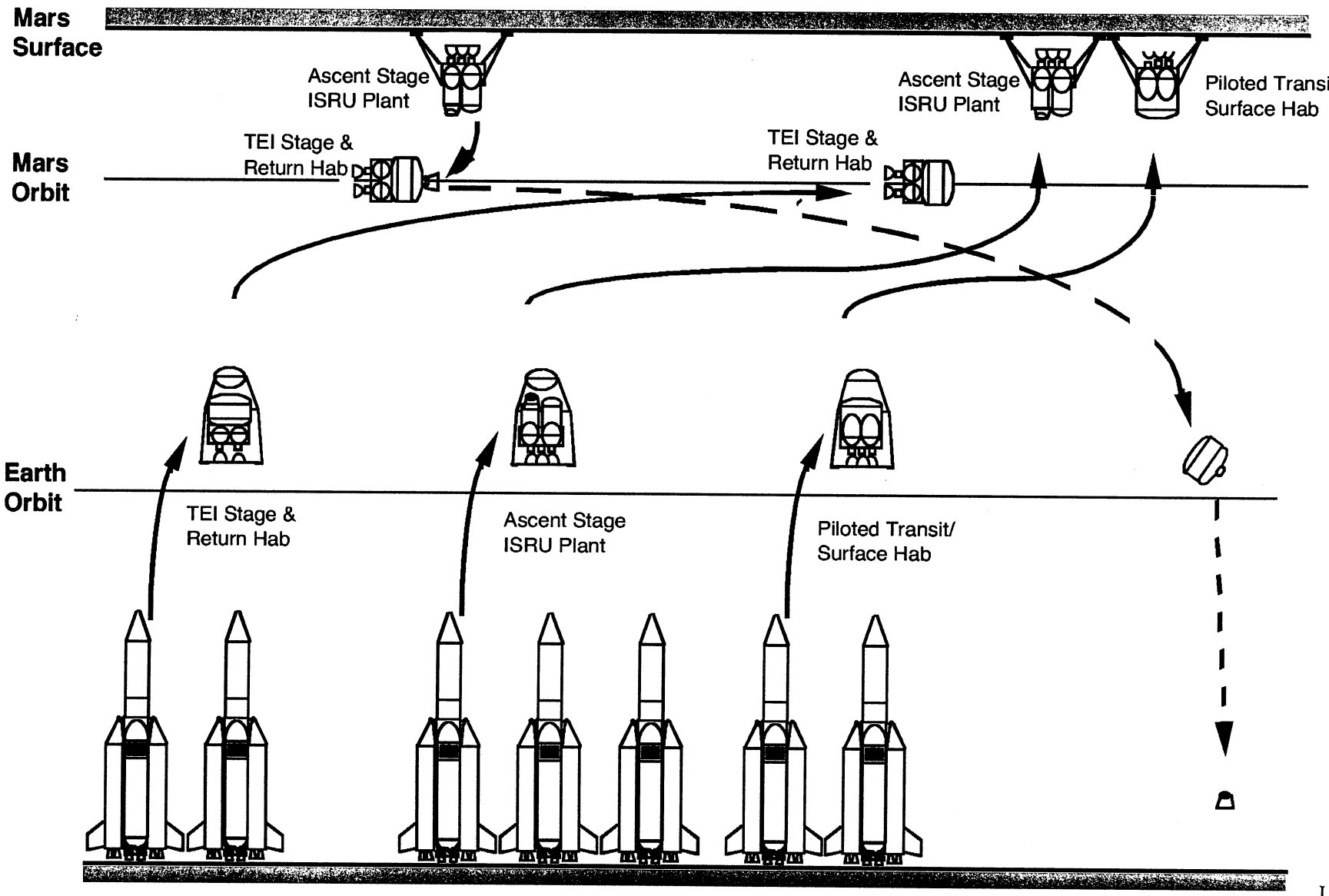

Two 80 mt Launches (Six – Seven 80 mt LV Launches to include backup vehicles)

Larry Kos
MSFC / PD32
7/10/97

ASSUMPTIONS

- Mars arrival
  - Aerocapture
    - arrival speed limit 8.7 km/s
  - 250 x 33,793 altitude
- Mars departure (piloted only)
  - Depart from same orbit
  - TEI (Lox/Methane)
    - Isp = 379 secs, two 15,000 lb thrust engines
- Ballistic reentry at Earth (piloted only)
  - Arrival speed limit 14.5 km/s

ASSUMPTIONS

- Cargo mission priority is minimum cost (minimum initial mass from LEO)
  - normally Type II
- Piloted missions limited to 180 days TOF each leg
  - normally type I

HMM 2014 Piloted DRM Trajectory

Flight Profile, 161 day Transit Out, 154 day Return

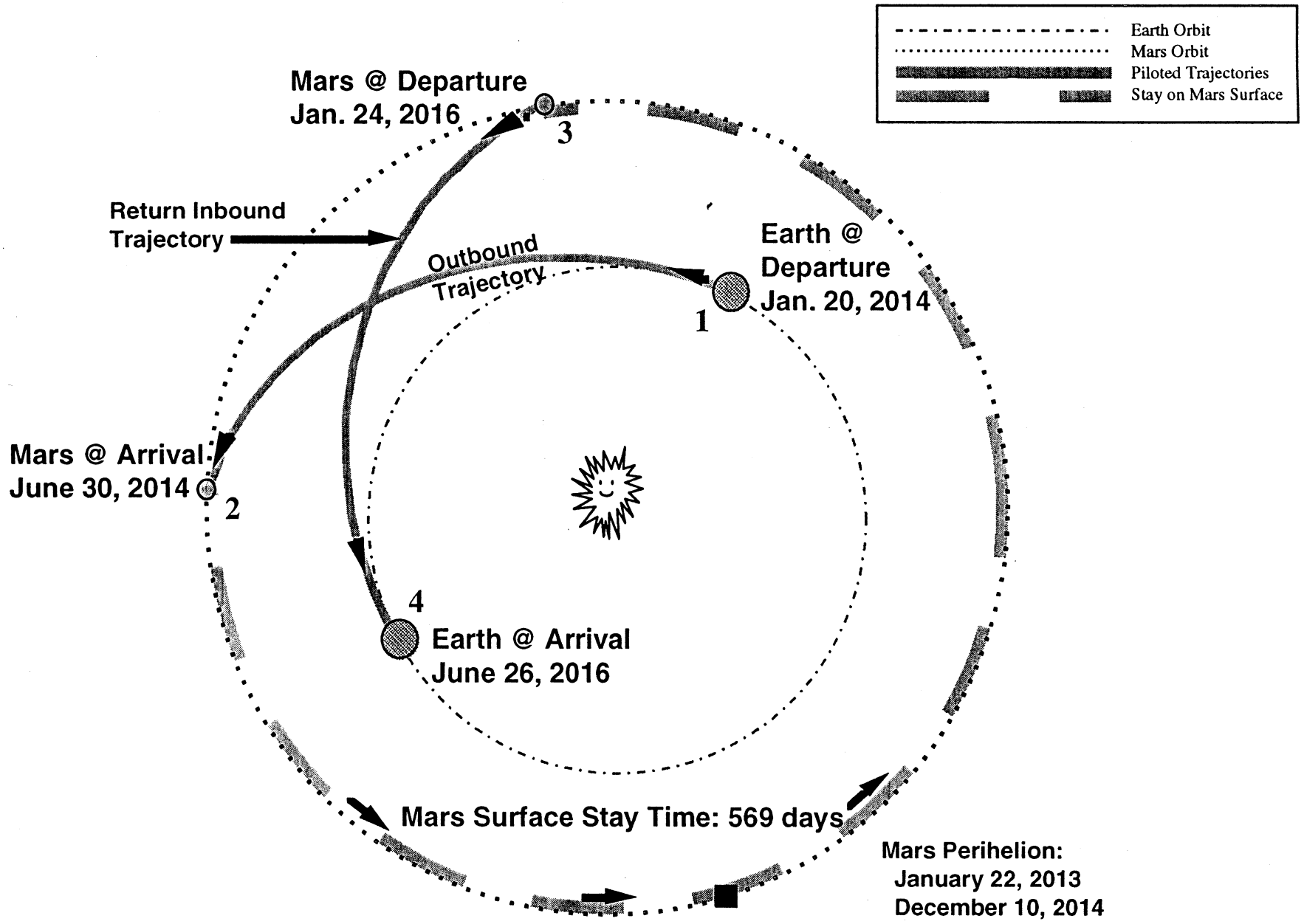

DESIGN REFERENCE MISSION TRAJECTORIES

Primary Cargo Mission Opportunities 2009:

Mission	Launch Date	TMI Delta V (m/s)	Velocity Losses (m/s)	C_3 (km^2/s^2)	Mars Arrival Date	TOF (days)
Cargo 1	11/8/11	3673	92	8.95	8/31/12	297
Cargo 2	11/8/11	3695	113	8.95	8/31/12	297

Primary Piloted Mission Opportunities 2014:

Launch Date	TMI Delta V (m/s)	Velocity Losses (m/s)	C_3 (km^2/s^2)	Mars Arrival Date	TOF (days)	Mars Stay (days)	Mars Departure Date	TEI Delta V (m/s)	Return Time (days)	Total Duration (days)
1/20/14	4019	132	15.92	6/30/14	161	573	1/24/16	1476	154	888
1/22/14	4018	131	15.92	7/21/14	180	568	2/9/16	1476	180	928
Window: 3 days							17 days			

TOOLS USED/APPROACH

- Mission Analysis Environment for Heliocentric High Thrust Missions (MAnE)
  - 1st developed mass models and used to verify
    - Older trajectories
    - JPL "porkchop" plots

Human Mars Mission: Design Reference Mission

DRM "Scrub v3.0" Architecture: 2011 / 2014 Opportunity

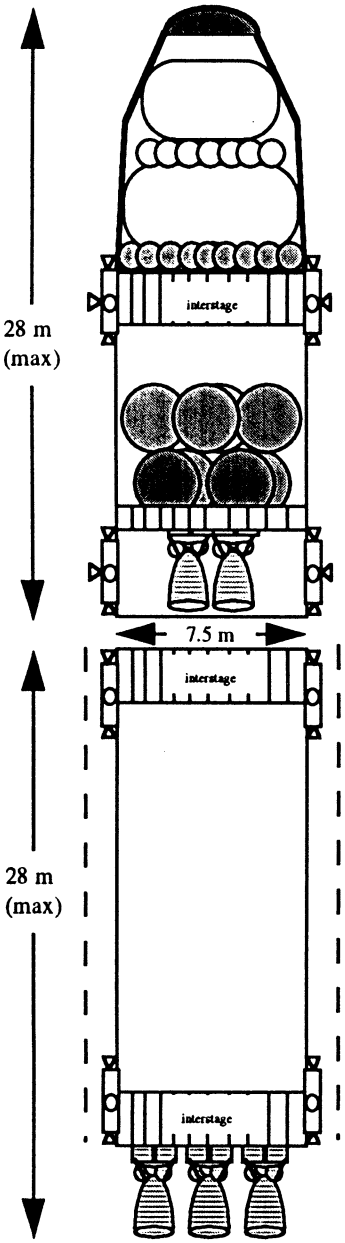

–62 days / TMI:

m_{ab} = 10.6 mt

m_{retHab} = 21.6 mt

TEI Stage (2 RL–10s):
(boil-off: 0.3%/mo ave.)
m_{dry} = 4.6 mt
m_p = 31.3 mt
24 RCS thrusters

m_{pyld} = 68.2 mt

–32 days / TMI:

MLI ETO shielding
L_{tank} = 20 m (typ)

TMI Stage:
(boil-off: 1.6%/mo LEO)
m_{dry} = 22.4 mt
m_p = 46.3 mt

m_{stage} = 68.7 mt

3 15 klb_f NTP engines
12 RCS thrusters

2011 TMI Stack 1: 136.9 mt

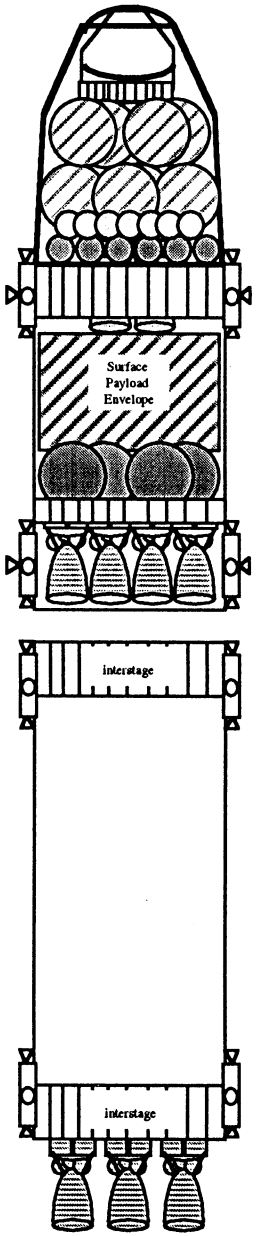

–92 days / TMI:

m_{ab} = 16.0 mt
m_{ecrv} = 5.5 mt

Ascent Stage (2):
m_{dry} = 2.6 mt
m_p = 38.2 mt

Surface Payload:
m_{cargo} = 32.5 mt
(incl. m_{LH2} = 4.5 mt)

Descent Stage (4):
m_{dry} = 4.2 mt
m_p = 17.1 mt
24 RCS thrusters

m_{pyld} = 77.9 mt

–2 days / TMI:

TMI Stage:
m_{dry} = 22.4 mt
m_p = 50.6 mt

m_{stage} = 73.0 mt

3 15 klb_f NTP engines
12 RCS thrusters

2011 TMI Stack 2: 150.8 mt

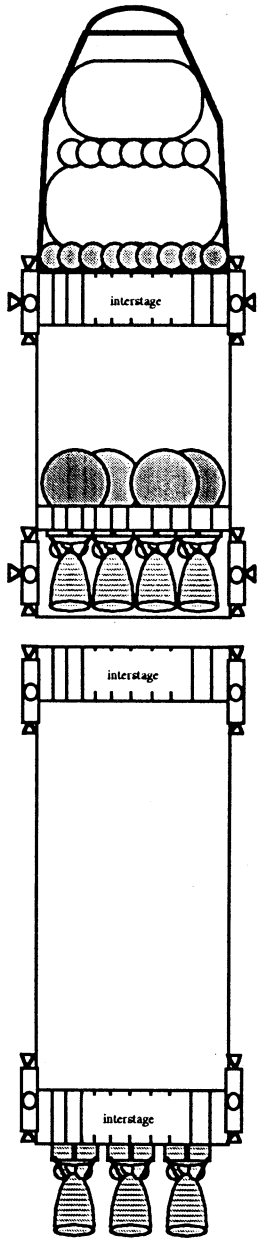

–62 days / TMI:

m_{ab} = 14.0 mt

m_{crew} = 0.5 mt

Surface Payload:
$m_{transHab}$ = 19.3 mt
m_{misc} = 9.8 mt

Descent Stage (4):
m_{dry} = 4.2 mt
m_p = 17.3 mt
24 RCS thrusters

m_{pyld} = 65.1 mt

–32 days / TMI:

TMI Stage:
m_{dry} = 25.6 mt
m_p = 51.7 mt

m_{stage} = 77.3 mt

3 15 klb_f NTP engines
12 RCS thrusters

2014 TMI Stack (5): 142.4 mt

Larry Kos
MSFC/PD32
v3.1.1, 7/10/97

TOOLS USED

- MAnE modeling
  - Inputs
    - Mass models (DRM used)
    - Estimated departure and arrival dates
    - End criteria (net spacecraft delivery mass, TOF, departure or arrival excess speed)
    - Optimization criteria (minimum initial mass, TOF, or total Delta V)

TOOLS USED

- MAnE
  - Output
    - Optimal trajectory along with departure and arrival data
      - Delta Vs
      - Velocity losses
      - Departure and arrival excess speeds

Cargo mission Departure Energies

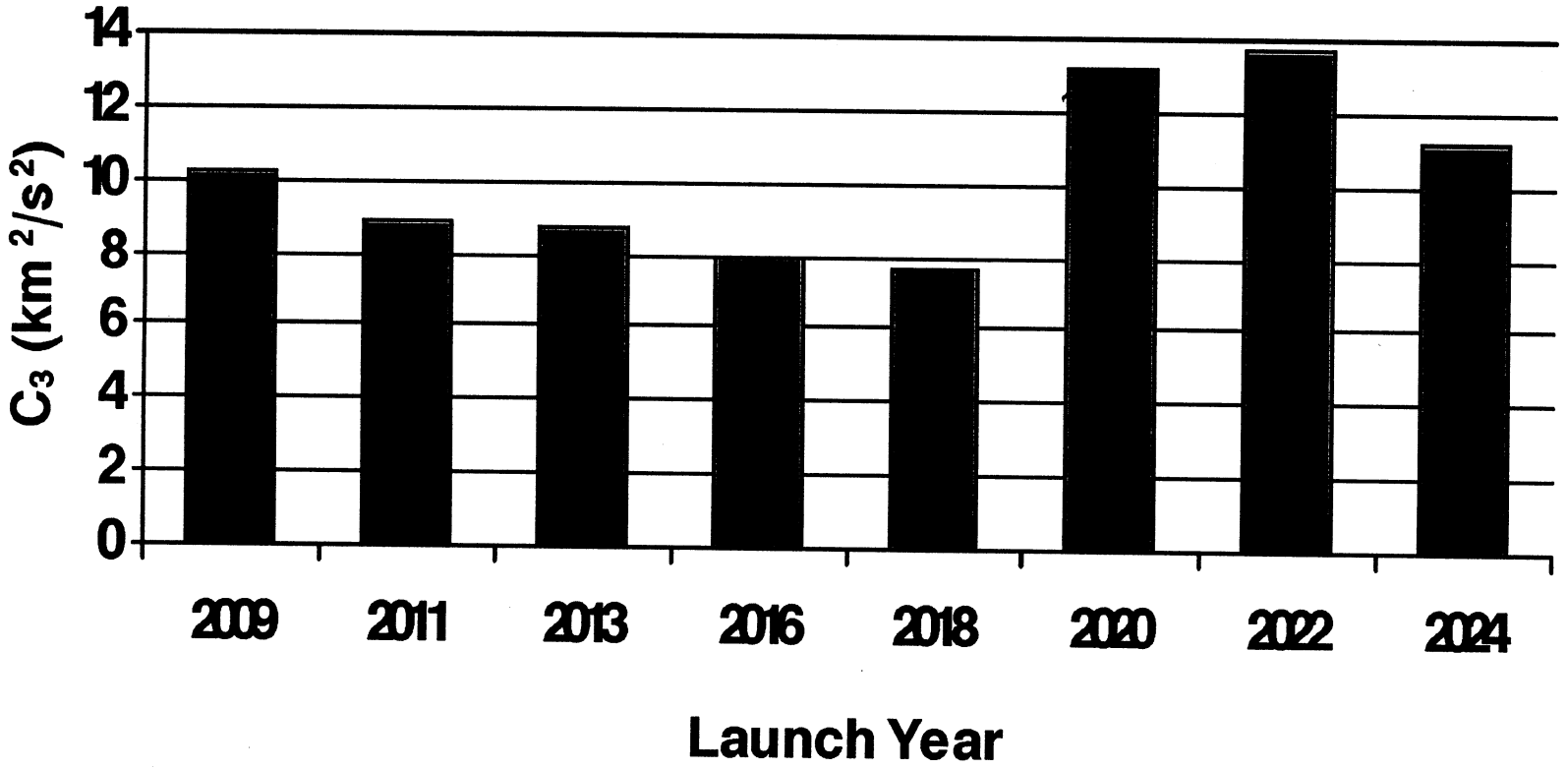

Cargo mission Durations

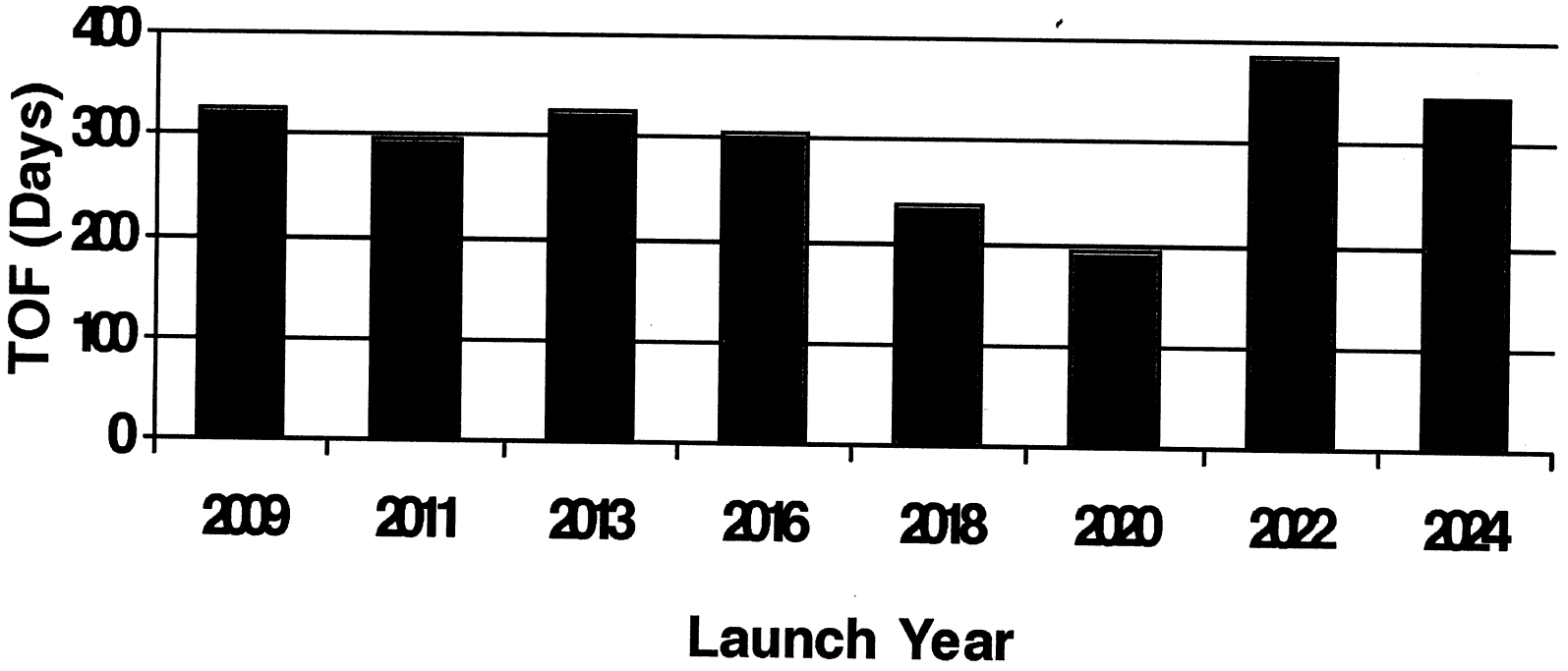

Piloted Optimal Mission Departure Energies

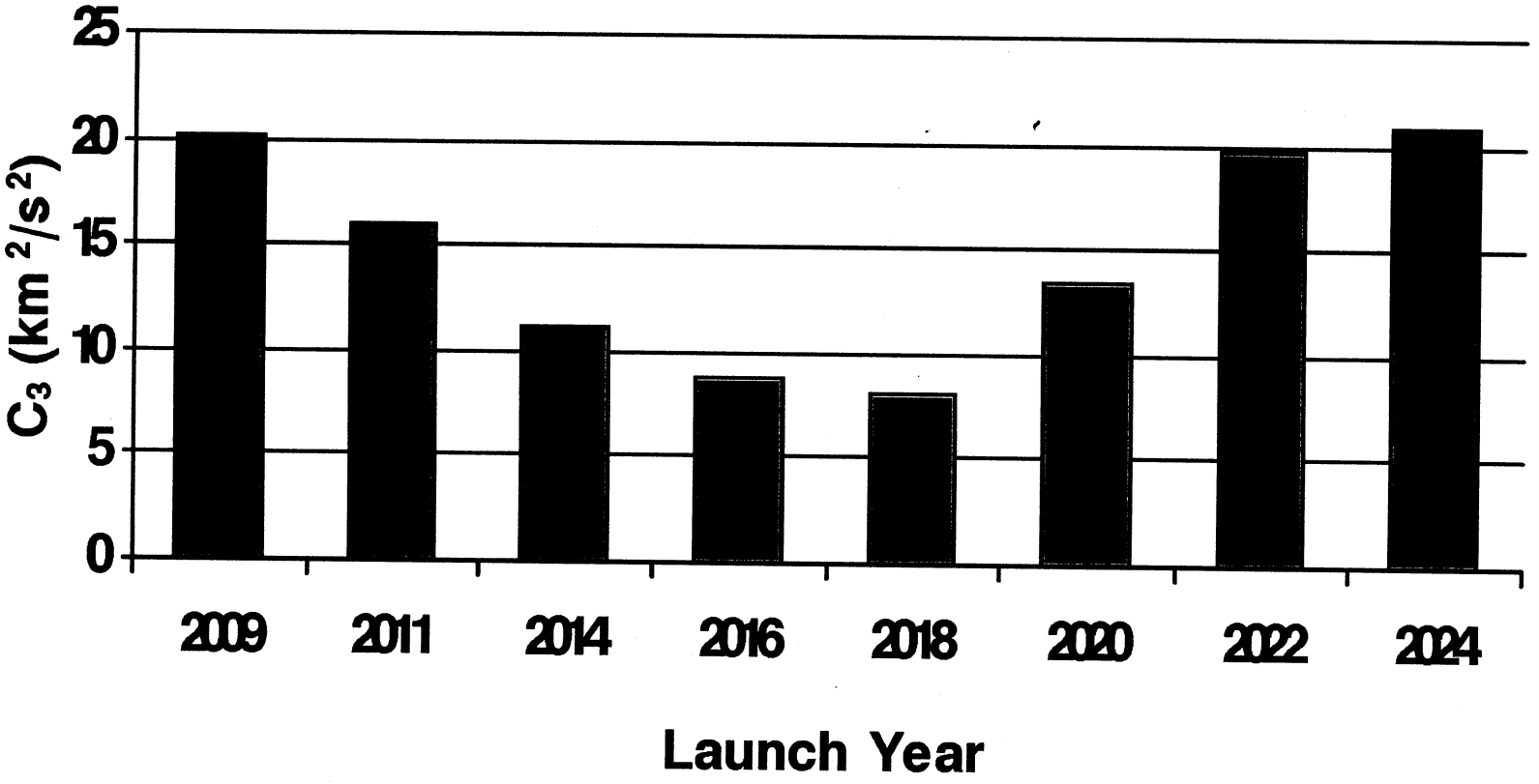

TOOLS USED/APPROACH

- Began developing baseline trajectories
  - Developed "porkchop" plots showing C_3s and other parameters for each opportunity
  - Used plots to determine starting areas for optimization of trajectories
    - Cargo missions: Minimum initial mass in LEO
    - Piloted missions:
      - Minimum initial mass for 180 day TOF
      - Minimum in-flight time at 2011 C_3s

Earth-Mars Trajectories

2011 Conjunction Class

C_3 (Departure Energy) km^2/s^2

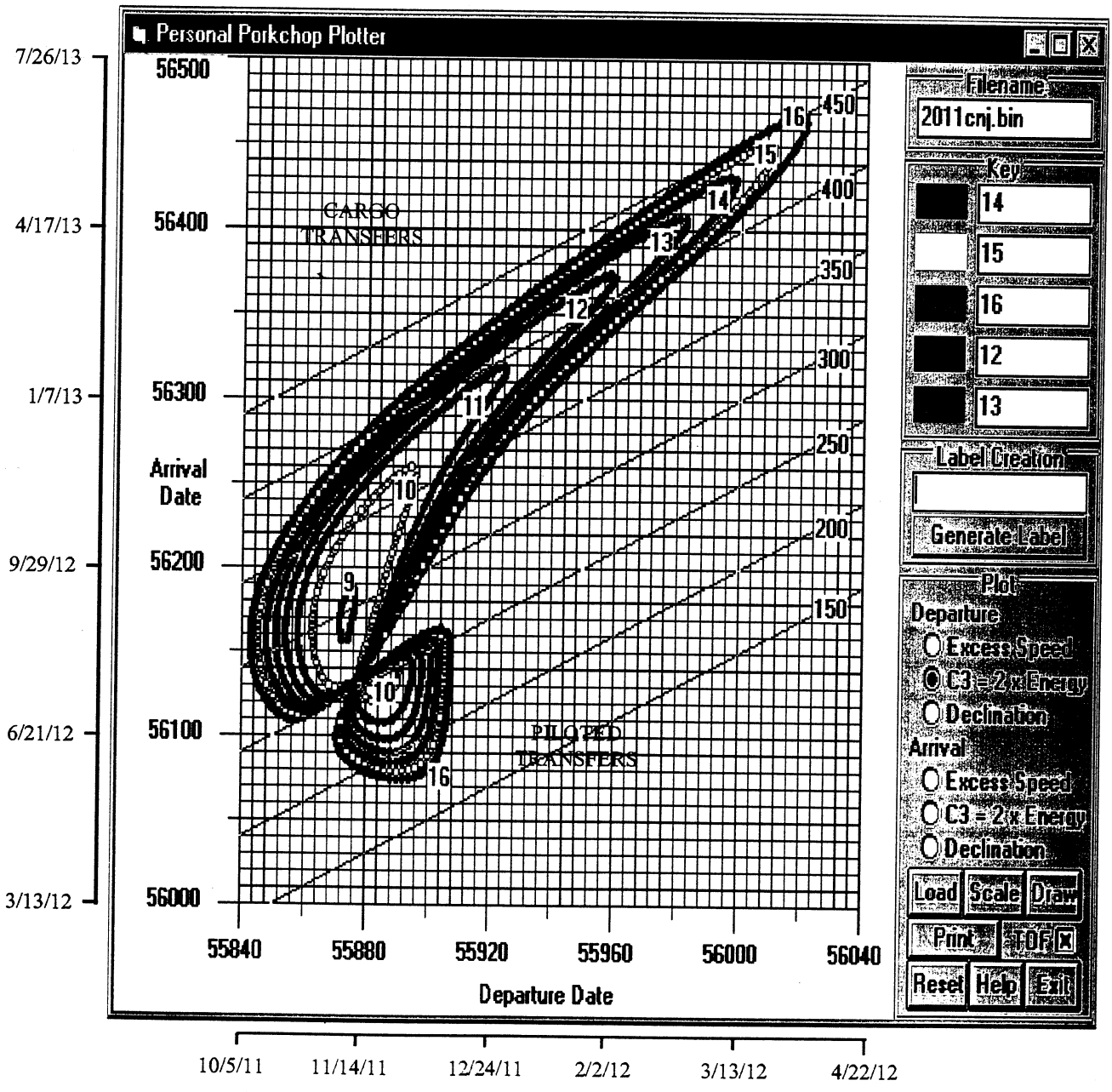

Earth-Mars Trajectories
2013/14 Conjunction Class
Departure Excess Speed (km/s)

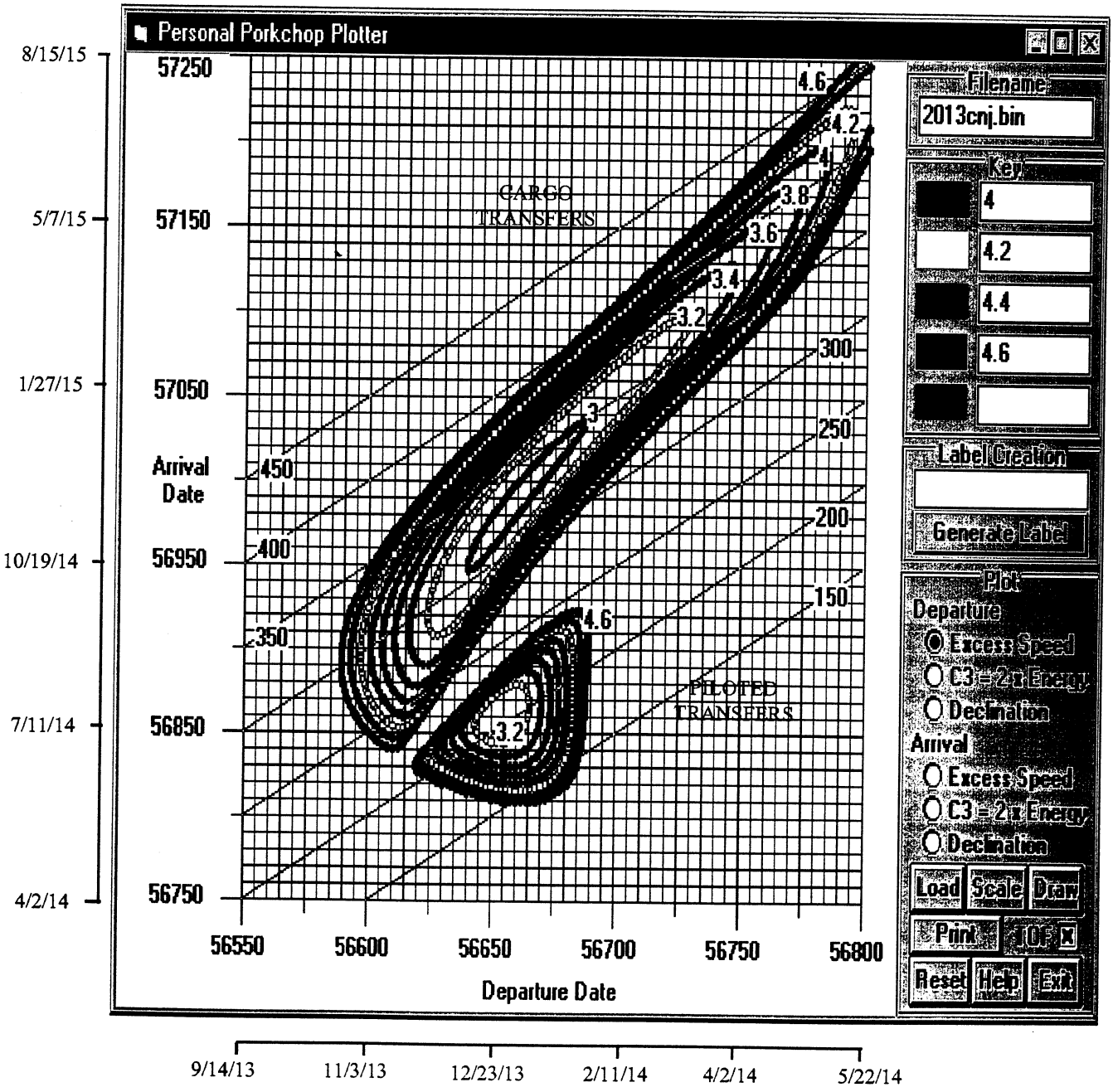

Earth-Mars Trajectories
2013/14 Piloted Missions
Baseline Mission Designed to 2011 Departure Excess Speed

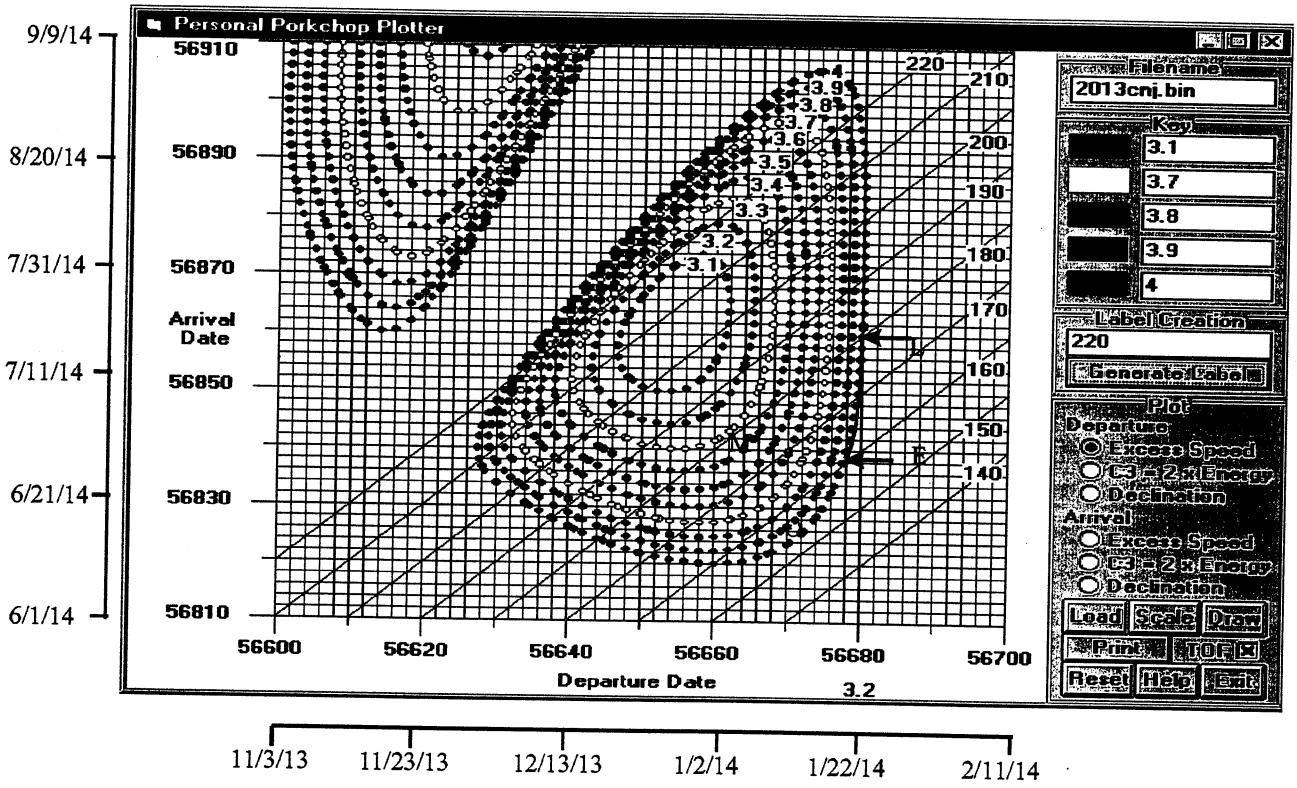

E = Minimum flight time trajectory using 2011 Piloted Mission Departure Excess Speed (3.99 km/s) and while maintaining acceptable Mars entry velocity needed for aerobraking.
Departure: 1/20/14 (56678J) Arrival: 6/30/14 (56839J)

L = Latest possible trajectory to keep flight time limited to 180 days. The acceptable window of opportunity for launch will be along the arc from E to L
Latest Departure: 1/22/14 (56679J) Arrival: 7/21/14 (56859J)

O = Minimum flight time trajectry using 2011 Piloted Mission Departure Excess Speed (3.99 km/s). Mars arrival excess speed = 8.56 km/sec, which exceeds the limit of 7.167 km/sec

M = Minimum departure excess speed and initial mass trajectory for 2014 opportunity for a flight time of 180 days
Departure: 1/4/14 (56662J) Arrival: 7/3/14 (56842)

REDUCED PILOTED MISSION DURATIONS

Year	Mission Duration	Mars Arrival Velocity (km/s)	Earth Arrival Velocity (km/s)	Departure window (days)	Return window (days)
2014	161*	7.17	8.91	3	17
2016	137*	7.17	8.91	8	30
2018	115	6.85	4.38	27	10
2020	151	4.27	5.28	12	1

* Arrival excess speed at Mars exceeded at shorter flight times

Msn Type	Launch Date (m/d/yy)	TMI Delta V (m/s)	Vel Losses (m/s)	Mars Arrival Date (m/d/yy)	Outbd Flight Time (days)	Mars Stay Time (days)	Mars Dep Date (m/d/yy)	TEI Delta V (m/s)	Return Time (days)	Return Date (m/d/yy)	Total Msn Durn (days)	C_3 (km/s)	Total Delta Vs (m/s)
Cargo 1	10/14/09	3,737	97	9/6/10	327	—	—	—	—	—	—	10.27	3,737
Cargo 2	10/14/09	3,760	120	9/6/10	327	—	—	—	—	—	—	10.27	3,760
Piloted	10/30/09	4,219	153	4/28/10	180	536	10/16/11	1,780	180	4/13/12	896	20.06	5,999
Cargo 1	11/8/11	3,673	92	8/31/12	297	—	—	—	—	—	—	8.95	3,673
Cargo 2	11/8/11	3,695	113	8/31/12	297	—	—	—	—	—	—	8.95	3,695
Piloted	12/2/11	4,019	132	5/30/12	180	538	11/19/13	1,476	180	5/18/14	898	15.92	5,495
Cargo1	12/31/13	3,665	91	11/24/14	328	—	—	—	—	—	—	8.78	3,665
Cargo 2	12/31/13	3,686	112	11/24/14	328	—	—	—	—	—	—	8.78	3,686
Piloted	1/20/14	4,019	132	6/30/14	161	573	1/24/16	1,476	154	6/26/16	888	15.92	5,495
Cargo 1	3/21/16	3,627	88	1/20/17	305	—	—	—	—	—	—	7.99	3,627
Cargo 2	3/21/16	3,647	109	1/20/17	305	—	—	—	—	—	—	7.99	3,647
Piloted	3/14/16	4,019	132	7/29/16	137	630	4/20/18	1,476	130	8/28/18	897	15.92	5,495
Cargo 1	5/17/18	3,615	87	1/8/19	236	—	—	—	—	—	—	7.74	3,615
Cargo 2	5/17/18	3,635	108	1/8/19	236	—	—	—	—	—	—	7.74	3,635
Piloted	5/18/18	4,019	132	9/10/18	115	651	6/22/20	1,314	158	11/27/20	924	15.92	5,333
Cargo 1	7/18/20	3,877	109	1/27/21	193	—	—	—	—	—	—	13.17	3,877
Cargo 2	7/18/20	3,903	135	1/27/21	193	—	—	—	—	—	—	13.17	3,903
Piloted	7/24/20	4,019	132	12/22/20	151	586	7/31/22	1,706	180	1/27/23	917	15.92	5,725
Cargo 1	9/14/22	3,906	112	10/2/23	383	—	—	—	—	—	—	13.79	3,906
Cargo 2	9/14/22	3,933	138	10/2/23	383	—	—	—	—	—	—	13.79	3,933
Piloted	9/10/22	4,198	152	3/9/23	180	543	9/2/24	1,860	180	3/1/25	903	19.63	6,058
Cargo 1	10/5/24	3,782	101	9/15/25	345	—	—	—	—	—	—	11.19	3,782
Cargo 2	10/5/24	3,805	124	9/15/25	345	—	—	—	—	—	—	11.19	3,805
Piloted	10/17/24	4,257	158	4/15/25	180	535	10/2/26	1,841	180	3/31/27	895	20.85	6,098

ADDITIONAL STUDIES

- Velocity losses for various Thrust-to-weight ratios
- Piloted total time-of-flight trades
- All chemical configurations (LOx/LH_2)

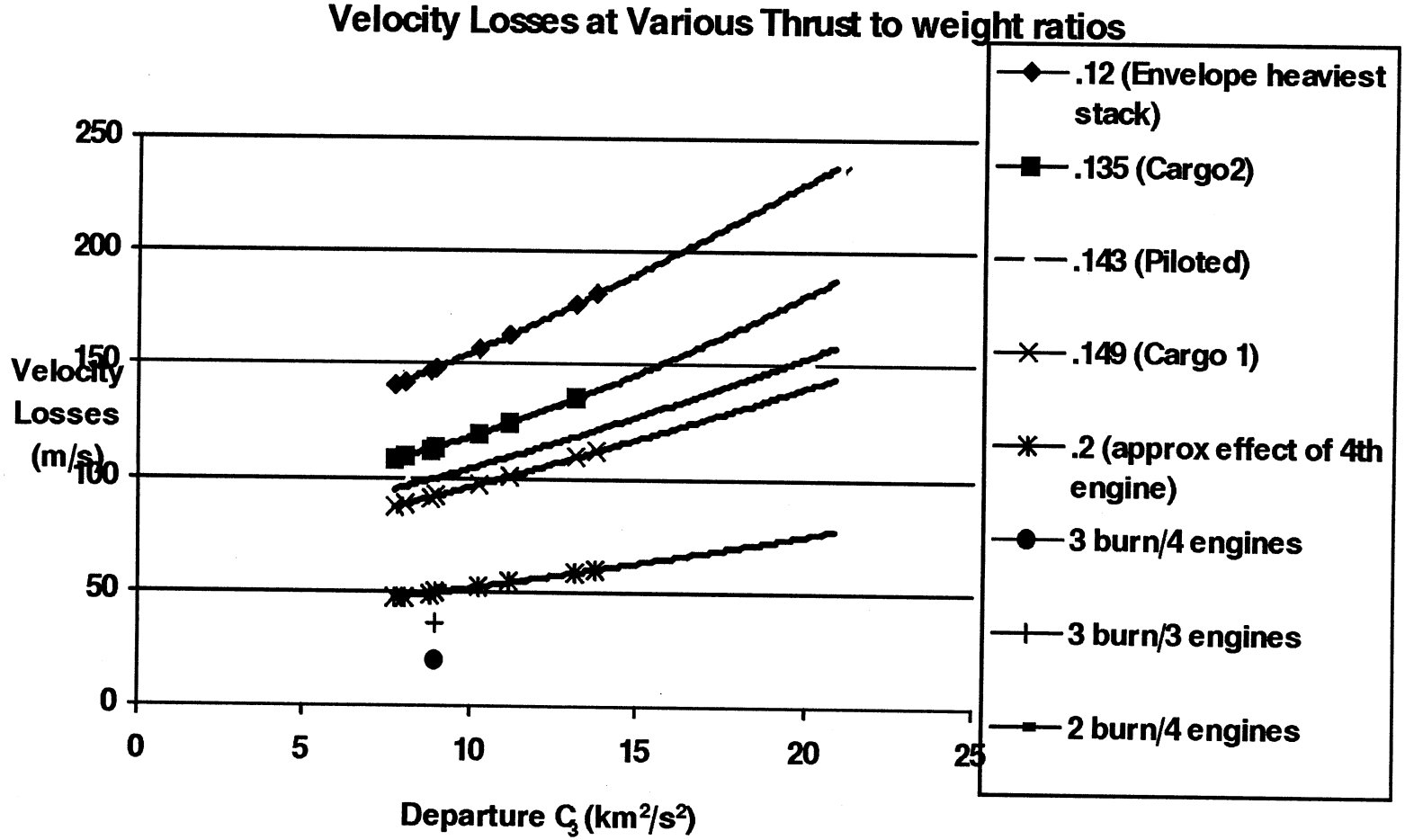
Velocity Losses at Various Thrust to weight ratios
Velocity Losses (m/s)
250
200
150
100
50
0
0
5
10
15
20
25
Departure C_3 (km^2/s^2)
.12 (Envelope heaviest stack)
.135 (Cargo2)
.143 (Piloted)
.149 (Cargo 1)
.2 (approx effect of 4th engine)
3 burn/4 engines
3 burn/3 engines
2 burn/4 engines

TIME-OF-FLIGHT TRADES - 2014

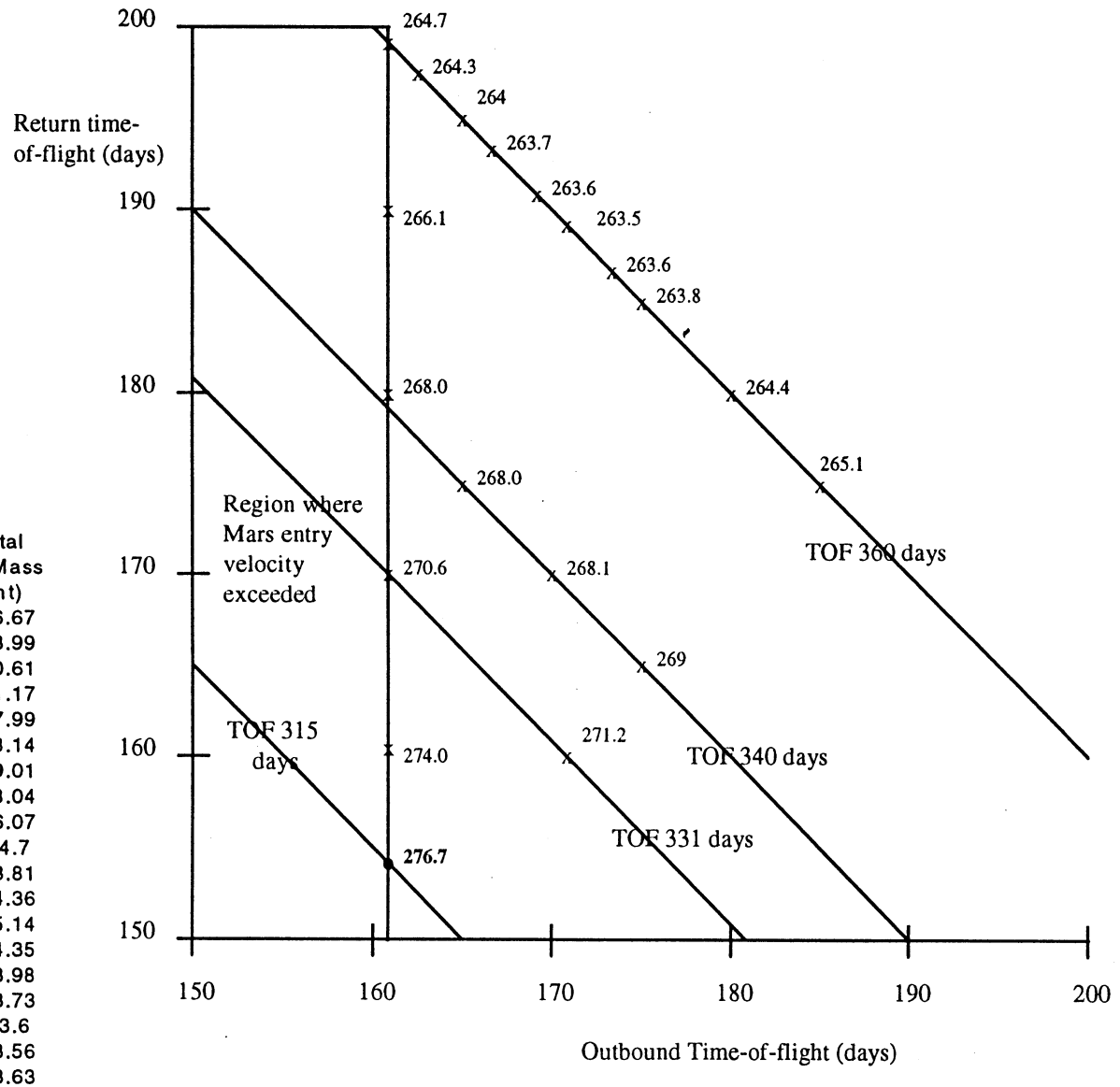

PLOT DATA:

TOF Outbnd (days)	TOF Inbnd (days)	Total TOF (days)	Total InitMass (mt)
161	154	315	276.67
161	160	321	273.99
161	170	331	270.61
171	160	331	271.17
165	175	340	267.99
170	170	340	268.14
175	165	340	269.01
161	180	341	268.04
161	190	351	266.07
161	199	360	264.7
175	185	360	263.81
180	180	360	264.36
185	175	360	265.14
163	197	360	264.35
165	195	360	263.98
167	193	360	263.73
169	191	360	263.6
171	189	360	263.56
173	187	360	263.63

2014 Tradeoffs/Launch Dates

TOF Outbnd (days)[1]	Dep Date	TMI Prop Reqd (mt)	Earth Minit (mt)[2]	Prop Redn (mt)[3]	Total TMI Mass (mt)[4]	TOF Inbnd (days)	Dep Date	Total TOF (days)	TEI Prop Reqd (mt)	Prop Redn (mt)[5]	Cargo 1 Delivery (mt)[6]	Cargo 1 Minit (mt)	Total Init Mass (mt)[7]	Total Delta	
161	**1/20/14**	**50.43**	**141.19**	**0**	**76.086**	**154**	**1/24/16**	**315**	**18.386**	**0**	**57.589**	**135.48**	**276.672**	**0**	**Baseline**
161	1/20/14	50.43	141.19	0	76.086	160	1/20/16	321	16.678	-1.708	55.881	132.8	273.986	-2.686	
161	1/20/14	50.43	141.19	0	76.086	170	1/14/16	331	14.421	-3.965	53.624	129.42	270.611	-6.061	
171	1/9/14	47.618	138.38	-2.812	73.274	160	1/20/16	331	16.678	-1.708	55.881	132.8	271.174	-5.498	
165	1/16/14	49.017	139.78	-1.413	74.673	175	1/11/16	340	13.503	-4.883	52.706	128.21	267.985	-8.687	
170	1/10/14	47.796	138.56	-2.634	73.452	170	1/14/16	340	14.421	-3.965	53.624	129.58	268.136	-8.536	
175	1/6/14	47.096	137.86	-3.334	72.752	165	1/17/16	340	15.472	-2.914	54.675	131.15	269.008	-7.664	
161	1/20/14	50.43	141.19	0	76.086	180	1/7/16	341	12.7	-5.686	51.903	126.85	268.038	-8.634	
161	1/20/14	50.43	141.19	0	76.086	190	1/1/16	351	11.382	-7.004	50.585	124.88	266.067	-10.61	
161	1/20/14	50.43	141.19	0	76.086	199	12/27/15	360	10.468	-7.918	49.671	123.51	264.7	-11.97	
175	1/6/14	47.096	137.86	-3.334	72.752	185	1/4/16	360	11.997	-6.389	51.2	125.96	263.812	-12.86	
180	1/4/14	46.596	137.36	-3.834	72.252	180	1/7/16	360	12.7	-5.686	51.903	127.01	264.363	-12.31	
185	1/3/14	46.168	136.93	-4.262	71.824	175	1/11/16	360	13.503	-4.883	52.706	128.21	265.136	-11.54	
163	1/18/14	49.671	140.43	-0.759	75.327	197	12/28/15	360	10.652	-7.734	49.855	123.92	264.348	-12.32	
165	1/16/14	49.017	139.78	-1.413	74.673	195	12/29/15	360	10.846	-7.54	50.049	124.21	263.984	-12.69	
167	1/14/14	48.46	139.22	-1.97	74.116	193	12/30/15	360	11.051	-7.335	50.254	124.51	263.734	-12.94	
169	1/12/14	47.996	138.76	-2.434	73.652	191	1/1/16	360	11.269	-7.117	50.472	124.84	263.596	-13.08	
171	1/9/14	47.618	138.38	-2.812	73.274	189	1/2/16	360	11.498	-6.888	50.701	125.18	263.56	-13.11	
173	1/7/14	47.323	138.08	-3.107	72.979	187	1/3/16	360	11.741	-6.645	50.944	125.55	263.628	-13.04	

Notes:

1) Italicized trajectories have a constraint that the arrival velocity at Mars = 7.167 km/s (otherwise would be greater)
2) Minitial for piloted outbound = 90.76 mt + TMI propellant required (from MAnE run for baseline trajectory)
3) Propellant reduction for Mars outbound = 50.43 - propellant required (from MAnE run for baseline trajectory)
4) Total TMI mass = 25.6 mt (dry weight of TMI engine) + propellant required
5) Propellant reduction for Earth return flight = 18.386 - propellant required (from MAnE run for baseline trajectory)
6) Cargo 1 delivery required = Total payload delivery to Mars (57.589 mt) - propellant reduction
7) Total Departure Initial mass in Low Earth orbit = piloted outbound + cargo 1 missions

ALL CHEMICAL PROPULSION

- Chemical TMI Stage (LOx/LH_2)
  - Isp 480 secs, thrust 100,000 lbs, dry mass 18.3mt

	Cargo 1	Cargo 2	Piloted
Mass (mt)	190.47	211.84	196.9
T/W	.238	.214	.230
Aerobrake (mt)	10.6	16	14.04
Delta V (m/s)	3606	3612	3920
Vel losses	24	30	33

LESSONS LEARNED

- Classroom versus application
- Exposure to NASA
- Handbook

2018 Opportunities

Msn Type	Launch Date	TMI Delta V	Vel Losses	Mars Arrival Date	Outbd Flight Time	Mars Stay Time	Mars Dep Date	TEI Delta V	Return Time	Return Date	Total Msn Durn	C_3	Total Delta Vs	Dep Vinf Earth	Arrival Vinf Mars	Arrival Vel@ Mars	Dep Vinf Mars	Arrival Vinf Earth	Arrival Vel@ Earth
	(m/d/yy)	(m/s)	(m/s)	(m/d/yy)	(days)	(days)	(m/d/yy)	(m/s)	(days)	(m/d/yy)	(days)	(km/s)	(m/s)	(km/s)	(km/s)	(km/s)	(km/s)	(km/s)	(km/s)
Piloted[1]	5/8/18	3,641	97	11/4/18	180	586	6/12/20	1,314	180	12/9/20	946	8.11	4,955	2.8475	3.256	5.909	3.419	3.498	6.046
Cargo 1	**5/17/18**	**3,615**	**87**	**1/8/19**	**236**	—	—	—	—	—	—	**7.74**	**3,615**	2.7824	3.263	5.914	---	---	---
Cargo 2	**5/17/18**	**3,635**	**108**	**1/8/19**	**236**	—	—	—	—	—	—	**7.74**	**3,635**	2.7824	3.263	5.914	---	---	---
Piloted	**5/18/18**	**4,019**	**132**	**9/10/18**	**115**	**651**	**6/22/20**	**1,314**	**158**	**11/27/20**	**924**	**15.92**	**5,333**	3.9894	6.848	8.439	3.688	4.385	6.599
Piloted[2]	6/13/18	4,019	132	12/10/18	180	569	7/1/20	1,476	180	12/28/20	929	15.92	5,495	3.9894	6.848	8.439	3.688	3.025	5.785

1) Optimal piloted trajectory (minimum initial mass)
2) Latest possible launches designed to 2011 C_3s/180 day TOF

27 day Earth-Mars Departure Window:

Depart:	TOF	Arrive:
5/18/18	115	9/10/18
6/13/18	180	2/10/18

10 day Mars-Earth Return Window:

Depart:	TOF	Arrive
6/22/20	157	11/27/20
7/1/20	180	12/28/20

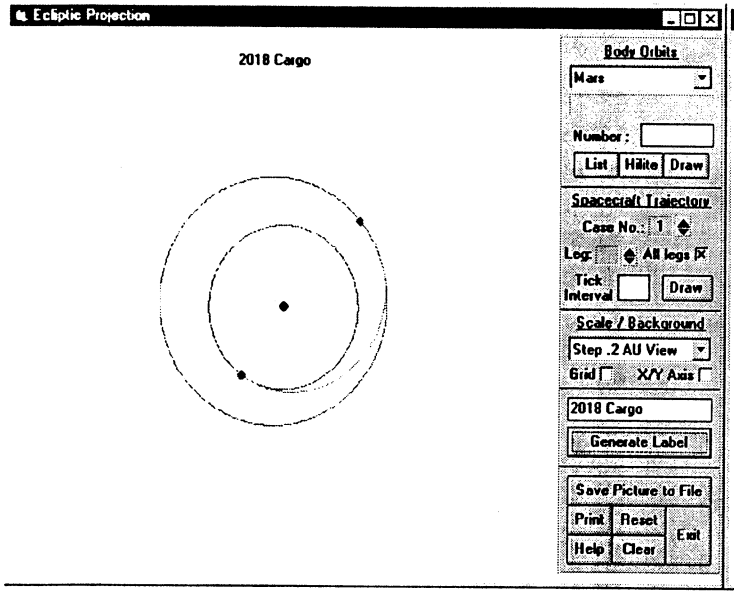

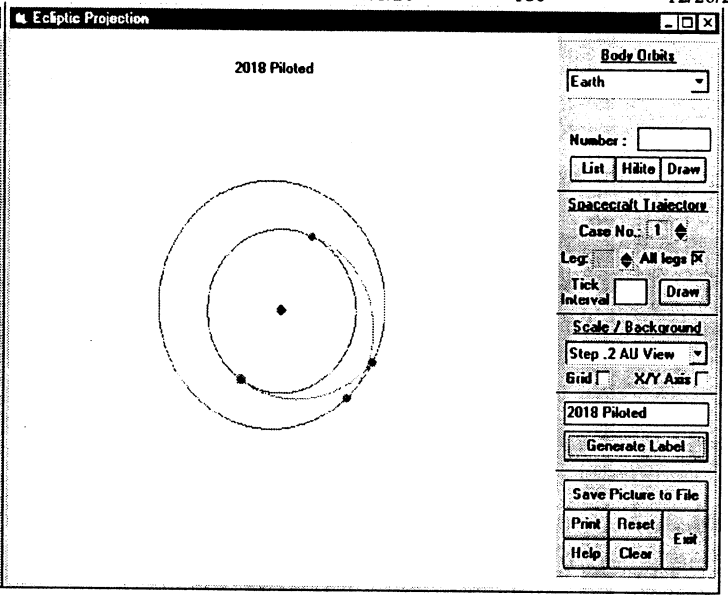

TABLE OF CONTENTS

INTRODUCTION 5

HUMAN MARS DESIGN REFERENCE MISSION OVERVIEW 5

GENERAL TRAJECTORY CHARACTERISTICS 7

MISSION OPPORTUNITIES 12

ADDITIONAL STUDIES AND APPENDIX INFORMATION 20

DESCRIPTION OF TRAJECTORY CHARACTERISTICS 24

EARTH DEPARTURE VARIABLES 26
MARS ARRIVAL VARIABLES 26
MARS DEPARTURE VARIABLES 27
EARTH ARRIVAL VARIABLES 27

CONCLUSIONS 27

REFERENCES 28

ACKNOWLEDGMENTS 29

APPENDICES 29

APPENDIX A 29
APPENDIX B: FLIGHT TIME STUDIES 138
APPENDIX C: GRAVITY LOSS STUDIES 141
APPENDIX D: FREE RETURN TRAJECTORIES 141
APPENDIX F: ASSUMPTIONS 143
APPENDIX G: OVERVIEW OF MANE 145
APPENDIX H: VERIFICATION OF MANE RESULTS 147

1997

NASA/ASEE SUMMER FACULTY FELLOWSHIP PROGRAM

MARSHALL SPACE FLIGHT CENTER
THE UNIVERSITY OF ALABAMA IN HUNTSVILLE

OPTIMAL CONTROLLER DESIGN FOR THE MICROGRAVITY ISOLATION MOUNT (MIM)

Prepared By:	R. David Hampton, Ph.D., P.E.
Academic Rank:	Assistant Professor
Institution and Department:	McNeese State University Engineering Department (Mechanical)

NASA/MSFC:

Team:	Precision and Pointing Team
Branch:	Flight Dynamics, Precision Pointing, and Mechanical Systems Control Branch
Division:	Guidance and Control Systems Division
Laboratory:	Structures and Dynamics Laboratory

MSFC Colleague:	Mark S. Whorton

Introduction

Acceleration measurements on the U.S. Space Shuttle and the Russian Mir Space Station show acceleration environments that are noisier than expected (DeLombard et al., 1997). The acceleration environment on the International Space Station (ISS) will likewise not be as clean as originally anticipated; the ISS is unlikely to meet its microgravity requirements without the use of isolation systems (DeLombard et al., 1997, and System Specification (no author), 1995). While the quasi-static acceleration levels due to such factors as atmospheric drag, gravity gradient, and spacecraft rotations are of the order of several micro-g, the vibration levels above 0.01 Hz are likely to exceed 300 micro-grams, with peaks typically reaching milli-g levels (DelBasso, 1996). These acceleration levels are sufficient to cause significant disturbances to many science experiments that have fluid or vapor phases, including a large class of materials science experiments (Nelson, 1991).

The Microgravity Isolation Mount (MIM) is a six-degree-of-freedom (6-DOF) magnetic-levitation system which was designed by the Canadian Space Agency (CSA). Its purpose is to isolate experiments from the high-frequency (>0.01 Hz) vibrations on the Space Shuttle, Mir, and ISS, while passing the quasi-static (<0.01 Hz) accelerations to the experiment (Tryggvason, 1994). The performance limit depends primarily on the character of the umbilical required between the MIM base (stator) and the MIM flotor on which the experiment is mounted. The emphasis with the MIM design is on isolation at the experiment level, with isolation ideally accomplished on only the sensitive elements of an experiment; this limits the need for a heavy umbilical. In the current implementation, the umbilical provides power to experiments mounted on the flotor, along with data-acquisition and control services (Tryggvason et al., 1997).

The first MIM unit was launched in the Priroda laboratory module which docked with Mir in April 1996. The system has been operational on Mir since May 1996, and has supported several materials science experiments. An upgraded system (MIM II) will be flown on the U.S. Space Shuttle Discovery on mission STS-85 in August 1997.

MIM (both the original and the upgraded unit) consists of two major components: a fixed stator and a free flotor. The system includes eight wide-gap Lorentz-force (voice-coil) actuators with the magnets on the flotor and the current coils on the stator. By controlling the currents independently in each of the coils, full 6-DOF control is achieved of the flotor with respect to the stator. The system includes three light-emitting diodes (LEDs) imaged onto three position-sensing devices (PSDs) which together allow position tracking of the flotor, relative to the stator. The system also includes six accelerometers for monitoring the stator and flotor accelerations. (Only the flotor-mounted accelerometers are currently used for control.)

The control system used with MIM on Mir uses simple proportional-derivative (PD) control with relative position measurement to suspend the flotor as an equivalent spring-mass-damper system typically tuned for near-critical damping; acceleration feedback can be added to tune the system by increasing its effective mass. It is desired to improve the isolation capabilities of MIM by using various more sophisticated control approaches. One such approach, pursued by this investigator, is the application of H_2 controllers which use standard linear quadratic gaussian (LQG) theory augmented by appropriate frequency

weighting. H_2 controllers have the advantage of using a quadratic (rms) performance index, which measures performance in terms of an energy measurement (state covariance plus control covariance). This is a very reasonable performance measure for a microgravity isolation problem (Hampton et al., 1996; see Saberi et al, 1995, for a thorough discussion of H_2 theory). However, H_2 theory does not allow the "up-front" incorporation of stability-robustness- or performance demands into the controller design "machinery." H_∞ synthesis and μ synthesis, on the other hand, allow such constraints to placed directly on the controller in the design process; however, the performance measure that is used must be an infinity-norm (Stoorvogel, 1995). The newer mixed-norm theory allows the controls engineer to design a compensator that minimizes a 2-norm of the closed-loop transfer-function matrix from one set (vector) of plant inputs to a set of plant outputs, subject to an ∞-norm constraint on the closed-loop transfer function from a second (not necessarily different) set of inputs to a second (again, not necessarily distinct) set of outputs (Whorton, 1997). This approach is a logical sequel to an H_2 (or H_∞/μ approach), and is expected to produce controllers superior to those achievable by either of the former methods.

Mixed-norm controller design

Mixed H_2/μ design can be achieved using the general procedure outlined below (Whorton, 1997). This is the procedure being applied to controller design for MIM.

1. *Develop a model for the H_2 problem.*
   (The fundamental problem is typically an H_2 problem, because typically the performance measure is to be a quadratic (rms) measure. An initial H_2 controller, of the final desired order for the mixed H_2/μ controller, and satisfying the robust stability constraints, will be useful as a starting point for the H_∞ homotopy algorithm entered below at step 7.)
2. *Synthesize an H_2 (full-order) controller, with good nominal performance.*
   (A full-order controller is needed because no direct path exists to synthesize a reduced-order controller with guaranteed stability.)
3. *Develop an uncertainty model for robust stability analysis.*
4. *Form the generalized plant for mixed-norm design.*
5. *Reduce the control authority to result in a full-order H_2 controller which satisfies robust stability (at the expense of some nominal performance).*
   (Low-authority control is needed because order-reduction techniques tend to work best for low-authority. Within the limits imposed by order reduction and robust stability, the loss of performance will be recovered via mixed-norm H_2/μ homotopy, i.e., alternating homotopies on ρ and λ, with γ fixed at unity.)
6. *Reduce the full-order controller to the desired order. (Reduction in controller order may result in loss of closed-loop stability. Consequently, it may be necessary to reduce the control authority before order reduction in order to ensure closed-loop system stability.)*
   (A controller of reduced order is needed to provide a starting point for the fixed-order mixed H_2/μ controller to be developed by H_∞ homotopy.)

[NOTE: At this point a reduced-order H_2 controller will have been obtained which satisfies robust stability, but has suffered a loss in nominal performance in order to satisfy robust stability and closed-loop stability after the order-reduction step.]

7. *Transform the controller into canonical form.*
   (The canonical form is needed to minimize the number of free parameters, in order (1) to produce a unique solution, and (2) to produce a static feedback-gain form of the five first-order equations expressing the necessary conditions for nominal performance and robust stability.)
8. *Fix* γ (at $\gamma = 1$) *and* ρ, *and perform a homotopy on* λ *until the closed-loop system* H_2*-norm* $\left(\left\|T_{z_p w_p}\right\|_2\right)$ *reaches a minimum or the closed-loop system* H_∞*-norm* $\left(\left\|T_{z_i w_i}\right\|_\infty\right)$ *approaches unity.*
9. *Compute the* μ*-measure* $\left(\left\|T_{z_p w_p}\right\|_\mu\right)$. *If it is appreciably less than one, compute and approximate the optimal D-scales, absorb them into the plant, and continue with the homotopy on* λ *until the robust stability (unit) boundary is reached again. Repeat as necessary to obtain a controller* $G(\rho, \lambda, \gamma)$ *for which the* μ*-measure is unity.*
   (At this point the controller-gain matrix $G(\rho, \lambda, \gamma)$ will have been found which places the closed-loop system on the robust-stability "boundary" for the given value of ρ and the assumed plant and uncertainty models. In effect, λ-homotopy has been used to solve the five matrix equations expressing the first-order sufficient conditions for nominal performance and robust stability, for the given value of ρ.)
10. *With* γ *fixed at a value of one, and* λ *fixed at the value determined above, perform a homotopy on* ρ *to increase the control authority (by decreasing* ρ*).*
11. *Repeat steps 8 through 10 to obtain a set of controller feedback gains G as a function of decreasing* ρ *(increasing control authority). These gains all yield nominal performance, for the given value of* ρ*, while ensuring robust stability. The value of* ρ *can be decreased in this fashion either until* $G(\rho)$ *yields the desired closed-loop nominal performance, in terms of the* H_2 *norm* $\left(\left\|T_{z_p w_p}\right\|_2\right)$*, or until no further decrease in* ρ *is possible without sacrificing robust stability.*

Effectively, what is done in the above process is iteratively to use homotopy on ρ and homotopy on λ to solve the five first-order necessary conditions for nominal stability and robust performance in terms of the chosen plant, disturbance, and uncertainty models, design frequency weights, and tuning parameter ρ. This yields a set of fixed-order controllers $G(\rho)$ that can be evaluated, for decreasing values of ρ, until a satisfactory (or until the best achievable) nominal performance has been obtained.

Current Status

A dynamic model of MIM II (Hampton et al., 1997) was created in Matlab, and used (with appropriately-selected frequency weightings) to develop three full-order and six reduced-order high-authority, high performance H_2 controllers. The controllers were spot-checked for robust performance and robust stability using Monte Carlo methods. Simulations by CSA indicate the controller performance to be as predicted, and they have been installed on MIM II for testing on STS-85. The first figure below shows the predicted open- and closed-loop transmissibilities, for a typical controller, from stator acceleration disturbances through umbilical to flotor acceleration, with both accelerations directed along the axis of one of the flotor accelerometers. (The plots are very similar for the other flotor accelerometer directions.) The second figure shows the predicted closed-loop transmissibilities, for the same controller and in the same direction, due to acceleration disturbances applied directly to the flotor. (The lower curve in each figure is the closed-loop curve.) Note that both types of disturbance experience significant attenuation in the 0.01 Hz to 10 Hz frequency range. As indicated by the first figure, the indirect (umbilical-induced) disturbances must be simply transmitted without attenuation in the range below 0.01 Hz, due to rattlespace constraints.

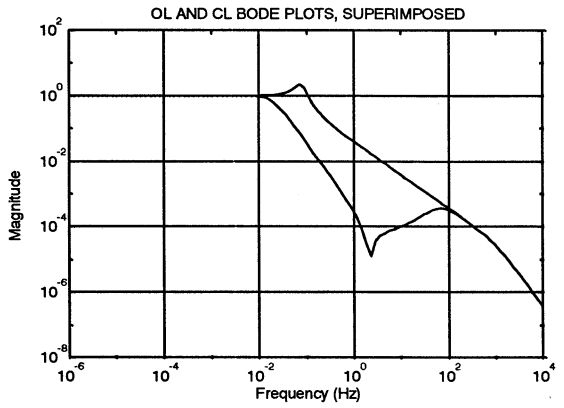

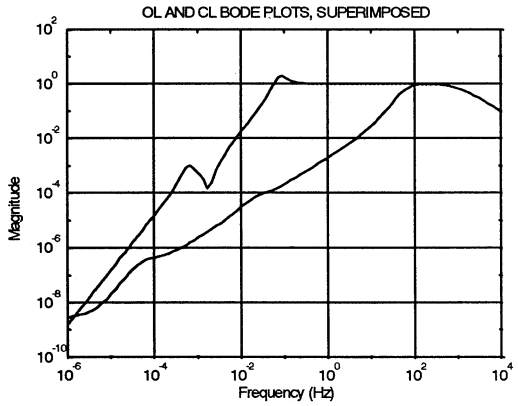

A modal uncertainty model was developed for the MIM and implemented in a Simulink model suitable for mixed-norm controller design.

Conclusion and Future Work

H_2 controllers, when designed using an appropriate design model and carefully chosen frequency weightings, appear to provide robust performance and robust stability for MIM. The STS-85 flight data will be used to evaluate the H_2 controllers' performance on the actual hardware under working conditions. Next, full-order H_∞ controllers will be developed, as an intermediate step, in order to determine appropriate H_∞ performance weights for use in the mixed-norm design. Finally the basic procedure outlined above will be used to develop fixed-order mixed-norm controllers for MIM.

Acknowledgments

This investigators are grateful to the American Society for Engineering Education, Marshall Space Flight Center, and the University of Alabama in Huntsville for the privilege of being able to pursue this summer of research.

References

DelBasso, S., "The International Space Station Microgravity Environment," AIAA-96-0402, January 1996.

DeLombard, R., Bushnell, G.S., Edberg, D., Karchmer, A.M., and Tryggvason, B.V., "Microgravity Environment Countermeasures Panel Discussion," AIAA 97-0351, January 1997).

Hampton, R.D., Tryggvason, B.V., DeCarufel, J., Townsend, M.A., Wagar, W.O., "The Microgravity Vibration Isolation Mount: A Dynamic Model for Optimal Controller Design," accepted for the *Proceedings of the MAG '97 Industrial Conference and Exhibition*, August 1997.

Hampton, R.D., Knospe, C.R., Allaire, P.E., and Grodsinsky, C.M., "Microgravity Isolation System Design: A Modern Control Synthesis Framework," *Journal of Spacecraft and Rockets*, Vol. 33, No. 1, January-February 1996, pp. 101-109.

Nelson, E.S., "An Examination of Anticipated g-Jitter in Space Station and Its Effects on Materials Processes," NASA TM-103775, April 1991.

Saberi, Ali; Sannuti, Peddapullaiah; and Chen, Ben M.; *H_2 Optimal Control*, Prentice Hall, Englewood Cliffs, NJ, 1995.

Stoorvogel, Anton, *The H_∞ Control Problem*, Prentice Hall, Englewood Cliffs, NJ, 1995.

"System Specification for the International Space Station," Specification number SSP41000, Rev. D, Nov. 1, 1995, NASA Johnson Space Center.

Tryggvason, B.V., "The Microgravity Vibration Isolation Mount (MIM): System Description and Performance Specification," MIM Critical Design Review, May 11, 1994.

Tryggvason, Bjarni V.; DeCarufel, Jean; Stewart, Bill; Salcudean, S.E.; and Hampton, R.D.; "The Microgravity Vibration Isolation Mount: System Description and On-Orbit Performance," in preparation for submission for publication.

Whorton, Mark S., *High Performance, Robust Control of Flexible Space Structures*, Ph.D. dissertation, Georgia Institute of Technology, Atlanta, GA, August 1997.

1997

NASA/ASEE SUMMER FACULTY FELLOWSHIP PROGRAM

MARSHALL SPACE FLIGHT CENTER
THE UNIVERSITY OF ALABAMA IN HUNTSVILLE

1-D NUMERICAL ANALYSIS OF RBCC ENGINE PERFORMANCE

Prepared By:	Samuel S. Han
Academic Rank:	Professor
Institution and Department:	Tennessee Technological University Department of Mechanical Eng.
NASA/MSFC:	
Branch:	Combustion Physics
Division:	Engine Systems
Laboratory:	Propulsion
MSFC Colleague:	S. Don Bai, Ph.D.

Introduction

RBCC engine combines air breathing and rocket engine into a single engine to increase the specific impulse over an entire flight trajectory. Considerable research pertaining to RBCC propulsions was performed during 1960's and these engines were revisited recently as a candidate propulsion system for either a single-stage-to-orbit (SSTO) or two-stage-to-orbit (TSTO) launch vehicle (Foster, et. al., 1988). There are variety of RBCC configurations that had been evaluated and new designs are currently under development. However, the basic configuration of all RBCC systems is built around the ejector scramjet engine originally developed for hypersonic airplane. In this configuration, a rocket engine plays as an ejector in the air-augmented initial acceleration mode, as a fuel injector in scramjet mode and the rocket in all rocket mode for orbital insertion (Escher, 1995).

Computational fluid dynamics (CFD) is a useful tool for the analysis of complex transport processes in various components in RBCC propulsion systems. The objective of the present research was to develop a transient 1-D numerical model that could be used to predict flow behavior throughout a generic RBCC engine following a flight path.

1-D Numerical Model

One dimensional transient compressible flow equations used in the model are mass, linear momentum and energy equations. They are :

$$\frac{\partial \rho A}{\partial t}+\frac{\partial \rho u A}{\partial x}=m_{inj}A$$

$$\frac{\partial \rho u A}{\partial t}+\frac{\partial}{\partial x}\left[A\left\{\rho u u-\left(2\mu+\lambda\right)\frac{\partial u}{\partial x}\right\}\right]=-A\frac{\partial p}{\partial x}-\tau_w p_w+m_{inj}Au_{inj}$$

$$\frac{\partial \rho u e}{\partial t}+\frac{\partial}{\partial x}\left[A\left(\rho u e-\kappa\frac{\partial T}{\partial x}\right)\right]=-p\frac{\partial u A}{\partial x}+u\tau_w p_w+m_{inj}h_{inj}A+q_{gen}A+uu_{inj}m_{inj}A-1.5u^2m_{inj}A$$

In these equations, ρ density, u velocity, p pressure, e internal energy, x axial coordinate , t time, and A(x,t) is the cross-sectional area. Ejector mass flow rate, m_{inj}, was the primary rocket mass flow rate, and h_{inj}, was calculated by using primary rocket nozzle exit temperature and Cp of the primary rocket combustion products. Exit velocity of the gas at the primary rocket nozzle, u_{inj}, was calculated via ideal gas equation with known primary rocket exit pressure and exit area. Energy release from hydrogen injection, q_{gen}, was treated as uniform energy input. Stoichiometric reaction of hydrogen and oxygen was assumed.

For the present study, molecular viscosity of the fluid, μ and λ, are negligible and therefore wall friction was neglected. τ_w represents minor losses due to sudden area change modeled after incompressible flow case,

$$\tau_w = c_d \frac{1}{2} \rho u^2$$

where c_d is a form drag coefficient ranging from 0.05 to 0.2 and p_w is the wetted perimeter of the cross section.

Numerical scheme used was a variant of SIMPLE method that incorporates compressibility of the fluid. A staggered grid was used. Time accuracy of the solution was obtained by choosing time steps slightly larger than those dictated by CFL conditions. Mass, momentum and energy addition from primary rocket and hydrogen injectors were uniformly distributed over the chosen control volumes using source term linearization.

Imposition of numerical boundary conditions depend not only on the nature of the problems but also on the numerical methods used and often creates erroneous solutions. In RBCC operation, primary rocket was used to initiate the flow and thus disturbance to the initially static condition in the engine began internally and propagated to the inlet and exit of the engine. At the engine inlet, static pressure was extrapolated by using static pressures next to inlet boundary. The remaining flow properties were then calculated by using free stream conditions assuming that the process from the free stream to the inlet was isentropic. If there was a shock ahead of the inlet, flow properties of the free stream must be readjusted accordingly. This step was not taken in the present calculation. At the end of the exit nozzle, atmospheric pressure was imposed if the flow at the exit was subsonic and extrapolated pressure was used otherwise.

Simulation Results

Table 1 shows bypass ratio of an ideal ejector calculated by the present numerical model in comparison with analytical solution (Heiser and Pratt, 1994). Numerical results agreed well with the analytical solution up to free stream Mach number 1.0. Results deviated rapidly with increasing free stream Mach number beyond 1.0. In the numerical model, primary flow pressure and the induced air flow pressures were not assumed equal at the inlet plane of the mixer while they were assumed equal in analytical method.

Table 1. Ideal Ejector Bypass Ratio

Free stream Mach no	Numerical	Analytical
0.0	1.65	1.68
0.5	1.94	1.92
1.0	2.98	2.93
1.5	4.47	5.66
2.0	6.00	12.10

Another calculations were performed to obtain the bypass ratio and the ejector stagnation pressure ratio for the Pratt-Whitney test rig. Numerical results obtained by the present model for three free stream Mach numbers following a flight trajectory were compared with the results RJPA code of John Hopkins University. A reasonable agreement was obtained. This was expected since both models were based on the same equations except the time dependent terms in the present model.

To validate the accuracy of the numerical model, numerical results were next compared with the test data. Test data of a duel-mode ejector scramjet engine developed by Marquardt (Congelliere, et. al., 1968) was used for that purpose. Fig. 1 shows flow area along the axis of the engine; diverging inlet, combuster and after-burner-exit nozzle and constant area mixer (ejector). Flow areas were changed abruptly at the strut and where pressure probes were located. Free stream Mach numbers were varied from 0 to 6.0. Test results were presented in terms of pressures and induced air flow rate. A bell mouth was placed at the inlet for the static test only.

Fig. 2 shows the static pressure distributions for four cases along the engine at M_0=0. Flow speed remained subsonic throughout the engine. Experimental wall pressure distribution (broken line) showed static pressure was increased through the ejector, decreased in the constant area mixer, increased in the combustor and further increased through the after-burner-exit nozzle. Sharp pressure changes due to the presence of pressure probes were apparent. Ideal case (-Δ-) assumed no form drag due to area changes and the mixer area was assumed constant as the actual geometry. Without form drag, pressure at the inlet was much lower than the test data and no pressure bumps were shown at the probe locations. Since the flow was subsonic, pressure in the constant area mixer remained constant and increased smoothly through the diverging part of the remaining engine. Tested pressure in the mixer, however, decreased rapidly along the mixer indicating that the flow accelerated in the mixer. This implies that active cross sectional area of the mixer was progressively reduced. This is similar to accelerating flow through an isolator in a dual-mode scramjet engine. A supersonic flow (Heiser and Pratt, 1994) entering a constant area isolator remains supersonic at the mixer outlet because of reduced flow area. Active flow area decreases because of boundary layer that is generated by series of oblique shocks. Isolator acts as a buffer when the engine switches from a ramjet to a scramjet modes in a dual-mode scramjet engine. In ejector mode, flow in the mixer is subsonic but oblique shocks are created by the high pressure primary flow and the low pressure induced air flow (Daines, 1995). The exit area of the mixer was thus reduced by 20 % in subsequent calculations and the results showed a better agreement with the test data. Overall pressure distribution was higher with a form drag (c_d=0.05) than without. Even without a form drag, numerical results were higher than the test data. This might be explained by the fact that measured pressure was wall pressure which was much lower than the pressure at the center of the mixer. Numerical results were obtained at free stream Mach numbers, 0.8, 1.6 and 3.0 without hydrogen injections. Table 2 shows the bypass ratios calculated by ideal ejector analysis and the present model in comparison with the test data.

Fig. 3 shows the effects of hydrogen injections at two locations: "A" at the end of combustor and "B" at the beginning of combustor. Injection of hydrogen was 0.0165 kg/s and a stoichiometric reaction with oxygen in the induced air was assumed.

Table 2. Bypass Ratio for Marquardt Test Engine

M_0	Ideal (H&P)	Numerical (w/o drag)	Numerical (w drag)	Test data
0.0	5.14	3.6	3.6	2.67
0.8	7.81	5.4	4.2	5.01
1.6	21.61	14.43	10.76	12.5

Energy release in the combustion chamber increased the static pressure before the injection points and caused flow acceleration and rapid pressure drop after injection points as expected in a subsonic flow. Pressure distribution however agreed only qualitatively with the test data. Fig. 4 shows pressure and Mach number distributions with "A" injection and without injection at M_0=3.0. Again with injection pressure increased and the flow became subsonic before the injection point and choked in the after-burner followed by supersonic expansion. This is an example of ramjet mode operation. Without hydrogen injection, flow is choked at the end of mixer and the flow become supersonic in the combustor (M=1.5) and remained supersonic.

Conclusions and Recommendations

A transient 1-D numerical model was used to study fundamental mechanisms involved in RBCC propulsion systems. Numerical results obtained by the present model for the ejector mode agreed well with other available analytical data. Comparison with test data showed that inlet interactions, mixing processes in the ejector and energy release in the combustor have dominant effects on the performance of the engine. Additional studies are recommended for the inlet interactions, and the chemical reactions in the combustor before simulating modes transition following a actual flight path and parametric study on various engine configurations.

References

Congelliere, J., Prevatte, N., and Lime, J., Advanced Ramjet Concepts: Volume 2-Ejector Scramjet Technology, AFAPL-TR-67-118, Vol.2, 1968.

Daines, R. L., Computational Fluid Dynamic Analyses of Rocket Based Combined Cycle Engine Flowfields, Ph.D. Thesis, Penn State Univ, 1995.

Escher, W. J. D., Rocket-Based Copmbined-Cycle RBCC Powered Spaceliner Class Vehicles Can Advantageously Employ Vertical Takeoff and Landing (VTOL) AIAA paper 95-6145, 6th Int. Aerospace Plane and Hypersonic Conf., Chattanooga, Tenn., April, 1995.

Foster, R. W., Escher, W. J. D., and Robinson, J., Air Augmented Rocket Propulsion Concepts, AFL-TR-88-004, Jan., 1988.

Heiser, W. H., and Pratt, D. T., Hypersonic Air breathing Propulsion, AIAA Education Series, 1994.

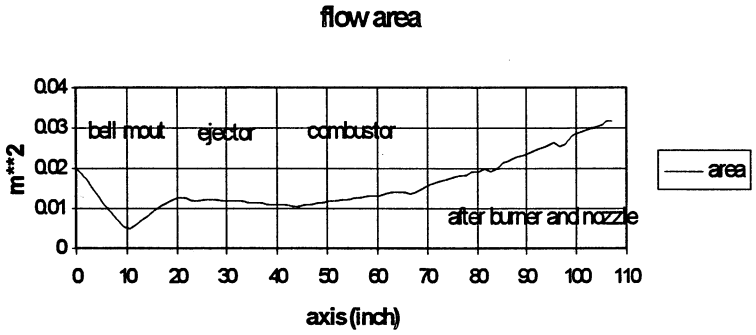

Fig. 1

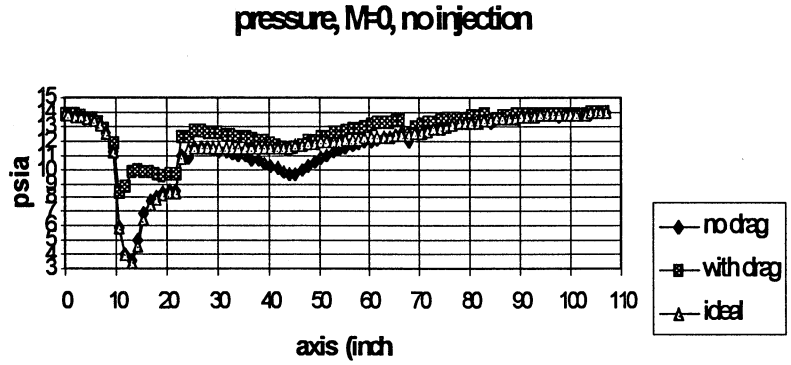

Fig. 2

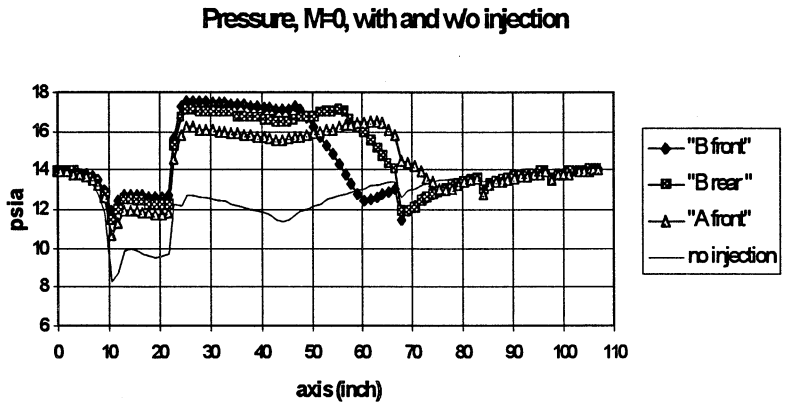

Fig. 3

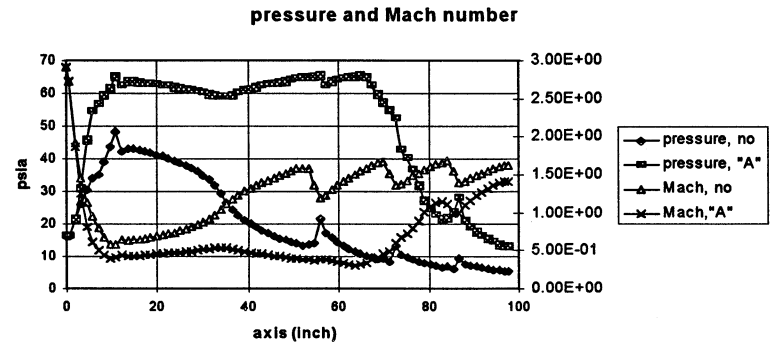

Fig.4

1997

NASA/ASEE SUMMER FACULTY FELLOWSHIP PROGRAM

MARSHALL SPACE FLIGHT CENTER
THE UNIVERSITY OF ALABAMA AT HUNTSVILLE

"EDCATS: AN EVALUATION TOOL"

Prepared By:	Pamala D. Heard
Academic Rank:	Assistant Professor
Institution:	Langston University
Department:	Department of Mathematics
NASA/MSFC:	
Office:	Education Program Office
MSFC Colleague:	Mr. Jim Pruitt

INTRODUCTION

The purpose of this research is to explore the development of Marshall Space Flight Center Unique Programs. These academic tools provide the Education Program Office with important information from the Education Computer Aided Tracking System (EDCATS). This system is equipped to provide on-line data entry, evaluation, analysis, and report generation, with full archiving for all phases of the evaluation process. Another purpose is to develop reports and data that is tailored to Marshall Space Flight Center Unique Programs. It also attempts to acquire knowledge on how, why, and where information is derived. As a result, user will be better prepared to decide which available tool is the most feasible for their reports.

RESEARCH APPROACH

The initial approach to this research was to look at the NASA-Wide programs. Because EDCATS has many facets, I needed to explore the variety of information that could be generated from the data feedback reports, program sessions, and field center final reports. I had to examine how the information was currently being collected, tabulated, reported and disseminated. Looking at the six indicators for the system, I needed to determine whether or not all information was being collected. I discovered there were specific performance indicators used in the evaluation system. The indicators included the target population, indefinite program techniques, content, data collected and analyze supplementary material being distributed. These essentials provided a first- hand account of NASA's accomplishments of its education goals and objectives that pertained to the program.

After the information is gathered it could be used in a plethora of areas. Some of the areas of utilization are reports, follow-up studies, changes in existing programs, and development of new programs. Recently, I examined the Center-Unique Programs. It is comprised of the Discover Lab, Project Laser Database, Explorer Post, and Moon Buggy. This examination required research into different types of programs. I had to determine the type of information that was necessary for these programs. An analysis of the goals set forth by NASA and the program managers were vital. For each program, I looked at the participants and data/feedback report, program session report, and the field center final report. This examination was necessary to determine what questions to address that was related to each program. Each program has unique information that is useful for the program manager. To better understand this uniqueness, I talked to the program managers to better determine what data is important for a particular program. After this information was gathered, I "tackled" the task of going through each data feedback form to explore whether or not the criteria were met by the objectives of EDCATS and by the program manager.

Next, I had to view the program session and determine what was needed for the reports and choose the most feasible way of gathering data. The information for the program session required that data be entered by the program manager with no input from participants. The success of using on-line evaluations was another consideration. In making this determination, I asked several questions related to the evaluation. What would the information be used for? If the information was entered correctly, how would a true result be realized? I had to determine how the programs would be operated/reported and who was responsible for the different forms? Does EDCATS have the necessary ability for reporting, data collection and keeping track of budget procedures? A plethora of forms was examined in effort to determine if any difference existed. The participant's opinion on whether or not to complete on-line evaluations are another consideration that can't be ignored. After seeing how the data was collected and generated into different reports, I better understood the internal functions of the program.

RESULTS

While conducting my research, I immediately perceived the evaluation forms as being somewhat lengthy, but I would later discover how quickly the forms could be completed. It is much more feasible with the aid to computer to enter the necessary information. After completion of the form it is then ready for immediate feedback. However, the current setup makes it more difficult for the participant to make corrections. Any changes are usually made by the program manager. Once the information is compiled and stored, it is easier to develop different types of databases. This database is helpful with follow-up in the educational community for programs.

The next area of concern involves the program session, these questions do not coincide with the teacher/student feedback. The program manager will be responsible for entering this information. There is no linkage between forms. If the information was asked on the evaluation form it could automatically be mapped to other forms and prevent a duplication of entry. Oftentimes, trying to generate a report from the information gathered is difficult because the evaluation may not have asked relevant questions. If a pre-define summary is used for each component then the data and vital information would be in place. The field center final center report is generally based on funds. This form would be filled out by the program manager and /or resource manager. In looking at these components we need pre-define summaries to realize a report that is functional. Also, using the Ad-Hoc user reports will help to develop an illustrated report. When using the Ad-hoc report tools you have no totals of the information you have gathered.

EDCATS and Microsoft Excel or Microsoft Access programs can be used to develop databases. These are valuable tools that provide linkage and helps gather information for reports. Excel makes it easier to develop spreadsheets and graphs that highlight gathered information. This method helps the center conduct follow-ups on participants in different programs.

Information about participants in other programs would also be included. Information gathered can be used to support the programs' effort aimed at the betterment of education, needed improvements, and the reporting of data as a team. Monthly reports can be generated with information collected from the evaluations. This information can be used as an update for all programs in the Education Program Office. The total can be used to develop statistical data for the center and numbers the office might need. The different reports offer variety for the individual and help to better relay the message.

CONCLUSION

Evaluations are important to the development and implementation of programs that are designed to aid education. The system (EDCATS) is an important step in gathering the opinions of educators who are embarking on new and real-time experience in space. The exploration of these avenues, in my opinion, couldn't be more urgent. The following are suggestions that I strongly believe would be helpful: make sure information gathered from teachers and students via EDCATS will help make needed changes and provide additional programs. Programs that are not useful should be "scratched". Inform participants that the forms seem lengthy but only take a short period of time to complete. Office reporting should be done monthly using spreadsheets to keep track of activities within the office from a team perspective. Other suggests would be to develop a linkage between the programs, have training for users, and gather information from EDCATS programmers. These suggestions would make it possible to view the entire sphere of EDCATS and take full advantage of the system's capabilities. Knowing the capabilities will only further assist user. The Program Inventories are very helpful because they highlight NASA's efforts in the area of Education. The information that is used in the program inventory, the number of participants, and applicant is also valuable for prospective participants. This data helps to make determinations related to the competitiveness of the program. In using EDCATS we need to implement a system of checks-and-balances. EDCATS is a good program but should not be viewed as a "cure all"

ACKNOWLEDGMENT

I would like to thank Mr. Jim Pruitt and the Education Program Office team for their support. I was truly accepted as a team member. I also appreciate the time and effort the team members contributed to my project.

1997

NASA/ASEE SUMMER FACULTY FELLOWSHIP PROGRAM

MARSHALL SPACE FLIGHT CENTER
THE UNIVERSITY OF ALABAMA IN HUNTSVILLE

THE EFFECT OF JETTING PARAMETERS ON THE PERFORMANCE OF DROPLET FORMATION FOR INK-JET RAPID PROTOTYPING

Prepared by: Wayne Helmer

Academic rank: professor

Institution and Department: Southern Illinois University
Carbondale, Illinois
Mechanical Engineering and
Energy Processes

NASA/MARSHALL:

Laboratory: Materials and Processes
Division: Nonmetallic Materials & Processes
Branch: Nonmetallic Materials

MSFC Colleague: Floyd E. Roberts, III

Introduction

Heinzl et al. (1985) reports that experiments in ink-jets to produce drawings or signals occurred as early as 1930. Various companies such as IBM and Pitney-Bowes have conducted extensive studies on these devices for many years. Many such reports are available in such journals as the IBM Journal of Research and Development. While numerous articles have been published on the jetting characteristics of ink and water, the literature is rather limited on fluids such as waxes (Gao & Sonin 1994) or non-water based fluids (Passow, et al. 1993). This present study extends the knowledge base to determine the performance of molten waxes in "ink-jet" type printers for rapid prototyping.

The purpose of this research was to qualitatively and quantitatively study the droplet formation of a drop-on-demand ink-jet type nozzle system for rapid prototyping.

Apparatus

The jet test station used in this study provided the operator with the ability to set, control and record the jetting parameters for an ink-jet drop-on-demand type molten material deposition system. See figure 1.

A frequency generator controlled the firing frequency input to the PC board electronics. A square wave was used to dictate the firing frequency of the droplets. A strobe light illumined the droplets as they were emitted from the piezo-jet. The strobe frequency was adjustable from 500 to 15,000 Hz. The strobe frequency was usually set equal to the jetting frequency except in cases where a lower strobe frequency was used to enable better visual distinction of the droplets on the monitor screen.

An oscilloscope provided the measurement of the firing voltage and firing wave form for the jet. These two parameters were controlled by adjusting two potentiometers on the PC board. The frequency generator controlled the jetting frequency, of course. A frequency counter provided a check on the frequency generator.

A reservoir provided molten material for the jet. Heated and insulated tubing delivered the molten material to the jet. The reservoir, lines and jet were all heated and temperature controlled. Solid build material was periodically added to the reservoir as needed. The reservoir was adjusted so that the liquid level was about 0.5 inches below the tip of the jet.

A video camera fitted with a special lens enabled the high speed images of the droplet jetting to be transmitted to the TV monitor and recorded on the VCR.

Materials and Methods

All equipment was turned on for at least two hours before any data were taken. These data were taken at the following operating conditions representative of this type of RP system:

Voltage ratio = 0.60, 0.70, 0.80, (Voltage ratio = voltage/reference voltage)
Frequency ratio = 2 to 9, (Frequency ratio = frequency/reference frequency)
Duty cycle = min, max, optimum (Duty cycle = firing time/total cycle period)

The duty cycle is defined as the firing time/total time for one cycle. See figure 2. Minimum and maximum duty cycle points were determined visually when the jet stream started to deteriorate. The "optimum" point was some where in between. Voltage readings, and firing times were measured from the oscilloscope. Jet frequency was indicated from the frequency generator as well as the oscilloscope.

Room conditions were approximately: $T_{dry\ bulb}$ = 72 F, 75 % relative humidity. The build material was a proprietary wax that had a melting temperature of about 120 C. All test points were recorded on video tape. Reference distances on the video screen were also recorded on the tape for later determination of droplet diameter, etc.. The time period for each operating point was from 4 to 15 minutes, depending on the frequency. Droplet mass was collected for a given period and weighed on a digital scales to determine the build rate.

Results

Figure 3 illustrates the effect of duty cycle on the build rate at a specific frequency ratio (other frequencies are similar). As expected the build rate has a maximum at some point between the maximum and minimum duty cycles. (Beyond the maximum and minimum points the jet does not fire or the jetting is so poor that it is unacceptable.) On the lower duty cycle end the deterioration of the jet is probably due to the lack of adequate refill time required by the surface tension forces to refill the jet. Poor jet performance on the high end may be due to not having adequate time for the piezo to eject the drop from the nozzle. The optimum jetting conditions are the only ones plotted on the following figures.

Figure 4 illustrates the effect of frequency on duty cycle. It appears that the range of acceptable duty cycles cluster in a range from about 85% on the low frequencies to about 60% at the high frequencies. This seems to indicate that more time is needed to fire the droplet of wax than it does to refill the jet passage with new wax. This effect gradually changes as the frequency increases.

Figure 5 indicates the build rate dependency on frequency. (Ignore for the moment the data at a frequency ratio of 6 and 7.) It is seen that the build rate is approximately linear with frequency; the greater the number of drops (frequency) the

greater the amount of build mass. It is also apparent that higher voltages produce a slightly greater build rate. This would seem reasonable since higher voltages would mean greater displacement (volume) of the piezo and therefore greater drop diameter per cycle.

Note that irregular jetting occurred at frequency ratios of 6 and 7. Video inspection of these points indicated that several jet streams were being emitted from the jet at slightly different angles and frequencies. The jet stream was very irregular. It appears that several higher or lower resonant frequencies are existing in the jet at these points which cause the irregular (and unacceptable) jetting. This behavior caused the build rate to be much lower than expected as is indicated in Figure 5.

One operating point was duplicated at a 25 minute interval and the results seemed identical to the smaller time period.

Conclusions

The following general conclusions can be made consistent with the range of variables studied in this program.

1. The build rate (mass/time) is approximately proportional to the frequency of the jet for stable jetting conditions, as expected.

2. The build rate increases with increasing voltage.

3. The droplet diameter increases with increasing voltage.

4. At higher frequencies certain irregularities in the jet stream occur possibly due to particular resonance frequencies occurring in the nozzle. These conditions cause the build rate to decrease.

5. The range of acceptable jet duty cycle for good jet performance ranges from about 60% to 85% with a band width of about 10 to 15 %. The level of the duty cycle decreases with increasing frequency.

References

Heinzl, J. and Hertz, C. H. (1985), Ink-Jet Printing. Advances in Electronics and Electron Physics, v. 65, pp: 90-171.

Passow, C. H., and Chun, J. -H., (1993) "Droplet-Based Manufacturing," CIRP Annals. v. 42, n. 1, pp. 235-238.

Gao, F. And Sonin, A. 1994. Precise deposition of molten microdrops: the physics of digital microfabrication. Proc. R. Soc. London. A (1994) v. 444, pp. 533-554.

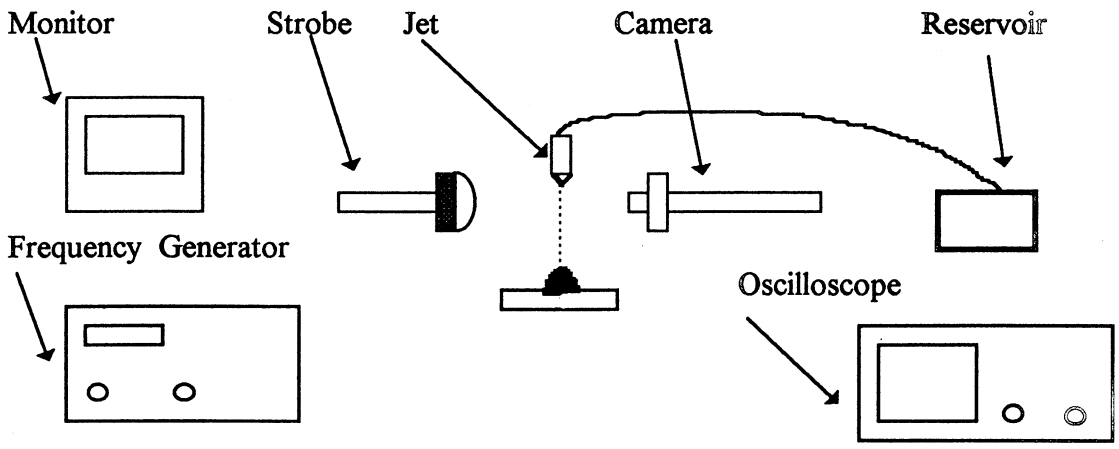

Figure 1 Jet test station.

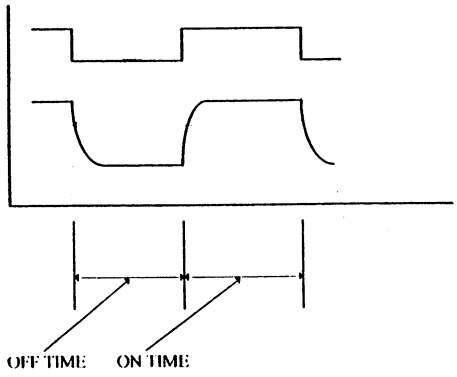

Figure 2. Jet firing profile.

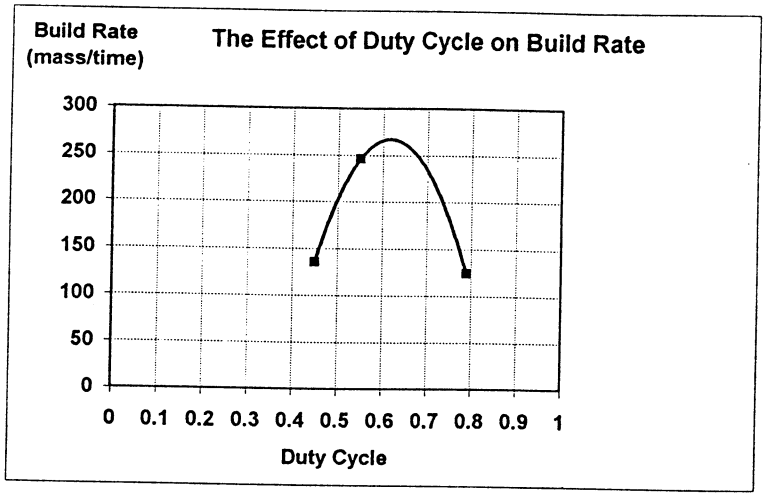

Figure 3. Variation in build rate with duty cycle at a frequency ratio of 9.

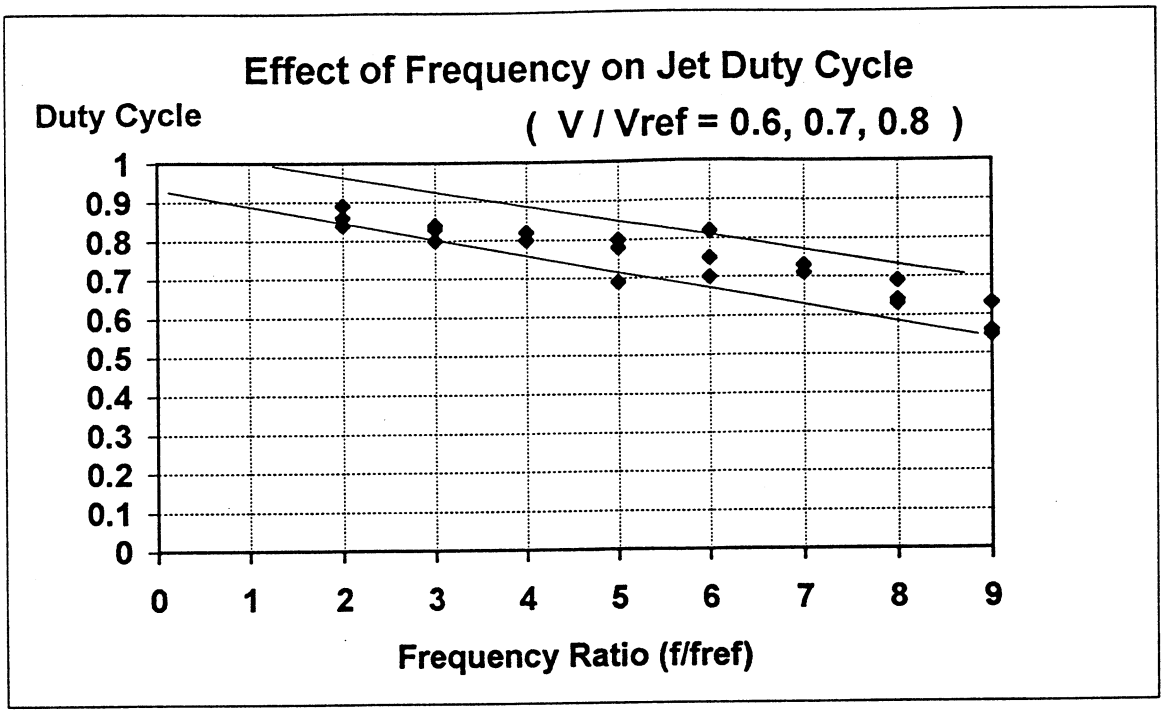

Figure 4. Variation in duty cycle with frequency

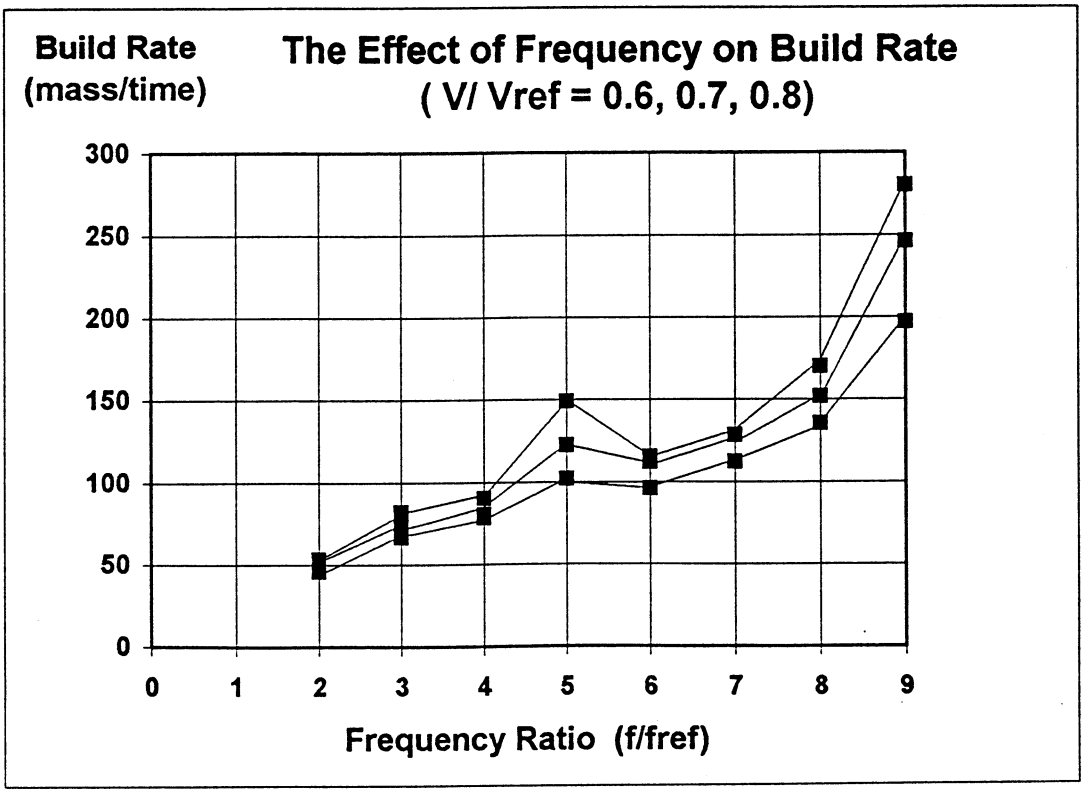

Figure 5. Variation in build rate with frequency.

1997

NASA / ASEE SUMMER FACULTY FELLOWSHIP PROGRAM

MARSHALL SPACE FLIGHT CENTER
THE UNIVERSITY OF ALABAMA IN HUNTSVILLE

UNCERTAINTY IN CALIBRATION, DETECTION, AND ESTIMATION OF METAL CONCENTRATIONS IN ENGINE PLUMES USING OPAD

Prepared by: Randall C. Hopkins / Daniel A. Benzing

Academic Rank: Instructor / Graduate Research Assistant

Institution and Department: University of Alabama - Tuscaloosa
Dept. of Aerospace Engineering and Mechanics

NASA / MSFC:

Office: Instrumentation and Control Branch
Division: Astrionics Laboratory

MSFC Colleagues: Anita Cooper
W. T. Powers
William White

Introduction

The idea of extracting chemical data from the analysis of the electromagnetic (EM) spectrum is not new. Holding a copper wire in a sufficiently hot flame produces a characteristic green region in the flame. The copper atoms are exited to such a high energy state that they emit electromagnetic radiation at several wavelengths, with green light being dominant. The atomic structure determines the wavelengths of EM emitted, and since all elements are unique, no two elements will emit EM at exactly the same wavelengths. Thus each element has its own unique spectral signature. For example, in the same flame, the element nickel will emit EM at wavelengths different than copper. A plot of radiant intensity versus wavelength is the electromagnetic spectrum of nickel, as shown in Fig. 1. Since this spectrum is unique, a spectrometric detector some distance from the flame would allow a user to determine the presence of nickel, copper, or both, in the flame.

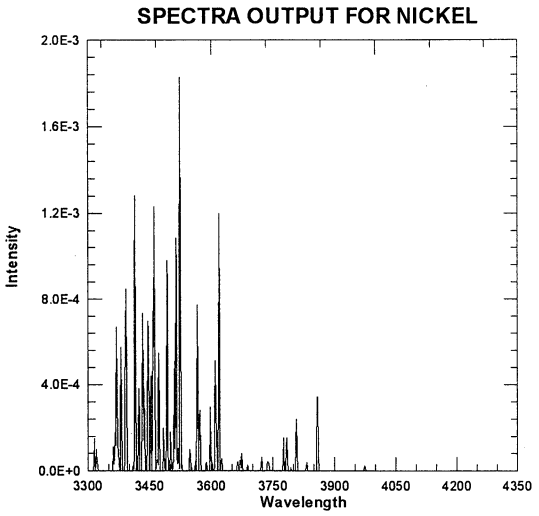

Fig. 1. Example Emission Spectra for Nickel.

Individual spectra for other elements vary in complexity, some having few atomic transitions (peaks), others having many. Three germane points of importance to this paper result from Fig. 1 and the associated radiation physics: 1) *every element has it's own "spectral signature,"* 2) *the emission will contain atomic transitions at wavelengths which may not be part of the visible spectrum, and* 3) *the* ***intensity*** *of the emission is a function of the* ***quantity*** *of emitting matter present in addition to the system temperature and other quantum variables.*

Rocket plumes are emissive events subject to the same physics (with more complications of course) as burning nickel or copper over an open flame. The Optical Plume Anomaly Detection (or OPAD) program (Cooper, *et al*, 1997) was initiated by researchers at MSFC as an effort to take advantage of the wealth of information contained in the exhaust plume of a rocket engine. The initial idea was to identify anomalous spectral events which were consistent with known mechanical failures and then use them as templates in the health monitoring of future engine tests (ground or in-flight). This could then be coupled with the anomalous events found in the vibrational and other sensor data to determine the overall state, or health, of the engine.

The "template idea," however, was soon replaced by even more ambitious goals as a result of some initial findings in the TTB experimental program (Benzing, *et al*, 1997). The spectral data from one test in particular revealed a major occurrence of a metallic species which was indigenous to the SSME

preburner faceplate. An even closer evaluation of the amount of metallic species present versus time showed an initial erosive event of the metal followed by numerous other anomalous emissions, all leading up to an engine-threatening erosion of the faceplate. This meant that anomalous events could be predicted.

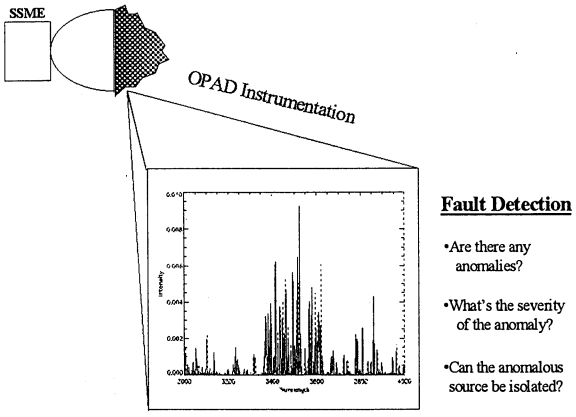

Fig. 2. Monitoring the SSME Exhaust Plume using the OPAD System.

As a result of these findings, the focus of the researchers turned to not only anomaly detection but also metal quantification. In other words, health monitoring now involved the simultaneous tasks of anomaly detection and determination of the severity of the anomaly, as illustrated in Fig. 2. This meant that the free atom densities of all the metals of interest within the engine would have to be predicted for every temporal scan taken by the instruments. The metal quantification process would essentially give metal concentration versus time. Spikes in this time trace would then be indicative of a metal erosion.

The neural network extracts radiant intensity data from the electromagnetic spectrum of the exhaust plume and uses these values to predict concentrations, as well as temperature and broadening parameter, of metals in the flame (Whitaker, *et al*, 1997). Fig. 3 illustrates the network's operation. As the intensities of the electromagnetic radiation are extracted from the spectrum, the uncertainties in those values are propagated through the network and result in uncertainties in the predictions of number density, broadening parameter, and temperature.

Calculation of the uncertainties begins with an examination of the procedure used to calibrate the instruments used in the OPAD system.

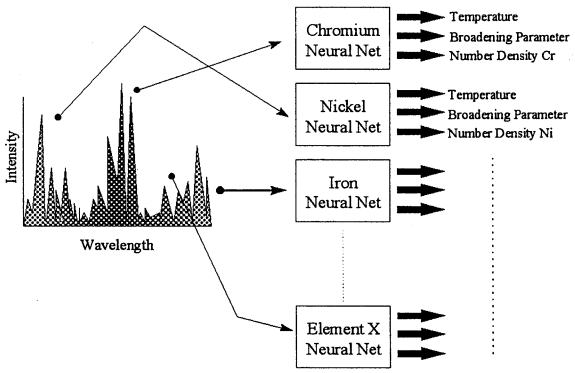

Fig. 3. Basic Operation of the Neural Network.

Uncertainties in Instrument Calibration

The purpose of instrument calibration is to determine the response of each photodetector, or the ratio of incoming radiation to outgoing voltage. During an engine test, the radiant intensity , I, at each photodetector is

$$I = (I_T - I_B) \cdot R \quad \text{(units are W/(str cm}^2\text{ ang))} \tag{1}$$

where I_T is the radiant intensity during engine firing and I_B is the radiant intensity of the background, or ambient light. These two values are measured in "counts" since the analog-to-digital converter installed in the computer converts the voltages released by each photodetector into an integer. In order to calculate the radiant intensity, I, during the test, the value of R must be determined from calibration.

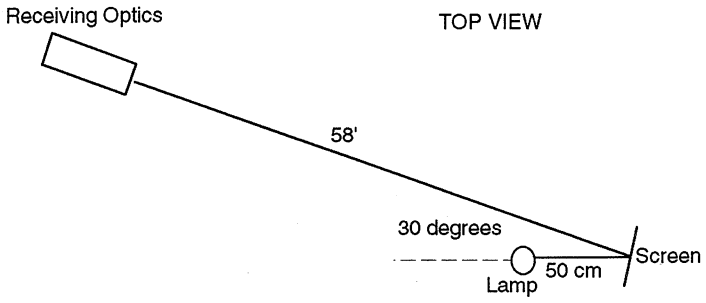

Fig. 4. Calibration Procedure for the OMA, One of Several OPAD Instruments.

Fig. 4 shows a typical calibration for the OMA, one of several spectrometers that can be used as part of the OPAD system. Using a calibrated irradiance lamp of known intensities across a segment of the electromagnetic spectrum allows the values of R in the above equation to be determined. During calibration, lamp radiation is reflected off of a screen of known reflectance properties at a certain distance from the receiving optics. Therefore, the only unknown in Equation 1 is R. Thus,

$$R(\lambda) = \frac{\left(I_{interpolated}\right)_\lambda}{\left(I_L - I_B\right)_\lambda} \tag{2}$$

where I_L is the lamp intensity (in counts) at the photodetector, and I_B is the background. Any uncertainty in R will be propagated though Equation 1 during an engine test.

Some of the sources of uncertainty in R include instrument noise, uncertainties in the lamp irradiance, uncertainties in the screen reflectance, the distance between the lamp and reflectance screen, the distance between the screen and the receiving optics, background fluctuations (such as sun and shade, time of day, changing surroundings, etc.), and others.

Due to time constraints, the uncertainty in R was determined using statistical methods. Several hundred sample calibration scans were taken at different times and the environmental factors (sun, temperature, humidity, etc.) noted. Then values of R were calculated for each photodetector for these scans. Values of R were determined by the mean of the data points and the uncertainties were reported as one standard deviation, as in Equations 3 and 4, respectively.

$$\mu = \frac{1}{n}\sum_{i=1}^{n} x_i \tag{3}$$

$$\sigma = \sqrt{\frac{1}{n-1}\sum_{i=1}^{n}\left(x_i - \mu\right)^2} \tag{4}$$

Uncertainties in the distances between the screen and lamp and the screen and the receiving optics were determined but not propagated through the calibration procedure due to time constraints; they will be included in future studies. Once these uncertainties were determined, then the uncertainties in the radiant intensity during an engine test could be determined.

Uncertainties in the Measured Photodetector Radiant Intensity

The uncertainty in I in Equation 1 can be determined mathematically using well known statistics. For each photodetector (there may be over 2000) in the instrument, the absolute uncertainty in I, expressed U_I, is

$$U_I^2 = \left[U_{I,T}\frac{\partial I}{\partial I_T}\right]^2 + \left[U_{I,B}\frac{\partial I}{\partial I_B}\right]^2 + \left[U_R\frac{\partial I}{\partial R}\right]^2 \tag{5}$$

where $U_{I,T}$ and $U_{I,B}$ are the uncertainties in the measured exhaust plume and background (pre-test) radiance, and U_R is the uncertainty in the photodetector response. Evaluating the partial derivatives results in a simple expression:

$$(U_I)^2 = (U_{I,T}R)^2 + (U_{I,B}R)^2 + (U_R(I_T - I_B))^2 \tag{6}$$

Use of Equation 6 allows one to not only evaluate the overall uncertainty, but also determine the major contributors. This shows the experimenter what areas of the experiment should be improved.

To evaluate these equations by hand would be extremely time consuming for experiments of several hundred scans using instruments of over 2000 photodetectors. Therefore, five ANSI standard C programs were written to convert raw data from the instruments a standard format, analyze the data for entire scans or for individual photodetectors, create histograms and temporal charts, and compute the mean, standard deviation, and absolute and relative uncertainties in any measurement, whether it be counts (such as I_L) or values of R. These programs can average several background scans, or randomly mix background (I_B) and calibration (I_L) or engine test (I_T) scans. The results of these programs are then substituted into Equation 6.

Analysis of each term for photodetector number 099 of the OMA instrument is shown in Table 1.

$$(U_I) = 7.501E-08 \frac{W}{str \cdot cm^2 \cdot ang}$$

$$(U_{I,T}R)^2 = 1.198E-16$$

$$(U_{I,B}R)^2 = 7.862E-18$$

$$(U_R(I_T - I_B))^2 = 1.170E-15$$

Table 1. Contributions to the Uncertainty for Photodetector #99 in the OMA Instrument.

The data used in the analysis in Table 1 are from an SSME test. The results clearly show that the uncertainty (expressed as 1σ) in background measurements contribute the least to the overall uncertainty. However, for photodetector number 99, U_R is 3.641E-10 (4.802%), and in the third term U_R is multiplied by a large number (I_T - I_B = 1030 counts on average). Thus if the exhaust plume is extremely bright, then this error term dominates, and the errors during the calibration process become very important.

Propagation Through the Neural Network

The neural network takes the intensity values from Equation 1 and predicts temperature, number density, and broadening parameter for the flow. What can be said of the uncertainties in these estimates? Generally speaking there are three main sources of uncertainty in the radial basis function neural network (RBFNN) estimation: 1) error due to the inability of the neural model to completely map the underlying physical relationship, 2) uncertainty in the training data as a result of the *Spectra6** models' inability to completely describe the physical nature of the flow emission, and 3) uncertainties introduced during the calibration/response function creation processes.

Typically, the statement of uncertainties in a neural network prediction involve only error estimates that are based on the neural model's inability to fit the training data. No consideration is given to the error component introduced through the acquisition of the actual testing or training data sets. The terse technical note described herein serves to highlight this error component and provide a means by which its effects can be quantified.

The general architecture of the RBFNN is given in Fig. 5 below. It is assumed that prior knowledge of the uncertainties in the inputs has been established. The figure shows a fully connected RBF network with radial kernels and associated weighting factors. The kernel function can be any radially symmetric function; that is, a function which has a "local" behavior such as the Gaussian, Cauchy, or Multiquadric. The output quantities (y_k) are then given by the basis function expansion of Equation 7.

$$y_k = \sum_{j=1}^{m} w_{jk}(g_j) \qquad (7)$$

* The *Spectra6* model is a computer program that produces the training data for the RBFNN. Inputs into the program are quantum variables; outputs are an electromagnetic spectrum and associated temperature, number density, and broadening parameter. (Cooper, *et al*, 1997)

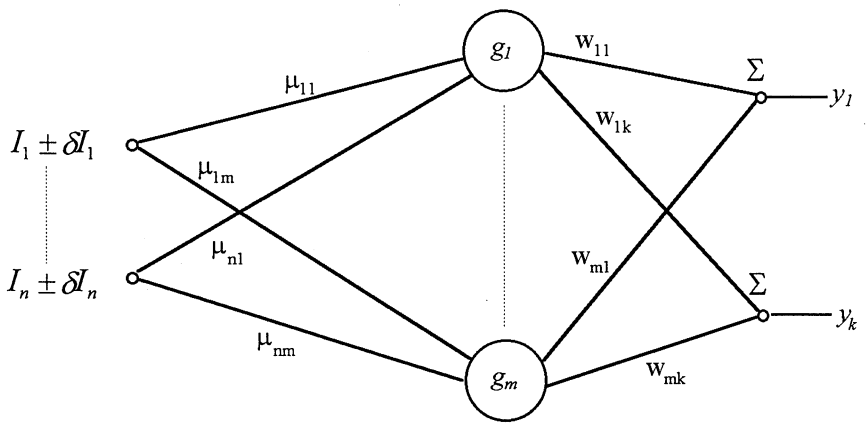

Fig. 5. RBFNN General Architecture.

Note, the bias term in Equation 7 is not included because it drops out in the partial derivative expansion. For the sake of analysis, assume the kernel function is a Gaussian (Equation 8) and that the network coefficients (w_{ii}, μ_{ii}) have already been established. Further assume that any uncertainties associated with the network inputs are independent and random. With these conditions, the uncertainty in an output variable can be obtained via Equation 9 below.

$$g_m = \exp\left\{-\frac{\sum_{i=1}^{n}\left(I_i - \mu_{mi}\right)^2}{R^2}\right\} \tag{8}$$

$$\left(\delta y_k\right)^2 = \sum_{i=1}^{n}\left(\delta I_i \frac{\partial y_k}{\partial I_i}\right)^2 \tag{9}$$

Through a trivial (just kidding) partial expansion, the partial derivatives can be evaluated as,

$$\frac{\partial y_k}{\partial I_n} = \sum_{j=1}^{m} w_{jk} \frac{\partial g_j}{\partial I_n} \tag{10}$$

As an example, the paritial expansion has been worked out for the Gaussian kernel below,

$$\frac{\partial y_k}{\partial I_n} = \sum_{j=1}^{m} w_{jk} g_j \bullet \left(-\frac{2}{R^2}\left(I_n - \mu_{jn}\right)\right) \tag{11}$$

Conclusions

Improvements in uncertainties in the values of radiant intensity (I) can be accomplished mainly by improvements in the calibration process and in minimizing the difference between the background and engine plume radiance. For engine tests in which the plume is extremely bright, the difference in luminance between the calibration lamp and the engine plume radiance can be so large as to cause relatively large uncertainties in the values of R. This is due to the small aperture necessary on the receiving optics to avoid saturating the instrument. However, this is not a problem with the SSME engine since the liquid oxygen / hydrogen combustion is not as bright as some other fuels. Applying the instrumentation to other type engine tests may require a much brighter calibration lamp.

References

Cooper, A.E., Powers, W.T., Wallace, T.L., Buntine, W., "Recent Results in the Analysis of Large Rocket Engine anomalies Utilizing State-of-the-Art Spectral Modeling Algorithms," 1997 JANNAF.

Benzing, Daniel A., Hopkins, Randall C., Whitaker, Kevin W., "OPAD: An Innovative Rocket Engine Health Monitoring System," *Proceedings of the 16th Annual Digital Avionics System Conference*, 1997.

Whitaker, K L., Moore, D., Benzing, D.A., "A Neural Network Approach to Anomaly Detection in Spectra," *35th Aerospace Sciences Meeting & Exhibit*, AIAA-97-0223, Reno, NV, 1997

1997

NASA/ASEE SUMMER FACULTY FELLOWSHIP PROGRAM

MARSHALL SPACE FLIGHT CENTER
THE UNIVERSITY OF ALABAMA

DYNAMIC MODELS OF INSTRUMENTS USING ROTATING UNBALANCED MASSES

Prepared By:	John Y. Hung, Ph.D.
Academic Rank:	Associate Professor
Accompanying Student:	Jason M. Gallaspy (M.S. candidate)
	Carlee A. Bishop (Ph.D. candidate)
Institution and Department:	Auburn University Department of Electrical Engineering
NASA/MSFC:	
Laboratory:	Astrionics Laboratory
Division:	Instrumentation and Control
MSFC Colleagues:	Michael E. Polites, Ph.D. Dean C. Alhorn

INTRODUCTION

The motion of telescopes, satellites, and other flight bodies have been controlled by various means in the past. For example, gimbal mounted devices can use electric motors to produce pointing and scanning motions. Reaction wheels, control moment gyros, and propellant-charged reaction jets are other technologies that have also been used. Each of these methods has its advantages, but all actuator systems used in a flight environment face the challenges of minimizing weight, reducing energy consumption, and maximizing reliability. Recently, Polites invented [1] and patented [2] the Rotating Unbalanced Mass (RUM) device as a means for generation scanning motion on flight experiments. RUM devices together with traditional servomechanisms have been successfully used to generate various scanning motions: linear, raster, and circular [3]. The basic principle can be described: A RUM rotating at constant angular velocity exerts a cyclic centrifugal force on the instrument or main body, thus producing a periodic scanning motion. A system of RUM devices exerts no reaction forces on the main body, requires very little energy to rotate the RUMs, and is simple to construct. These are significant advantages over electric motors, reaction wheels, and control moment gyroscopes.

Although the RUM device very easily produces scanning motion, an auxiliary control system has been required to maintain the proper orientation, or pointing of the main body. It has been suggested that RUM devices can be used to control pointing dynamics, as well as generate the desired periodic scanning motion. The idea is that the RUM velocity will not be kept constant, but will vary over the period of one RUM rotation. The thought is that the changing angular velocity produces a centrifugal force having time-varying magnitude and direction. The scope of this ongoing research project is to study the pointing control concept, and recommend a direction of study for advanced pointing control using only RUM devices.

This report is subdivided into three section. Three dynamic models and one proposed control principles are described first. Then, the results of model analyses and some experiments are discussed. Finally, suggestions for future work are presented.

DYNAMIC MODELS AND CONTROL

A sketch of one RUM system is shown in Figure 1. Two RUM devices are mounted on the main body so as to produce a circular scan with respect to the line-of-sight (LOS) vector. The RUMs rotate in the same direction, but are synchronized and positioned 180° apart to eliminate reaction forces at the center of mass. (In a zero-gravity environment, a single RUM is adequate.)

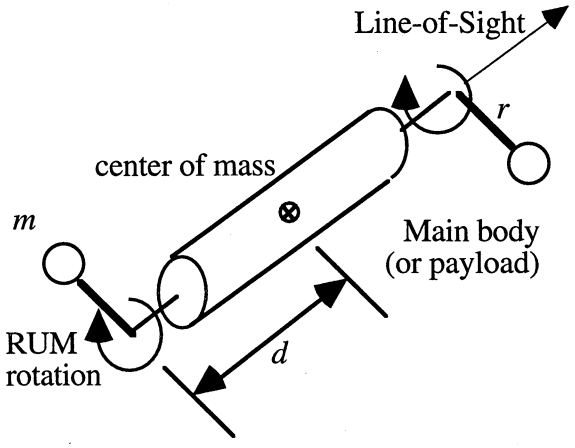

Figure 1. Sketch of a body using 2 RUMs to generate scanning.

Several models describing the main body and RUM device dynamics are summarized below. Key parameters and variables are defined as follows:

m	RUM mass
r	RUM radius of rotation
d	distance between RUM and payload center of mass, measured along the LOS.
I	main body inertia
θ_E	main body elevation angle
θ_X	main body cross-elevation angle
θ_R	RUM angular position

The local coordinate system is shown in Figure 2. The axis $\vec{P}_1$ is aligned with the main body line-of-sight (LOS). Axis $\vec{P}_2$ is associated with the main body elevation angle θ_E, while the main body cross-elevation angle θ_X is associated with axis $\vec{P}_3$. All three axes pass through the main body center of mass.

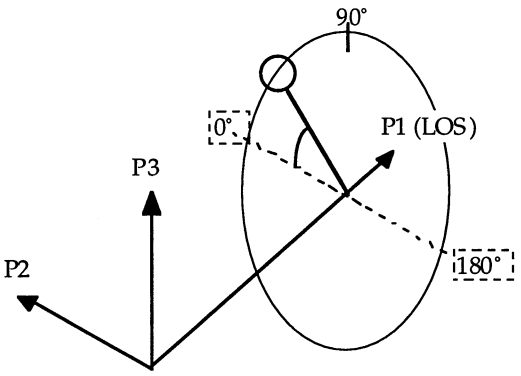

Figure 2. Coordinate system

Torque Developed by RUMs

Centrifugal force exerts a torque about the main body center of mass by acting through a moment arm of length d. In the system of Figure 1, the two RUM devices are controlled to rotate in synchronized fashion, but always pointing 180° opposite each other. Therefore, the total torque or moment exerted about the main body center of mass is doubled. The torque vector can be decomposed into elevation and cross-elevation components, expressed by the following relationship [1]:

$$\begin{bmatrix} T_E \\ T_X \end{bmatrix} = 2dmr\omega_R{}^2 \begin{bmatrix} -\sin\theta_R \\ \cos\theta_R \end{bmatrix} \tag{1}$$

Observation of the actual experiment motion verifies that the centrifugal forces generated by RUMs are the dominant effects when RUM angular velocity is constant [3]. But if the RUM angular velocity is not constant, then it appears that the main body also reacts to the RUM motor torques as the RUM accelerates and decelerates during each rotation. Further analysis of the RUM system suggests that a more complete model of the developed torques is of the following form [8]:

$$\begin{bmatrix} T_E \\ T_X \end{bmatrix} = 2dmr \begin{bmatrix} \cos\theta_R & -\sin\theta_R \\ \sin\theta_R & \cos\theta_R \end{bmatrix} \begin{bmatrix} \dot{\omega}_R \\ \omega_R{}^2 \end{bmatrix} \tag{2}$$

In other words, the torque on the main body about the center of mass is a function of RUM angular velocity (squared) AND the RUM acceleration.

Another observation is that both models (1) and (2) are derived under the assumption that there are no other cross-coupling effects. A more complete model has been derived by Bishop, using techniques from robot dynamic modeling [9]. The form of that model is as follows:

$$D(q)\ddot{q} + C(q,\dot{q})\dot{q} = T(q) \tag{3}$$

where

q :	4x1 vector of the cross-elevation, elevation, and two RUM position angles
$D(q)$:	4x4 matrix of inertia components
$C(q)$:	4x4 matrix of coriolis and centripetal force components
$T(q)$:	4x1 vector of applied torques

Bishop has also shown that the model can be reduced to three variables instead of four under the assumption that the two RUMs are perfectly synchronized. All three models (1), (2), and (3) predict similar scanning behavior. In fact, the model (1) can be recovered from both other models under suitable assumptions (e.g. small angular variations, ignoring cross-coupling, etc.).

Pointing Control Using RUM Rate Variation

Polites originally proposed to use a control signal that introduces periodic variations in the RUM rate ω_R. A heuristic explanation can be found in the report [4]. The logic of such an approach can also be analytically confirmed by applying the nonlinear control design technique known as input-output linearization. The interested reader is also directed to the references [5] - [7].

Polites suggested that control input be defined as:

$$\omega_r = \omega_{ro} + \Delta\omega_X \cos\theta_R - \Delta\omega_E \sin\theta_R \tag{4}$$

where

ω_{ro} : a constant (nominal RUM rate of rotation)

$\Delta\omega_X$: a rate variation to compensate for cross - elevation gimbal error

$\Delta\omega_E$: a rate variation to compensate for elevation gimbal error

The RUM rate variations $\Delta\omega_X$ and $\Delta\omega_E$ are small relative to the nominal RUM rate ω_{ro}. Notice that the rate variations are periodic and are synchronized to the RUM position θ_R through the $\sin(\theta_R)$ and $\cos(\theta_R)$ factors.

Summary of Model Analyses & Experiments

Extensive computer simulations of the three models have been performed. Also, a study of the total angular momentum of the system has been conducted. In addition, several experiments on the NASA RUM test bed located at Marshall Space Flight Center have been conducted for comparison. All of this summer's studies have focused on a control input of the form shown in Eq. (4). The

RUM rate variations $\Delta\omega_X$ and $\Delta\omega_E$ have been held constant, so the studies and experiments address the open-loop behavior of the system. The following conclusions are drawn:

a. All three models (1), (2), and (3) predict periodic scanning behavior of the instrument, and agree reasonably well with experimental behavior.

b. The control input (4) alone has little noticeable effect on the experimental system's pointing. That is, significant changes in the average cross-elevation angle and average elevation angle are not possible using the control input (4) alone. This experimental observation is in agreement with behavior predicted by Bishop's simulations of model (3).

c. Bishop's model (3) shows that cross-coupling effects have a significant role in the system response. The control (4) may have a very small, long term effect on the pointing angles. The predicted effect is small, however, and may be easily washed out by imperfections in the present experiment (e.g. nonlinear frictions at the gimbals, gravity, cable tensions, etc.).

d. The model (2) also predicts a small effect on the instrument model pointing when control input (4) is used alone. It is concluded that reactions to the RUM accelerations and decelerations cannot be ignored.

e. Curiously, the model (1) predicts significant effect on the instrument pointing by using the control input (4) alone. This simulation result is not in agreement with either the experiment, or the simulations of models (2) and (3). However, the analyses of model (1) DOES give insight to how instrument pointing can be achieved by a modified control. In other words, the control input (4) may not be suitable alone, but may be effective if augmented by other control effort. This is explained further in the recommendations for future work.

f. Finally, angular momentum conservation does not appear to be violated. Angular momentum of a system set up for linear scan using RUMs has been performed this summer. The preliminary results leave the door open for pointing control using RUMs alone.

RECOMMENDATIONS FOR FUTURE WORK

Analysis of the basic model (1) and an angular momentum model suggests that pointing control of the system should be possible. However, the more detailed models (2) and (3) predict that cross-coupling and other nonlinear dynamics are significant and cannot be ignored. From the controller design viewpoint, it is suggested that these nonlinear effects be cancelled by feedback control. The idea is very similar to feedback linearizing control, which has been proven in robotic control (but is called "computed torque control") to give linear closed-loop dynamics to systems that are inherently nonlinear. In the RUM application, linear closed-loop dynamics are not the goal. Rather, closed-loop dynamics consistent with that predicted by the nonlinear model (1) are the goal. Hence it is recommended that further analytical study be focused on the design of a nonlinear controller to cancel the undesirable dynamic components. These undesirable components are described in the model (3).

Implementation of the recommended nonlinear controller may not be feasible on the present experimental system at Marshall Space Flight Center. A chief concern is the limited computational capability of the microcontroller system. Although modifications were made last summer to improve the sampling rate and accuracy of the calulations, it is recommended that an electronic control system based on a floating-pointing digital signal processor be developed for future experimental work.

REFERENCES

[1] M.E. Polites, "New method for scanning spacecraft and ballon-borne/space-based experiment," AIAA Journal of Guidance, Control and Dynamics, vol. 14, no. 3, May-June 1991, p. 548-553.

[2] M.E. Polites, "Rotating-unbalanced-mass devices and methods of scanning balloon-borne experiments, free-flying spacecraft, and space shuttle/space station attached experiments," U.S. Patent #5,129,600, National Aeronautics and Space Administration, Washington, D.c. July 14, 1992.

[3] D.C. Alhorn and M.E. Polites, "Rotating unbalanced-mass devices for scanning: results from the proof-of-concept test," *Guidance and Control 1994*, Vol.86, *Advances in the Astronautical Sciences*, Edited by R.D. Culp and R.D. Rausch, American Astronautical Society, 1994.

[4] J. Y. Hung, D.A. McGee, M.E. Polites, D.C. Alhorn, "Pointing and scanning control of instruments using rotating unbalanced masses," Project summary report, ASEE/NASA Summer Faculty Fellowship Program, Marshall Space Flight Center, Huntsville, AL, Aug 1996.

[5] B. Friedland, Advanced Control Techniques, McGraw-Hill, 1995.

[6] A. Isidori, Nonlinear Control Theory, Springer-Verlag, 1984.

[7] J-J. E. Slotine and W. Li, Applied Nonlinear Control, Prentice-Hall, 1989.

[8] C.A. Bishop, J.Y. Hung, M.E. Polites, D.C. Alhorn, "Pointing and scanning control of optical instruments using rotating unbalanced masses," *Guidance and Control 1997*, Vol. 94, *Advances in the Astronautical Sciences*, Edited by R.D. Culp and S. B. Wiens, American Astronautical Society, 1997, pp. 251-265.

[9] C.A. Bishop, "Nonlinear modeling, analysis, and control of intruments using rotating unbalanced masses," Ph.D. dissertation, Dept. of Electrical Engineering, Auburn University, appearing Feb 1998.

1997

NASA/ASEE SUMMER FACULTY FELLOWSHIP PROGRAM

MARSHALL SPACE FLIGHT CENTER
THE UNIVERSITY OF ALABAMA IN HUNTSVILLE

APPLICATION OF FERSNEL ZONE TO CROSS TALK

Prepared By:	Hank Javan, Ph.D.
Academic Rank:	Associate Professor
Institution and Department:	North Carolina A&T State University Department of Electronics and Computer Technology
NASA/MSFC:	
Branch:	Electromagnetics and Aerospace Environments ,EL23
Lab:	System Analysis and Integration, EL01
Directorate:	Science and Engineering, EA01
MSFC Colleagues:	Mark E. Krome Tony Clark

Introduction

Unintentional radiation results in cross coupling to nearby cables. As frequency increases, the amount of this coupling becomes significant especially in high speed data transmission and space lab experiments. There has been considerable amount of research to model this radiation and design the electronic equipment accordingly so that operation of space lab instruments will be immune to unwanted radiation. Here at MSFC, Electromagnetics and Aerospace Environment Branch has the responsibility to analyze, test, and make the necessary recommendation as to the safe operation of instruments used in space program. Rules, regulation, and limits as set by this group are published in Electromagnetic Compatibility Design and Interference Control (MEDIC) Handbook (T.L. Clark, etl. 1995). This document contains both conducted and radiate emission rules and limits are set by NASA. However cross coupling have not been included. At the time of assigning research task for the author, the Group decided that a more in-depth investigation of Near Field is needed before establishing set of rules and limits for cross coupling. Thus this task was assigned to the author with hope that his work will be more beneficial to NASA's Space mission experiments. The model and the method which will be described shortly is intended to improve the present approach of this Group and suggests a method for measuring the cross field coupling capacitance.

Methodology

Basically three methods have been used to model unintentional radiation coupling. These are; Circuit model, Transmission Line Method, and Field Approach.

First method uses lumped element approach. This method is used by most of the authors for short length of cable i.e. $l < \lambda$, (λ is the wave length) and low frequency regions, (Mills, 1993, Paul, 1992). For cross talk consideration the distance is so short that cable looks infinitely long and thus in the frequency range of interest current can not be considered constant as is required by this method.

Second method was introduced by (C.R.Paul, 1976) and was published in his text book on INTRODUCTION TO ELECTROMAGNETIC COMPATIBILITY. In this method, after evaluating the capacitance and the inductance of multiconductor transmission line, he determines exact expressions for the calculations of Near End and Far End coupled voltages using distributed transmission line approach with sinusoidal steady state excitation, in matrix form. In his later work he also introduces Spice Model for coupled transmission lines. His work is quite remarkable but requires considerable amount of computer's memory and experienced programmer.

The third method was introduced by (A.A.Smith, Jr, 1977) in " Coupling of External Electromagnetic Fields to Transmission Line" with the latest edition in 1989. He uses transmission line exposed to radiated emission and calculates the transfer function of radiation, i.e. the ratio of induced current to incident electric field. This method is not suitable for industrial applications since it requires elaborate mathematics.

Time domain approach to distributed transmission line was introduced by (Sol Rosenstark, 1994). He separates coupling in to forward and reversed talk and calculates the corresponding coefficient under different termination. His method is quite recent and authors believe that it can be used to effectively determine the coupling capacitor and the inductor. His work is under the investigation by the authors.

Present Approach

Our method is concentrated on field equations using Fresnel Zone to analyze radiated emission and problem of cross coupling. It seems that this method has not been explored as yet even though it is a direct application of Near Field radiation. It is important to note that in the Fresnel Zone the wave front are no longer plane waves but rather spherical and thus electric and magnetic fileds have no simple relation of 377 Ohms as for plane wave but require some mathematics and applications of Maxwell equations. In spite of these difficulties we prefer to explore this method because cross talk is the result of Near Field radiation, it seems natural to apply field theory directly. Using field theory with careful approximations a very simple and useful result can be obtained which can be used without regarding the mathematics. This was the primary concern , to obtain a simple workable equation. There are, however, two ways to apply field equations to Near Field radiated emission; Vector Potential, and Electric Field methods.

Vector Potential Method: In this method the vector potential of a short element of a radiator is calculated first, then the total vector potential in the Fresnel Zone is determined by direct integration and by careful approximation. The magnetic and the electric field are then obtained by applying Maxwells' equations with no additional approximations.

Electric Field Method: This method involves the direct application of the electric field of elemental radiator to Fresnel Zone and obtaining the total electric field by integration and carefully using reasonable approximation.

We have derived rather simple expressions for magnetic and electric field using above methods. But the two methods have yielded different numerical results due to the nature of approximations. Vector potential method has yielded familiar and more accurate results than the second method. Thus in the following we will explain this method.

Vector Potential Method

Consider a radiator along the z-axis as shown in figure 1.

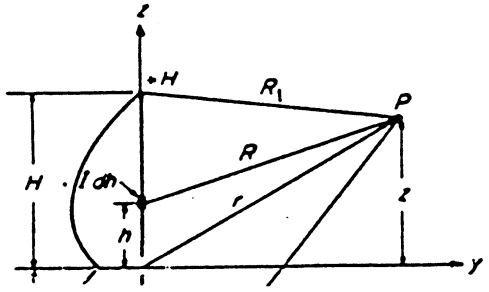

Fig. 1- Geometry for calculating vector potential

If the radiator is small, then in the vicinity of the radiator, (in the Fresnel Zone) the wavefront will be spherical and will reach the observer at point P with a time delay of t-R/c. The proper expression for the vector potential at point P for such a radiator is given by (Jordan, 1968):

$$A_z = \frac{\mu}{4\pi} \int \frac{I(z)\, e^{j\omega(t-R/c)}}{R}\, dz \qquad (1)$$

μ is the permeability of transmitting medium, ω is $2\pi f$ with f in Hertz, c is the speed of wavefront, and R is shown in figure 1. It is customary to write this equation in term of wave number as defined below;

$$k = \frac{2\pi}{\lambda}; \qquad \lambda = \frac{c}{f}; \qquad k = \frac{\omega}{c} \tag{2}$$

Thus equation (1) can be written as

$$A_z = \frac{\mu}{4\pi} \int \frac{I(z)\, e^{j(\omega t - kR)}}{R}\, dz \tag{3}$$

If we can determine I(z), current distribution along the radiator, then the magnetic and electric fields can be obtained from A_z by taking its curl and applying Maxwell's equation respectively. Following cases have been investigated by the author:

Case 1-$I(z) = I_o$
Case 2-$I(z) = I_o e^{j\omega t}$
Case 3-$I(z) = I_o e^{j\omega t} \mathrm{Sin}[k(H-z)]$

There are other expressions for current variation along the cable like $I(z) = I_o (1 - h/l)$ (Tesche 1997), but sinusoidal variation is more practical. The true current distribution can only be found from experimental measurements. We have carried out this experiment in the MEDIC Lab of our Branch, the results and the experimental setup are shown in figure 2 with the computer plots for two different terminations. It is concluded, from these plots, that the current distribution in fact is sinusoidal. Thus the expression for the vector potential becomes;

$$A_z = \frac{\mu I_o e^{j\omega t}}{4\pi} \int \frac{\mathrm{Sin}[k(H-h)]\, e^{-jkR}}{R}\, dz \tag{4}$$

for convenience we will drop $e^{j\omega t}$ as long as there is not operation on t. We now outline the evaluation of magnetic field H_x, and the electric field E as following.

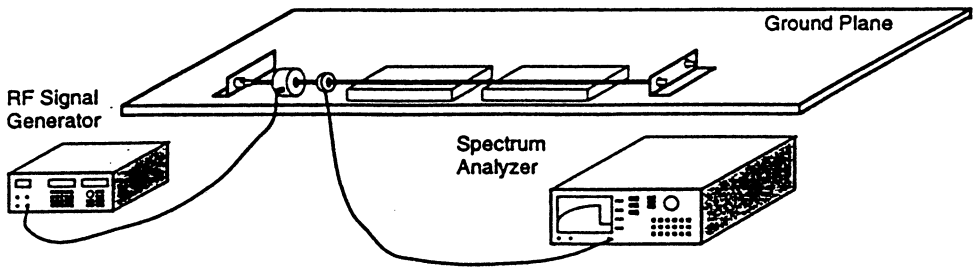

Fig. 2-Experimental setup for measuring I(z)

Table 1-Current Distribution

Location	dbm	
	short	open
18.75 cm	-21.5dbm	-20dbm
37.5	-27.5	-22
56.25	-35	-24
75	-44	-27
93.75	-49	-30
112.5	-30	-33
131.25	-21.5	-38
150	-21	-46

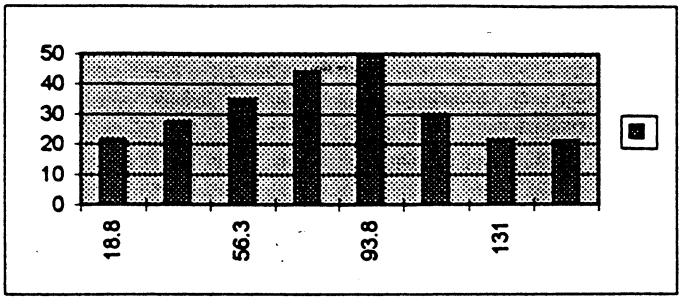

1.Evaluation of Magnetic Field: Using curl A, we obtain for H_x:

$$H_x = -\frac{\partial A_z}{\mu\,\partial y} = -\frac{I_o}{8\pi}\left[e^{jkH}\int\frac{\partial}{\partial y}\left(\frac{e^{-jk(R+h)}}{R}\right)dh - e^{-jkH}\int\frac{\partial}{\partial y}\left(\frac{e^{-jk(R-h)}}{R}\right)dh\right] \quad (5)$$

using the geometry of figure 1 and carrying out the indicated integration, we obtain

$$H_x = -\frac{I_o}{8\pi}\left[\frac{-2H\,e^{-jkR_1}}{R_1\,y} - \frac{y\,e^{-jkr}}{r(r-z)}\,2jSin(kH)\right] \quad (6)$$

2.Evaluation of Electric Field: Using curl H, components of electric field are calculated as followings:

$$E_z = \frac{1}{j\omega\varepsilon}(\nabla xH) = \frac{1}{j\omega\varepsilon y}\frac{\partial}{\partial y}(y\,Hx) = \frac{I_o\,e^{-jkr}}{4\pi\varepsilon c}\left[\frac{1}{y^2(1-1/2z^2)}\right]\frac{Sin\,(2\pi f/c)H}{(2\pi f/c)} \quad (7)$$

$$E_y = \frac{I_o\,ej\omega t}{4\pi\varepsilon c}\left[\frac{1}{z(1+y^2/2z^2)(1-1/2z2)}\right]\frac{Sin(2\pi f/c)H}{(2\pi f/c)} \quad (8)$$

In order to compare our results with the experimental values we must determine the total electric field as following;

$$|E|^2 = |E_y|^2 + |E_z|^2 \quad (9)$$

instrument will read the RMS value of this equation. We have used equation (7,8) and have calculated this value. The results are shown in table 2. Figure 3,4 show these results in graphical forms. The frequency plots agree with plots given by (Mills, 1993)

Case 3 - $I(z) = I_o e^{j\omega t} \sin[k(H-z)]$

TABLE 2 - COMPARISON OF THEORETICAL AND EXPERIMENTAL RESULTS

	H = 1met., Io = 177μa@f = 1Mhz		H=1met.,Io=56μ@f= 10MHz	
Model	y = 0.5met.	y = 1met.	y = 0.5	y = 1met.
Present Model	0.02 V/m	0.0064V/m	0.0067V/m	0.0017V/m
Point Source	2	0.25	0.2	0.025
Experiment (Evans, 1995)	0.03	0.02	0.01	0.01
Experiment (McCollum, 1997)		0.003		0.017

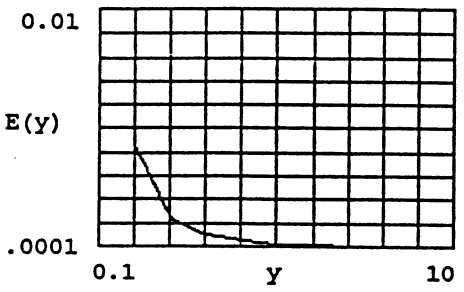

(a)

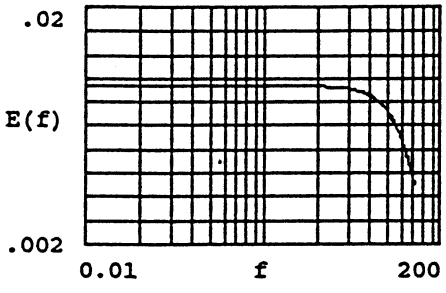

(b)

Fig. 3- Variation of $|E_z|$, equation (7) for z = H/2,
f = 1MHz. I_o = 177μa, (b) y = 0.5, I_o = 116μa

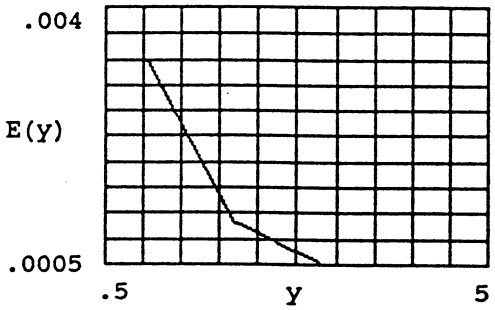

(a)

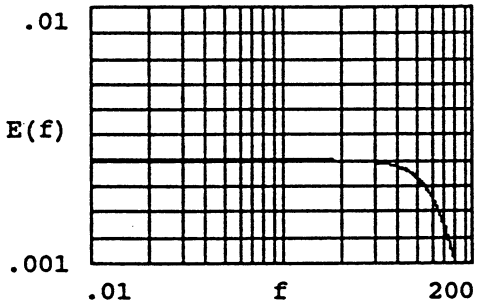

(b)

Fig. 4- Variation of $|E_y|$, equation (8) for z=H/2.
(a) f = 1MHz, I_o = 177μa, (b) y = 0.5, I_o = 116μa

Evaluation of Coupling Capacitor: Coupling capacitor is the most important parameter of cross talk. It is the distributed capacitance along the cables between them. It is necessary to obtain an expression for its dependence on distance and the frequency in order to reduce its effect efficiently. Our method yield direct expression for it as following;

$$C = \frac{dQ/dz}{dV/dz} \qquad (10)$$

dV/dz is equal to $-E_z$ and is given by equation (7), no further math is needed. DQ/dz can be evaluated as following;

$$dQ/dz = \frac{d}{dz}\int I(z)\,dt = \frac{d}{dz}\int Io\, e^{j\omega t}\, Sin[k(H-z)] \qquad (11)$$

using the result of this integration and equation (7) for E_z, capacitance c, can now be written as;

$$|C| = \frac{8\pi^2 \varepsilon f}{c}\, y^2 (1-1/2z^2)\, \frac{Cos[k(H-z)]}{Sin(kH)} \qquad (12)$$

Figure 5 is a plot of this equation. The values computed from this equation range between 0.5 to 5 pf, in excellent agreement with (Paul, 1992).

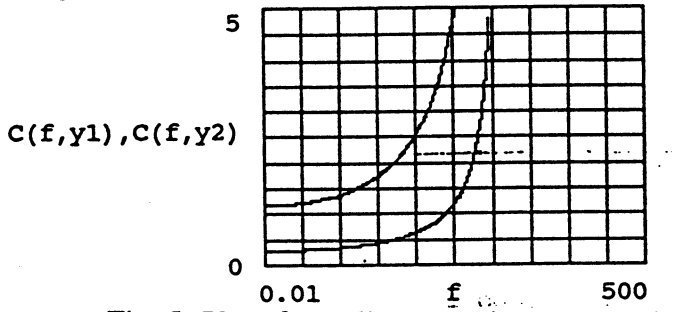

Fig. 5- Plot of coupling capacitance, equation (12)

Conclusion

In conclusion I have applied field theory and investigated the radiated emission and cross coupling in the Fresnel Zone. I have provided:

1. Simple expressions for magnetic and electric fields. It is shown that electric field decreases with inverse square distance modified by current distribution function.
2. Expression for the coupling capacitance, it is shown that this parameter in addition to its dependence on inverse square distance also depends on frequency. This is a new finding.
3. Near End or the Far End effect by simply changing the coordinate of observation point.
4. Our results apply for worst case termination, i.e. open circuit

Our work, however does not include:

1. Losses in the cable or the dispersion effects, thus the propagation constant, k, has been taken $2\pi/\lambda$.
2. Skin effect. This effect will increase the effective AC resistance of the cables, and thus the cable losses. Its effect becomes significant at higher frequencies.
3. Matched termination
4. In applying the results of this work we should adhere to the following constraints:

$$z/\lambda < 1, \qquad y/z << 1$$

Acknowledgment

The author would like to thank Dr. Gerald Karr, from UAH, University Program Co-Director for 1997 NASA/ASEE Summer faculty fellowship Program and Dr. James Dowdy from MSFC/NASA for their encouragement and supporting this work. I also would like to thank the Branch Manager, Chief Engineer Steve Pearson for providing the state of the art lab equipment for the experimentation. Finally I would like to thank Mr. Ross Evans for his assistance and discussions.

References

Clark, T.L., McCllum, M.B., Trout, D.H., and Javor, K., (1995), Marshll Space Flight Ce Center Electromagnetic Compatibility Design and Interference Control, (MEDIC) Handbook, CDDF Final Report, Project No. 93-15, June 1995.

Evans, R.W., (1995), International Space Station Electromagnetic Compatibility Analysis (ISEAS), Validation Study, Physitron, Alabama, pp. 84-86.

Jordan, E.C., (1968), Electromagnetic Waves and Radiating Systems, Prentice - Hall, Inc. New Jersey, pp. 316-322, 333-338.

Mills, J.P., (1993), Electromagnetics Interference Reduction in Electronic Systems, Prentice-Hall, Inc., New Jersey, pp. - 125-166.

Paul, C.R., (1992) Introduction to Electromagnetic Compatibility, John Wiley & Sons, Ne New York, pp. 491- 631.

Rosenstark, S., (1994) Transmission Lines in Computer Engineering, McGraw-Hill, Inc., New York, pp. 113-132.

Smith, A.A. (1989), Coupling of External Electromagnetic Fields to Transmission Lines, I Interference Control Technologies, Inc., New York, pp.21-45.

Tesche, F.M., Ianoz, M.V., Karlsson, T.K., (1997), EMC Analysis Methods and Computational Models, John Wiley & Sons, Inc., New York, pp. 117-120.

1997

NASA/ASEE SUMMER FACULTY FELLOWSHIP PROGRAM

MARSHALL SPACE FLIGHT CENTER
THE UNIVERSITY OF ALABAMA

FLAMMABILITY OF HETEROGENEOUSLY COMBUSTING METALS

Prepared By: Peter D. Jones, Ph.D., P.E.

Academic Rank: Associate Professor

Institution and Department: Auburn University
Mechanical Engineering Department

NASA/MSFC:

Laboratory: Materials and Processes
Division: Metallic Materials and Processes
Branch: Metallurgical Research and Development

MSFC Colleague: Biliyar N. Bhat, Ph.D.

INTRODUCTION

Most engineering materials, including some metals, most notably aluminum, burn in homogeneous combustion. 'Homogeneous' refers to both the fuel and the oxidizer being in the same phase, which is usually gaseous. The fuel and oxidizer are well mixed in the combustion reaction zone, and heat is released according to some relation like

$$q_c = \Delta H_c C \left(\frac{p}{p_o}\right)^a \exp\left(\frac{-E_c}{RT}\right) \qquad (1)$$

where the pressure exponent a is usually close to unity. As long as there is enough heat released, combustion is sustained. It is useful to conceive of a threshold pressure beyond which there is sufficient heat to keep the temperature high enough to sustain combustion, and beneath which the heat is so low that temperature drains away and the combustion is extinguished.

Some materials burn in heterogeneous combustion, in which the fuel and oxidizer are in different phases. These include iron and nickel based alloys, which burn in the liquid phase with gaseous oxygen. Heterogeneous combustion takes place on the surface of the material (fuel). Products of combustion may appear as a solid slag (oxide) which progressively covers the fuel. Propagation of the combustion melts and exposes fresh fuel. Heterogeneous combustion heat release also follows the general form of Eq.(1), except that the pressure exponent a tends to be much less than 1. Therefore, the increase in heat release with increasing pressure is not as dramatic as it is in homogeneous combustion. Although the concept of a threshold pressure still holds in heterogeneous combustion, the threshold is more difficult to identify experimentally, and pressure itself becomes less important relative to the heat transfer paths extant in any specific application. However, the constants C, a, and E_c may still be identified by suitable data reduction from heterogeneous combustion experiments, and may be applied in a heat transfer model to judge the flammability of a material in any particular actual-use situation.

In order to support the above assertions, two investigations are undertaken: 1) PCT data are examined in detail to discover the pressure dependence of heterogeneous combustion experiment results; and 2) heterogeneous combustion in a PCT situation is described by a heat transfer model, which is solved first in simplified form for a simple actual-use situation, and then extended to apply to PCT data reduction (combustion constant identification).

PROPAGATION RATE DATA

PCT burned length is difficult to predict with a heat transfer model because of the dripping phenomena. As the rod burns, a ball of molten metal covered by slag forms at its tip. When the slag is heavy enough, it sloughs off, pulling some of the molten metal with it. If there is enough molten metal left behind, and if it is hot enough, then

combustion will continue because there is enough heat released by the combustion reaction over the active surface to defeat radiative and other losses. If the molten remainder is too small or too cool, it will extinguish. The temperature of the remainder, even if given knowledge of the transient temperature field in the melt, is governed by the time or conditions under which separation (sloughing) occurs. The size of the remainder is governed by the complex viscous and attractive interactions of the sloughing slag and the fixed solid sample. Models have not yet been developed which can predict either phenomenon with any precision. Therefore, burned length results cannot at present be used to identify the constants of the combustion reaction rate equation.

Heat transfer models of heterogeneous combustion situations [2,3] are more readily written to simulate the approximate temperature fields and the propagation rates of the flame front or melt interface for a steadily advancing combustion, given the physical and thermophysical properties of the metal and the form and constants of the combustion reaction rate. The propagation rate is an experimentally observable quantity, and can be used to correlate simulation with experiment. (Temperature fields in the burning, slag-covered molten metal are difficult to observe. Infrared measurements of the molten region in some PCTs have been acquired [4], though these measurements average radiant intensity over the entire molten region, and thus represent a bulk mean of T^4. This could also be a useful quantity for correlation, though capability for this measurement is not yet present at MSFC.)

The propagation rate of a PCT test may be determined from a suitable video record of the test by measuring the length of the unconsumed rod as a function of time (using a 0.01 s resolution time display, a jog VCR, and a scale factor for length measured on the video screen). This has been done for a variety of materials and is reported in ref.[5]. It is found that the propagation rate as a function of test time is fairly constant, and that there is relatively little scatter in the propagation rate from one observably identical sample to another. Therefore, propagation rate is a conveniently observable quantity which may be conveniently used to correlate between experimental and simulated results in order to identify the constants of the combustion reaction rate equation.

Propagation rate as presently reported on MSFC PCT data sheets shows a large uncertainty. This is because propagation rate is presently derived from the measured burn length divided by the difference between very nominal test start and stop times. To make propagation rate data useful, a more automated version of the above procedure must be instituted. For instance, clear (well filtered) video records could be made of all tests (currently, only one test cell has an adequate video setup), and visible pointers at a measured distance apart could be placed in the plane of the sample. Change in length over change in time could then be easily computed.

The propagation rate data in ref.[5] are presented as functions of PCT chamber pressure, and exponential functions are fit. It is found that in heterogeneous combustion of the samples considered (low alloy steels, stainless steels, nickel alloys, cobalt alloys),

the pressure exponent of this fit is between 0.18 and 0.49. Thus pressure dependence is relatively flat (as compared to homogeneous combustors), and threshold pressure will be difficult to identify experimentally.

PCT THERMAL MODEL

A heat transfer (thermal) model of the PCT test is presented in ref.[3]. This model does not include slag build-up on the fuel/oxidizer interface, and is thus subject to temperature instabilities. The instabilities were temporarily solved with an ignition temperature (imposed constant temperature for the combustion reaction). This model is completed with the addition of combustion-limiting slag build-up terms. In the solid zone, energy conservation is written

$$\rho_s c_s A_s\left[\frac{\partial T}{\partial t} + (s-1)\frac{V}{l_s}\frac{\partial T}{\partial s}\right] \tag{2}$$

$$= \frac{k_s A_s}{l_s^2}\frac{\partial^2 T}{\partial s^2} - P_s h_s (T - T_w) - P_s \varepsilon_s \sigma_b (T^4 - T_w^4)$$

The left side of Eq.(2) represents advective transport (the phase interface between solid and liquid is fixed and serves as the origin). The coordinate system thus moves and stretches (as the solid is consumed), and the von Mises transformation must be applied. The right side first term is conduction, the second term is convection from the surface, and the third is radiation. The boundary conditions are adiabatic at the far end, and melting temperature at the phase interface. Variables are $T(s)$ and V. The convection coefficient arises from a cold vertical surface heated by a hot vertical surface below it [6]. In the liquid zone, energy conservation is written

$$\rho_\ell c_\ell A_\ell\left[\frac{\partial T}{\partial t} + (1-x)\frac{V}{l_x}\frac{\partial T}{\partial x}\right] \tag{3}$$

$$= \frac{k_\ell}{l_x^2}\left(A_\ell \frac{\partial^2 T}{\partial x^2} + \frac{dA_\ell}{dx}\frac{\partial T}{\partial x}\right) - P_\ell h_\ell (T - T_w)$$

$$- P_\ell \sigma_b (T^4 - T_w^4) + P_\ell q_c$$

where combustion heat release has been added to the right side. The variables are $T(x)$ and V. Boundary conditions are adiabatic at the far end, and melting temperature at the phase interface. The propagation rate V is defined by the interface condition

$$V = \frac{1}{\rho_s h_{s\ell}}\left[\frac{k_s}{l_s}\frac{\partial T}{\partial s}\bigg|_{s=0} + \frac{k_\ell}{l_x}\frac{\partial T}{\partial x}\bigg|_{x=0}\right] \tag{4}$$

The combustion heat release is moderated by build-up of slag (combustion product), which reduces the concentration of oxygen on the molten metal surface. Oxygen penetrates the slag by diffusion, and the slag layer acts as a diffusive resistance to oxygen concentration, thus

$$q_c = \Delta H_c \left\{ \left[C \left(\frac{\rho}{\rho_o} \right)^a \exp\left(\frac{-E_a}{RT} \right) \right]^{-1} + \frac{\delta}{\rho_{ox} D} \right\}^{-1} \quad (5)$$

The slag thickness is related to the combustion reaction rate and is also defined on the moving, stretching coordinate system

$$\frac{\partial \delta}{\partial t} + (1-X) \frac{V}{l_x} \frac{\partial \delta}{\partial X} = \frac{1}{\rho_s} \left\{ \left[C \left(\frac{\rho}{\rho_o} \right)^a \exp\left(\frac{-E_a}{RT} \right) \right]^{-1} + \frac{\delta}{\rho_{ox} D} \right\}^{-1} \quad (6)$$

In the solid rod, cross sectional area and perimeter are constant. In the liquid ball, these are functions of x

$$A_s = \pi (1-X)(r^2 + X l_x^2) \quad (7)$$
$$P_s = 2(\pi A_s)^{1/2}$$

where the length of the liquid zone is defined from continuity by

$$\frac{dl_x}{dt} = \frac{2 \rho_s A_s V}{\pi \rho_s (l_x^2 + r^2)} \quad (8)$$

The model of Eqs.(2-8) is solved in discrete form using a full matrix solver for $T(s)$, $T(x)$, and V. (Iterative solution between T and V tends to diverge). Nonlinear terms, including T/V cross terms are linearized by Taylor series about set points, and the solution is iterated to converge the linearization points. After convergence, the simulation is marched in time.

The model was initially simplified to steady state, with constant liquid cross section and perimeter, to provide a solution development case. Such a case represents a simple actual-use situation of steady combustion of a flat sheet with a line of combustion going all the way across it. Simulations were successful, showing a positive propagation rate, a solid temperature profile rising to the interface, a liquid temperature profile rising from the interface under the influence of combustion and then falling as the building slag layer inhibited further combustion, and a slag layer thickness building to a downstream asymptote (resolidification downstream was not simulated). If the combustion rate constants were reduced, the propagation rate slowed or went negative (negative rate is a degenerate case in the model, and physically represents extinguishment). The simple simulation was found to be very sensitive to D, which is itself a function of temperature [7]

$$D = D_o \exp\left(\frac{-\Delta H_D}{RT} \right) \quad (9)$$

Equation (9) represents an extrapolation to combustion temperatures (1800 to 3000 K for iron) from data peaking at 1500 K. This is a shortcoming of the model, since oxygen diffusion through slag has a great impact on the simulation, and yet very little is known about diffusion through high temperature oxides lying on liquid metals. It must be kept in mind that accurate simulation requires good physical understanding, and that the mechanisms of heterogeneous combustion are at the edge of our knowledge. High temperature diffusion through combustion products is one of the detailed issues which lie on this edge. Further study of high temperature diffusion through oxide is warranted.

The model of Eqs.(2-8) was then prepared for transient PCT simulation to roughly identify the combustion rate constants. This application proved to be less stable than the steady, one-dimensional simplification. Stable solutions could only be obtained through careful selection of starting linearization points and ultra-slow under-relaxation (successive under-relaxation coefficient of 0.02). Since the model was implemented on WATFOR Fortran on a 33 MHz PC, this meant a run of at least overnight for the first time step, and several days to complete a full drop growth and separation cycle. Unfortunately, it was discovered after these runs that the time and stretching terms in Eq.(6) had been neglected (the slag thickness was solved as a function of x only, using a Runge-Kutta projection at each linearization point). Correcting this oversight will require more time than remains to the author at MSFC, at the time that this report is written.

RECOMMENDATIONS

In the near term, it is recommended that the MSFC PCT operational procedure be modified to allow presentation of data as in ref.[5]. Knowledge of the variation of combustion propagation rate with pressure will allow an extra dimension of understanding in the material selection of heterogeneous combustors. Thermal models of a few generic actual-use situations should be constructed, such as burning edge, burning wedge, and burning plate (two-dimensional) should be built. These generic models would help in quantifying the correlation between hanging rod (burning pin) PCT experiments and actual-use situations.

In the middle term, the use of PCT experiments and simulations to identify combustion rate equation constants should be put on a firmer computational and intuitive basis. Computational aspects include more appropriate software, hardware, and optimal parameter identification algorithms. Intuitive aspects include justifiable model simplifications and a basic understanding of result sensitivities. With these in hand, consideration might be given to replacement of threshold pressure material ranking with combustion rate equation comparisons.

In the longer term, the fundamentals of heterogeneous combustion should be better understood. In particular, high temperature diffusion through oxide layers, a key to heterogeneous combustion behavior, requires investigation.

1997
NASA / ASEE SUMMER FACULTY FELLOWSHIP PROGRAM

MARSHALL SPACE FLIGHT CENTER
THE UNIVERSITY OF ALABAMA IN HUNTSVILLE

MODELING THE MECHANICAL BEHAVIOR OF CERAMIC MATRIX COMPOSITE MATERIALS

Prepared by: William Jordan, Ph.D., P.E.

Academic rank: Associate Professor

Institution and Program: Louisiana Tech University
Mechanical Engineering

NASA/MSFC:

Laboratory: Materials and Processes Laboratory
Division: Nonmetallic Materials and Processes Division
Branch: Nonmetallic Materials Branch

MSFC Colleagues: Dr. Corky Clinton
Mike Effinger

Introduction to Project

Ceramic matrix composites are ceramic materials, such as SiC, that have been reinforced by high strength fibers, such as carbon. Designers are interested in using ceramic matrix composites because they have the capability of withstanding significant loads while at relatively high temperatures (in excess of 1000 °C). Ceramic matrix composites retain the ceramic materials ability to withstand high temperatures, but also possess a much greater ductility and toughness. Their high strength and medium toughness is what makes them of so much interest to the aerospace community.

This work concentrated on two different tasks. The first task was to do an extensive literature search into the mechanical behavior of ceramic matrix composite materials. This report contains the results of this task. The second task was to use this understanding to help interpret the ceramic matrix composite mechanical test results that had already been obtained by NASA. Since the specific details of these test results are subject to the International Traffic in Arms Regulations (ITAR), they are reported in a separate document (Jordan, 1997).

Three excellent sources of general information about ceramic matrix composites are Evans' paper (Evans, 1997), Solti's Ph.D. dissertation (Solti, 1996a), and Nair and Jakus' book (Nair and Jakus, 1995). Evans paper examines a number of design issues for high temperature applications of ceramic matrix composites. He discusses fiber pull out, the effect of pin–loaded holes, notch sensitivity, fiber bridging, and inelastic strains caused by fiber/matrix microcracking.

The book edited by Nair and Jakus provides an excellent introduction to the high temperature behavior of ceramic matrix composite materials. There are sections in the book dealing with both short term behavior (impact) as well as long term behavior (creep and fatigue).

The first two chapters of Solti's dissertation provide an excellent introduction to ceramic matrix composite materials. An engineer unfamiliar with high temperature ceramic matrix composite behavior should probably start with the beginning of Solti's dissertation (if available), then Nair and Jakus book, and finally proceed to Evans article.

Modeling Mechanical Behavior of Ceramic Matrix Composites

There are two very broad approaches to modeling material behavior. A macroscopic approach attempts to predict future performance based on prior macroscopic tests. Examples of such macroscopic tests are tensile tests, impact tests, creep tests, and fatigue tests. A second basic approach is to model on a microscopic level. This approach looks at such issues as fiber properties, matrix properties, fiber/matrix bonding, etc. These properties are then used to predict composite material behavior. This approach is frequently combined with a finite element analysis of the structure in question. Using either approach, modeling the behavior of ceramic matrix composite materials is intrinsically a difficult task (Solti, 1996a).

For any failure theory to there needs to be good mechanical test data. Any theory is no more precise than the basic mechanical property measurements that are used within it. Testing of brittle materials is much more difficult than ductile materials, since very small flaws can promote premature failure. Testing at the high temperatures of interest is also more difficult than at room temperature. One research group (Curtin, et al., 1994) has developed techniques to perform tensile and fatigue tests on composites up to 1500 °C.

NASA is interested in how ceramic matrix composites respond to high velocity impact loads. Such tests can be performed at NASA's facility at White Sands, NM. Stoltzfus describes their capability in a 1988 paper (Stoltzfus, et al., 1988). They exposed a cup shaped sample to high velocity particle impact at temperatures over 400 °C.

Estimating Toughness from Mechanical Tests

Impact toughness results can be estimated from particle impact tests. It was assumed that all of the impact energy went into creating a hole in the base of the cup. G_{IC} is the energy released per unit area of crack growth. By dividing the impact input energy by the area of the newly cracked surface, we can estimate the G_{IC} of a material that just failed by the impact. The more commonly used critical stress intensity (K_{IC}) can be calculated from G_{IC} .

The approach described above is the maximum toughness material that can be broken by the impact tests. The next step was to estimate the toughness from room temperature tensile tests. The deformation energy in the material is the energy under the stress–strain curve in each test. The total energy absorbed by the cup would be the strain energy per unit time the volume of the cup base. This energy term was divided by the newly cracked area to get a value for G_{IC}.

The toughness of these materials when exposed to oxygen at elevated temperatures can be approximated. This can be done using the stressed in oxygen data and calculating the strain energy that was input into these samples. The energy per unit volume that the material could withstand was then used as the input energy into the cup shaped samples that were used in the particle impact test.

Modeling Tensile and Creep Behavior

There are several macroscopic failure theories available. Use of tensile strength or the creep based Larson Miller Parameter to predict strength are both macroscopic models. A number of researchers have proposed various micromechanical models. Several (Curtin, et el., 1994) have proposed a micromechanical model for high temperature tensile and fatigue behavior. They amplified this approach in a 1996 conference paper (Materials Science Corporation, 1996). While this method looks promising, it is not possible to verify without getting a copy of their computer code and running it with some of the data generated by NASA.

One interesting approach to mechanical behavior is a mixed macroscopic / microscopic approach that has been taken by a group of researchers at NASA's Lewis Research Center (Murthy, et al., 1996, and Mital, et al., 1996). They have created a software called CEMCAN, which stands for Ceramic Matrix Composite Analyzer. This software uses both macroscopic and microscopic tensile type data. The user inputs the laminate structure which includes such things as fiber type, matrix type, loading, and stacking sequence. The software then calculates what is occurring on an individual fiber level. It then rebuilds itself back up to the laminate level and produces macroscopic results (such as moduli for the laminate). Their model incorporates the stress redistribution that occurs when the material progressively fails. It can be used to monitor the damage initiation and progression as the load increases. It has the capability of dealing with the non–linear stress strain behavior that is characteristic of many of these CMC materials. This software was not designed for analyzing fatigue loading. One of the benefits of this is that it produces engineering properties that can directly be used by design engineers. While this method looks promising, it is not possible to verify without getting a copy of the computer code they have created and running it with some of the data generated by NASA.

Modeling Fatigue Behavior

There are a number of models that have been used to represent fatigue data. The most common macroscopic method uses what is called the S–N curve, where the maximum applied stress is plotted as a function of lifetime. For many materials there is a stress level below which an infinite lifetime is expected. This value is called the endurance limit.

The S–N curve approach is limited because it does not distinguish between issues such as varying the amplitude stress while keeping the maximum applied stress the same. These issues are frequently dealt with using variations of the Goodman plot (which is another macroscopic model). In the Goodman plot the amplitude stress is plotted as a function of the mean stress. The safe region is below a line that connects the endurance limit for a pure tension/fatigue test (on the amplitude scale) and the tensile strength (on the mean stress scale). This approach is based on the idea that fatigue crack growth is dependent on the size of the maximum applied stress. A part that is experiencing a high mean stress does not have to have a very high amplitude stress before the stress required to grow the crack is reached. Conversely, a material with a low mean stress, will require a higher amplitude stress before it will fail.

The Goodman approach is commonly used along with a fracture mechanics approach. The Goodman approach is used to estimate the maximum allowable stress (and therefore the maximum crack size) before final failure occurs. Fracture mechanics is then used to estimate the subcritical crack growth. This is illustrated in Hertzberg's book (Hertzberg, 1996).

One important parameter used in describing fatigue behavior is the value of R. R represents the ratio of the minimum applied stress to the maximum applied stress. At high

values of R, there have been cases of premature failure in what otherwise would be seen as the safe region (Nicholas and Zuiker, 1996).

There have been several micromechanical based approaches to modeling fatigue behavior. Curtin's approach (Curtin, et al., 1994 and Materials Science Corporation, 1996) looks promising, it is not possible to verify without getting a copy of the computer code they have created and running it with some of the data generated by NASA.

Another micromechanical approach to fatigue has been described by Solti (Solti, 1996a and Solti, 1996b). Solti's approach has the advantage that it can be tried out without using a complicated computer code. He refers to this as a "simplified approach". One disadvantage of his approach is that it is for unidirectional systems. It will need to be expanded to the more complicated layups that need to be used in actual aerospace applications.

Conclusions

Many of the equations that are used to model fiber reinforced polymers can be used for fiber reinforced ceramic matrix composites as well. However, the very different property values of ceramic matrix composites compared to polymeric based ones indicate that something different is occurring on a microscopic level.

Toughness can be estimated from tensile tests, particle impact tests, and elevated temperature stress tests. These yield values that are consistent with more direct measurements of toughness.

The Goodman approach to modeling fatigue failure appears to work well as long as the R value is not too large. Large R values tend to promote premature failure. A number of micromechanical approaches to fatigue failure have been developed. Their precision cannot be estimated until the specific software has been tested using results already obtained by NASA.

References

Curtin, W.A., Reifsnider, K.L., Oleksuk, L.L., and Stinchcomb, W.W. (1994), Investigation of Properties and Performance of Ceramic Composite Components: Final Report on Phase II, DE95–004737 and ORNL/SUB–87–SA946C/04, 40 pages, 1994.

Evans, A.G. (1997), Design and Life Predictions Issues for High–Temperature Engineering Ceramics and the Composites, Acta Materialia, Volume 46, No. 1, pp. 23–40.

Hertzberg, Richard (1996), *Deformation and Fracture Mechanics of Engineering Materials*, John Wiley & Sons, New York, pp. 529–531.

Jordan, William (1997), Failure of Ceramic Matrix Composite Materials, unpublished report subject to ITAR restrictions, submitted August 15, 1997 to Nonmetallic Materials Branch, Nonmetallic Materials and Processes Division, Materials and Processes Laboratory, Marshall Space Flight Center, 32 pages.

Materials Science Corporation and Virginia Polytechnic Institute and State University (1996), An Overview of Life Prediction Tools for CFCCs, presented at The 20th Annual Conference on Ceramic, Metal and Carbon Composites, Materials, and Structures, Cocoa Beach FL, January 23–25, 1996, pp. 891–938.

Mital, Subodh, and Murthy, Pappu (1996), CEMCAN–Ceramic Matrix Composites Analyzer User's Guide–Version 2.0, NASA Technical Memorandum 107187, 8 pages, 1996.

Nair, Shanti, and Jakus, Karl, editors (1995), *High Temperature Mechanical Behavior of Ceramic Composites*, Butterworth–Heinemann, Boston.

Murthy, Pappu, Chamis, C.C., and Mital, Subodh (1996), Computational Simulation of Continuous Fiber–Reinforced Ceramic Matrix Composites Behavior, NASA Technical Paper 3602, 15 pages, 1996.

Nicholas, T., and Zuiker, J.R. (1996), On the use of the Goodman diagram for high cycle fatigue design, International Journal of Fracture, Volume 80, pp. 219–235.

Solti, James (1996a), *Modeling of Progressive Damage in Fiber–Reinforced Ceramic Matrix Composites*, Ph.D. Dissertation, Air Force Institute of Technology, March 1996, 337 pages. Also found as reports AD–A304782 and AFIT/DS/ENY/96–2.

Solti, James (1996b), A Simplified Approach for Modeling Fatigue of Unidirectional Ceramic Matrix Composites, Journal of Composites Technology and Research, Volume 18, No. 3, July 1996,. pp. 167–178.

Stoltzfus, J.M., Homa, J.M., Williams, R.E., and Benz, F.J. (1988), ASTM Committee G–4 Metals Flammability Test Program: Data and Discussion, in *Flammability and Sensitivity of Materials in Oxygen–Enriched Atmospheres: Third Volume, ASTM STP 986*, American Society for Testing and Materials, Philadelphia, pp. 28–53.

1997

NASA/ASEE SUMMER FACULTY FELLOWSHIP PROGRAM

MARSHALL SPACE FLIGHT CENTER
THE UNIVERSITY OF ALABAMA IN HUNTSVILLE

SPECTRUM PREPROCESSING IN THE OPAD SYSTEM

Prepared by:	Dr. Constantine Katsinis, Ph.D.EE
Academic Rank:	Associate Professor
Institution:	University of Alabama in Huntsville
Department:	Electrical and Computer Engineering
NASA/MSFC:	Astrionics Laboratory Instrumentation Branch
MSFC colleagues:	W.T. Powers and Anita Cooper

Introduction

To determine the readiness of a rocket engine, and facilitate decisions on continued use of the engine before servicing is required, high-resolution optical spectrometers are used to acquire spectra from the exhaust plume. Such instruments are in place at the Technology Test Bed (TTB) stand at Marshall Space Flight Center (MSFC) and the A1 stand at Stennis Space Center (SSC). The optical spectrometers in place have a wide wavelength range covering the visible and near-infrared regions, taking approximately 8000 measurements at about one Angstrom spacing every half second.

In the early stages of this work, data analysis was done manually. A simple spectral model produced a theoretical spectrum for given amount of elements and an operator visually matched the theoretical and real spectra. Currently, extensive software is being developed to receive data from the spectrometer and automatically generate an estimate of element amounts in the plume. It will result in fast and reliable analysis, with the capability of real-time performance. This software is the result of efforts of several groups but mainly it has been developed and used by scientists and combustion engineers, in their effort of understanding the underlying physical processes and phenomena and creating visualization and report generation facilities.

Most of the software has been developed using the IDL language and programming environment which allows for extensive data visualization. Although this environment has been very beneficial, the resulting programs execute very slowly and are not easily portable to more popular, real-time environments. The need for portability and high speed of execution is becoming more apparent as the software matures moving out of the experimentation stage and into the production stage where ease of use and short response time are the most desirable features.

The purpose of the work described here is to assist the scientists who developed the original IDL-based version in the conversion of the software into the real-time, production version. Specifically, a section of the software devoted to the preprocessing of the spectra has been converted into the C language. In addition, parts of this software which may be improved have been identified, and recommendations are given to improve the functionality and ease of use of the new version.

Facilities

The Diagnostic Test Facility (DTF) at Stennis Space Center has a small rocket engine with different characteristics to the SSMEs that has been seeded with known amounts of alloys during firing. DTF data were produced with the OMA Spectrometer, and will be used to confirm the spectral model and methods for handling the OH component. The TTB (Technology Test Bed) data is gathered at MSFC using the OPAD instrument, together with engine data on the tests. There is also data from High RAS, which is the new resolution spectrometer with 3 banks.

Data from different instruments is stored in the directories dffdata (DTF data), rawdata (TTB data), raw3data (TTB data from High RAS 3), omadata (TTB data from the OMA), engdata (engine data for TTB). Tests are identified by two parameters. The first one defines an integer indicating the instrument and engine from which the data taken. The

available options are: 1=ttb, 2=dtf, 2= high/ras, 3= oma from TTB. The second parameter defines the test, an integer number for the TTB test or a string representing the DTF test.

The naming convention of data files is not always obvious since they were created by different scientists at different locations and times. For example, in one case names were used to indicate the level of "plume seeding" which took place during the test.

Preprocessing of spectra

Spectrum preprocessing is the first of a sequence of steps, the final purpose of which is to determine the amounts of metals present in the plume. The input of the preprocessing step is the data produced by the spectrometer. Its output is a refined version (defined below) of the spectrum, which in following steps is further processed by the neural-network code and the SPECTRA code.

Each spectrum of the engine plume has a component due to metal erosion, but it also has components due to the emission of the OH and H_2O molecules generated by the burning of hydrogen in the engine. In addition, scattered background light produces another spectrum component. The major purpose of the initial stages of the software, the preprocessing stages, is to extract the first component (due to metal erosion) of the spectrum. Subsequent stages of the software use the theoretical model to predict the metal amounts in the plume. The OH component can vary from test to test, and is generally indicative of the power level, the fuel mixture ratio, and of change in power level. Unfortunately, the complex interaction of the OH and water vapor emissions are poorly understood and little quantitative data are available that would permit development of an accurate model. Currently a basic understanding of the process has resulted in the development of a simple method to extract the OH component of a spectrum and leave an estimate of the metallic component. This method is being improved since it is not successful during the critical start-up and shut-down phases of an engine test.

As Figure 1 shows, the preprocessing step is implemented by the following major routines (which in turn use numerous other routines for file handling and data processing):

1) GETTEST(test_number, wave_array, time_array, data_array)

Reads a wave array with wavelengths of the spectra, a time array with the time of each spectrum and a data array with a sequence of spectra. Data is in files originating from experiments at TTB (RAS or Highras or OMA) or DTF specified by test_number.

2) STANDARD_SCAN(wave_array,sscan)

Reads a clean metal-free spectrum from disk for use by the CLEAN program. The supplied wave array indicates the desired wavelengths at which the metal-free spectrum should be returned.

3) START_CLEAN(dist,magn,grid,wavarray,sscan)

Routine CLEAN is called repeatedly to process a sequence of spectra. It needs a set of data (interpolation parameters) which stays permanently in memory until the wavelength array is changed. Routine START_CLEAN initializes the data set for the CLEAN routine.

4) CLEAN(datarray,cleanarray)

Receives a sequence of spectra in data array and produces a cleaned sequence of spectra in clean array by removing the OH portion of a spectrum to leave the metal region.

5) SMOOTHAWAY(cleanarray,newarray)

Routine CLEAN may cause negative values to occur in the clean array. Routine SMOOTHAWAY smoothes the clean array to remove the negative values.

File data formats

Data format of the TTB files

The TTB (Technology Test Bed) data appears over a broad wavelength range of 280 nm (2800 Angst) to 718 nm (7180 Angst) thus covering the short UV to Visible wavelength range. The instrument has two detectors covering the 2800 to 5010 Angstrom, and 5010 to 7180 Angstrom range. The representative pixel width of 24.4 μm. It is possible, due to the efforts made to maximize sensitivity of each detector by various focus enhancing optical elements, to observe distortions in line shape and position. If the input optics do not fill the entrance slit with light, or if the divergence through the slit is insufficient to fill the mirrors and the grating, the line may shift sideways or become distorted. Detector 2 (B), which covers the 5010 to 7080 Angstrom range, has a skewed instrument profile as well as some non-linear behavior in wavelength shift. Each test firing is assigned a three-digit number (xxx). The detectors are calibrated at the start of each test firing and the resulting data files are stored at directory "rawdata/rascals/" with file names "inrespl.xxx" and "inresp2.xxx". One source of error is that the calibration factors, which allow conversion of data from Volts to Counts, are hard coded with the assumption that there is no drift in such instrument dependent parameters.

Two data files, with sampled data and corresponding time, are stored in binary format in the directory "rawdata/rasxxx" with names "ras.052" and "time.052".

Based on the detector to wavelength grid relation established by calibrations performed in the lab, the wavelength array corresponding to sample points is deduced. This conversion can be a source of error. The sampled data points for each scan are recovered, and processed to account for background data. The data is also calibrated with respect to the detectors which are re-calibrated at the start of the test firing.

Data format of the DTF files

The DTF (Diagnostic Test Facility) data files are supplied in binary format and located in the directory "dtfdata". The spectral coverage range for DTF is 300 nm to 430 nm. The first record in the data file contains the test number, total number of scans, total number of sample points, sample scan rate, time of engine start, and type. Files created at later times contain a more extensive first record. After the first record, subsequent data is organized into a record of four numbers indicating the wavelength at the sample point, the response function point value, the measured background data, and the data with the background subtracted.

Data format of the OMA data of the TTB

The OMA is the same kind instrument used to gather the DTF data, but the data files have a different format. For each test (xxx), there are two files omaxxx.bin with the raw data and caixxx.bin with the calibration data.

Conclusions and Recommendations

The major function of the preprocessing code is to remove the effect of the OH lines

on the spectrum and extract the spectrum part due to metal erosion. It appears to have grown within a relatively long period of time as scientist sought to experiment with different ways of implementing various subfunctions. In addition, some programs have a large number of options (keywords) which select one of many possible processing paths. Although such software can be useful during experimentation, the resulting size and complexity make maintenance and optimization difficult. It would be very useful to closely examine the processing steps in this software and identify the ones that are absolutely necessary for the real-time (production) version of the software. Activities should be separated into "experimental" or "debugging" activities and "production" or "real-time" activities and two programs should be developed, one for each set.

Since experiments have been performed over a long period of time at different places and by different people, it is unavoidable that a multitude of file formats would be present. This complicates processing and results in maintenance difficulties. It would be very beneficial to create a generic file format, to play the role of the standard, and require all newly developed software to adhere to this standard. To support the standard format, a set of programs must be created to convert all old file formats. This entails no difficulty, as the current file processing routine contains all the necessary code.

Suggestions for additional changes to the code

1) In gettest(), most of the code is performing the same task in a slightly different way for each of the instruments. Having a consistent interface between the code and the input files would make for much cleaner, easier to read, and easier to maintain code.

2) Gettest() has three major parts: a) retrieval of the TESTSTUFF structure b) retrieval of (and some processing on) the wavarray[], timarray[], and datarray[][] structures. c) cleaning of timarray, adjusting of wavarray[] and (based on keywords) the ability to perform the cleaning and smoothing operations within gettest. It would be better to make gettest() a smaller more specific function. The TESTSTUFF structure could be obtained by a separate function. The TESTSTUFF structure would then be an input into the gettest function. Gettest would then be limited to obtaining the timarray[], wavarray[] and datarray[][] structures and a minimal amount of processing on these arrays.

3) The number of keywords to the routines should be limited.

Credits

Some information on instruments and file data formats is summarized from the OPAD web page.

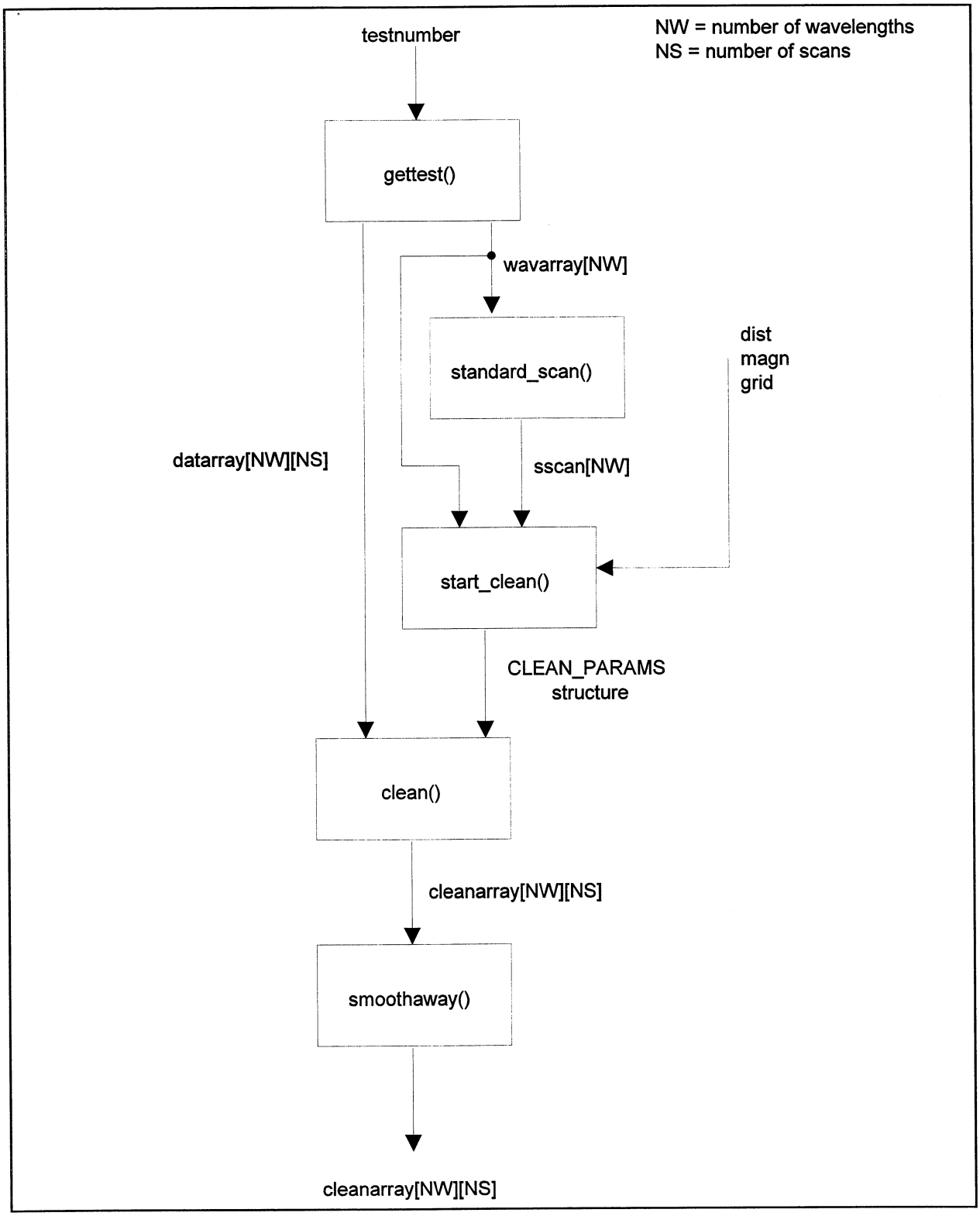

Figure 1: Preprocessing major routines.

1997

NASA/ASEE SUMMER FACULTY FELLOWSHIP PROGRAM

MARSHALL SPACE FLIGHT CENTER

THE UNIVERSITY OF ALABAMA IN HUNTSVILLE

INVESTIGATION OF SOLUTION POLYMERIZATIONS IN MICROGRAVITY AND 1G.

Prepared By:	Alvin P. Kennedy, Ph.D.
Academic Rank:	Associate Professor
Institution and Department	North Carolina A&T State University Department of Chemistry
NASA/MSFC	
Office:	Space Sciences Laboratory
Division:	Microgravity Science & Applications
MSFC Colleagues:	Donald Frazier, Ph.D. Steve Paley, Ph.D.

Introduction

Only a few investigations have been performed on polymer reactions in a microgravity environment. The majority of microgravity investigations have involved biological and inorganic materials and processes. Polymeric systems have not been extensively investigated because most polymers are too viscous for any microgravity effects such as convection or sedimentation to be important.(3) However in the case of solution phase polymerization these effects are more important. Resent results from two separate solution polymerization experiments have indicated the importance of gravitational effects on polymerization.

Recently a UV polymerizable prepolymer solution of Cyclotene was flown on a KC-135 flight. The sample was irradiated for 15 sec intervals at 0.2 G for 40 times. A control sample was irradiated under similar conditions using the same UV cell on the ground. The low gravity UV polymerized sample was a yellowish fluid and similar in viscosity to the starting prepolymer solution. The 1-G sample was dark orange with brown inclusions, and had begun to develop a crosslinked network structure. It had a much higher viscosity than the low gravity sample. Typically in thermosets sedimentation and phase separation occur near the gel point and the high molecular weight polymer separates from the liquid monomer or solvent. These processes determine the variation in molecular weight which is obtained in an earth based environment. Since this process is a result of the gravitational effect on the higher molecular weight material, higher molecular weight polymers and possibly different polymer morphologies might be obtained under microgravity conditions. Similar effects can occur during the polymerization of crystalline polydiacetylene (4). Dielectric spectroscopy has been used to monitor the solution polymerization of polydiacetylene.

Many different techniques have been used to investigate the polymerization process, however dielectric spectroscopy provides a simple yet powerful technique for following the polymerization process from monomer to polymer. Dielectric spectroscopy has been used to study a variety of thermoset resins, however most research has been conducted on epoxy thermosets. The dielectric behavior of epoxy resins can be adequately described by the Debye model (2), in which the dielectric constant ε' is given by:

Eq.1

$$\varepsilon' = \varepsilon_u + \frac{(\varepsilon_r - \varepsilon_u)}{1 + (\omega\tau)^2}$$

where ε_u and ε_r are the unrelaxed and the relaxed dielectric constants, respectively, ω is the angular frequency given by $\omega = 2\pi f$, and τ is the characteristic relaxation time. The dielectric loss ε'' is given by:

Eq.2
$$\varepsilon'' = \frac{\sigma}{\omega\varepsilon_o} + \frac{(\varepsilon_r - \varepsilon_u)\omega\tau}{1+(\omega\tau)^2}$$

where σ is the ionic conductivity, and ε_o is the permittivity of free space. The first term represents the ionic conductivity of the material and becomes dominate at low frequencies. This term will vary with the viscosity of the material and the ionic concentration, which can also change during cure. The second term is the dipolar component of the dielectric loss. This term should change as the network forms and as the viscosity changes. A maximum is observed in the dielectric loss spectra when $\omega\tau = 1$, and experimentally the relaxation time can be determined from the loss peak. In the case of a curing resin, ε_r and ε_u would correspond to the neat resin and cured polymer, respectively. This model is based on a static number of dipoles which respond to variations in the applied frequency. Although of the dipoles in the monomer and curing agent are consumed during the polymerization process, this model has worked well for epoxy resins (1,5). How applicable this model is in describing the solution polymerization of polydiacetylene will have to be determined.

Experimental

The dielectric measurements were made using a HP4274A LCR meter. The unit measures capacitance and dissipation factor (tan D) from 100 Hz to 100 kHz in steps. The LCR meter was interfaced to the PC using Labview software. The program allows measurements to be taken at 30 sec or larger intervals for the duration of the run. Typical runs used 5 minute intervals for at least 24 hours. Measurements were taken at 1, 2, 4, 10, 20, 40, and 100 kHz. Gold plated glass interdigitated electrodes were purchased from DekDyne and used to measure the impedance of the solutions. A 1000W UV lamp was used at a distance of 4-5" from the cell.

Two different sample cells were used. For the bulk measurements a rectangular aluminum cell was used. It consisted of a solid rear block with small holes drilled for the leads to feed through and a front cover with a rectangular area drilled out to permit irradiation through a glass slide. The electrode was positioned facing the UV source and glued to the back of the cell with RTV rubber. Leads were soldered onto the electrode with either silver paste or indium solder. The indium solder was more resistant to solvent

attack. In this position the electrode was measuring the bulk solution. Enough sample was added to cover the electrode but not fill the cell. The feed through holes were sealed with RTV rubber. A brown solid was always observed near the solder joints of the electrode. It appeared to be vapor deposited crystalline polydiacetylene. Attempts to attached the electrode face up on the glass slide and irradiate through the back were unsuccessful because the total absorbance of the slide and electrode was too high for reaction to occur. For surface polymerization the electrode was attached face down on to a cylindrical aluminum test cell using a tie down. The sample was injected through a hole in the back and sealed with RTV rubber after the cell was filled. Electrical contact was made using alligator clips.

Results and Discussion

Results for the bulk experiments are shown in figure 1. Data was collected for the first 40 minutes without irradiation. During this time the capacitance and dissipation factor remained nearly constant. As soon as the lamp was turned on there was a large increase in the capacitance and dissipation factor for the lower frequencies. This indicates that the changes are due to the photopolymerization reaction. The bulk sample has a peak in the capacitance at 590 minutes for the 1 kHz data (Fig. 1A). The dissipation factor increases rapidly and goes off scale for the 1kHz data in the first 250 minutes and then decreases again. There is no peak observed in the capacitance data at 100 kHz (figure 1B). The initial decrease in the 100 kHz data is due to the partial heating of the cell by the UV lamp. This change was also observed when only the solvent was heated. The dissipation factor raises rapidly then levels off for 300 minutes and peaks near 590 minutes at the same time observed in the 1 kHz capacitance data.

Figure 1A and 1B

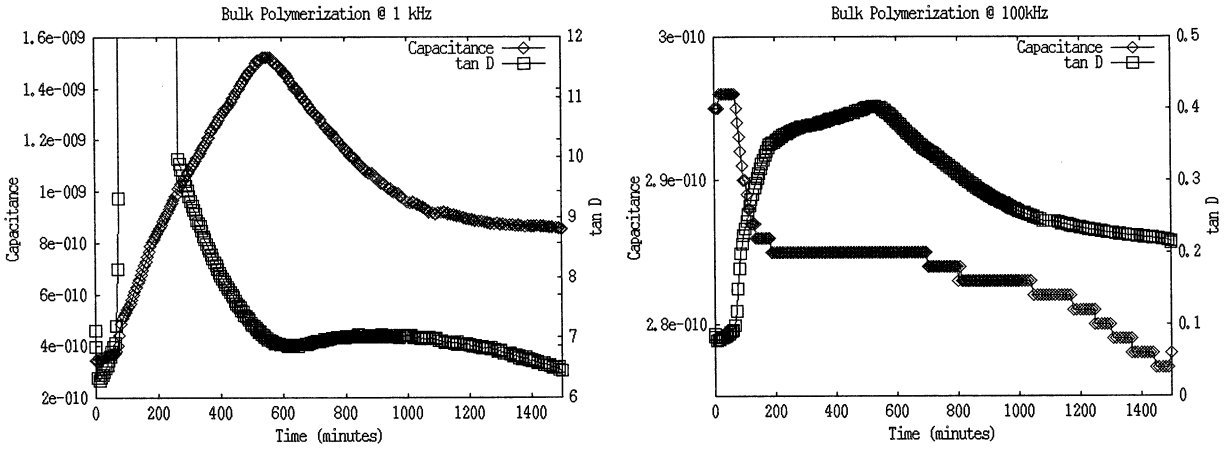

The peak in the capacitance at 590 minutes is present at 10 kHz but completely diminished at 20 kHz and above. The peak in the dissipation factor at 200 minutes is present in the 2 kHz but has diminished in size at 4 kHz. And the peak in the dissipation factor at 590 minutes is present at 4 kHz and higher frequencies. Since the observed peaks occur at the same time it suggests a single process is affecting the different frequencies.

The results for the surface experiments are shown in figure 2. There is an increase in the capacitance during the first 400 minutes at 1 kHz, after which the capacitance levels off instead of decreasing as was observed in the bulk data (figure 2A). The dissipation factor has a peak at 200 minutes similar to the one observed in the bulk data. The decrease in intensity is probably due to the smaller available surface area of the cylindrical cell. The capacitance at 100 kHz is exactly like the bulk data (figure 2B). And suggests that the reaction is not producing any products which are active at the higher frequency. The dissipation factor has the same form as the capacitance at 1 kHz. However the dissipation factor clearly decreases at longer times at 100 kHz.

Figure 2A and 2B

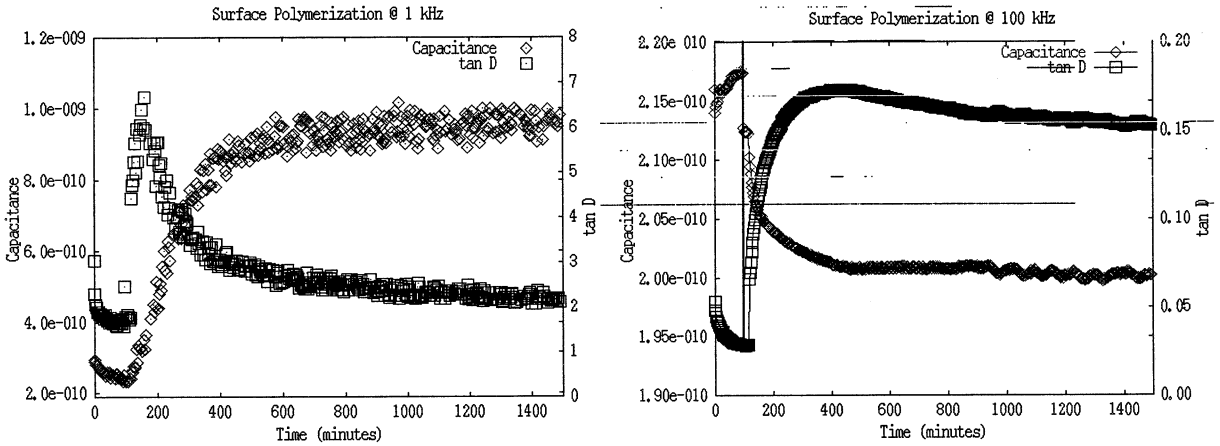

The response in the capacitance diminishes as the frequency increases and is completely diminished at 40 kHz. The peak in the dissipation factor at 200 minutes is not present at 4 kHz and higher. At 4 kHz the dissipation factor rises rapidly in the first 300 minutes, then peaks near 350 minutes and gradually decreases over time.

The peak observed in the capacitance of the bulk sample clearly indicates that the polymerization process has either decreased in rate or terminated. This decrease could be the result of the film growing on the surface decreasing the light intensity. There is a more gradual decrease in the capacitance for the surface measurement, which peaks 315 minutes after irradiation begins. This

decrease cannot be due to attenuation since the film should increase the capacitance as it continues to grow on the surface. The peak observed at 250 minutes in the dissipation factor at low frequencies is present in both the surface and bulk measurements. This suggest that the same process is active at both the surface and the bulk.

Conclusions

The in-situ dielectric spectra for the solution polymerization of polydiacetylene has been successfully measured. The results show a distinct difference between the response for the bulk solution and surface polymerization. It also shows a low frequency peak in the dissipation factor which is present in both the bulk and surface polymerizations. These features may prove to be significant indicators for important polymerization processes. Future studies will investigate the mechanisms responsible for this dielectric responses. This technique will eventually be used to monitor microgravity polymerizations and provide in-situ data on how microgravity affects solution polymerization.

References

1. M. E. Baird, G. T. Goldworthy, C. J. Creasey, *J. Polym. Sci.* **(B) 6**, 737 (1968).

2. A. R. Blythe, "Electrical Properties of Polymers", Cambridge University Press, 1979.

3. D. O. Frazier, C. E. Moore, NASA Conference Publication 3250 (1993).

4. D. O. Frazier, R.J. Hung, M.S. Paley, Y.T. Long, *J. Crystal Growth,* 175, 172 (1997).

5. D. Kranbuehl, S. Delos, E. Yi, *ANTEC '85*, 311 (1985).

ORBITAL PROCESSING OF EUTECTIC ROD-LIKE ARRAYS

David J. Larson, Jr.
Department of Materials Science & Engineering,
University at Stony Brook,
Stony Brook, NY 11794-2275
NASA Summer Faculty Fellow

Frank Szofran, Palmer Peters and Richard Grugel
Space Sciences Laboratory
George C. Marshall Space Flight Center 35812
NASA Colleagues

I. **Introduction**

The eutectic is one of only three solidification classes that exist. The others are isostructural and peritectic-class reactions, respectively. Simplistically, in a binaryeutectic phase diagram, a single liquid phase isothermally decomposes to two solid phases in a cooperative manner. The melting point minimum at the eutectic composition, isothermal solidification temperature, near-isocompositional solidification and refined solidification microstructure lend themselves naturally to such applications as brazing and soldering; industries that eutectic alloys dominate.

Interest in direct process control of microstructures has led, more recently, to in-situ eutectic directional solidification with applications in electro-magnetics and electro-optics. In these cases, controlled structural refinement and the high aspect ratio and regularity of the distributed eutectic phases is highly significant to the fabrication and application of these in-situ natural composites. The natural pattern formation and scaling of the dispersed phase on a sub-micron scale has enormous potential application, since fabricating bulk materials on this scale mechanically has proven to be particularly difficult. It is thus of obvious importance to understand the solidification of eutectic materials since they are of great commercial significance.

The dominant theory that describes eutectic solidification, Jackson and Hunt, was derived for diffusion-controlled growth of alloys where both solid eutectic phases solidify metallically, i.e. without faceting at the solidification interface. Both high volume fraction (lamellar) and low volume fraction (rod-like) regular metallic arrays are treated by this theory. Many of the useful solders and brazements, however, and most of the regular in-situ composites are characterized by solidification reactions that are faceted/non-faceted in nature, rather than doubly non-faceted (metallic). Further, diffusion-controlled growth conditions are atypical terrestrially since gravitationally-driven convection is pervasive. As a consequence, it is important to determine whether these faceted/non-faceted composites behave in the same manner as their doubly non-faceted counterparts, particularly in the presence of convection.

Prior analytical convective sensitivity testing of this theory predicted insensitivity, Verhoeven, Gibson and Homer. Prior experimental testing of this theory offered broad-based agreement between theory and experiment, though most results were for high volume fraction lamellar eutectics that solidified without faceting at the solidification interface. Directional solidification experiments of low volume fraction rod eutectics under damped (microgravity or magnetic field) conditions,

however, have demonstrated significant sensitivity, challenging this fundamental theory. More recent theories have been proposed which introduce kinetic undercooling, faceting, fluid shear of the solute redistribution zone and the possibility that the interface composition is not the same as the bulk liquid composition. This program tests the established and proposed analytical theories and addresses the origins of discrepancies between the experimental and analytical results.

II. Experiment

II.1 Proposed Research Program

This program will directionally solidify low volume fraction regular eutectic structures in orbit (μ-g), under diffusion-controlled growth conditions. Complementary in-situ diagnostics will be applied to monitor and/or perturb the solidification interface velocity and to precisely monitor the solidification interface temperature (undercooling) and shape. Post-flight analyses will determine, quantitatively, the relations between the solidification interface velocity, solidification interface temperature (undercooling), and microstructural parameters (rod diameter, inter-rod spacing and volume fraction) that are enumerated in the eutectic theoretical relationships. Identical experiments will be conducted terrestrially, under damped (thermal, gravitational and applied magnetic field stabilization) and undamped conditions to provide a comprehensive quantitative one-g baseline for comparison.

The experiments enumerated above will develop critical data, under both diffusion-controlled and convection-dominated conditions. These data sets will be used to test analytical theories describing the solidification of regular, low volume fraction, eutectic alloys. Specific efforts will be made to quantitatively compare these results with the diffusion-controlled Jackson-Hunt theory and the Verhoeven, et al, modification which predicts convective insensitivity. These results will also be compared to the analytical formulation of Drevet, et al, which attempts to incorporate within the Jackson-Hunt formulation kinetic undercooling, faceting, convection and the possibility that the interfacial composition is not the same as the bulk liquid eutectic composition.

As a critical part of this task, a directional solidification model that describes current interface demarcation will be developed and validated experimentally. This model will predict interface shape and location during the current pulse and post-pulse transient, as well as eutectic rod-like structure within these regions and during steady state

growth. This insight will allow us to optimize the microstructural observation, while maintaining steady-state growth conditions between pulses. This model will include thermoelectric contributions (Peltier, Thomson, Joule, and Seebeck), as well as solute redistribution (including Soret diffusion), current-induced magnetic field effects, applied magnetic field effects, and gravitationally-driven convection. This model will predict responses under damped and undamped conditions and will differentiate between the microgravity damping and the applied magnetic field damping.

II.2 Description Of Anticipated Summer Research

Previous work conducted by the Principal Investigator, under NASA contract, has established that gravitationally-dependent convection substantially impacts the scaling dimensions of the Bi/MnBi eutectic microstructures under investigation. This structural modification occurs on damping the natural convection, not on accelerating the convection. This has been demonstrated by damping gravitationally-dependent convection in microgravity as well as by applying transverse or longitudinal magnetic fields in unit gravity. This convective sensitivity is not predicted by the existing eutectic solidification theories noted above.

The proposed work is intended to investigate the microstructural refinement experimentally, under damped conditions. Previously used magnetic field facilities are no longer available to the Principal Investigator. The Applied Magnetic Field Facility housed at the Space Sciences Laboratory of the NASA George C. Marshall Space Flight Center is an ideal location at which to conduct this study. Dr., Frank Szofran of the NASA Space Sciences Laboratory graciously offered to act as the NASA Research Colleague.

Our plan was to directionally solidify Bi/MnBi eutectic samples with and without applied magnetic fields, under conditions of thermal and gravitational stabilization. Simultaneous in-situ temperature measurements will be made, using sub-miniature Chromel -Alumal sheathed thermocouples. Complementary current interface demarcation experiments will be conducted under identical growth conditions, and simultaneous current interface demarcation experiments will be attempted. In the latter case, the generation of large Lorentz forces, which might significantly disturb experiments of this type, will be a major concern. Failure of this approach will render the microgravity experiments unique. Quantitative microstructural measurements will be conducted on the processed samples.

II.3 Revised Research Plan, Results and Discussion

On arrival at the NASA/MSFC/SSL facilities, it became apparent that facilities other than the previously described Applied Magnetic Field facility would also be of great utility to the program. One of the difficult aspects of this experimental program is to fabricate homogeneous alloys of the correct eutectic composition. This is a problem because of the large difference in melting point between the two constituent species combined with their relatively large differences in density, which allows the non-melted Mn to separate from the liquid Bi by Stokes flow. A candidate solution to this problem was found at SSL in the form of a rocking furnace that resided in the laboratory. It was decided to utilize this furnace to fabricate homogeneous alloys for the investigations. Empirical tests demonstrated that 8 hours of mixing at 525°C was totally ineffective, but that 100 hours at 925°C was sufficient to create a homogeneous alloy. The latter conditions were adopted as the baseline. Evacuated ampoules of correct alloy composition were fabricated at the State University of New York and transported to SSL by the PI. Four boules have been homogenized and additional castings will be fabricated throughout the Fall on an as-needed basis.

Further discussions with SSL personnel indicated that a new program was being initiated at SSL studying precision temperature measurement using the Seebeck technique. This technique had been proposed in our original proposal as a candidate to measure the interfacial undercooling that are fundamental to the theories being investigated. This technique is particularly valuable since it uses the solid/liquid solidification interface as a thermocouple without employing intrusive hardware and can measure the interface temperature, in some cases, to with 0.1°C. This is an ideal technique for achieving our ends, but the technology had to be extended to the two phase eutectic case, since it had previously been demonstrated for single phase solidification. These complementary programmatic interests offered an opportunity to advance both programs by collaborating.

Discussions with Drs. Peters, Sen, and Kaukler suggested that the ideal sample geometry for their apparatus was a single crystal of the sample material approximately 0.1 cm in diameter and 15 to 20 cm long. This posed a serious practical problem of growing such crystals. The first steps were taken with the assistance of Dr. Grugel of SSL. He provided facilities to aspirate liquid Bi and Bi alloys into the requisite fused silica capillaries. Initial successful attempts were made using 0.999 Bi and subsequent samples were fabricated using 0.999999 Bi. This provided samples to initiate the Seebeck work and allowed additional time to

fabricated Bi/MnBi eutectic alloys. The latter work is in progress.

Initial measurements on the 0.999999 Bi samples suggested the signal from the sample was of the correct order of magnitude (i.e. 8 to 10 microvolts) and we were encouraged to note that the signal noise was 0.1 to 0.2 microvolts, which was tolerable. Experiments are underway to measure the Seebeck Coefficient for pure Bi to compare with published values, and to make similar measurements on the Bi/MnBi eutectic alloy. Experiments on the eutectic alloy will determine whether Soret Transport is a problem with respect to the surface composition and output voltage of the reference thermocouple junction. Further experiments on the eutectic alloy will determine whether the distributed second phase inherent to the eutectic creates output noise that overwhelms the Seebeck signal or decreases the signal/noise ratio to the point where interpretation of the temperature unambiguously is impossible. These experiments are continuing.

Finally, the Applied Magnetic Field experiments were also undertaken. First homogeneous alloys were fabricated, as described previously. The next step was to calibrate the temperature field within the growth furnace. This was accomplished with the help of Mr. Curtis Bahr and the final value selected was a thermal gradient of 35°C/cm at the solidification temperature of 265°C. Experimental conditions selected were solidification velocities of 4, 9, and 16 cm/h with and without the applied fields. Success with this experimental matrix would cue the initiation of the current interface demarcation experiments with and without the applied fields. To date the 4.0 and 9.0 experiments, with and without the magnetic field have been completed. The remainder of the program will be conducted over the next several months.

III. Conclusions

This was a unique opportunity to advance the research program of the Summer Faculty Fellow. Results in homogeneous alloy fabrication were excellent. Similarly, the fabrication of Bi and Bi/MnBi samples with a very high aspect ratio were successfully accomplished. Initial Seebeck measurements were encouraging both with respect to output signal magnitude and signal cleanliness. Lastly, initial samples under damped and undamped growth conditions have been fabricated and are under analysis. More work is necessary, and collaboration in each of these areas will continue throughout the 1997/1998 academic year.

1997

NASA/ASEE SUMMER FACULTY FELLOWSHIP PROGRAM

MARSHALL SPACE FLIGHT CENTER
THE UNIVERSITY OF ALABAMA IN HUNTSVILLE

DEVELOPMENT OF AN OUTREACH PROGRAM FOR NASA: "NASA AMBASSADORS"

Prepared by:	George Lebo, PhD
Academic Rank	Associate Professor
Institution and Department	University of Florida Department of Astronomy
NASA/MSFC	
Laboratory: Division:	Space Sciences Physics and Astronomy
MSFC Colleague	N. Frank Six, PhD

DEVELOPMENT OF AN OUTREACH PROGRAM FOR NASA: "NASA AMBASSADORS"

INTRODUCTION AND BACKGROUND

For the last two decades United States government and business institutions have been scrambling to recapture "marketshare" lost to other countries (mostly to Japan). They have instituted new "ways of doing business" such as "Total Quality Management", "Continuous Improvement" and "ISO 9000", all of which find some elements in the economic theories proposed after World War II by Dr. Duane Deming. Among the concepts which he proposed we find requirements that we "determine who our customers are" and "be sure that we are satisfying our customers". Government agencies have adopted elements of the above policies but they have found that it is easier to enunciate a policy than it is to implement it. In order to reach out to its customers NASA has introduced a policy that requires each mission to set aside a fraction of its budget to do "education and outreach". However, while NASA does have an office of education that is responsible to disseminate NASA information to the school systems, and an office of Public Affairs that reaches the general public through the media, there is no one NASA office that is responsible to reach directly and personally to the general public. The "NASA Ambassadors" program is designed to do just that.

During the summer of 1996 Dr. Malcolm McDonald and I, under the guidance of Dr. Frank Six, initiated the development of the program labeled "NASA Ambassadors". Pre-packaged presentations consisting of visual and textual materials describing NASA's science and missions were assembled and made available to members of MSFC's summer programs. The intent was that those who requested copies of a given talk would give it to general audiences in their hometowns during the following year. Four presentations were prepared but not and applications to receive them were completed by forty members of the MSFC summer programs. The topics of the completed packages, those under development and new talks under consideration are described in the final report of Dr. Malcolm McDonald who has also prepared a NASA SFFP report for the summer of 1997.

THE NEED FOR THE PROGRAM

It is widely recognized by NASA's publicists that NASA needs to do a better job of advertising. However, since NASA is a government agency, it cannot actively advertise in the commercial media, as a business, would but instead has to rely on other forms of communications to reach out to its customers: the voters and taxpayers. Currently NASA's outreach is accomplished primarily through its office of education. Educational institutions offer a well established infrastructure which can be used to "tell NASA's story". However, the educators are not talking to NASA's customers but to their children. In fact teachers, whether they teach at the K-12 level or at the college or university level, rarely venture outside of their own institutions to make presentations. It is this separation that gives rise to the idea of the "Ivory Tower" which the teachers, especially those at the post secondary education level, rarely leave.

Major colleges and universities are recognizing this isolation from the general public (more exactly, from their alumni) and are setting up speakers bureaus to reach out, not to educate, but to raise funds. The NASA Ambassador Program provides a speakers bureau using members of MSFC summer programs, not to raise funds, but to reach out to the general public to convey the excitement of NASA's activities and to enlist support for its programs. There are several advantages to using summer programs' participants:

1. They are generally good communicators (teachers).
2. They are available at no cost. They require no honoraria nor travel funds.
3. They are creditable speakers. They do not receive NASA salaries so their enthusiasm for their topics is free of any self-serving agenda.

Dr. Neal Lane, director of the National Science Foundation, recently wrote a letter to the presidents of the country's major universities calling for them to support him as "we strive together to communicate the role that research plays in our nation's present and future". In a recent address to university public affairs professionals he proclaimed;

> "We are enjoying a golden age of discovery, as exciting research continues to uncover new knowledge about our universe. However, a different kind of golden age - - that of ever increasing funding for American science and engineering - - is clearly over.....
>
> Today, public support must be earned. We can no longer expect it in the form of a blank check and an undefined agenda. This is entirely appropriate. At the same time, I remain very concerned that the nation will not be doing enough to maintain and strengthen it position as a world leader in science and engineering over the next several years.
>
> It is now more vital than ever for us, the research community, to make a convincing case to the public about the tangible societal benefits that flow from science and technology, and the importance of investing adequately in research and education.
>
> At the National Science Foundation, our surveys continue to show that more than two-thirds of the public believes that science is a net good. But the vast majority of people have no understanding of the scientific process; 98% of them don't know what research means. This gap should trouble all of us.
>
> It is also troubling that many scientists and engineers, while concerned, do not think they can do anything about the gap. This may be because traditional scientific education does not prepare its graduates very well to assume a role as an activist in society, an **ambassador for science** (my emphasis).
>
> I well understand the discomfort, from my own career experience. But during my years as director of NSF, I've come to understand the need for the research community to reach out to the public. In more personal terms, we need to engage in genuine public dialogues with our local communities, in the mold of what I call the 'civic scientist'.....

It is true that the climate for science has changed forever. But change brings opportunity. If the sobering budget outlook prompts us all to communicate more broadly, more frequently and more effectively, then we have learned an important and necessary lesson that will serve the science and engineering community well in any climate."

OPERATIONAL DETAILS

In Dr. McDonald's final report (pages XXXII-1 to XXXII-4) he outlines five task areas: preparation of new presentations, updating of existing presentations, recruitment of NASA Ambassadors, production, and operations. Many of these tasks can be accomplished during the summer. The following is a description of procedures that need to occur during the rest of the year (end of summer until the beginning of the next summer) when the summer faculty and teacher program participants are not at the Marshall Space Flight Center. These represent details that would have to be managed either by the Office In Charge of the program or by some other contracting group.

The procedural details listed below are associated with the areas of: a) the production phase of newly-written talks, b) the production phase of updating the "boilerplate" materials which are integrated into each NASA AMBASSADOR (NA) talk, c) the production phase related to the updating of previously existing talks, and d) the general management operations of the program.

I. The Production of New Presentations.

(This assumes that new presentations (have) been developed by the end of the summer through the efforts of the summer participant volunteers.)

1. Has the talk been reviewed by a NASA Technical Expert (NTX) for accuracy (YES or NO)? (It is expected that this will already have occurred during the summer writing.)
2. **If "NO",** the text and visual materials are delivered to the NTX for approval.
3. The materials must be retrieved from the NTX after review.
4. **If "YES",** the Office In Charge (OIC) authorizes the reproduction of the new talk. This involves determining the number of copies to be reproduced and handling the paperwork for the necessary work order.
5. The "raw" visual materials must be delivered to the photo lab for reproduction.
6. The "raw" textual material must be delivered to the reproduction department.
7. The textual and visual copies must be retrieved from the respective locations.
8. The presentation packages must be assembled:
    a) Number the 35-mm slides individually in sequential order.
    b) Acquire the necessary vinyl slide holders.
    c) Insert the slides into the slide holder pockets. (This will include the "boilerplate" slides and the talk subject slides.)
    d) Collate and staple the text pages (if not already done).
    e) Prepare the envelopes with the slide sets, the textual materials, a "welcoming letter" which explains the candidacy aspects of the NA program, and instructions for the use of the presentation package.

9. Delivery of the ready-to-mail envelopes to the Teacher Resource Center (TRC) for storage and eventual distribution.
10. The OIC directs the TRC to mail or distribute the presentation packages.

II. The Review/Updating of "Boilerplate" Materials.

1. Is the boilerplate material still up-to-date with regard to content (YES or NO)?
2. **If "NO",** the OIC needs to review and bring the materials up to date.
3. **If "YES",** the OIC determines the reproduction needs of the material and processes the necessary work order(s) to the photo lab and the textual reproduction facility.
4. Repeat steps 5, 6, 7, and 8 in the procedure above.

III. The Updating of Existing Presentations.

1. Does an existing presentation require updating (YES or NO)? Refer to an appropriate NTX to determine the answer. This determination will have been handled during the summer while the summer programs participant volunteers are involved.
2. **If "YES",** the summer volunteers and the NTX will make the necessary changes. This procedure will create new update materials which must be incorporated with existing talks on that topic.
3. The OIC must certify the reproduction needs for the update materials and proceed with the reproduction steps 4 - 7, in I.
4. The assembling of update "kits":
    a) Compose step-by-step instructions for integrating the update kits into the existing talks.
    b) Number and insert the update slides into vinyl holders in the update kits.
    c) Insert the updated text into the update kits.
    d) Deliver the update kits to the TRC.
    e) The OIC issues orders for mailing update kits to affected NA's.
5. The update kit materials must be integrated into the previously-existing inventory of packages on that presentation topic at the TRC.
6. **If "NO",** no action is required.

IV. General Operations.

1. The OIC must make available a point of contact (person and phone number) to respond to NA inquiries and requests.
2. Evaluations:
    a) Evaluate whether any of the presentation topics should not be supported (dropped from the system). (This decision will be made during the summer by the summer volunteers and coordinators in consultation with a NTX.)
    b) Evaluate the feedback information available in the Public Affairs Office NA database concerning the performance and presentation style of active NA's. (It is hoped that this function will be handled as a project by the NASA Alumni League (NAL) members.)

3. The 2(b) evaluation will entail gathering the available feedback information from the PAO database and determining individualized helpful criticisms and comments that should be sent to the NA's. The results will be furnished to the OIC.
4. The OIC is responsible for communicating the results of the evaluations to the NA's.
5. The maintenance of the NA feedback database is the responsibility of the PAO. For each presentation made by a NA the following steps should occur:
   a) The NA returns a postcard feedback form listing simple facts and statistics for the talk,
   b) The program chairperson of the organization to which the talk is presented returns members' evaluation forms.
   c) The PAO database manager logs the receipt of the various forms and passes them on to the OIC.
   d) The OIC stores the forms until the evaluation of the forms is done (by the NAL).
6. The NA database should contain information including: each NA's name, address, and affiliated institution, presentation topics in the NA's possession, and the statistics related to each talk delivered (*e.g.*, date, group hearing the presentation, presentation topic, number in attendance, and the number of returned evaluation forms, *etc.*).

CONCLUSION

The NASA Ambassadors Program is designed to present the excitement and importance of NASA's programs to its customers, the general public. Those customers, which are identified in the "Science Communications Strategy" developed by the Space Sciences Laboratory at the MSFC, are divided into three categories:

1. Not interested and not knowledgeable
2. Interested but not knowledgeable
3. Science attentive.

In it they recognize that it makes the most sense to attempt to communicate with those described in the last two categories. However, their plan suggests that the media and the educational institutions are the only means of outreach. The NASA Ambassadors Program allows NASA to reach its target audience directly.

Steps to be taken in order for the program to commence:

1. MSFC chooses to support the NASA Ambassadors Program. - **decision point**
2. Designate an "Office In Charge".
3. Assign the "Operation" phase to in-house MSFC personnel or to a contractor. - **decision point**
4. Name a point of contact.
5. Identify partners in the program and enlist their assistance.
6. Process an unsolicited proposal from an outside sourceto accomplish those tasks which MSFC chooses to out-source.

1997
NASA/ASEE SUMMER FACULTY FELLOWSHIP PROGRAM

MARSHALL SPACE FLIGHT CENTER
UNIVERSITY OF ALABAMA AT HUNTSVILLE

TITLE

OBJECT CREATION AND HUMAN FACTORS EVALUATION FOR VIRTUAL ENVIRONMENTS

Prepared By:	Patricia F. Lindsey, Ph.D.
Academic Rank:	Assistant Professor
Institution and Department:	East Carolina University School of Human Environmental Sciences
NASA/MSFC:	
LABORATORY:	Mission Operations Laboratory
DIVISION:	Training and Crew Systems Division
BRANCH:	Systems Engineering Branch
TEAM:	Crew Systems Team
MSFC Colleague:	Joseph P. Hale

Introduction

The main objective of this project is to provide test objects for simulated environments utilized by the recently established Army/NASA Virtual Innovations Lab (ANVIL) at Marshall Space Flight Center, Huntsville, Al. The objective of the ANVIL lab is to provide virtual reality (VR) models and environments and to provide visualization and manipulation methods for the purpose of training and testing.

Visualization equipment used in the ANVIL lab includes head-mounted and boom-mounted immersive virtual reality display devices. Objects in the environment are manipulated using data glove, hand controller, or mouse. These simulated objects are solid or surfaced three dimensional models. They may be viewed or manipulated from any location within the environment and may be viewed on-screen or via immersive VR. The objects are created using various CAD modeling packages and are converted into the virtual environment using dVise (Division, Inc., 1997). This enables the object or environment to be viewed from any angle or distance for training or testing purposes.

In order to provide environments with the objects used in testing and training, models were created that focused on the primary project or task. Building on comparison and human factors projects completed during a previous NASA Summer Faculty Fellowship in 1993-1994, objects individualized for the X-34 virtual model and X-34 virtual maintenance environment were created using AutoCAD Release 13 (AutoDesk, 1995) and 3-D Studio (AutoDesk, 1994). These models included dVise's Manikin human figure models) of 5th, 50th, and 95th percentile American males, graphic representation of reach envelopes for each of these Manikins, and a manipulatable flexible air hose for the X-34 environment. The X-34 model and environment were created by Orbital Sciences Corporation and Marshal Space Flight Center.

The current primary task of the ANVIL laboratory is to use VR technology to enhance, animate, test, and document a design of the engine cavity, engine access hatch area, and maintenance environment for the X-34 sub-orbital vehicle. However, the general purpose nature of VR technology makes it an intelligence enhancing tool for a wide range of disciplines (Rheingold, 1991b) and the creation of manipulative input devices have simplified the interaction process between user and computer. These innovative input devices use hand or body movements instead of using complicated computer commands. The ease of interaction, and the use of wearable display equipment make it possible for the participant to view and to move through a simulated environment (Chung, 1989). VR's primary effect is to place a person into a simulated environment that looks and feels to some degree like the real world" (Psotka, 1994, p.1). however, reveals the motion of the hose as it is moved by the user.

The flexible hose will be incorporated into the latest version of the X-34 virtual maintenance environment where human factors testing will occur pertaining to its Using VR simulation of objects and environments, interactive computer programs have utilized the computer's advantage in memory and calculation

along with the human advantage in evaluation and putting ideas into context (Brooks, 1988). These advantages are magnified with the use of VR enhancement tools. These tools permit the user to utilize natural movement rather than typed instruction or symbols and words picked from a menu (Rheingold, 1991b). Among VR's advantages are opportunities for viewing and evaluating a selected object or environment that is difficult or expensive to access due to a remote or inaccessible location or one that is planned but does not yet exist. The importance of these factors interaction, simulation, and natural movement) lies largely in their potential for achieving economic efficiency in understanding the nature of human-environment interaction (Craik & Feimer, 1987).

Volume Visualization

Three-dimensional objects are necessary for volume visualization, concept that is difficult for most individuals. While we see in three dimensions, we are accustomed to looking at consolidated information on two dimensional media, whether it be graphic of text. A method of extracting information from a three-dimensional environment is necessary and is available in virtual reality environments which are essentially volumetric data sets. Information may be extracted from volumetric data sets through interactive graphics and imaging (Kaufman, 1996, p.1). Meaningful information that aids the understanding of volume and may be extracted from computer graphics by using transformations segmentations, translucency, and measurements (Kaufman, 1996). Two of these methods--translucency and measurement--will be utilized by the Manikin models and reach envelopes to extract information about X-34 engine extraction and maintenance. Measurement can be used when incorporating the flexible hose into a test or training session, or example on engine extraction.

Process

The process of creating three dimensional models and incorporating them into virtual environments is a time consuming and labor intensive one. It is important, however, that objects be in the scale of the parent environment and be as much like the real object being replicated as is possible (Lindsey, 1995). Inaccurate scale or representation can skew test results or provide ineffective training. Each segment of each model must be carefully dimensioned and then reproduced accurately along the x, y, and z axes so that it may be placed properly into the environment..

Creating and Testing Manikins and Reach Envelopes

The dVise standard male Manikin was used as a starting point to develop sample test human figures across the range of body sizes required for NASA development of NASA engineering designs. Using NASA standards NASA (1989) were used to modify the dVise Manikin represent a fifth, fiftieth, and ninety-fifth percentile American male as closely as possible. Each of the three Manikins was placed within the

test environment at a specified point at the X-34 engine maintenance hatch and using the dVise inverse kinematics, the reach capabilities of each of the three Manikins were compared by specifying individual engine parts could be reached.
A graphic representation of a reach envelope was used for comparison or reach inclusive areas, rather than specific objects (Figure 1). During this process, it was discovered that the dVise reach envelope exceeded the reach of the Manikin human figure, causing skewing of the information being gathered. New graphic representations of reach envelopes for each Manikin was developed using AutoCAD (AutoDesk, 1993). The newly designed envelopes were anthropometrically correct for each of the Manikins used for testing.
Again, each Manikin was placed at the engine cavity hatch of the X-34 virtual model and tested with the graphic reach envelope engaged and intruding into the engine cavity. By observing the reach envelope shell, information was gathered on which of the engine components might be reached by Manikins of the specified body sizes. The components that could be reached were determined by their inclusion in the reach envelope shell..

Flexible Air Hose

Compressed air powered wrenches will be used for maintenance of the X-34. The hoses are space consuming and kinetic. The motion of the hose is created by the user, but is passed on down the length of the hose due to its somewhat rigid nature and its rotation on the two axes only. This motion characteristic presents potential problems for technicians working at the engine cavity aperture. In order to test for problems that may occur in handling this motion and space intensive piece of equipment, a test model was created.

The original object, one three inch long segment, was created in AutoCAD. Copied multiple times, the segments were and aligned end-to-end until a usable length of hose was created. This CAD drawing was then imported into 3D Studio where links between each segment and a hierarchial structure was were established. The flexibility of the hose was restricted to 30 degrees. The rotation along the length of the hose was then set to zero so that the hose would rotate only around the y and the z axes, emulating accurate motion. The hose was presented via two types of animation: automatic and interactive. The automatic animation simply demonstrates the range of motion of the hose as it moves along a pre-determined path. The interactive hose,
however, reveals the motion of the hose as it is moved by the user.
The flexible hose will be incorporated into the latest version of the X-34 virtual maintenance environment where human factors testing will occur pertaining to its

function and spatial needs. It will be controlled by a data glove so that the user may move the hose at will in the X-34 environment and observe how the hose reacts the user-generated motion. The hose, maintaining its kinematic capabilities, may be scaled up or down and have its rotation restrictions modified to represent similar pieces of equipment

such as cables and hoses of alternate size and flexibility.

Conclusions and Expectations for the Future

This decade has been a succession of study, research, writing and activity in the evaluation and use of virtual reality technology for predicting the success of behavioral environments. Object creation for the use of human factors evaluation is the least time effective part of setting up an environment to be observed via VR technology. While there are commercial templates on the market, many times templates must still be customized. The object creator must understand scale and function of the subject environment and must stay in constant contact with the person who will convert the CAD objects into components of the VR environment. Specific elements must be included or deleted from A CAD drawing in order to convert it. Additionally, it is helpful for the object creator to be able

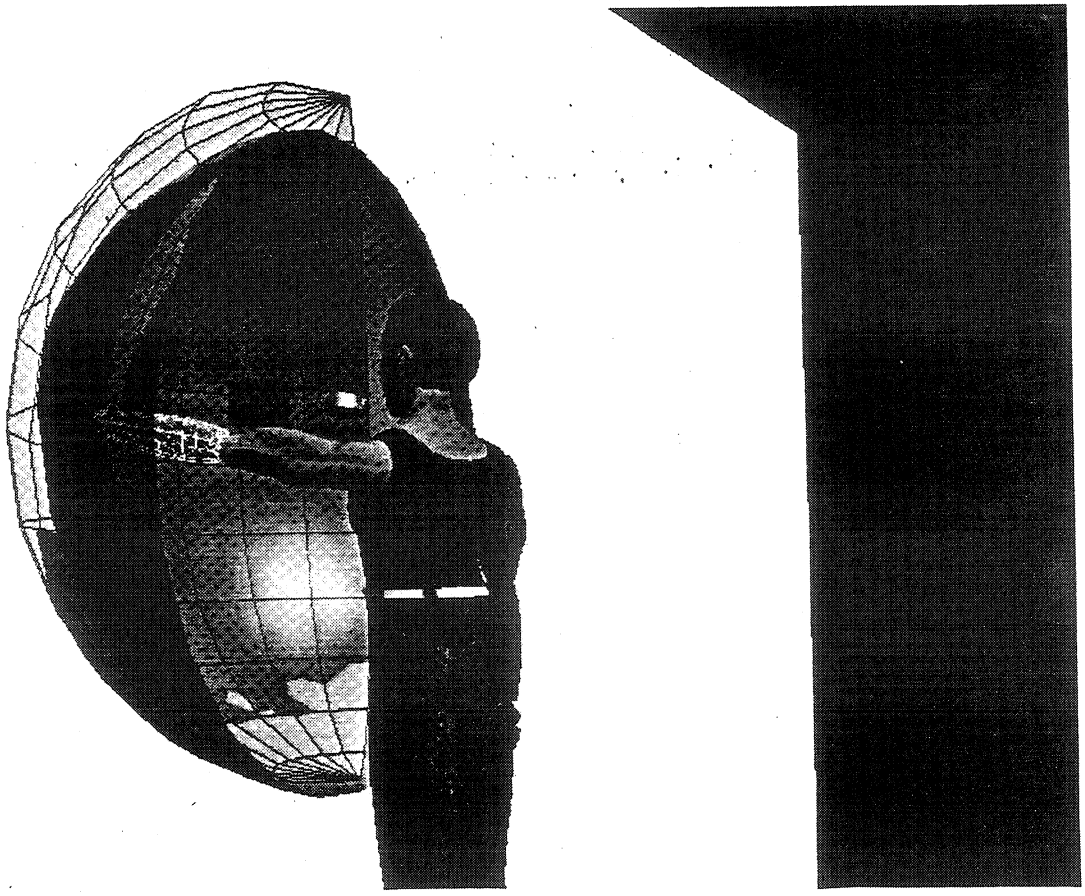

Figure 1.

to run the animation system in order to test our the success of the object within the environment, so that needed adjustments may be made.
It appears that ease of use of primitive shapes will increase in CAD packages in the future to reduce the time expended creating three dimensional objects. Since VR software necessitates the conversion of objects from CAD and modeling packages, a more sophisticated and interactive conversion method should be developed. Too many times, part of an object or its surface texture is lost during the translation from CAD to VR. As with all uses of electronic graphics, more uses will be found for the technology and the temporal problems will become less accute.

Collaborations

Efforts in to create and include necessary objects into the X-34 virtual environment and to establish them in an interactive mode could not have taken place with out the efforts of Leigh Lunsford, Ph.D.,and Joe Dumas, Ph.D., Summer Faculty Fellows in the ANVIL lab. Dr. Lunsford manipulated and animated the X-34 environments via software customization Dr. Dumas wrote devise drivers that incorporated the interactive VR equipment making the environments immersive and responsive to user manipulation.
We all worked under the guidance and with the help and advise of NASA mentor, Joe Hale and permanent ANVIL engineers, Mark Blassingame and Chris Daniel.

References

AutoDesk, Inc. (1990). 3D Studio. Autodesk, Inc. Publication, Sausalito, CA.

AutoDesk, Inc. (1993). AutoCAD. Autodesk, Inc. Publication, Sausalito, CA

Brooks, F. P., Jr. (1988). Grasping reality through illusion. In E. Soloway, D. Frege, & S. Sheppard (Ed.), CHI Proceedings, 1-11. Reading, MA.

Chung, J. C. et al. (1989). Exploring virtual worlds with head mounted display. Non-holographic, true 3-dimensional, display technologies. SPIE Proceedings, Vol. 1083, Los Angeles.

Division Inc. (1997), dVISE 4.0.0.

Kaufmann, A. E. (1996). Volume visualization. ACM Computing Surveys, 28, 1, 1-3.

NASA (1989). Man-system integration standards. NASA-STD-3000. Volume I, Revision A. National Aeronautics and Space Administration. Scientific and Technical Information Office.

Lindsey, P.F. (1996). A comparison of spatial interpretations of NASA's payload operations control center, marshall space flight center, using real world and virtual reality observations. Unpublished doctoral dissertation, Virginia Polytechnic Institute and State University, Blacksburg, VA.

Psotka, J. (1994). Immersive tutoring systems: Virtual reality education and training. Available: http://alex-immersion.army.mil/its.html.

1997

NASA/ASEE SUMMER FACULTY FELLOWSHIP PROGRAM

MARSHALL SPACE FLIGHT CENTER
THE UNIVERSITY OF ALABAMA IN HUNTSVILLE

REMOTE SENSING IN ARCHAEOLOGY: CLASSIFYING BAJOS OF THE PETEN, GUATEMALA

Prepared by:	James D. Lowry, Jr., Ph.D.
Academic Rank:	Assistant Professor
Institution and Department	East Central University Department of Cartography and Geography
NASA/MSFC:	
Office:	Global Hydrology Research
Division:	ES41, Earth System Science
MSFC Colleague:	Thomas L. Sever, Ph.D.

Introduction

This project focuses on the adaptation of human populations to their environments from prehistoric times to the present. It emphasizes interdisciplinary research to develop ecological baselines through the use of remotely sensed imagery, in situ field work, and the modeling of human population dynamics. It utilizes cultural and biological data from dated archaeological sites to assess the subsistence and settlement patterns of human societies in response to changing climatic and environmental conditions. The utilization of remote sensing techniques in archaeology is relatively new, exciting, and opens many doors (El-Baz 1997).

The cultural group examined is the Mayans of Mesoamerica (Guatemala, Mexico, Belize, Honduras, and El Salvador). We analyzed satellite data to address issues dealing with Mayan archaeology relating to climate and climatic change resulting from deforestation. At the time of the Mayan collapse they had almost completely cleared the forests (Coe 1993; Sever 1997) and suffered from tremendous population pressures (Coe 1993; Culbert 1993; Garrett 1989; Sever 1997; Stuart 1989). Current deforestation in the area is examined in light of the Mayan deforestation and collapse. Specifically we are concerned with the potential impact of deforestation on both the classic Mayan civilization and current Mesoamerican civilizations. Through the use of remote sensing we are attempting to unravel the past in order to protect the future.

We looked at early Mayan farming practices vis-à-vis current practices. There are no rivers or lakes in the study area, only seasonally flooded areas (bajos). When Westerners visit the area they are able to identify only two or three types of bajos, while the natives are able to identify seven. However, only two or three (of the seven) are good for agriculture. If the natives are able to identify all seven, satellites should be able to see them as well. We, thus, attempted (via ground truths) to identify all seven types on satellite images, with the purpose of identifying those which are good agricultural sites. The purpose of this is twofold: we would like to see if the Mayans selected the appropriate bajos and if the current civilizations have as well, and if these areas are/were threatened by deforestation and overpopulation.

History of the Maya

Mayan civilization is commonly divided chronologically into three general periods; the Preclassic, which began with the first appearance of pottery about 1800 B.C. and ended around 250 A.D. with the beginning of dated inscriptions, the Classic, which began with the dated inscriptions and ended around 900 A.D. with the disappearance of dated inscriptions, and the Post Classic, which ended with the Spanish Conquest. In addition, each of these periods has been further subdivided (Coe 1993, Culbert 1993). The period of specific interest here is the Terminal or Late Classic. Mayan population by the end of the Classic period is thought to have reached 500 people per square mile (Culbert 1993; Sever 1997), which is higher than almost any place in the world today. This, along with almost exponential population growth, is believed to have led to the disastrous and rapid (<100 year) collapse. Although there were most certainly multiple factors which led to the collapse (e.g., warfare (Demarest 1993; Sabloff 1995), food shortages (Sabloff 1995; Sever 1997; Stuart 1989), environmental degradation (Curtis, et. al.

1996; Hodell, et. al. 1995; Sabloff 1995; Sever 1997; Stuart 1989), etc.), all point to overpopulation as the root. The importance of this lies in the fact that this process (i.e., high population density along with tremendous population growth) is being replicated in Mesoamerica (in the Department of the Peten in Guatemala population today is twenty times the size of its 1950 population (Stuart 1992)), and elsewhere, today. Overpopulation is a result of many things, but an increasing scarcity of resources, including food, is one of the keys. The Mayans surely suffered from food shortages as their population and population density increased rapidly. How did they react to these shortages? Did they intensify their traditional milpa (slash and burn) agricultural practice? Did they extend agriculture into land previously thought to be marginal at best. And, if so, to where did they extend agriculture? Evidence (Coe 1993; Culbert 1993; Culbert, et. al. 1995a; Culbert et. al. 1995b; O'Neill 1993) exists to indicate that they both intensified milpa and moved into bajos. We need to know how and why they selected certain bajos. Did they select those most amenable to agriculture? And, if not, did this hasten their demise? Finally, is they pattern to be repeated?

The archaeological record has provided us with a wealth of information on Mayan life, yet there is much yet to learn. Why, exactly, did Mayan civilization collapse? The archaeological record will likely never definitively answer this question. Although the Mayans developed writing (hieroglyphics) we will likely never read their historical accounts. Unfortunately, the great body of Mayan texts was destroyed by Friar Diego de Landa , Bishop of Yucatan in the mid 16th century, in an attempt to eradicate "paganism" and "idolatry" (Culbert 1993; Hammond 1990; Sever 1997). Landa was recalled to Spain to answer for his crimes, and in the process of his defense in 1566 penned Yucatan before and after the conquest (1978). Landa, thus, destroyed almost all Mayan records, while at the same time providing us with the most complete account we have of Mayan history. This history, however, tells us nothing about the collapse. We must, therefore, reconstruct this as best we can, from the archaeological record.

Searching for Answers

As stated above, there are seven types of bajo known to Mesoamericans, two or three of which remain sufficiently moist enough in the dry season to sustain agriculture. Westerners are able to discern only two or three types (not necessarily the two or three favorable to agriculture) of the seven, but we must find a way to see all seven if we are to examine agricultural practices of the past and the present. Since we are unable to see these different bajos with our eyes, we decided to attempt to "see" them with satellite imagery. This required several steps. We first acquired satellite imagery of part of the Peten, we obtained transect data (ground truths) of vegetation from archaeological field work, and then attempted to classify the satellite imagery based upon vegetation classifications to determine if the satellite could, in fact, "see" the bajos.

The satellite imagery employed comes from the Thematic Mapper (TM) from Landsat 4. We examined data from bands 2-5, which includes both visible and infrared segments of the electromagnetic spectrum. The transect data comes from field data collected by Culbert and his team during their May 1995 field session. They conducted vegetation surveys along two transects in the Bajo la Justa, Peten, Guatemala, one a trail of approximately 7 km, the other along a road of approximately 17 km. They were assisted in the vegetation survey by a native

(Sr. Don Felipe Lanza) employed by the Forestry Division of the Tikal National Park (who could see all seven types of bajo). During this session they learned that there are two primary classifications of vegetational associations. These were termed "palm bajo" and "scrub bajo." Within each of these two major types are "sections characterized by a predominance of particular species which provide subtypes such as "escobal", "corozal", and "botonal" within the palm bajo, and "jimbal", tintal", navajuelal", and "huechal" within scrub bajo" (Culbert, et. al. 1995a, 1). Additionally, there are three distinctions that relate to ground surface characteristics and inundation. These are "bajo plano," which has a flat surface and no noticeable slope, "bajo borbolal," which has an undulating surface, and "bajo inundable," which is at an elevation where seasonal flooding occurs and seems to be characterized by scrub vegetation. Sr. Lanza also informed them that palm bajo is excellent for milpa and is one of the environments of choice among the native Pateneros. Along both transects they recorded vegetation according to Sr. Lanza's classification and gathered global positioning system (GPS) readings.

Armed with TM data of the Peten and the vegetation surveys and GPS readings, we launched our project to "see" bajos with satellites. Our first task was to truncate our study area from the larger image. In doing so we encountered our first minor problem, we lost georeferencing. We were able to overcome this by manually re-georeferencing the data using easily identifiable points. Once we had this task completed, we subjected the data to several classification schemes. We then plotted the GPS readings. For all vegetation types for which we had two readings, we compared results of our classification. Our best classification resulted in only about 50% of the pairs being classified together. Thus, so far we have been unsuccessful in seeing all of the various types of bajo with satellite imagery, although we feel yet that it can be accomplished. We are optimistic because our success was impeded by two major problems, addressed below, that we can, and will, overcome.

Problems, Solutions, and the Future

Both of our major problems are related to the quality of our data. The first of the problems is related to the image itself. The TM image of the Peten with which we were working was gathered in May of 1993. Landsat 4 was launched in July of 1982 (Richarson 1983), which places the sensor well beyond its expected lifetime. This had a tremendous effect on bands two and three, both visible, of the sensor in that they were subject to quite notable banding (i.e., noise). The effect was minimal on bands four (near infrared) and five (middle infrared), thus we were forced to settle with employing only these two bands. We, therefore, were not able to fully maximize the image.

The second problem is related to the vegetation survey data. As was mentioned before, one transect is only approximately seven kilometers long, the other only about seventeen. In addition, they are located very close to each other. The problem with this is that these points are all located along a road or trail where there is obvious clearing, which results in a less than optimal vegetational signal. Thus, for example, a sample of palm bajo along the road surely had a difference reflectance, and signal, than palm bajo miles from any clearing. These sites are simply too close to each other and too close to areas cleared for human transportation.

Solutions to both of these problems are quite simple to address. We are currently in the process of securing older TM data (i.e., data from before the sensor began to decay). This should alleviate the banding (noise) problem we have been experiencing. In addition, as regards Sr. Lanza's description of non-vegetational attributes of bajos, we are also looking at obtaining Shuttle Imaging Radar-A (SIR-A) or Spaceborne Imaging Radar-C (SIR-C) data. Radar has the ability to look beneath the canopy at the ground, thus it may help us with topographic and hydrologic features. We also need to obtain more transect vegetational survey data. Ideally we need multiple observations of each type of bajo. These observations need to be well within the bajo in question (at least 100 meters from the edge to counteract GPS selective availability and to ensure that that point will be well within a pixel corresponding to that type of vegetation on the image), and, if possible, areas within the bajo should be collected instead of points (to provide more information for classification).

We are, as was mentioned above, in the process of obtaining "better" imagery. Vegetational survey data, however, will be harder to collect. We will, however, continue to use the transects we have until we are able to secure new information. For the immediate future we are focusing on the image, for this is something better under our control. However, once we have new images and new vegetational survey data, we feel sure that we will be able to fully address our basic question: can a satellite "see" the various types of bajos? Answering this question will help us in our quest to discover what led to the collapse of Classic Mayan civilization, and may help us prevent a recurrence in the future.

Acknowledgments

In addition to Dr. Tom Sever, my NASA mentor, to whom goes a world of thanks and admiration, we received technical assistance in remote sensing classification and interpretation from Mr. Burgess Howell, also of the GHCC at MSFC. Throughout the text, whenever "we" are mentioned, it includes my very capable student Chad Landgraf. His assistance has been invaluable. I also owe a great deal of gratitude to Drs. Bruce Weems and Duane Anderson, both of East Central University, for their encouragement, support, and patience. In addition, I would like to thank my wife Lori and my girls, Abby and Jesse, for "releasing" me for the summer.

References

Coe, Michael D. 1993. The Maya (5e). Thames and Hudson, New York.

Culbert, T. Patrick. 1997. Vegetation surveys. Personal correspondence with Dr. Tom Sever.

-----. 1993. Maya Civilization. Smithsonian Books, Washington, D.C.

-----, Laura Levi, Brian McKee, and Julie Kunen. 1995a. Investigaciones arquelogicas en el bajo La Jusat entre Yaxha y Nakun, (unpublished manuscript, in English).

-----,-----,-----,-----, and Kerry Sagebiel. 1995b. The Bajo la Justa field season, May 1995, (unpublished manuscript).

Curtis, Jason H., and David A. Hodell. 1996. Climate variability on the Yucatan Peninsula (Mexico) during the past 3500 years, and implications for Maya cultural evolution, Quaternary Research 46:37-47.

de Landa, Friar Diego. 1978. Yucatan before and after the conquest. Dover, New York.

Demarest, Arthur A. 1993. The violent saga of a Maya kingdom, National Geographic 183(2):94-111.

El-Baz, Farouk. 1997. Space age archaeology, Scientific American 277(2):60-65.

Garrett, Wilbur E. 1989. La Ruta Maya, National Geographic 176(4):424-479.

Hammond, Norman. 1990. Ancient Maya civilization. Rutgers U. Press: New Brunswick, N.J.

Hodell, David A., Jason H. Curtis, and Mark Brenner. 1995. Possible role of climate in the collapse of classic Maya civilization, Nature 375(June):391-394.

O'Neill, Thomas. 1993. New sensors eye the rain forest, National Geographic 183(9):118-130.

Richardson, Benjamin F. Jr. (ed.). 1983. Introduction to remote sensing of the environment (2e). Kendall/Hunt, Dubuque, Iowa.

Sabloff, Jeremy A. 1995. Drought and decline, Nature 375(June):357.

Sever, Thomas L. 1997. Various personal correspondences (June-July).

Stuart, George E. 1989. City of kings and commoners, National Geographic, 176(4):488-505.

-----. 1992. Maya heartland under siege, National Geographic, 182(5):94-107.

1997

NASA/ASEE SUMMER FACULTY FELLOWSHIP PROGRAM

MARSHALL SPACE FLIGHT CENTER
THE UNIVERSITY OF ALABAMA IN HUNTSVILLE

EVALUATION OF GPS COVERAGE FOR THE X-33 MICHAEL-6 TRAJECTORY

Prepared By: John B. Lundberg, Ph.D.

Academic Rank: Assistant Professor

Institution and Department: Auburn University
Department of Aerospace Engineering

NASA/MSFC:

Branch: Flight Mechanics, Guidance, Navigation, & Control Systems

Division: Guidance & Control Systems

Laboratory: Structures & Dynamics

MSFC Colleagues: John M. Hanson, Ph.d.

Introduction

The onboard navigational system for the X-33 test flights will be based on the use of measurements collected from the Embedded Global Positioning System (GPS)/INS system. Some of the factors which will affect the quality of the GPS contribution to the navigational solution will be the number of pseudorange measurements collected at any instant in time, the distribution of the GPS satellites within the field of view, and the inherent noise level of the GPS receiver. The distribution of GPS satellites within the field of view of the receiver's antenna will depend on the receiver's position, the time of day, pointing direction of the antenna, and the effective cone angle of the antenna. The number of pseudorange measurements collected will depend upon these factors as well as the time required to lock onto a GPS satellite signal once the GPS satellite comes into the field of view of the antenna and the number of available receiver channels. The objective of this study is to evaluate the GPS coverage resulting from the proposed antenna pointing directions, the proposed antenna cone angles, and the effects due to the time of day for the X-33 Michael-6 trajectory from launch at Edwards AFB, California, to the start of the Terminal Area Energy Management (TAEM) phase on approach to Michael AAF, Utah.

Procedure

To evaluate the GPS coverage, the parameters of interest are assumed to be the minimum possible (optimal) GDOP (Geometric Dilution of Precision) and the number of satellites that the receiver locks onto at any particular point in the trajectory. Using the current baseline Michael-6 trajectory, these parameters are computed at equally spaced intervals in time. Parameter permutations include four antenna positions, two cones angles, and 24 launch times. The time of day is varied to generate 24 profiles for each antenna and cone angle combination. The results are summarized by computing the percentage of time during this trajectory that each of the two parameters fall within a specified range of values.

Assumptions

1) The Michael-6 trajectory has the following time characteristics: main engine cut-off (MECO) at 200 seconds after launch and TAEM entry at 476 seconds after launch. The trajectory has bounded attitude rates, and the vehicle is assumed to have a perfect response to guidance command inputs. Periods of significant maneuvering for energy management occur near 260 seconds after launch and from 300 to 380 seconds after launch.

2) The GPS receiver has 5 tracking channels; 4 of these channels are used to lock onto the "primary" GPS satellites and the remaining channel is to lock onto another GPS satellite whose data will be used in the event that signal lock to one of the primary satellites is lost. There is assumed to be a 6 second delay between the time that a GPS satellite comes into the field of view and the time when the receiver is able to lock on to the signal and generate valid measurements. The receivers are assumed to record measurements at intervals of one second.

3) There are 4 possible antenna positions on the current X-33 vehicle configuration. All 4 are located on the forward part of the vehicle in a symmetrical arrangement about the center line

(2 to port and 2 to starboard). Since only the pointing directions of the antennas affect the results, the actual positions of the antennas are immaterial. The body-fixed pointing directions of the antennas are assumed to be:

Antenna Position	ID	Pointing Direction		Body-fixed Unit Vector		
		zenith	azimuth	x	y	z
Front/Port	1	11.8°	-30°	0.1771	-0.1022	-0.9789
Front/Starboard	2	11.8°	30°	0.1771	0.1022	-0.9789
Back/Port	3	9.5°	-30°	0.1429	-0.0825	-0.9863
Back/Starboard	4	9.5°	30°	0.1429	0.0825	-0.9863

Note: the x direction is forward, the y direction is to starboard, and the z direction is down.
Note: antenna 2 is currently reserved for the JPL GPS experiments while antennas 1, 3, and 4 will feed the three GPS/INS units.

4) The antennas are assumed to have two possible cone angles: 120° and 150°. There is assumed to be no masking of the antenna field of view by the body of the vehicle or any other object other than the Earth's disk.

5) The orbital parameters for the GPS constellation are those from the Yuma almanac for week 784. During the 476 second flight, the actual positions of the GPS satellites in an Earth-fixed system change very little although there will be significant changes from one hour to the next.

6) To consider the effect of the time of day, 24 scenarios were considered with launch occurring at the beginning of every hour (0000 to 2300).

Software Tools

The truth trajectory for the X-33 was generated using MAVERIC in 3 DOF mode. A file of time, position, velocity, acceleration, and attitude was generated at one second intervals from 1 second after launch to 476 seconds after launch.

The parameters associated with the coverage analysis were computed using GPS-RCM (GPS Digital Statistical Receiver and Constellation Model) which simulates GPS measurements along a user specified trajectory and using user specified information about receiver characteristics, environmental parameters, and antenna characteristics. Currently, GPS-RCM is capable of simulating two receivers each on separate trajectories with up to 12 channels and 4 antennas per receiver. Options in GPS-RCM include the capability to compute navigational solutions using a Kalman filter or using a static positioning approach.

Results

Since the receiver under consideration has only five channels and exports data from only four of these channels, the optimal (minimum possible) GDOP is selected from the set of all possible GDOP values computed using permutations of four GPS satellites selected from the set

of all GPS satellites within the field of view of the antenna. No assumption is made as to whether or not the receiver has locked onto the satellites which produce the optimal value. The GDOP corresponding to the measurements exported by the receiver will depend on which satellites the receiver is actually locked onto as opposed to which satellites are in the field of view. The satellite selection algorithm employed by the receiver and the time required to lock onto a satellite once it comes into the field of view (lock delay interval) will result in some degradation of the GDOP of the exported data when compared to the optimal GDOP.

A profile of optimal GDOP values was generated for each combination of time of launch, antenna position, and cone angle. For each profile, the number of optimal GDOP values in the following groups were counted: (0-5), (5-10), (10-20), (> 20), and (no GDOP available: < 4 GPS satellites in the field of view). It is noted that when only 4 GPS satellites are considered, the minimum possible value of GDOP is approximately 1.57; thus the lower limit of the first group in Tables 1 and 2 should read 1.57 rather than 0. Tables 1 and 2 show the distribution of GDOP values for antenna 1 using cones angles of 120° and 150°, respectively.

For a maneuvering vehicle that is carrying a GPS receiver, the number of satellites that the receiver is able to lock onto at any time is a critical parameter in evaluating the effect of the satellite cone angle and the lock delay interval on the overall navigational performance. The actual satellites that are locked onto will depend on the particular satellite selection algorithm. For the following results, the receiver is initialized by locking onto all satellites within the field of view at the start of the trajectory. If more than five satellites are visible at the start of the trajectory, the satellites are selected in terms of their usefulness in reducing the value of the GDOP. After initialization, the receiver locks an open channel onto the next GPS satellite that has been in the field of view beyond the lock delay interval. Once a channel has been locked onto a particular GPS satellite, it remains locked on that satellite until the GPS satellite is no longer in the field of view. This approach tends to maximize the number of locked channels rather than minimizing the GDOP of the primary GPS satellites. From this information, two parameters which measure the quality of GPS coverage are the total time during which fewer than four channels are locked on GPS satellites and the maximum duration during which there are fewer than four locked channels. Figures 1 and 2 show these two parameters for antenna 1 using cone angles of 120° and 150° respectively.

Conclusion

Despite the general improvement in reducing the optimal GDOP values with a cone angle of 150° over the corresponding cases for a cone angle of 120°, there are still some periods during the day in which the GPS coverage is significantly degraded with high GDOP values and/or less than 4 GPS satellites visible. Also, despite the general improvement in increasing the number of locked channels with a cone angle of 150° over the corresponding cases for a cone angle of 120°, there are still some significant periods during which the number of locked channels is 3 or less. Even with a cone angle of 150°, these periods range from 1 second to as much as 51 seconds and generally occur around the times of maneuvers when the GPS satellites can quickly disappear from the field of view and before other GPS satellites can be acquired. However, some of these instances are also due to launch or near launch conditions when the antennas are pointing toward the horizon.

Table 1
Percentage of epochs for the minimum possible GDOP:
Antenna 1 with a 120° Cone Angle

Launch Time (hour)	GDOP Range				
	0-5	5-10	10-20	> 20	< 4 sat
00	4.2	32.4	24.4	3.6	35.5
01	6.7	32.6	28.2	4.8	27.7
02	9.2	45.5	17.9	2.7	25.2
03	0.2	76.3	0.0	4.4	19.1
04	0.8	36.8	0.0	17.6	44.7
05	17.6	39.1	4.8	0.0	38.4
06	4.4	64.9	0.0	1.1	29.6
07	1.1	62.2	11.6	2.7	22.5
08	15.1	23.1	20.4	3.6	37.8
09	2.3	51.9	3.4	3.6	38.9
10	1.1	38.2	17.2	9.2	34.2
11	5.9	65.8	2.9	0.8	24.6
12	5.5	29.4	23.9	2.7	38.4
13	9.9	42.6	23.9	6.1	17.4
14	10.5	43.7	17.9	2.3	25.6
15	0.0	74.6	0.0	4.8	20.6
16	0.6	34.7	0.0	17.9	46.8
17	19.3	30.7	12.4	0.0	37.6
18	5.0	61.8	0.0	0.0	33.2
19	1.1	72.7	8.0	1.5	16.8
20	11.8	21.8	23.1	4.2	39.1
21	1.7	49.4	6.3	3.6	39.1
22	1.5	36.6	17.0	10.3	34.7
23	5.9	63.9	2.7	0.6	26.9

Table 2
Percentage of epochs for the minimum possible GDOP:
Antenna 1 with a 150° Cone Angle

Launch Time (hour)	GDOP Range				
	0-5	5-10	10-20	> 20	< 4 sat
00	81.9	12.2	5.9	0.0	0.0
01	73.9	10.7	15.3	0.0	0.0
02	55.7	26.1	8.2	0.0	10.1
03	61.1	38.9	0.0	0.0	0.0
04	32.1	46.8	0.0	0.0	21.0
05	69.3	23.5	0.0	0.0	7.1
06	58.6	31.1	0.0	0.0	10.3
07	51.9	36.6	11.6	0.0	0.0
08	67.4	23.3	6.7	2.5	0.0
09	39.7	34.5	13.4	0.0	12.4
10	60.9	17.4	15.8	0.0	5.9
11	65.1	25.6	0.0	0.0	9.2
12	81.3	11.6	7.1	0.0	0.0
13	88.4	5.7	5.9	0.0	0.0
14	55.9	25.6	8.2	0.0	10.3
15	59.9	40.1	0.0	0.0	0.0
16	39.5	40.8	0.0	0.0	19.7
17	64.1	28.2	1.7	0.0	6.1
18	55.9	33.4	0.0	0.0	10.7
19	56.1	41.6	2.3	0.0	0.0
20	69.1	20.6	6.3	4.0	0.0
21	38.4	35.1	14.3	0.0	12.2
22	65.3	13.0	14.3	0.0	7.4
23	63.0	27.7	0.0	0.0	9.2

Figure 2
Antenna 1 with a 150 degree cone angle

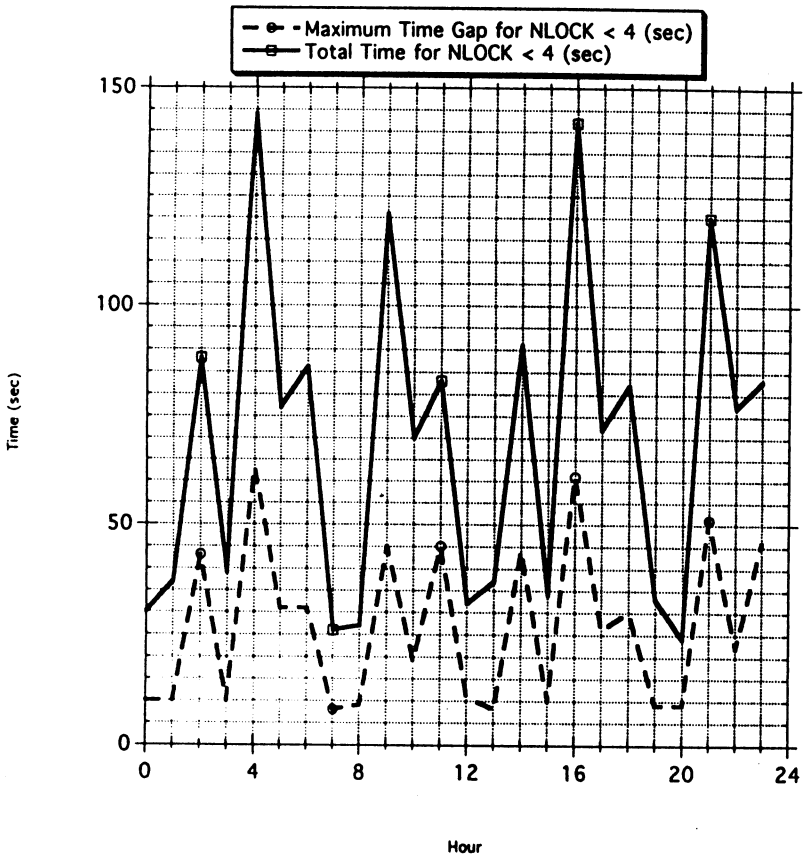

Figure 1
Antenna 1 with a 120 degree cone angle

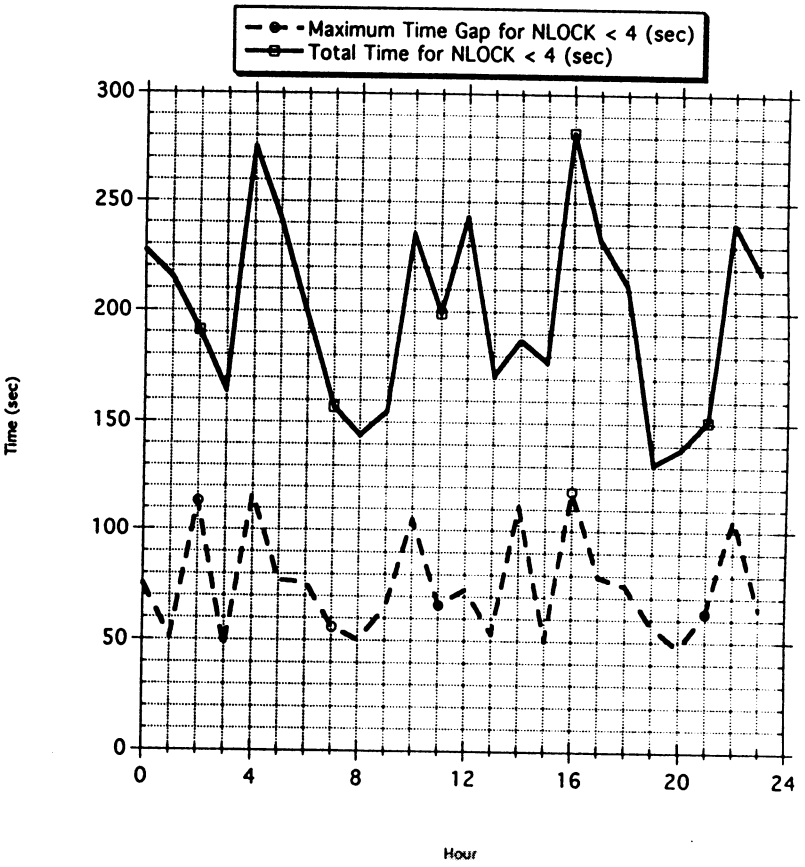

1997

NASA/ASEE SUMMER FACULTY FELLOWSHIP PROGRAM

MARSHALL SPACE FLIGHT CENTER
THE UNIVERSITY OF ALABAMA IN HUNTSVILLE

VIRTUAL ENVIRONMENT COMPUTER SIMULATIONS TO SUPPORT HUMAN FACTORS ENGINEERING AND OPERATIONS ANALYSIS FOR THE RLV PROGRAM

Prepared By:	M. Leigh Lunsford, Ph.D.
Academic Rank:	Assistant Professor
Institution and Department:	Alabama A & M University Dept. of Mathematics and Computer Science
NASA/MSFC:	
Branch:	Systems Branch
Division:	Training and Crew Systems Division
Lab:	Missions Operations Laboratory
MSFC Colleague:	Joseph P. Hale

Introduction

The Army-NASA Virtual Innovations Laboratory (ANVIL) was recently created to provide virtual reality tools for performing Human Engineering and operations analysis for both NASA and the Army. The author's summer research project consisted of developing and refining these tools for NASA's Reusable Launch Vehicle (RLV) program. Several general simulations were developed for use by the ANVIL for the evaluation of the X34 Engine Changeout procedure. These simulations were developed with the software tool dVISE 4.0.0 produced by Division Inc. [2] All software was run on an SGI Indigo2 High Impact. In the process of developing these simulations, the author worked with two Summer Faculty Fellows also assigned to the ANVIL. Dr. Pat Lindsay and the author analyzed the mannequin feature provided with the Division software [5]. Dr. Joe Dumas and the author worked on using various input devices with the Division software [3]. This paper describes the simulations, various problems encountered with the simulations, other summer activities, and possible work for the future. We first begin with a brief description of virtual reality systems.

Virtual Reality Systems and their Applications

Virtual Reality (VR) is a computer generated world in which the user can interact in real time. Typically this world will consist of three major components. The first consists of the various objects in the world which are represented by accessing their associated geometry files. The geometry files are CAD (Computer Aided Design) generated and consist of a description of vertices and polygons which define the shape of the object. The second component is the user. The user, who often wears immersive input devices such as a head mounted display (HMD) or data glove, is described by a body file. The body file contains the geometries of body parts and can be customized for various types of individuals. This implies one can take parameters such as reach and height into consideration. The third, and perhaps the most important, component of the virtual world consists of events and behaviors that govern the interactions between objects and the interactions between the user and objects. An example of this is the event of the user's hand touching an object which then generates a behavior such as a sound, message, or even an animation.

VR has great potential in the areas of human factors engineering and operations analysis. The greatest strength of VR is that it allows designers to visualize and interact with their products. Thus one can detect design flaws much earlier in the design and development process which can save substantial costs in the long run. Also, because one can perform the human factors analysis in the virtual world, costs incurred in the building a full-scale model of the product can be reduced.

Virtual Reality Simulations for the ANVIL

During the course of the summer, the author developed several VR simulations for use in the ANVIL. The main focus was to implement events and behaviors in these simulations which would allow interaction between the objects and interaction between the user and the objects. Two of these simulations were concerned with the evaluation of the X34 Engine Changeout procedure. The first was geared for human factors studies and the second addressed operations analysis of engine removal. In both simulations the X34 CAD files were generated by Orbital Sciences Corporation and MSFC. These CAD files were then imported into the Division software. It was at this point that the author began defining the various events and behaviors for the simulations. The dVISE program is intended to be a GUI (graphical user interface) based program. However, when designing customized simulations using dVISE, one often has to go to the level of the Division code (essentially function calls to their executable code written in the C Programming Language).

The simulation developed for human factors engineering was a virtual environment in which the user attempted to disconnect bolts from the X34 engine. This simulation allowed human subjects to interact with the virtual world for training purposes or for performing reach analysis.

The user is outfitted with a data glove which provides an immersive interface between the user's hand, and hence their body, and the virtual world. The data glove device drivers for use in the Division software were written this summer by Dr. Joe Dumas [3]. Features of the simulation include: the ability to move the user to any fixed starting point thus allowing for a common frame of reference when testing the same or multiple subjects; the ability of the user to reach and grab various objects in the world including a wrench and bolts; sounds and pop-up messages to let the user know when the wrench or the user's forearm has collided with other objects; and various animations such as the removal of a bolt when the user's hand touches the bolt. Currently we are using one body file, which means that arm length and height are the same for all users. Future work will be to develop several body files which fit the NASA 5th percentile female to 95th percentile male categories and to test these files with human subjects [6]. These body files would be usable in all of the simulations developed with the Division dVISE software.

The simulation developed for engine changeout analysis focused on providing support for operations and design analysis. The X34 Engine is a Fastrac 60K designed by the MSFC Propulsion Laboratory. The ANVIL has been asked to assist in the determination of engine removal paths and to provide demonstrations of these paths. These paths should include collision detection and close proximity detection for clearance assessment. With this in mind, the author developed the engine changeout simulation for the X34. Features of this simulation include: the ability of a user to try various engine removal paths; accurate measurement of removal, thus allowing for easy testing and verification; animation of removal paths; different camera angles from which to review various removal paths; accurate (polygonal) collision detection on individual engine parts during the engine removal process; and pop-up messages and visual cues such as color changes upon detection of collision of the engine with other parts of the spacecraft.

Two concerns became apparent in the development of the X34 Engine removal simulation. They were the determination and implementation of common reference points for measuring translations and angles of rotation of the engine and the implementation of close proximity collision detection. As described above, the geometries for all of the X34 objects are imported CAD files. This leaves the VR simulation designer somewhat at the mercy of the CAD designer as to where the geometrical origin of an object is located. In the case of the X34 engine, the origin of the geometry was directly in front of the nose of the aircraft which made it difficult to accurately describe movement of the engine. In this simulation we determined a way to get around this by fixing a common point of reference (inside the engine nozzle) from which we were able to accurately measure all translations and rotations of the engine. Certainly it is possible to change this point of reference. The author recommends an agreed-upon point of reference so that engineers can communicate effectively about the engine removal paths. In the process of moving the engine in the simulation, one sees various objects, such as the fuselage, change color when the engine collides with the object. Because we want accuracy in the engine removal process, we are using polygonal collision detection. Polygonal collision detection checks to see if any polygons of any two objects are colliding. Although strides have been made in this area and the Division software uses many of these advances [1, 4], polygonal collision detection is the most expensive computationally. We were able to avoid slow updates of the rendering window of the system by carefully choosing which parts of the engine to add collision properties. The more interesting problem encountered in this simulation was how to implement near collision detection. At the present we have found no existing software which can accurately perform near collision detection. We briefly discuss two ideas for future development in this area.

The first idea for performing near collision detection is to create a new geometry for an object called a "neighborhood". For instance, a one inch neighborhood about an object would consist of all points in space whose distance from the object is less than or equal to one inch. One could then use a one inch neighborhood geometry for the X34 Engine to see if engine removal could be accomplished with at least a one inch tolerance. The problem with this idea is generating the neighborhood, especially with complicated geometries such as the X34 Engine. The author believes the problem of generating a neighborhood geometry from an existing geometry is a hard (in the sense of not being computable in polynomial time, i.e. NP) problem. The second idea for performing near collision is to compute distances between objects as they move and then determine

the minimum distance. This is also a non-trivial problem. However, it is being addressed by some of the leading researchers in the field [7]. Future work could be developing and/or finding algorithms for near collision detection and then implementing them in the Division software.

In addition to the X34 simulations, the author also worked on a simulation developed for the Grand Opening of the ANVIL. This simulation was a virtual ribbon cutting and featured a fly-through of a virtual world that included helicopters, tanks, and various NASA spacecraft. The author principally worked on the animation sequence for the fly-through.

Other Projects

In addition to developing the above simulations, the author also worked with other Summer Faculty Fellows in the ANVIL lab in using the Division software for various tasks. Dr. Pat Linsdey and the author evaluated the Division mannequin (called "manikin") . We determined how to make a library of these mannequins that fit the NASA standards. We also determined how to import these new mannequins into the existing X34 simulations for the purpose of human factors engineering. The mannequin should not be confused with the user body described above. In fact, the mannequin is considered another object in the virtual world and does not use input devices such as the data glove. The purpose of the mannequin is to visualize and test human factors parameters such as reach envelope. For more information on the mannequin please see the paper by Dr. Pat Lindsey [5].

Dr. Joe Dumas, another ANVIL Summer Faculty Fellow, was assigned the task of writing device drivers for several input devices in the ANVIL. These included the space shuttle hand controllers, the data glove, and the HMD. Once he had written the device drives, the author helped him get the input devices working correctly with the Division software. Principally, the author worked on creating body files that would work with various combinations of input devices. For more information on the various input devices please see the paper by Dr. Joe Dumas [3].

Conclusions and Future Work

Although the author is pleased the simulations developed this summer are currently being used by the ANVIL, she believes more can be done to make these simulations easy to use for human factors, operations, and design engineers. The geometry models for the user need to be scaled to the NASA standards. These geometry models should also be tested with humans, wearing various input devices such as the data glove, who meet those standards. Once this is done, NASA will have a very nice library of body types for use in all immersive simulations which run the Division software package dVISE. The problem of near collision detection is interesting from both theoretical and practical points of view. Having this type of collision detection implemented in the Division software would be a real boon to the ANVIL. Lastly, there a several combinations of input devices available for the user (Fakespace, data glove, etc.). Some of these combinations of input devices have not been configured for use in the software. The different combinations should be tested to determine the best way for the user to have an immersive interface in the virtual world.

Before starting the Summer Faculty Fellowship Program, this author knew very little about VR and its applications. Upon completion of the program, she feels that VR is an up and coming technology that will be used for many types of applications. The author would like to thank NASA and in particular the Summer Education Programs for providing her with this excellent experience.

References

1. Cohen, J., Lin, M., Manocha, D. and Pnoamgi, K., Interactive and Exact Collision Detection for Large-Scale Environments, Technical Report TR94-005, Department of Computer Science, University of N. Carolina, Chapel Hill.

2. Division Inc., dVISE 4.0.0, 1400 Fashion Island Boulevard, Suit 510, San Mateo, CA 94404 [online] Available: http://www.division.com/ .
3. Dumas, J., Virtual Environment User Interfaces to Support RLV and Space Station Simulations in the ANVIL Virtual Reality Lab, *Research Reports, 1997, NASA/ASEE Summer Faculty Fellowship Programs*, Eds. G.R. Karr, L. M. Freeman, J. Dowdy, p. IX, 1997.
4. Lin, M., Manocha, D., Cohen, J., Gottschalk, S., Collision Detection: Algorithms and Applications, Appeared in Proc. of *Algorithms for Robotics Motion and Manipulation*, pp. 129-142, Eds. Jean-Paul Laumond and M. Overmaus, A.K. Peters (invited submission).
5. Lindsey, P., Object Creation and Human Factors Evaluation for Virtual Environments, *Research Reports, 1997, NASA/ASEE Summer Faculty Fellowship Programs*, Eds. G.R. Karr, L. M. Freeman, J. Dowdy, p. XXVII, 1997.
6. NASA Reference Publication 1024, Anthropometric Source Book, Vol. II: A Handbook of Anthropometric Data, NASA Scientific and Technical Information Office, 1997.
7. UNC Research Group on Modeling, Physically-Based Simulation and Applications, Univ. of N. Carolina, Chapel Hill, [online] Available: http://www.cs.unc.edu/~geom .

1997

NASA/ASEE SUMMER FACULTY FELLOWSHIP PROGRAM

MARSHALL SPACE FLIGHT CENTER
THE UNIVERSITY OF ALABAMA IN HUNTSVILLE

DEVELOPMENT OF TECHNOLOGY TRANSFER ECONOMIC GROWTH METRICS

Prepared By:	Christina M. Mastrangelo, Ph.D.
Academic Rank:	Assistant Professor
Institution:	University of Virginia Department of Systems Engineering
NASA/MSFC: MSFC Colleague:	Dave Cockrell Technology Transfer Office
	Bill Fieselman Tec-Masters, Incorporated

A. Introduction

The primary objective of this project is to determine the feasibility of producing technology transfer metrics that answer the question: Do NASA/MSFC technical assistance activities impact economic growth? The data for this project resides in a 7800-record database maintained by Tec-Masters, Incorporated. The technology assistance data results from survey responses from companies and individuals who have interacted with NASA via a Technology Transfer Agreement, or TTA.

The data are typically reported in three ways: economic impact, the number of products developed, and the number of jobs created or saved due to expansion, increased sales, or increased capital investment. Economic impact (EI) is calculated by the following method:

$$\text{EI (\$)} = \text{EI Due to Jobs} + \text{EI Due to Investment} + \text{EI Due to New Sales} + \text{Savings} \quad (1)$$

The number of products is simply summed, and the formula for calculating the number of jobs created or saved may be summarized as:

$$\text{Jobs} = \text{Jobs Due to Investment} + \max(\text{Jobs Saved or Created, Jobs Created by Sales}) \quad (2)$$

Criticisms of this metrics methodology (NAPA, 1997; Barnett and Thompson, 1996) focus on the use of jobs as part of the economic measure and the reporting of job creation in general. They suggest that data and measures that show evidence of wealth creation or growth are better measures of economic impact. They do, however, state that the creation of employment opportunities is an indicator of an increase in real national income.

There are several ways that wealth creation or growth may be defined:
-An increase in the wages of those impacted by tech transfer. This approach is also known as technology infusion and may be viewed as an element of productivity.
-An increase in the value of goods and services by customers outside the region, better known as exports (Sibert).
-An increase in the basic factors of production. This is characterized by increased investment in worker training to increase labor input, build more plants and equipment and improve technology to increase capital input, or discover more natural resources (Barron and Lynch, 1993).
-An increase in productivity. The best method of measuring productivity is debatable. At a minimum, it does require reporting of cost savings and new investment.
-An increase in the production of goods and services through capital formation. Capital stock includes factories, machinery, farms, offices, etc. In a general sense, it also includes less tangible products like education and scientific knowledge (Jones, 1982).

Since the database does not contain the information needed to address these definitions, the overall goal of this project is to analyze the technical assistance data for evidence of economic growth. Specific objectives are to study trends in the top SIC codes, to analyze job growth and compare to Department of Commerce values, and to analyze the effect of technology transfer efforts on wages.

B. Methodology

NASA/MSFC's TTA efforts have interacted with most of the industries as identified by 1987 SIC codes; the majority of which are in the manufacturing and engineering service industries. In examining the trends in jobs by SIC codes, the first step is to determine the top SIC codes. The top SIC codes were identified by total supported jobs–the sum of jobs created and saved. Figure 1

show these trends for the state of Alabama; other states are may be found in the Appendix. Figure 1 also indicates the problem with studying trends in SIC codes by state: limited data. Alabama significantly benefits from technical assistance, and the other states in the SE Alliance do not have enough job data to show continuous trends (positive, negative or otherwise). Note: The numbers reported in the figure are not cumulative but are the supported jobs realized that year.

Figure 1.

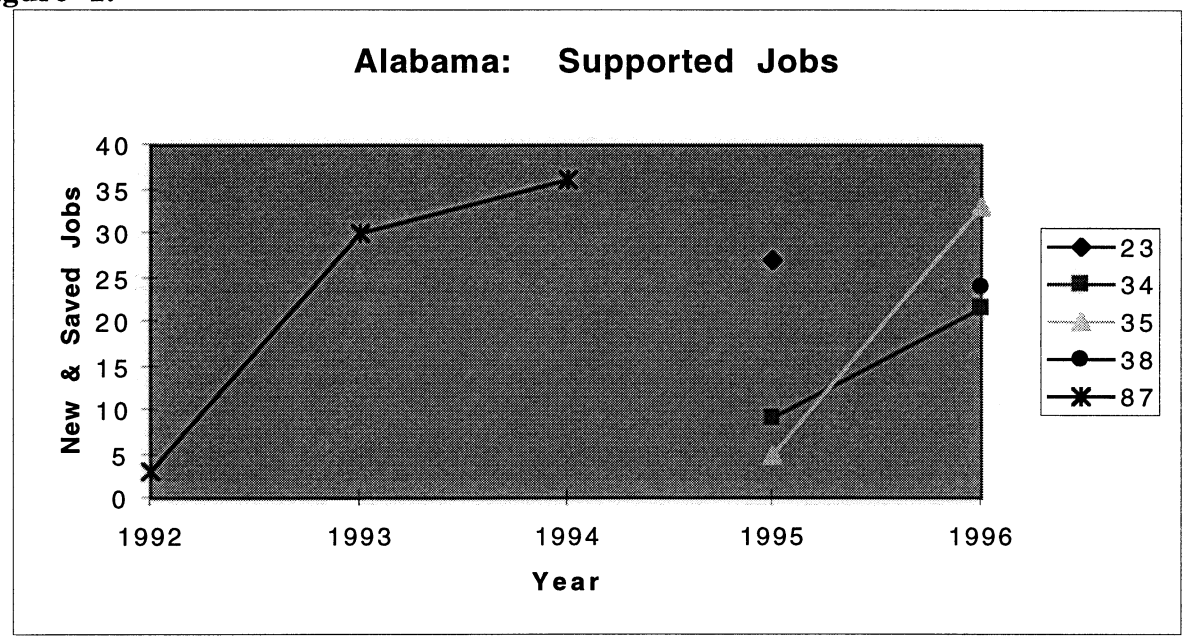

The top SIC codes, as identified by the number of supported jobs, for the SE region are shown in the first column of Table 1. As the table shows, while NASA has interacted with many industries, the majority of supported jobs are in the manufacturing industries. In attempting to determine the economic impact in these categories relative to Bureau of Economic Analysis values, a jobs-per-company approach was used. An example in support of this approach may be found in the apparel industry: the support of 361 jobs in this industry is a small perturbation when compared to the total employment in the SIC code: 393,000. However, comparing jobs/company in the key SIC codes supported by technical assistance to the equivalent national metrics may be of interest.

Table 1.

SIC Code	Description	Direct Primary Jobs	# of Companies	Jobs/Company
20	Food & Kindred Products	18.01	21	0.858
23	Apparel	361.06	123	2.935
25	Furniture & Fixtures	16.00	20	0.800
30	Rubber & Misc Plastics	14.31	71	0.202
34	Fabricated Metal Products	112.44	154	0.730
35	Machinery & Computer Equip.	79.21	143	0.554
36	Electrical Eqipment	13.62	66	0.206
37	Transporation Equipment	44.82	94	0.477
38	Instruments	34.86	83	0.420
51	Wholesale Trade	32.00	14	2.286
87	Engineering Services	24.59	133	0.185

To obtain these metrics, the number of unique establishments that NASA worked with needs to be calculated. This is not a simple task since NASA may work with a company on several TTAs. In addition, the SIC codes for the companies who did not respond to the survey need to be determined. The entire metrics database contains 7879 records; 2224 of which represent the closed, MSFC, SE states (P1-P6 MSFC data). Over a third of the records (837) did not have SIC codes. After many days, only 61 remained unidentified, and the last columns of Table 1 were complete. The number of companies (unique and total) for all SICs may also be found in the Appendix. In the table, Direct Primary Jobs differ from supported jobs. Direct Primary Jobs represent the max(jobs saved or created, jobs created by sales). Jobs created from sales represent de-RIM'd values.

For comparison purposes, overall economic values for wages and employment by industry were obtained from the REIS CD ROM and Stat-USA. The number of establishments by industry from the Census bureau.

C. Results

Figure 2 compares the direct primary jobs per company that result from technical assistance to the employment per company for all non-farm proprietors. In the figure, the job growth rate for non-farm proprietors is the bold black line (with the triangle symbol). 'Non-farm' includes both government and private industry for both the employment and the proprietor numbers. Overall, the figure shows that for the SE region, job growth rates, on a per company basis, are larger.

Figure 2. Comparison of Employment/Facility Growth Rate.

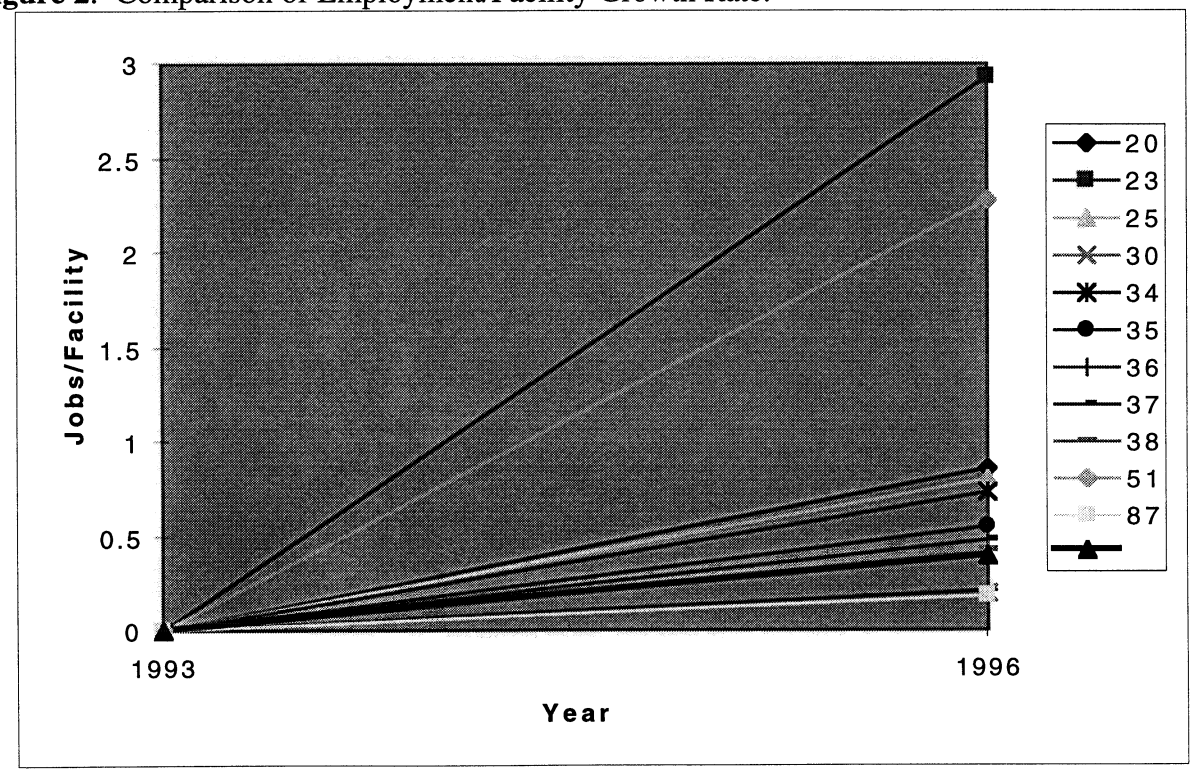

This means that in 1996, on average, a proprietor employed an additional .39 of a person than it did 4 years prior. This figure may be viewed as an upper bound, because it includes all industries as well as government employment. Ideally, the job growth resulting from technology transfer should be compared to job growth per 2-digit SIC code. In Figure 3, the comparison is shown for

the apparel industry (SIC 23). The data for the other industries studied may be found in the Appendix.

Figure 3. Job growth rate for the apparel industry.

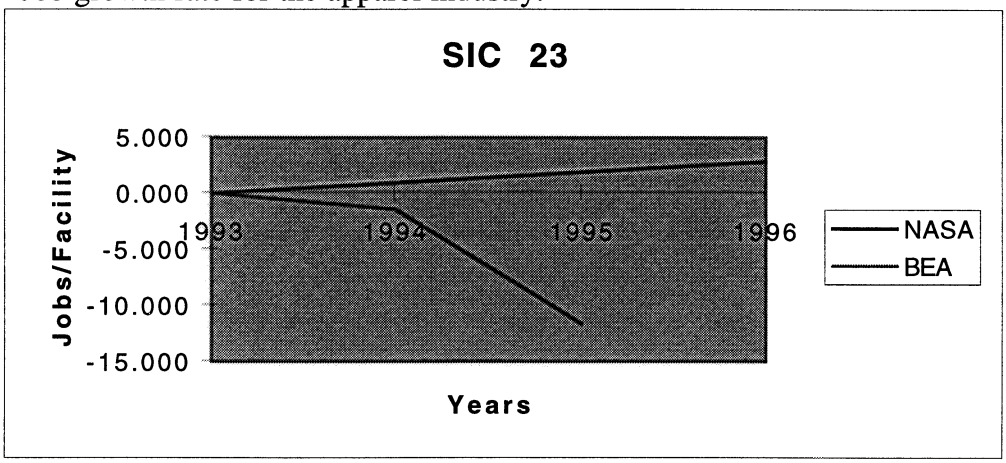

Figure 4 compares the per employee salary in the top NASA/MSFC SIC codes to that measure for private industry for the SE region. Except for apparel and furniture, the average salary is larger than that of private industry. In this figure, the bold comparison line differs from that of the previous figure in that it is private industry only and does not include government.

Figure 4. Comparison of Wages in Top SICs to Private Industry.

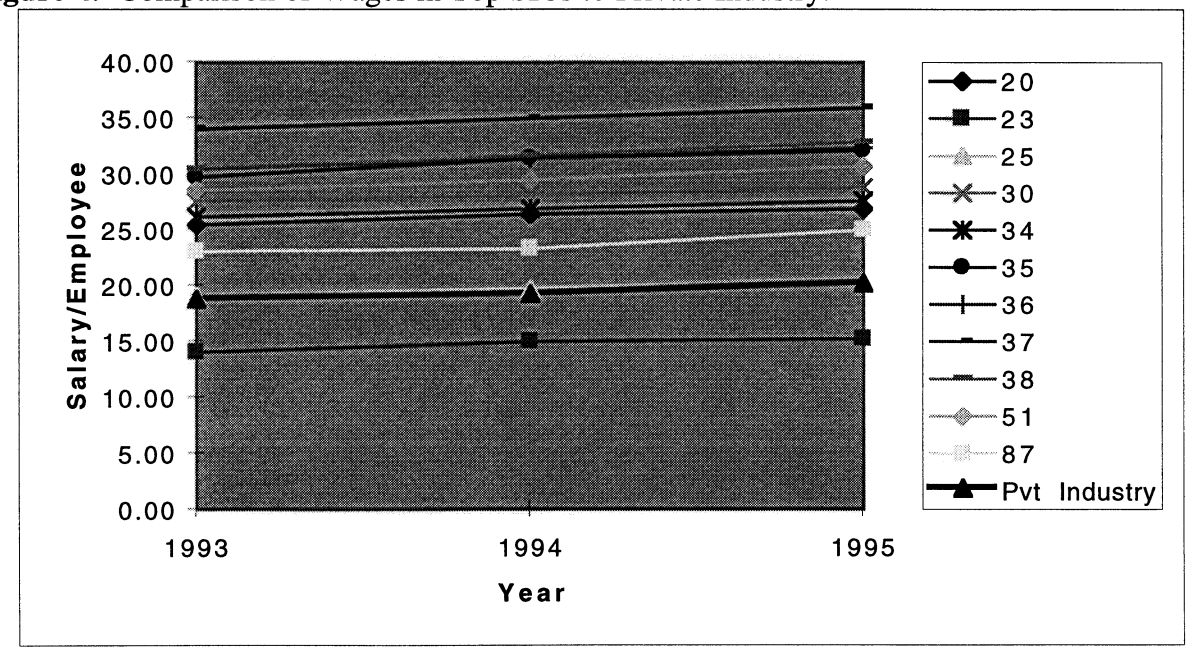

D. Conclusions

This goal of this project was to determine if the existing data could provide indications of increased wealth. This work demonstrates that there is evidence that companies that used NASA technology transfer have a higher job growth rate than the rest of the economy. It also shows that the jobs being supported are jobs in higher wage SIC does, and this indicates improvements in personal wealth. Finally, this work suggests that with correct data, the wealth issue may be addressed.

Future work in this area include expansion to other technology transfer interactions such as Space Act Agreements and expansion to regions beyond the SE Alliance. Other interesting work may involve the formulation of decision analysis models for determining candidate companies for licensing a technology by evaluating their capabilities.

E. References

Barnett, A. and H. Thompson. *Comments on Comments on Technology Transfer*. Unpublished paper, October 1996.

Barron, J.M. and G.J. Lynch (1993). *Economics*, 3rd Edition, Irwin, Boston, MA.

Harris State Manufacturers Directories. Harris InfoSource International, Twinsburg, OH.

Jones, B.W. (1982). *Inflation in Engineering Economic Analysis*, John Wiley & Sons.

NAPA (1997). *A Review of the Commercial Technology Division's Program.*

Regional Economic Information System (CD ROM), 1969-1994, Bureau of Economic Analysis, U.S. Department of Commerce.

Website: www.census.gov/datamap/www/index/html. U.S. Census Bureau. Select the 'State Profile' option and then 'County Business Patterns'.

Website: www.stat-usa.gov. Bureau of Economic Analysis, U.S. Department of Commerce.

1997

NASA/ASEE SUMMER FACULTY FELLOWSHIP PROGRAM

MARSHALL SPACE FLIGHT CENTER
THE UNIVERSITY OF ALABAMA AT HUNTSVILLE

NASA AMBASSADORS: A SPEAKER OUTREACH PROGRAM

Prepared By:	Malcolm W. McDonald, Ph.D.
Academic Rank:	Associate Professor
Institution and Department:	Berry College School of Math & Nat. Sciences Physics Department
NASA/MSFC:	
Office:	Public Affairs Office
Division:	Public Services
Branch:	Community Relations
MSFC Colleague:	Ed Medal

Introduction

The work done on this project this summer has been geared toward setting up the necessary infrastructure and planning to support the operation of an effective speaker outreach program. The program has been given the name, NASA AMBASSADORS. Also, individuals who become participants in the program will be known as "NASA AMBASSADORS". This summer project has been conducted by the joint efforts of this author and those of Professor George Lebo who will be issuing a separate report.

The description in this report will indicate that the NASA AMBASSADOR program operates largely on the contributions of volunteers, with the assistance of persons at the Marshall Space Flight Center (MSFC). The volunteers include participants in the various summer programs hosted by MSFC as well as members of the NASA Alumni League. The MSFC summer participation programs include: the Summer Faculty Fellowship Program for college and university professors, the Science Teacher Enrichment Program for middle- and high-school teachers, and the NASA ACADEMY program for college and university students. The NASA Alumni League members are retired NASA employees, scientists, and engineers.

The MSFC offices which will have roles in the operation of the NASA AMBASSADORS include the Educational Programs Office and the Public Affairs Office. It is possible that still other MSFC offices may become integrated into the operation of the program. The remainder of this report will establish the operational procedures which will be necessary to sustain the NASA AMBASSADOR speaker outreach program.

Program Operation

Participation as a NASA AMBASSADOR begins with the submission of an application to become a NASA AMBASSADOR candidate. It is planned that those who make application will come from the participants in the MSFC summer programs, though the possibility is open for current or former NASA employees to be included in the program. Application for candidacy to become a NASA AMBASSADOR involves signing an agreement which stipulates the commitment expected of both, the candidate and NASA.

The NASA AMBASSADOR candidate agrees to make at least two presentations per year to audiences external to the home institution for each presentation package requested. The candidate also agrees to provide essential feedback information to the office in charge at MSFC for each presentation made. The feedback is in the form of a reply card submitted by the candidate documenting simple pertinent statistics about the presentation and the audience and in the form of one-page evaluation forms filled in by members of the audience and returned by a member of the audience organization, presumably the program chair. If, at the end of one year, the performance and feedback support the decision the candidate becomes a NASA AMBASSADOR.

In the agreement signed by the NASA AMBASSADOR candidate NASA agrees to provide the pre-packaged presentation materials. NASA also agrees to keep the talks up to date by mailing to NASA AMBASSADORS update kits related to the topics for which they have been supplied presentation packages. NASA also agrees to provide contacts for the ambassadors with NASA technical experts knowledgeable of the presentation topics. NASA also will seek to recognize outstanding NASA AMBASSADOR performance with some type of commendation or award.

The operation of the program involves an annual cycle of five different task areas, with most of the tasks being undertaken during the summer months while the summer faculty and teachers are present at MSFC. The five task areas are: **preparation** of new presentations, **updating** of existing presentations, **recruitment** of NASA AMBASSADORS, **production** (duplicating of materials and assembling packages for distribution), and routine academic-year **operations** required to shepherd and maintain the program.

The **preparation** of new presentations will take place during the summers at MSFC. The NASA AMBASSADOR program will be promoted to the MSFC summer participants at the beginning of each summer. Volunteers will be enlisted to work with other volunteers throughout the summer to create informative and appealing talks for use in the program. The volunteers will review the talk contents for accuracy with NASA experts. They will also present the talks internally to the summer volunteer group in order to measure reaction. The textual and visual materials needed to create each talk will be collected by the end of the summer, and the presentation will be ready for the production phase.

The **updating** of the existing talks, as needed, will also occur during the summer months. In this cycle the feedback submitted from the NASA AMBASSADORS and their audiences will be analyzed to look for hints that any of the presentations might be improved or brought more up to date. The review process will also utilize the contributions of a local NASA technical expert in the area of the topic. The updating work will lead to the creation of update packets or kits which will be mailed to the NASA AMBASSADORS in possession of those topics. The update material will also be integrated into all copies of the presentation packages in inventory, awaiting distribution.

The **recruitment** of new NASA AMBASSADOR candidates will occur primarily during the summer. At the beginning of the summer, as the various MSFC participation programs get underway, visual promotion presentations will be made to the summer participants and materials describing the program will be distributed. The distributed materials will include forms for applying for candidacy in the NASA AMBASSADOR program. A final appeal will be made toward the end of the summer, and applications for candidacy will accepted and forwarded to the office in charge of the program.

The **production** phase will occur form the end of the summer into the early fall (approximately August to October). This phase will be conducted largely by the resources of the office in charge of the program, with some assistance available from the local branch of the NASA Alumni League. Production includes the reproducing of text and visual materials and the assembling of

the presentation packages with all the necessary enclosures (text, slide sets, welcoming letter explaining the candidacy program, and instructions for utilizing the package). The final step in the production process is to transport the ready-to-mail packages to the distribution center.

The general year-round **operations** of the program are concentrated during the non-summer months. This involves the "nuts-and-bolts" procedures which must be happening year round to enable the program to be maintained. The continuing procedures which must be happening during the operation phase would include the following:

1. The NASA AMBASSADOR schedules and delivers at least two talks per package per year.
2. The NASA AMBASSADOR returns the feedback form to MSFC for each presentation made.
3. The evaluation forms and feedback are received and logged by the MSFC office.
4. AN MSFC office maintains a database of information on each ambassador.
5. The evaluation forms are reviewed and analyzed on an annual basis and individualized feedback on the results are assembled and mailed to each ambassador.
6. The office in charge maintains a point of contact to field inquiries and requests from the ambassadors.
7. The office in charge issues mailing instructions for the distribution of packages.
8. The office in charge sends a letter to the president of the ambassador's home institution to acknowledge the selection and participation of the NASA AMBASSADOR.
9. The Public Affairs Office sends an annual press release to the home newspaper of the NASA AMBASSADOR.

Status of the planning

The summer of 1996 (last summer) served as a test bed for the summer activities described in the procedures above. Approximately a dozen volunteers from the summer programs met regularly (two times per week) throughout the summer. The results were the creation of four talks which were brought to fruition and the major work done on two other talks. Currently, the four completed talks have been reproduced and assembled into packages ready to be mailed or distributed. In addition, approximately forty summer participants from the summer of 1996 applied to be included in the NASA AMBASSADOR program. These facts make it clear that the program has a definite appeal to many of the summer faculty and teachers who are eager to have and to deliver the presentations.

The four ready-to-distribute talks are entitled:

"NASA: The Place Where Miracles Happen" (spin-offs of the space program),,
"Rocket Ships",
"Mars in Fact and Fiction", and
"Spacecraft Charging".

Two other presentation topics nearing completion are entitled:

"Extending Our Senses Beyond Our Reach" (Hubble and other space telescopes),
"To Lead, Or Not to Lead" (the wise investment in NASA programs).

Other topics under consideration for the creation of presentations include the areas of:
The International Space Station,
The Mission to Mars, and
The Quest for Origins of Life.

Conclusion

The NASA AMBASSADOR program is a speaker outreach effort whose time has arrived. It is able to capitalize on the considerable talents and enthusiasm for NASA programs displayed by many of the faculty and teachers who participate in the summer programs at the Marshall Space Flight Center. They have the ability and the willingness to take back to their home environments the NASA-related talks which the program is being geared to place in their hands. This outstanding outreach effort will be rendered by the NASA AMBASSADOR volunteers, at virtually no cost to NASA. They will offer to the public audiences the kind of information about NASA which a great majority of the public looks forward to hearing. Finally, the audiences to which the presentations will be made typically will include those members of the local community who are counted among the opinion makers in the community and who display an interest in all the happenings and decisions rendered at the local, state, and national levels.

1997

NASA/ASEE SUMMER FACULTY FELLOWSHIP PROGRAM

MARSHALL SPACE FLIGHT CENTER
THE UNIVERSITY OF ALABAMA IN HUNTSVILLE

PERFORMANCE OF A BOUNCE-AVERAGED GLOBAL MODEL OF SUPER-THERMAL ELECTRON TRANSPORT IN THE EARTH'S MAGNETIC FIELD

Prepared by:	Tim McGuire, Ph.D.
Academic Rank:	Assistant Professor
Institution and Department:	West Texas A&M University Department of Computer Information Systems
NASA/MSFC:	
Office:	Space Sciences Laboratory
Division:	Science Systems
MSFC Colleague:	Mike Liemohn, Ph.D.

Introduction

In this paper, we report the results of our recent research on the application of a multiprocessor Cray T916 supercomputer in modeling super-thermal electron transport in the earth's magnetic field. In general, this mathematical model requires numerical solution of a system of partial differential equations.

The code we use for this model is moderately vectorized. By using Amdahl's Law for vector processors (Fosdick, 1996), it can be verified that the code is about 60% vectorized on a Cray computer. Speedup factors on the order of 2.5 were obtained compared to the unvectorized code. In the following sections, we discuss the methodology of improving the code.

In addition to our goal of optimizing the code for solution on the Cray computer, we had the goal of *scalability* in mind. Scalability combines the concepts of *portabilty* with *near-linear speedup* (Sabot, 1995). Specifically, a scalable program is one whose performance is portable across many different architectures with differing numbers of processors for many different problem sizes. Though we have access to a Cray at this time, the goal was to also have code which would run well on a variety of architectures.

Additional Vectorization of the Code

The first step attempted was to examine the code carefully to see if the degree of vectorization could be increased. Typical consideration for improving vectorized codes include:

- Most vector-register architectures are designed to handle vectors of a given length; for instance, the vector registers of the Cray T90 series hold 128 elements of a vector. Using vectors of that approach that length is more efficient than using shorter vectors. In a nested loop, the inner loop is usually the one the compiler attempts to vectorize. Thus, if it is computationally equivalent to do so, the code should be arranged so that the longer vector operation occurs in the innermost loop.
- When dealing with multi-dimensioned arrays, the storage order can have an impact on the efficiency. Since FORTRAN stores arrays in column-major order, it is most efficient to access those arrays in that order. This allows us to process the array with a stride of one. It also reduces the memory and caching overhead, since the elements are being read and stored in a sequential manner.
- Compiler dependence analysis is of necessity conservative. Thus, the compiler might not detect all instances where an apparent dependence can be ignored. For example,

```
do i=2,n
   a(i-1) = a(i) + b(i)
end do
```

  can be vectorized and still generate the correct value. A more subtle instance is

```
do i=1,n
   a(i+1,j) = a(i,k) + b(i)
end do
```

which can be vectorized if is known that $j \neq k$. In most cases, however, the compiler is unable to make such an assumption and does not vectorize the loop. In these cases, most compilers have a "no dependence" directive that allows the code to be vectorized.

In practice, it was discovered that the Cray `f90` compiler performed quite well at exploiting the vectorization and as a result, the amount of performance increase on this code by hand vectorizing was not large ($\approx$ 5%.) When possible, loops containing recurrences (which are inherently scalar) were split so the portions which could be vectorized were separate.

Parallelization of the Code

Cray FORTRAN90 supports various levels of parallel processing through *autotasking*. In addition, it is possible to use *macrotasking*, since Cray provides a library of synchronization routines. This approach requires a major restructuring of the code to take advantage of parallelization. It has value when there is a large granularity to the code, but has considerable overhead cost. Because the resulting code is not portable, this approach was not used.

Autotasking directs the compiler to exploit parallelism in the code, typically by distributing loop iterations to multiple processors. The user may, if desired, insert directives in the form of comment lines (leading to transportable code) in some or all of the routines to enhance parallelization in the regions of the code where the preprocessor cannot determine, that parallelization is safe.

Utilizing the fully automatic method of parallelization only yielded a minimal improvement in the performance of the code ($\approx$ 5%.) This led us to pursue the insertion of directives into the code in an attempt to increase both the granularity and the average degree of multiprocessing.

Computational Results

The supercomputer used in this study was a Cray T916, a shared memory multiprocessor vector machine with up to 16 processors and a vector length of 128 64-bit words. The particular machine used was a 4-processor model with 256 megawords of main memory. Each processor has a peak performance of approximately 1.8 billion floating point operations per second (1.8 Gflops.) The operation system utilized was UNICOS 9.0.2.4 and the FORTRAN compiler `f90` version 3.0.0.

The problem considered for this study was a collisional three-dimensional interhemispheric flux tube model for photoelectrons (PE) (Khazanov *et al*, 1996). Using this model, initial calculations of the high energy PE distribution as a function of time, energy, pitch angle, and spatial location in the equatorial plane and along the field lines, are reported for different conditions of geomagnetic activity. To explore both the dynamic and steady behaviors of the model, the simulation starts with the abrupt onset of PE excitation, and is followed to steady state conditions. The results illustrate several features of the interaction of PE with typical magnetospheric plasmas and fields, including collisional diffusion of PE in pitch angle with flux tube filling, diurnal intensity and pitch angle asymmetries introduced by directional sunlight, and energization of the PE distribution in the evening sector.

This code had previously been run on an HP 9000 workstation with a run time greater than one month. The first port to the Cray ran longer than one week. Exact runtime data is not available, but it is obvious that improving the code is desirable.

For the sake of this project, we chose to use the original input data with a shorter runtime (i.e., 40 time units rather than 172800) so that many more runs could be done. On a non-optimized code, this lead to total wallclock time of 89.6 seconds. Utilizing the compiler's scalar optimization, we achieved a wallclock time of 35.7 seconds. Using the default level of optimization (which includes moderate scalar, vector, and tasking optimization) for the `f90` compiler led to a wallclock time of 17.5 seconds. Using aggressive scalar and vector optimization gave a wallclock time of 15.4 seconds. The addition of aggressive autotasking led to 14.7 seconds of wallclock time.

At this point is was determined that hand optimization would be necessary to achieve substantial performance gains. Hand vectorization of the code was attempted first. This was mainly done by splitting recurrences out of loops in which other operations could be vectorized. This gave a runtime of 14.1 seconds.

We concluded the work with an examination of how we may be able to help the compiler with directives. Aggressive autotasking found 20 loops in the code which could be parallelized. Because several loops contained subroutine calls, these were not parallelized by the compiler. Careful examination of the code revealed that no side effects resulted from many subroutine calls, so a compiler directive was inserted to allow those loops to be parallelized. In addition, it was discovered that on one occasion the autotasking preprocessor was unable to determine that an outer loop was safe to parallelize, and hence it parallelized the inner loops. We were able to reduce the overhead and increase the granularity by inserting compiler directives. By doing this we were able to double the amount of loop parallelized and reduce the wallclock time to 5.3 seconds.

It should be noted that each case was run three times and the median of the wallclock times were taken. This is help eliminate the machine load factor since we did not have a dedicated machine.

Concluding Remarks

The above results are summarized in the following table:

Non-vectorized code	89.6 seconds
Non-vectorized code, scalar optimization	35.7 seconds
Normal code (moderate scalar and vector optimization)	17.5 seconds
Aggressive vectorization	15.4 seconds
Aggressive vectorization and autotasking	14.7 seconds
Manual vectorization and autotasking	14.1 seconds
Manual tasking	5.3 seconds

We have shown that the Cray T916 can achieve substantial performance improvement in a "real-world" problem. The ability of the compiler to exploit vectorization is impressive. Code that is not designed specifically with parallelization in mind may be restructured to take advantage of parallel processing. Parallelization by hand is necessary in these cases.

The speed-up factor of 2.8 on a four-processor machine is reasonable for a problem of which is not inherently parallel. It is reasonable to expect that correspondingly faster performance would arise using additional processors, up to the number of grid points.

References

L. D. Fosdick, E. R. Jessup, C. J. C. Schauble, and G. Domik (1996), *An Introduction to High-Performance Scientific Computing*, Cambridge, MA: MIT Press.

G. V. Khazanov, T. E. Moore, M. W. Liemohn, V. K. Jordanova, M. C. Fok (1996), "Global, collisional model of high-energy photoelectrons," *Geophysical Research Letters* 23:331-334.

G. W. Sabot (1995), *High Performance Computing: Problem Solving with Parallel and Vector Architectures*, Reading, MA: Addison-Wesley.

1997

NASA/ASEE SUMMER FACULTY FELLOWSHIP PROGRAM

MARSHALL SPACE FLIGHT CENTER
THE UNIVERSITY OF ALABAMA IN HUNTSVILLE

A GEANT STUDY OF THE SCINTILLATING OPTICAL FIBER (SOFCAL) COSMIC RAY DETECTOR

Prepared By:	Ray B. Munroe, Jr., Ph.D.
Academic Rank:	Assistant Professor
Institution and Department:	University of Mobile Department of Natural Sciences
NASA/MSFC:	
Office:	Space Sciences Laboratory
Division:	Physics and Astronomy
MSFC Colleagues:	Thomas A. Parnell, Ph.D. John W. Watts, Ph.D.

Introduction

Recent energy measurements by balloon-borne passive emulsion chambers (3) indicate that the flux ratios of protons to helium nuclei and of protons to all heavy nuclei decrease as the primary cosmic ray energy per nucleon increases above ~ 200 GeV/n, and suggest a "break" in the proton spectrum between 200 GeV and 5 TeV (1,2,8). However, these passive emulsion chambers are limited to a lower energy threshold of ~ 5 TeV/n, and cannot fully explore this energy regime. Because cosmic ray flux and composition details may be significant to acceleration models (7), a hybrid detector system called the Scintillating Optical Fiber Calorimeter (SOFCAL) has been designed and flown. SOFCAL incorporates both conventional passive emulsion chambers and an active calorimeter utilizing scintillating plastic fibers (6) as detectors. These complementary types of detectors allow the balloon-borne SOFCAL experiment to measure the proton and helium spectra from ~ 400 GeV/n to ~ 20 TeV.

The fundamental purpose of this study is to use the GEANT simulation package to model the hadronic and electromagnetic shower evolution of cosmic rays incident on the SOFCAL detector. This allows the interpretation of SOFCAL data in terms of charges and primary energies of cosmic rays, thus allowing the determinations of cosmic ray flux and composition as functions of primary energy.

Detector Description

SOFCAL consists of four functional detector modules and the electronics required to operate the instrument, and to telemeter and record the data (5).

The upper detector module is a Cerenkov radiator in a diffusion box viewed by six photomultiplier tubes. The radiator is virgin Teflon™ with a refractive index of 1.36 and dimensions of 60 cm X 50 cm X 1.27 cm. The main purpose of this detector component is to resolve the primary cosmic ray as a proton, helium, or Carbon-Nitrogen-Oxygen (CNO) nucleus for lower energy (below ~ 5 TeV/n) events.

The second detector module is the upper emulsion chamber with an area of 50 cm X 40 cm, which consists of two major sub-components: a target section, and a passive emulsion calorimeter. The target section consists mostly of double coated (proton and helium sensitive) emulsion plates, 0.51 mm thick lead sheets, acrylic plates, and dividing layers of paper. Two sheets of plastic nuclear track detectors (CR-39) are used for identifying the charge of higher energy (above ~ 5 TeV/n) or heavy ($Z \geq 6$) primary particles. The target section has 0.11 interaction lengths for vertical protons and 0.9 radiation lengths. The emulsion calorimeter section is composed of five 1.1 mm and ten 1.95 mm thick lead plates separated by double-coated emulsion plates, x-ray films, and sheets of paper. This emulsion section has 0.13 interaction lengths for vertical protons and 4.3 radiation lengths. The x-ray film sets a threshold of ~ 1 TeV on the energy (ΣE_γ) of a detected cascade, thus fixing a lower scale on the observed primary cosmic ray energy of ~ 5 TeV/n. The emulsion plates do not have this limitation, but locating the numerous small cascades randomly distributed throughout the emulsion chamber would require a tremendous amount of microscope scanning without the scintillating fiber hodoscope.

The next detector module is the scintillating optical fiber calorimeter containing a stack of ten 4.0 mm thick lead plates separated by two orthogonal layers of 0.5 mm square scintillating optical fibers. These are BICRON polystyrene base fibers (BC-12) with acrylic cladding and coated with an extramural absorber to reduce signal cross talk between fibers. Two layers of 1.0 mm square scintillating optical fibers near the top and middle of the module serve as triggers and discriminators. Data processing is accomplished by coupling the fiber bundles to two dual-stage image intensifying 8-bit CCD camera systems. This detector module has an area of 50 cm X 50 cm, and has 0.39 interaction lengths for vertical photons and 7.1 radiation lengths.

The final detector module is a thin passive emulsion calorimeter consisting of five 1.95 mm thick lead plates separated by double-coated emulsion plates, x-ray films, and sheets of paper. This detector module has an area of 50 cm X 40 cm, and is 2.0 radiation lengths thick.

Simulation Packages

Aside from thorough experimental testing with beams of known composition and momenta (which could take years!), the best way to determine the propagation of cosmic rays through a complex detector geometry such as SOFCAL (SOFCAL contains over 21,000 detector elements) is via computer-generated simulations. Past SOFCAL simulations have employed a combination of electromagnetic simulators: EGS3 by the Stanford Linear Accelerator Center (SLAC), and SIBATA by the Japanese-American Cooperative Emulsion Experiment (JACEE); and a hadronic simulator, MCM2, also by JACEE. However, this study will utilize the GEANT simulation package, compare with previous studies, and attempt to extend the details of SOFCAL detector simulations.

The GEANT *Detector Description and Simulation Tool* (4) was written by and is maintained by CERN, the European Organization for Nuclear Research. GEANT is designed to be able to simulate all of the dominant hadronic, electromagnetic, and muonic processes in the energy range from 10 keV to 10 TeV. GEANT simulates the following hadronic interactions: decay in flight, multiple scattering, ionization and δ-ray production, hadronic interactions, and Cerenkov radiation. Simulated photonic interactions include: electron-positron pair production, Compton scattering, the photoelectric effect, photo-fission, and Rayleigh scattering. Simulated processes involving electrons and positrons include: multiple scattering, ionization and δ-ray production, bremstrahlung, positron annihilation, Cerenkov radiation, and synchrotron radiation. And simulated muonic interactions include: decay in flight, multiple scattering, ionization and δ-ray production, ionization by heavy ions, bremstrahlung, electron-positron pair production, nuclear interactions, and Cerenkov radiation.

The GEANT detector description package allows a thorough definition of detector materials, tracking parameters, geometries, and cuts. GEANT subroutines permit the definition of any type of cosmic ray, its initial momenta, and decay modes. And the GEANT graphics package allows the visualization of detector components and geometrical dimensions, particle trajectories, and hits recorded in the sensitive elements of the detector. An interactive version called GEANT++ is also available.

Results

For this initial stage of the study, the entire SOFCAL geometry was programmed and linked with the GEANT++ interactive simulation package. Figure 1 is a simulated example of a 400 GeV proton normally incident at the top of the upper emulsion chamber. For clarity, only a 8 cm X 8 cm area of the detector is shown, and the Cerenkov detector module and "filler" materials such as styrofoam, plywood and air are omitted. The solid (red) lines are charged particles and virtually all of the dashed (blue) lines are photons. The shower consists of many photons and charged particles (only distinguishable in the color version). The left frame view is parallel to the x-axis, the right frame view is parallel to the y-axis, and the top of the detector is "up" in both views. Note that some of the square cross-sections of the scintillating fibers are discernible at this scale.

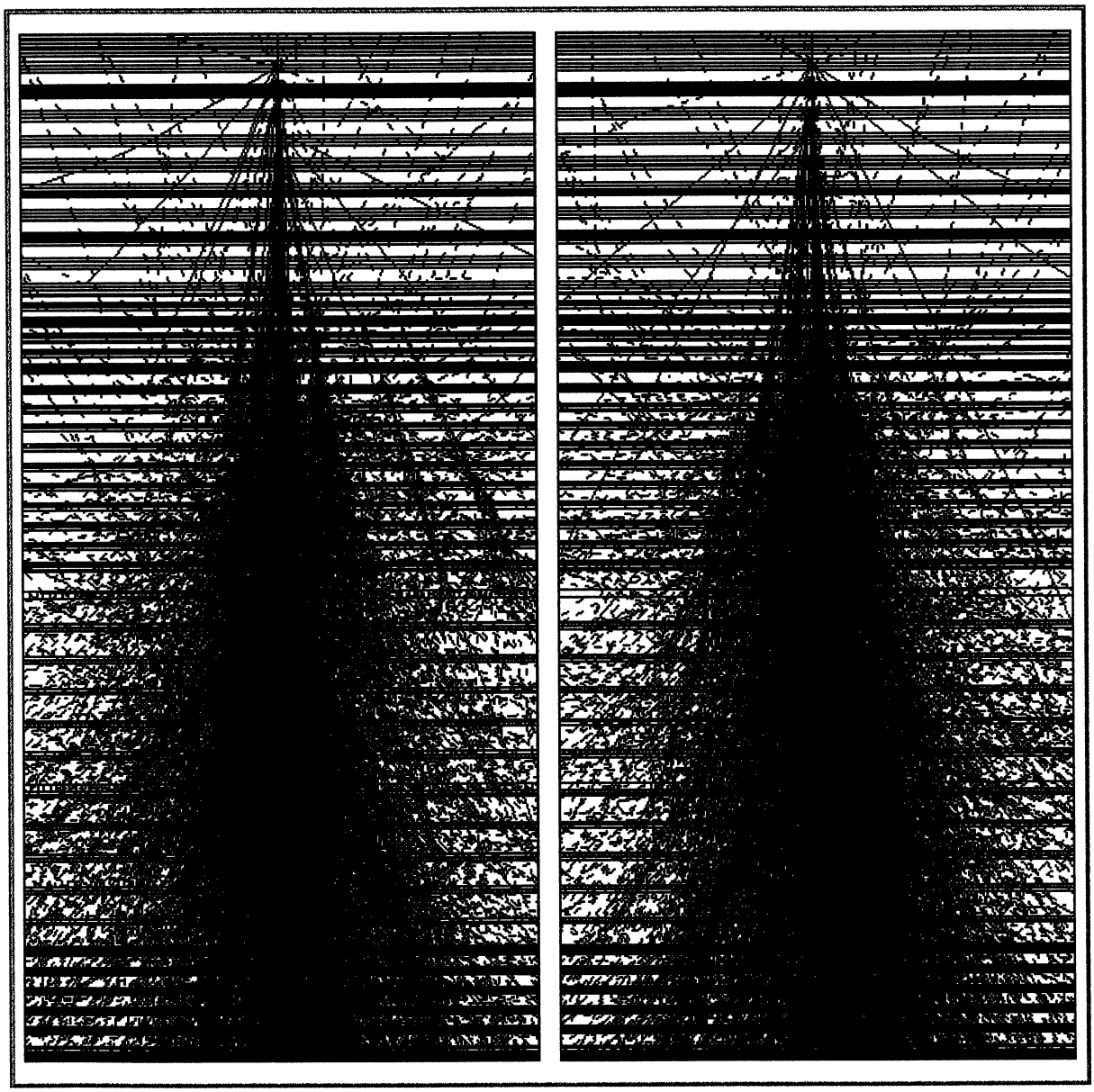

Figure 1 - A GEANT simulation of a 400 GeV proton incident on the SOFCAL detector.

Conclusions

GEANT is a convenient and comprehensive simulation package that can be applied to the study of lower energy cosmic ray detectors. The initial stage of this study highlights only one of GEANT's many capabilities and more detailed simulations of the SOFCAL detector are anticipated.

Proposals are ongoing for the design of and research on the Advanced Cosmic-ray Composition Experiment on the Space Station (ACCESS). Because standard emulsion chamber experiments are not designed for long exposures, at least one of the proposals for ACCESS will utilize a scintillating optical fiber calorimeter. So a modified version of SOFCAL may have a bright future!

Acknowledgments

The author would like to thank Dr. Thomas A. Parnell, Dr. John W. Watts, and Mark J. Christl of the Space Sciences Laboratory, Marshall Space Flight Center for many helpful conversations; and Dr. Gerald R. Karr and the staff and administration at the University of Alabama in Huntsville, Department of Mechanical and Aerospace Engineering for their part in organizing the 1997 NASA/ASEE Summer Faculty Fellowship Program. This work was performed at the Space Sciences Laboratory, Marshall Space Flight Center under NASA contract number NGT8-52836.

References

1. Asakimori, K. et al., 22nd International Cosmic Ray Conference Papers (Dublin), 2, 97-99 and 57-60 (1992).
2. Asakimori, K. et al., 23rd International Cosmic Ray Conference Papers (Calgary), 2, 21-24 and 25-29 (1993).
3. Burnett, T.H. et al., NIM, A251, 583-595 (1986).
4. CERN, GEANT - Detector Description and Simulation Tool (Geneva) (1993).
5. Christl, M.J., Fountain, W.F., Parnell, T.A., Roberts, F.E., Benson, C., Berry, F.A., Gregory, J.G., and Takahashi, Y., SPIE - The International Society for Optical Engineering Proceedings (Denver), 2806, 155-163 (1996).
6. Connell, J.J., Binns, W.R. et al., NIM, A294, 325-350 (1990).
7. Ellison, D.C. et al., Publication of the Astronomical Society of the Pacific, 106, 780-797 (1994).
8. Muller, D. et al., Ap. J., 374, 356 (1991).

1997

NASA/ASEE SUMMER FACULTY FELLOWSHIP PROGRAM

MARSHALL SPACE FLIGHT CENTER
THE UNIVERSITY OF ALABAMA IN HUNTSVILLE

CURRENT AND FUTURE CRITICAL ISSUES IN ROCKET PROPULSION SYSTEMS

Prepared by:	Homayun K. Navaz	Jeff C. Dix
Academic Rank:	Assistant Professor	Student
Institution and Department:	GMI Engineering & Management Institute Department of Mechanical Engineering	

NASA/MSFC:

Office:	Combustion Physics Laboratory
Division:	Engine Systems
MSFC Colleagues:	Klaus W. Gross

INTRODUCTION

The objective of this research was to tackle several problems that are currently of great importance to NASA. In a liquid rocket engine several complex processes take place that are not thoroughly understood. Droplet evaporation, turbulence, finite rate chemistry, instability, and injection/atomization phenomena are some of the critical issues being encountered in a liquid rocket engine environment. Pulse Detonation Engines (PDE) performance, combustion chamber instability analysis, 60K motor flowfield pattern from hydrocarbon fuel combustion, and 3D flowfield analysis for the Combined Cycle engine were of special interest to NASA. During the summer of 1997, we made an attempt to generate computational results for all of the above problems and shed some light on understanding some of the complex physical phenomena. For this purpose, the Liquid Thrust Chamber Performance (LTCP) code (Navaz, et al. 1994), mainly designed for liquid rocket engine applications, was utilized. The following test cases were considered:

1. Characterization of a detonation wave in a Pulse Detonation Tube.
2. 60K Motor wall temperature studies.
3. Propagation of a pressure pulse in a combustion chamber (under single and two-phase flow conditions)
4. Transonic region flowfield analysis affected by viscous effects
5. Exploring the viscous differences between a smooth and a corrugated wall
6. 3D thrust chamber flowfield analysis of the Combined Cycle engine.

CFD ANALYSIS

1. Pulse Detonation Tube

Over the last few years, the pulse detonation engines (PDE) have received a considerable amount of attention, due to their high specific impulse and reduced specific fuel consumption (SFC). These engines can potentially offer high performance due to the rapid detonation process. In this test case, a 2-inch diameter, 6-feet long tube is filled with premixed hydrogen and oxygen at stoichiometric mixture ratio initially at atmospheric pressure, closed at the left and subject to atmospheric back pressure from the right. Slip wall conditions are assumed on the tube wall to simulate a one dimensional flow. The analytical solution of this test case showed a good agreement with the experimental data (Navaz, et al, 1997).

Figure (1a) shows the variation of pressure along the centerline in time. The pressure distribution within the detonation tube has a characteristic form. The reaction process is initiated on the left wall by raising the temperature to 5400 °R for one iteration, i.e., a temperature impulse is imposed momentarily. The resulting detonation wave travels toward the open end while a low pressure wake is formed behind the peak pressure that does not move at the same speed. As a result, the region being at the peak pressure expands in size, therefore, prolonging the time that power can be extracted from the detonation pressure. The blow-down process starts when the detonation front reaches the

open end where a backward traveling wave is also initiated. This wave combines with the still incoming pressure wave and forms a rather complex wave form traveling in both directions. A few milliseconds after the blow-down the pressure decreases and asymptotically reaches the atmospheric pressure.

The pressure history on the closed end wall is shown in Figure (1b). The pressure during the detonation and part of the blow down processes on the closed end wall remains constant. However, when the backward traveling wave initiated at the open end reaches the closed end, the pressure decreases. The pressure at the closed end drops to less than one atmosphere, thereafter, and a pressure oscillation in the tube develops which will eventually decay due to viscous effects.

Several test cases were run varying the oxidizer/fuel (O/F) ratio and the temperature impulse for ignition. By changing the O/F ratio, the value of the peak pressure changed, however, the basic characteristics of the detonation wave remained unchanged. An animation video tape has been generated for this test case and our NASA colleague Mr. Klaus W. Gross can be contacted to provide further information. Figures (2) demonstrate the pressure contours in the tube and the pressure along the centerline at several time intervals during the calculations.

2. 60K FASTRAC Motor Wall Temperature Studies

NASA/MSFC is performing some tests to support the design of the 60K motor. This engine uses liquid RP-1 as fuel and liquid oxygen (LOX) as oxidizer. RP-1 is mostly composed of $C_{12}H_{26}$ which is a rather heavy hydrocarbon. The oxidization process for RP-1 is very complex and can easily involve more than 100 species and 1000 reactions and the formation of soot. Reactions producing soot are numerically stiff and may cause numerical instability. The LTCP code is very robust in treating problems with stiff chemistry. Four different cases were considered for this analysis:

a. 60K motor with RP-1/LOX reaction products being at equilibrium conditions with a mixture ratio of 2.34 and temperature of 6391 °R, uniformly distributed at the injector face. This analysis was performed with 8 species finite rate reactions and an adiabatic wall to calculate the maximum possible temperature on the wall. This test case is referred to as the **One-Zone** 60K motor test case.

b. 60K motor with RP-1/LOX reaction products being at equilibrium conditions at two different mixture ratios; 2.64 for the core flow with a temperature of 6520 °R, and 1.12 for the near wall region at 12.6% of the total mass flow rate with a temperature of 2983 °R. The analysis was performed with 8 species finite rate reactions and adiabatic wall conditions. This test case is referred to as the **Two-Zone** 60K motor test case.

c. 60K motor with RP-1/LOX reaction products being at equilibrium conditions with a mixture ratio of 2.64 uniformly distributed at the injector face except the near wall

region where pure RP-1 is injected in the gaseous phase at 6.67 lbm/s. This test case was performed with 22 species and a mechanism for soot formation. The geometry was similar to the one used in the TDK program, i.e., shorter chamber with two cylindrical arcs connected at throat region with no straight section in between as is the case in the real geometry. This test case is referred to as **TDK-Like Geometry**.

d. This test case is similar to the part (c) except that the real geometry of the 60K motor is ported into the LTCP code. This geometry contains a straight cylindrical section connecting the two arcs at the throat region and slightly elongated combustion chamber. This test case is referred to as **Real Geometry**.

The temperature contours and wall temperature for all of the 60K motor test case are shown in Figures (3). The two-zone test case with 12.6% mass flow rate near the wall region shows the lowest temperature achieved along the wall. Figures (4a) and (4b) show the soot mass fraction contours for test cases (c) and (d). It can be seen that slightly less soot is formed in test case (d). This can be attributed to the fact that some of the soot being formed may have enough time in the chamber to react with residues of oxygen to form carbon oxides.

3. Propagation of a Pressure Pulse in a Combustion Chamber

This test case was selected to study a pressure wave propagation in a combustion chamber. In practice, an artificial explosion is initiated in a combustion chamber, and the pressure wave propagation is monitored. This particular study is oriented toward future instability analysis to mark the threshold of an engine mechanical break down. The following test cases were selected for gaseous and two phase flows:

a. The subsonic and transonic portion of a combustion chamber is operating at steady state in gaseous phase for LOX/RP-1. The total pressure of the chamber is 630 psia. At this time a pressure pulse of 12000 psia at the injector face centerline is introduced for one iteration to simulate an explosion. The pressure wave starts to propagate and reflect. Figures (5) shows a series of snap shots from the pressure contours, pressure across the injector face, at the throat, along the centerline, and along the wall. After the explosion, the high pressure wave front generates a wake behind it that will invoke in a secondary wave originating from the location of explosion. This wave follows the first one and collides with the reflected one from the wall. In this case the pressure wave interacts with the finite rate chemistry calculations. It can be seen that the pressure and subsequently the mass flow rate will change significantly as the pressure disturbance passes through the throat.

b. The subsonic and transonic portion of a combustion chamber is running at steady state in two phase flow mode. H_2/O_2 in gaseous form at mixture ratio of 2 is mixed with 60 μm-diameter oxygen droplets. The droplet number density is assumed to be 10^7droplets/cc. This mixture is uniformly injected to the combustion chamber and burned. At this point, a 12000 psia pressure pulse is momentarily introduced at the

centerline. Figures (6) show the pressure pulse development contours and pressure distribution at the injector face, throat, along the centerline, and along the wall. We have considered hydrogen instead of RP-1 for this test case to simplify the chemistry and also reduce the computer run time . However, we can still observe that the pattern of the pressure wave is quite different from the gaseous flow in part (a) above. The existence of droplets has a damping effect on the pressure wave and reduces the strength of this wave considerably. Figures (7) show the oxygen mass fraction during this disturbance and comparing with the undisturbed state, it can be seen that the evaporation rate of the oxygen droplets will change as they come into contact with the pressure wave front. In this case the atomization process is not affected but the evaporation of the droplets and the finite rate chemistry are coupled with the pressure wave propagation.

An animation video tape of this test case can be requested from our NASA/MSFC colleague Mr. Klaus W. Gross.

4. Transonic Region Flowfield Analysis for the Extent of Viscous Effects

The purpose of this test case was to specify the validity of inviscid or Euler solvers in the throat region of a nozzle. Series of runs were made for small throat radii and varying chamber pressures. It was found that for low chamber pressures the viscous layer becomes thicker in the throat region. If the throat radius is of the same order of magnitude as the viscous layer thickness, any solution with an inviscid code will not be valid. Therefore, a CFD analysis must be performed for small throat engines to observe the extent of the viscous layer, before any Euler equation solution is acceptable.

5. Smooth Versus Corrugated Nozzle Wall

It has been speculated that for nozzle walls with corrugation in flow direction the trapped fluid in the gaps of the wall may act like a buffer between the core flow and the wall surface, thus, reducing the viscous effects and losses associated with such a phenomenon. The LTCP-3D code was employed to conduct this study. A typical corrugated wall is shown in Figure (8a). To simplify the geometry for our study, the geometry was assumed to have two planes of symmetry, one on the top of the circular arc and a second one between the two arcs. Figure (8b) shows the geometry for our computational studies. Four test cases were considered by varying the curvature of the arc from quarter of a circle to a flat plate as shown in Figure (8b).

6. 3D Flowfield Analysis of the Rocket Thrust Chamber in a Combined Cycle (CC) Engine

For this test case LTCP-3D with finite rate chemistry was used to evaluate the performance of the thrust chamber. The combustion chamber of this engine is axisymmetric but the nozzle requires a 3D analysis. The 3D effect in the nozzle is fairly significant such that a coarse grid in circumferencial direction will produce numerical

instability. The analysis was performed on a 65x23x71 grid. This number of grid points is not sufficient enough to resolve the boundary layer, but it is adequate for a first order estimate. Furthermore, our goal was to demonstrate the capability of the LTCP-3D in solving complex 3D flowfield equations with near equilibrium (stiff) finite rate chemistry. Figures (9a) through (9c) exhibit the Mach number contours. A fairly coarse grid in the radial direction was used for this case which made the subsonic viscous layer rather thick causing the information to travel backward from the nozzle to the combustion chamber. Therefore, for a coarse grid some 3D effects in the combustion chamber can be expected. Figures (9d) through (9f) shows the water, H_2, and O_2 mass fractions, respectively. A computer run is being made with a finer mesh to evaluate the specific impulse of the thrust chamber for this engine.

CONCLUSION

During the ten week time period of the Summer Faculty Fellowship Program (SFFP) a variety of important topics were addressed. Some of them were completed, others were started and brought to a state to effectively continue further analysis. It was shown that the LTCP-2D and LTCP-3D codes are capable of solving complex and stiff conservation equations for gaseous and droplet phases in a very robust and efficient manner. These codes can be run on a workstation and personal computers (PC's). Further studies in the area of pulse detonation are necessary to understand the effects of the mixture ratio on the detonation wave characteristics. Furthermore, the conditions at which a Chapman-Jouget detonation wave is initiated should be marked. In combustion chamber instability analysis, the effects of a pressure pulse on the atomization process should be studied. The shear stress analysis for the corrugated walls should be further followed, and last but not least, a 3D analysis for the combustion chamber of the combined cycle engine on a fine mesh is necessary to properly estimate the performance characteristics of this engine.

ACKNOWLEDEMENT

The authors wish to thank NASA/MSFC for their support of the Summer Faculty Fellowship Program (SFFP) and University of Alabama in Huntsville for coordinating the program. The research performed during the summer of 1997, will provide NASA with some guidelines in the design process and is mutually beneficial to us. It is intended to incorporate the above topics in a new Modern Compressible Flow course that is going to be offered at GMI Engineering & Management Institute during the Spring 1998 term.

REFERENCES

Navaz, H. K., and A. D. Dang, Engineering and Numerical Analysis/Users' Guide to the Liquid Thrust Chamber Performance (LTCP) Program, Prepared for NASA/MSFC, Contract No. NAS8-38798, January 1994.

Navaz, H. K. and R. M. Berg, "A Solution to Multi-Phase Flow Equations with Chemistry and Stiff Source Terms for Liquid Rocket Engines," Submitted *to J. of Propulsion and Power*, Aug., 1997.

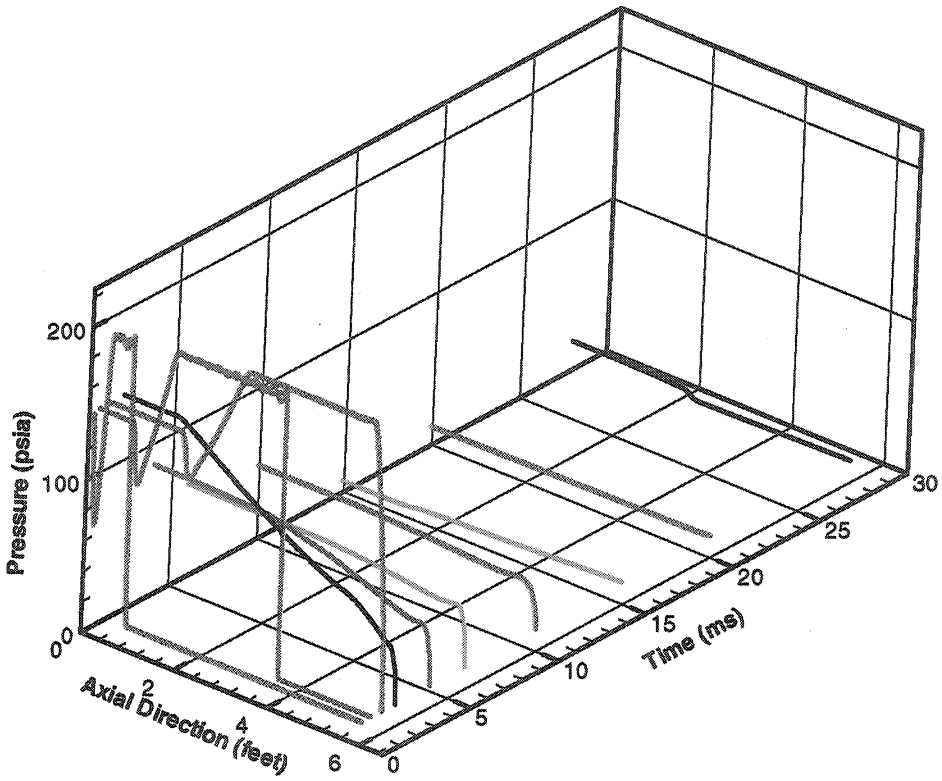

Figure 1a: Pressure history along the tube centerline as a function of time.

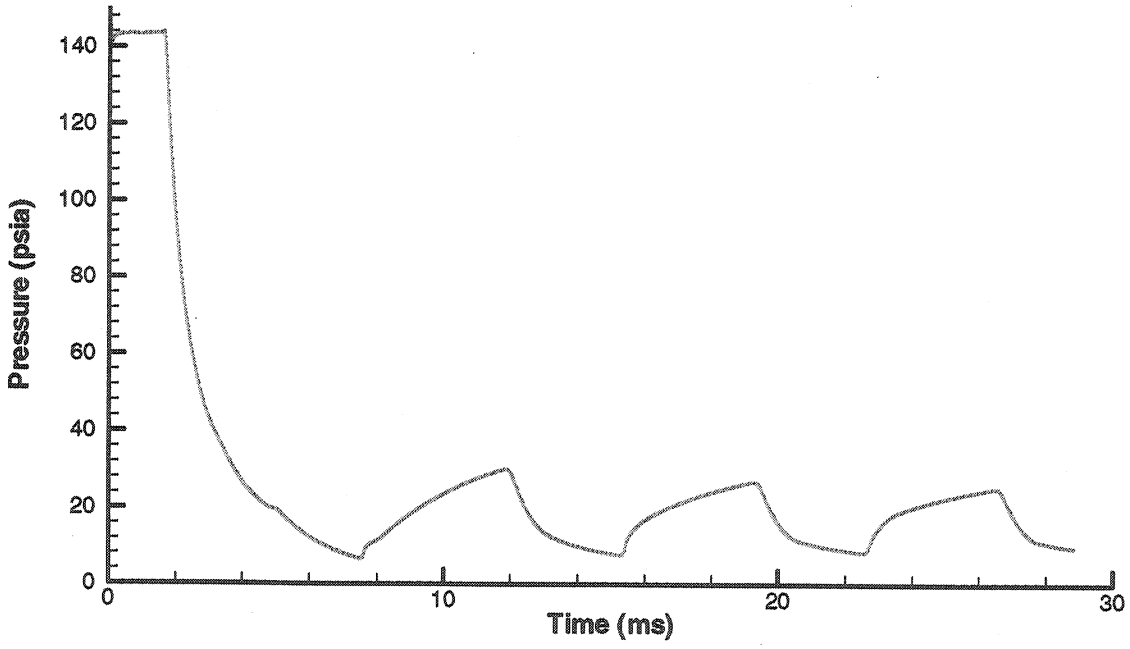

Figure 1b: Pressure history at the closed end of the tube.

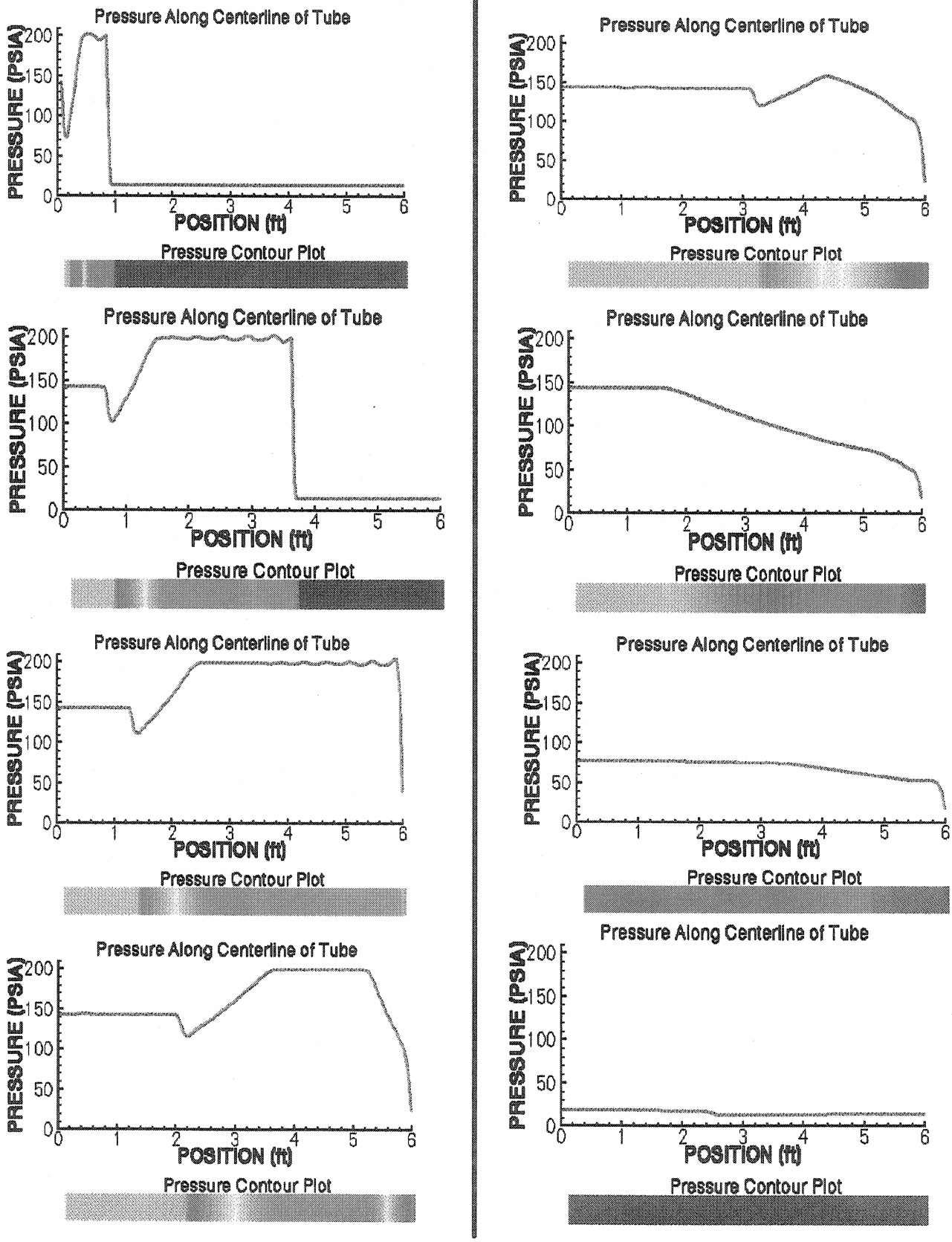

Figure 2: Detonation wave contour and pressure along centerline at several time intervals

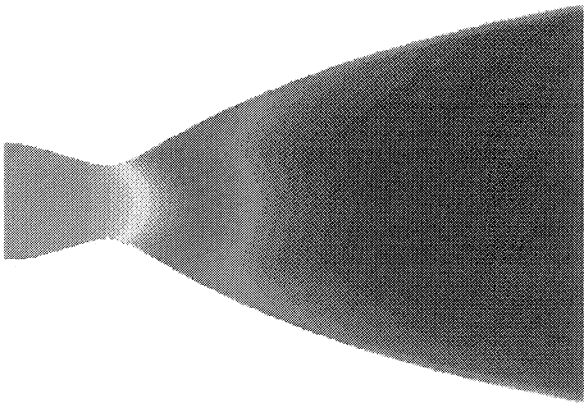

Figure 3a Temperature contours Case (a)

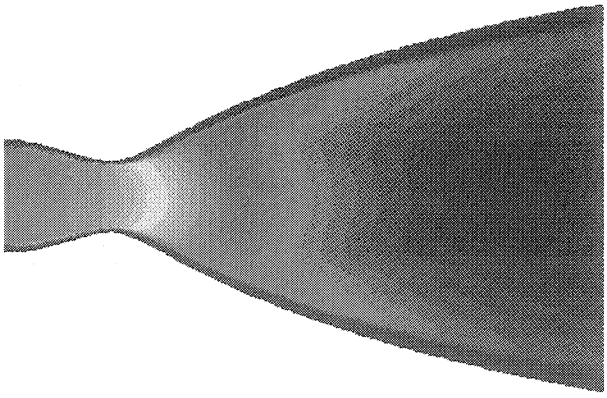

Figure 3b Temperature contours Case (b)

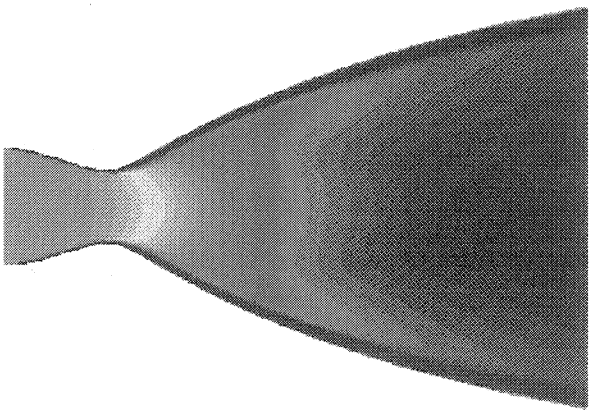

Figure 3c Temperature contours Case (c)

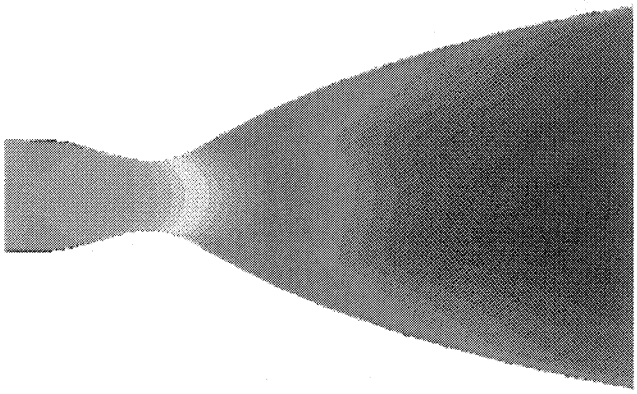

Figure 3d Temperature contours Case (d)

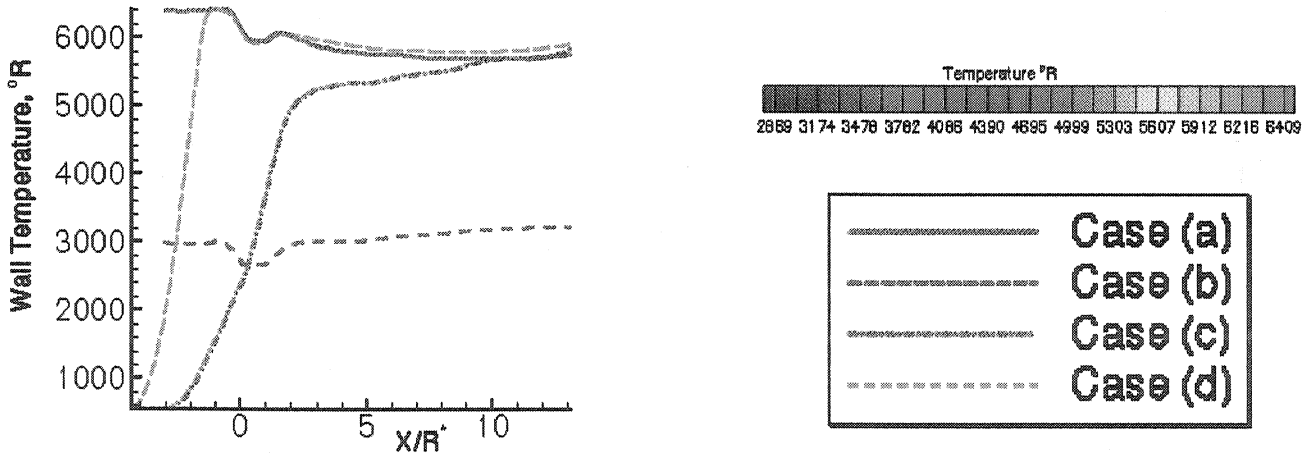

Figure 3e Temperature along the nozzle wall

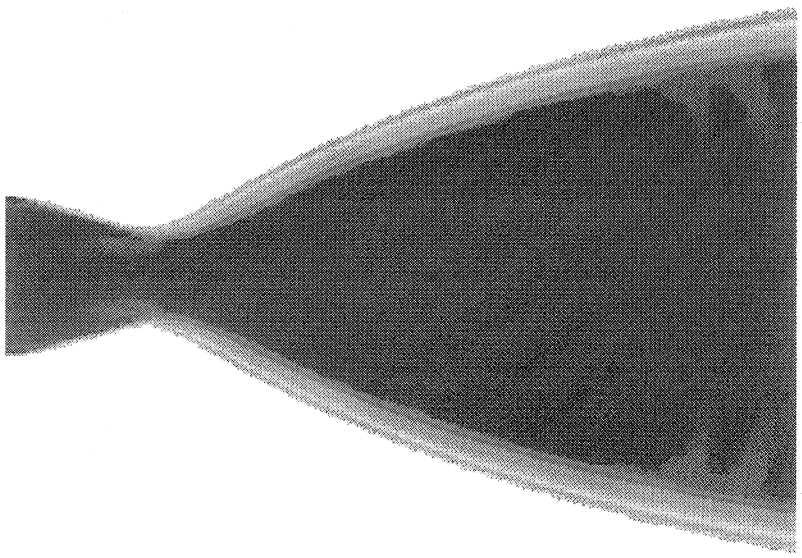

Figure 4a: Mass fraction contours of soot for Case (c).

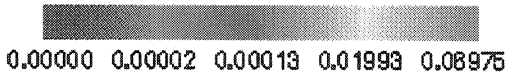

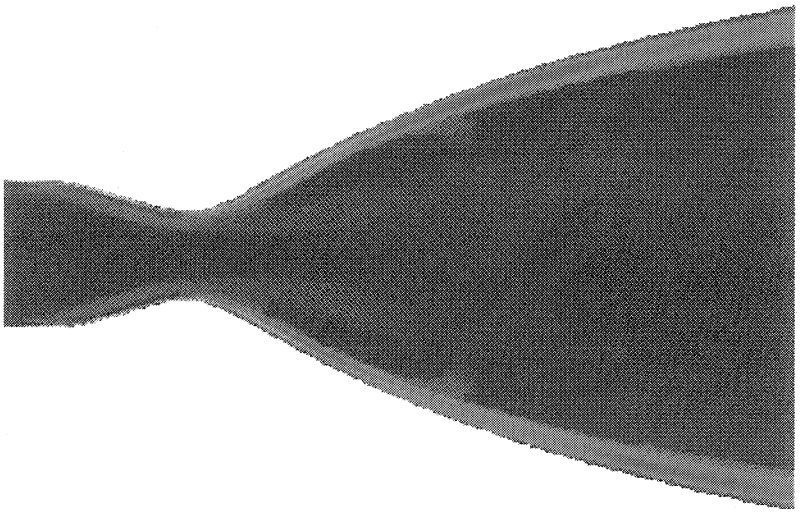

Figure 4b: Mass fraction contours of soot for Case (d).

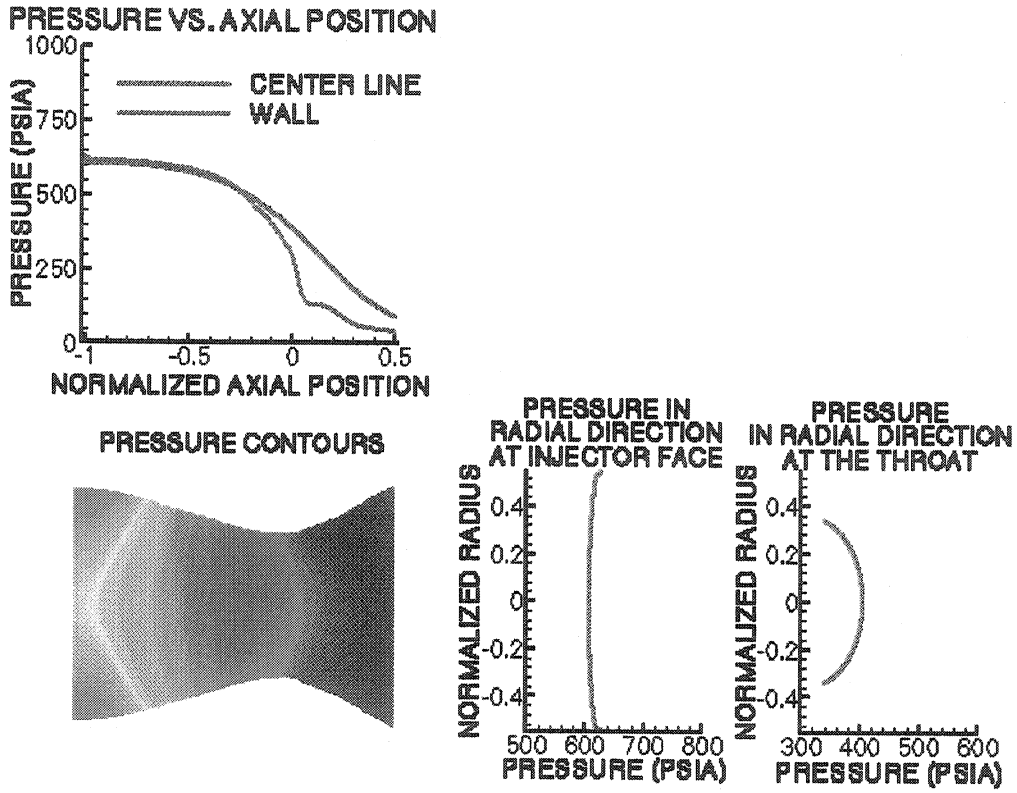

Figure 5a: Pressure pulse propagation in a combustion chamber in gaseous phase at a time interval.

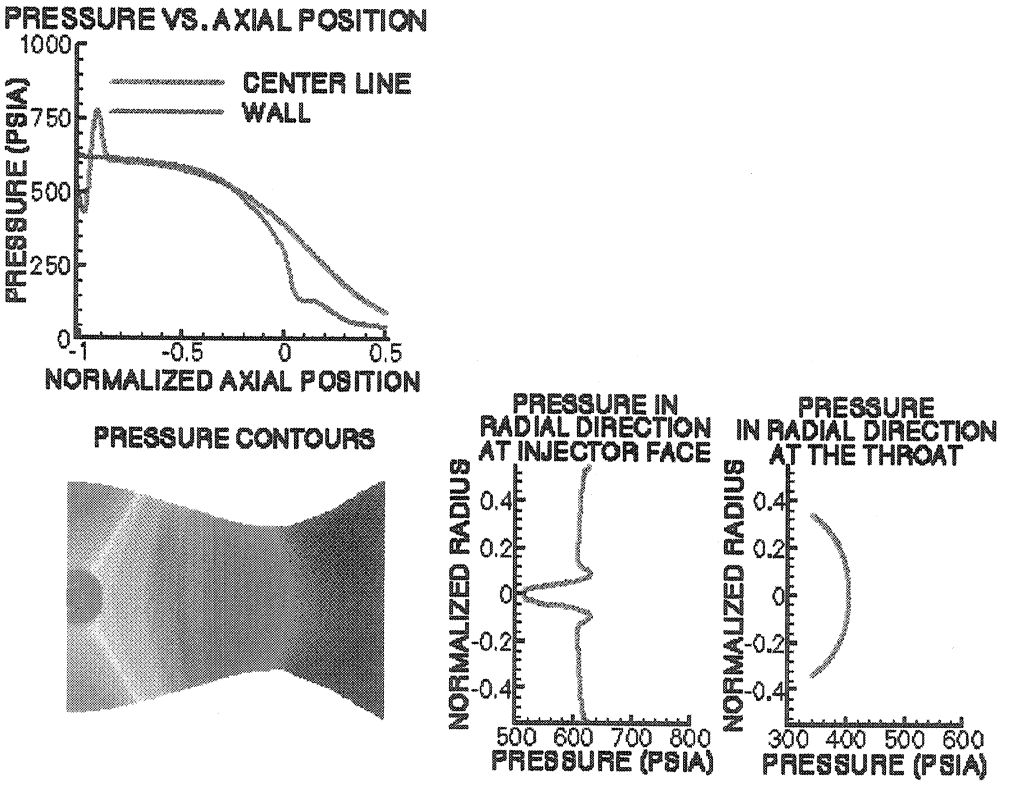

Figure 5b: Pressure pulse propagation in a combustion chamber in gaseous phase at a time interval.

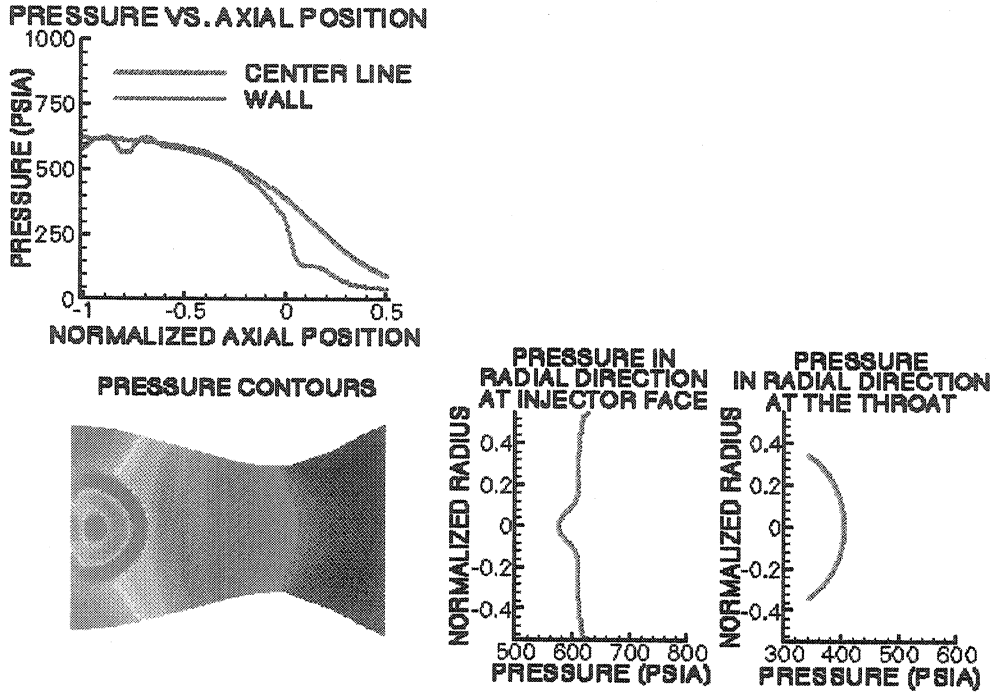

Figure 5c: Pressure pulse propagation in a combustion chamber in gaseous phase at a time interval.

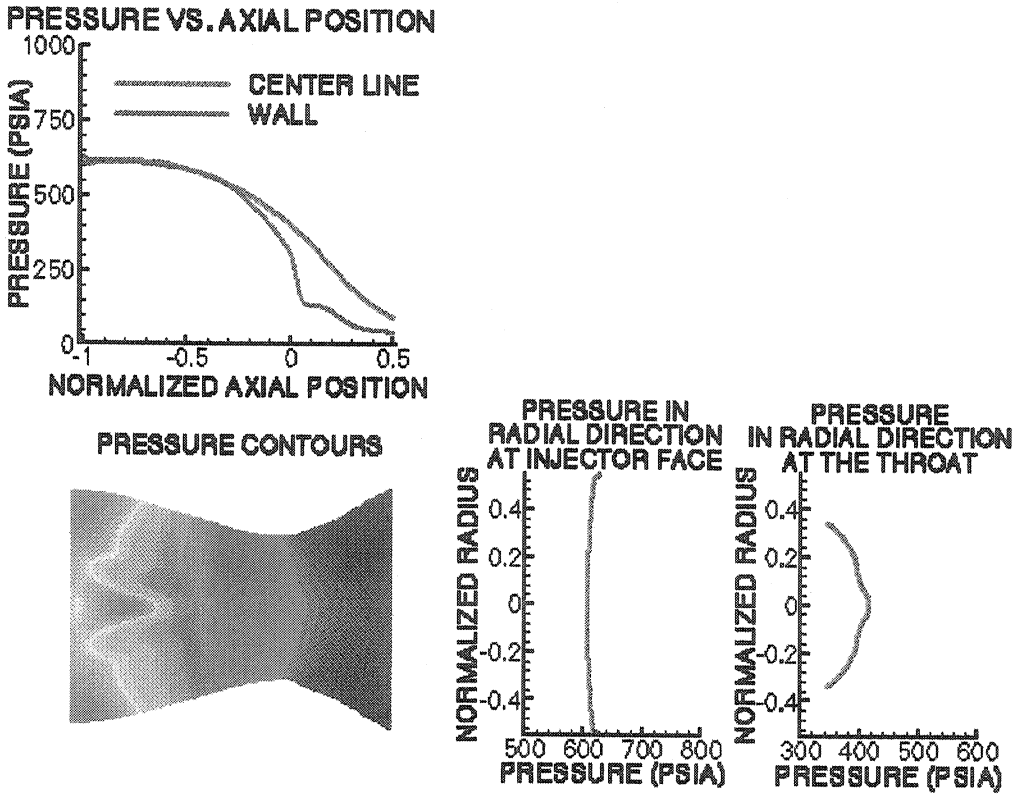

Figure 5d: Pressure pulse propagation in a combustion chamber in gaseous phase at a time interval.

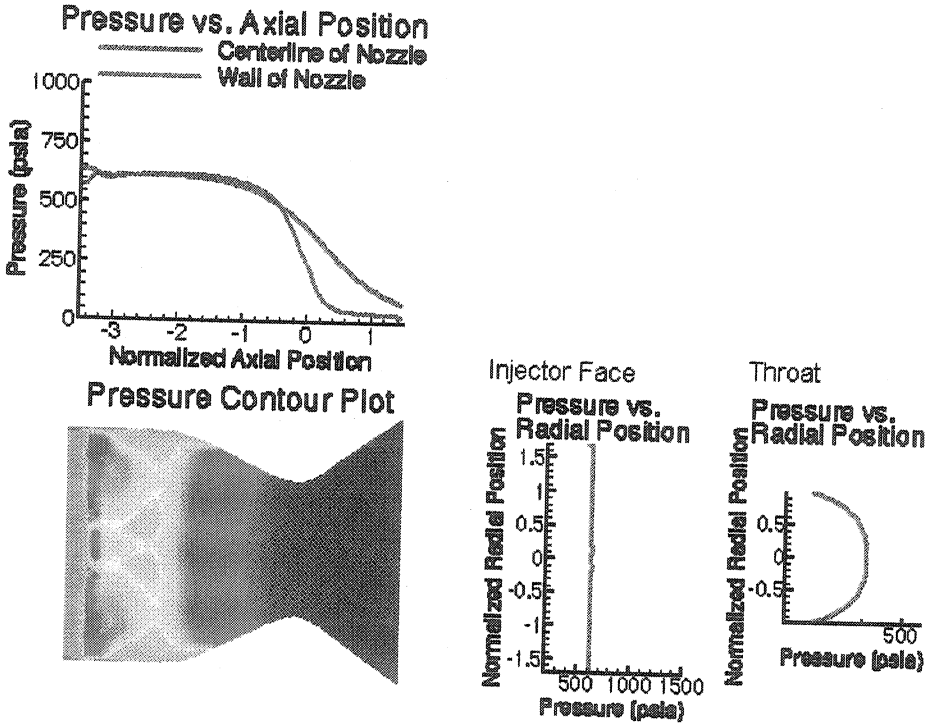

Figure 6a: Pressure pulse propagation in a combustion chamber in two phase flow at a time interval.

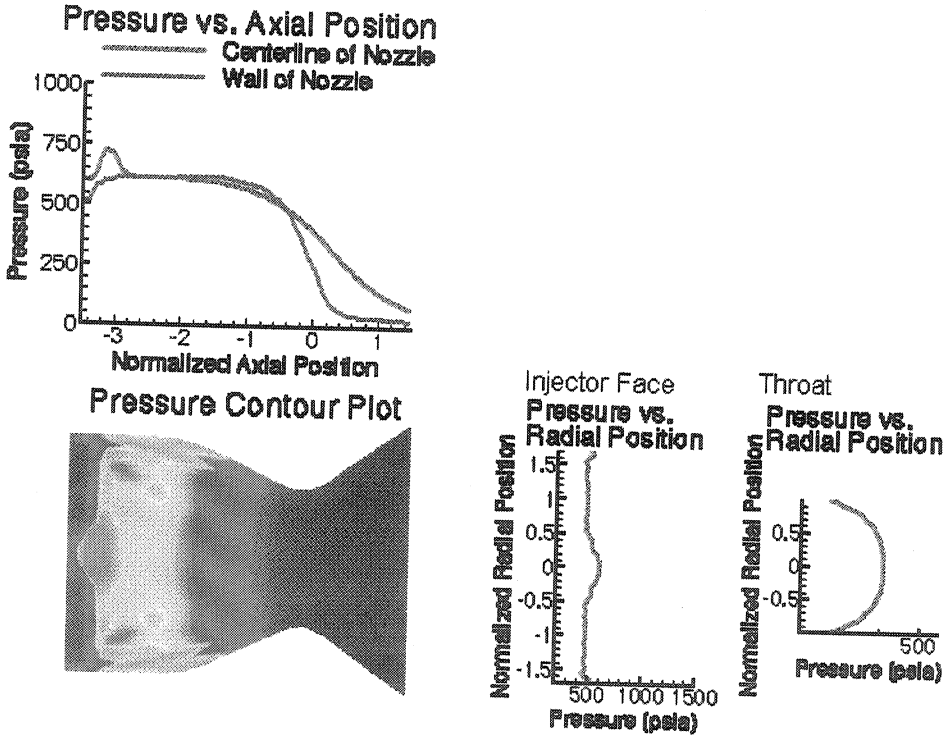

Figure 6b: Pressure pulse propagation in a combustion chamber in two phase flow at a time interval.

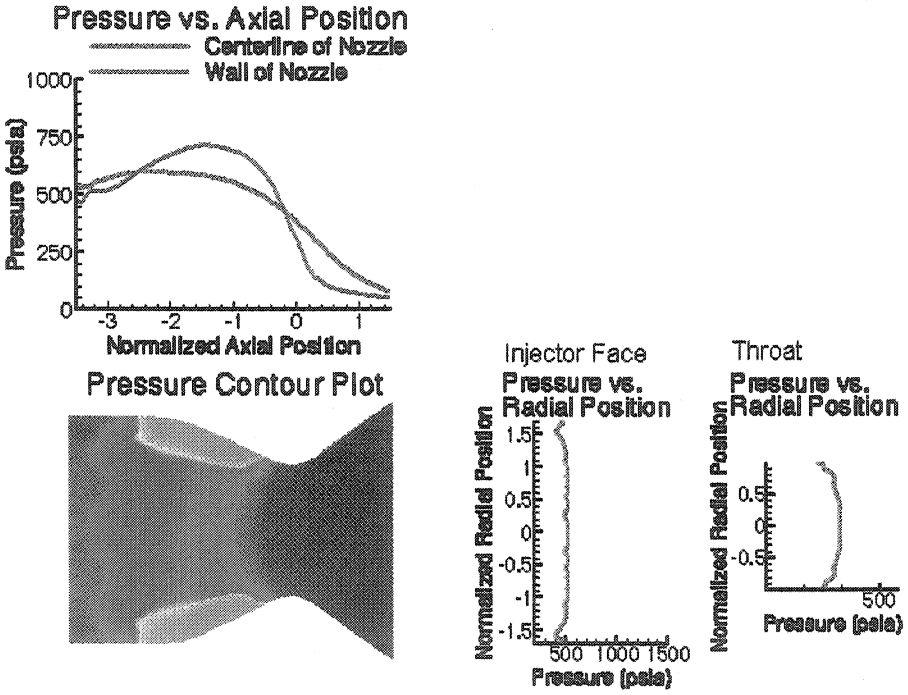

Figure 6c: Pressure pulse propagation in a combustion chamber in gaseous phase at a time interval.

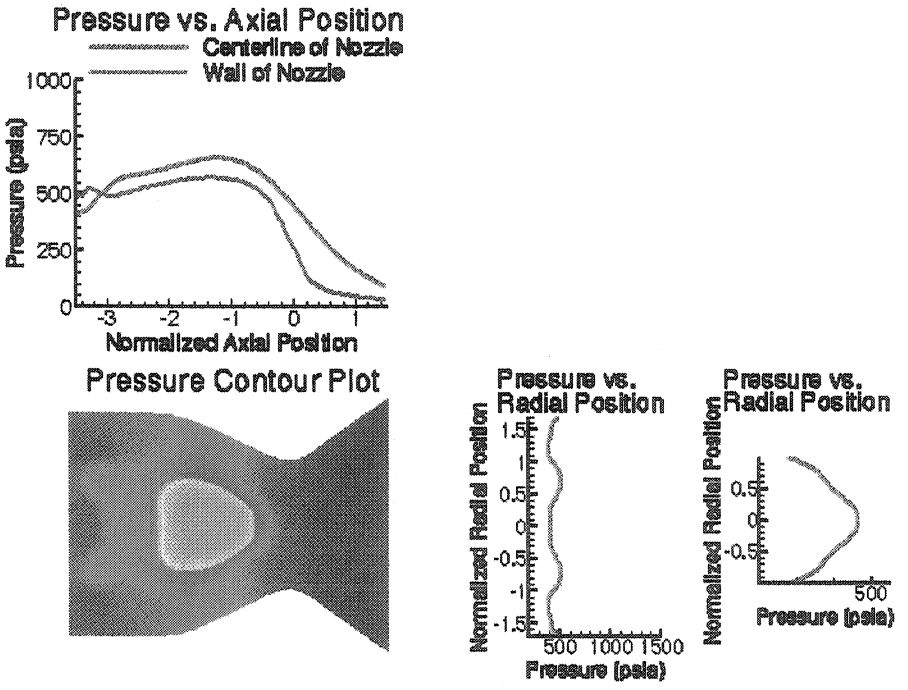

Figure 6d: Pressure pulse propagation in a combustion chamber in gaseous phase at a time interval.

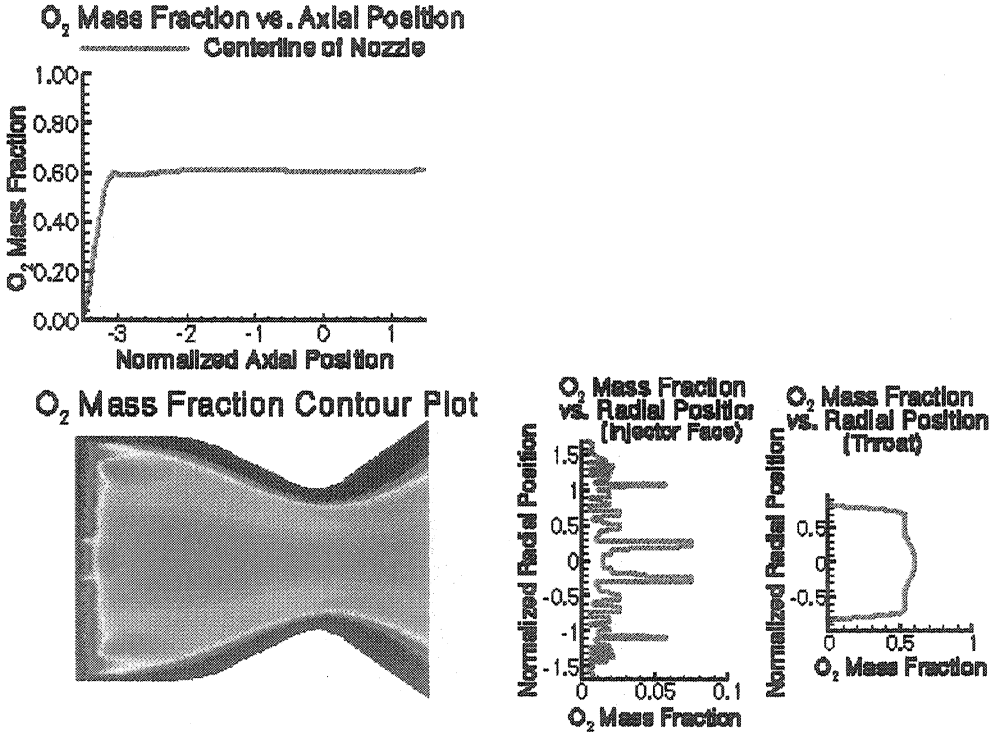

Figure 7a: O_2 Mass Fraction for two phase flow at steady state conditions.

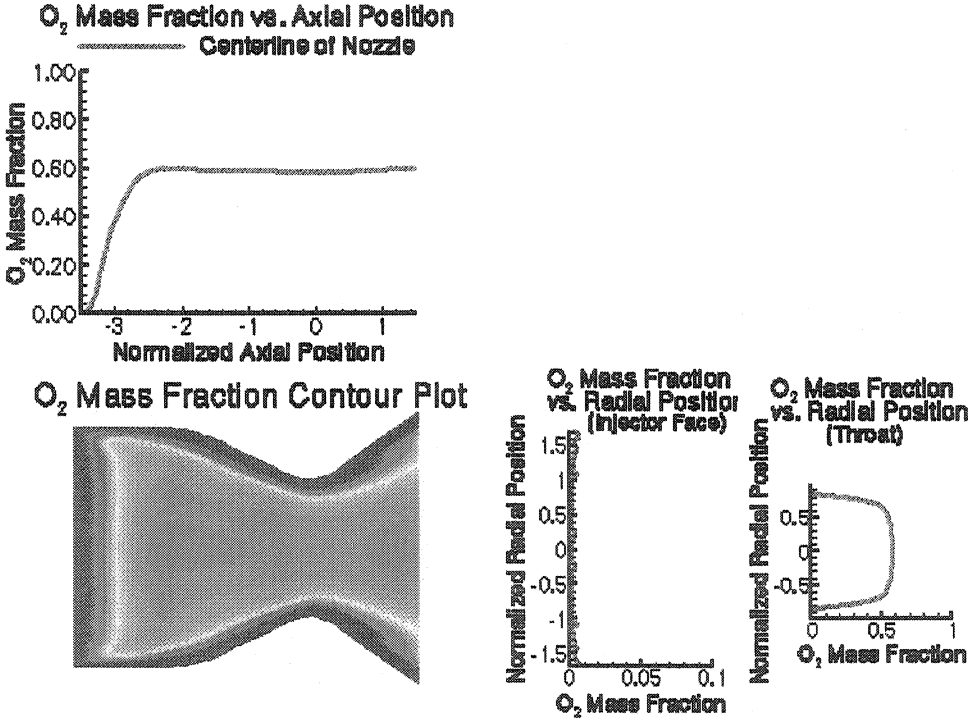

Figure 7b: O_2 Mass Fraction for two phase flow after the pressure pulse has been initiated.

Figure 8a: Schematic of a corrugated wall.

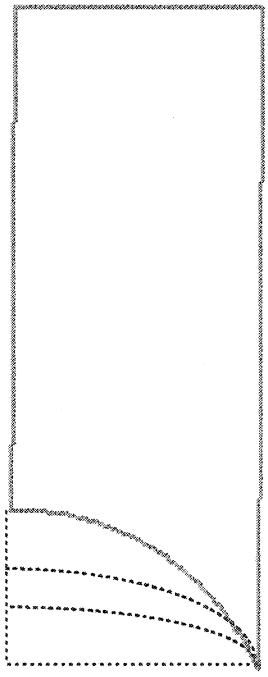

Figure 8b: Four variations of the lower wall, from circle to a flat plate.

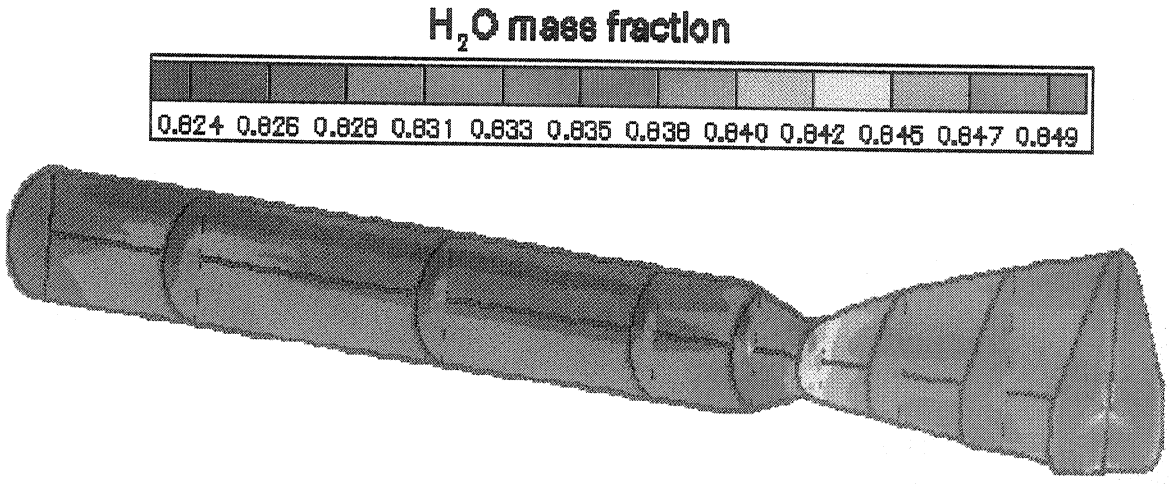

Figure 9d: Combined Cycle 3d analysis, contour plot of H_20 mass fraction.

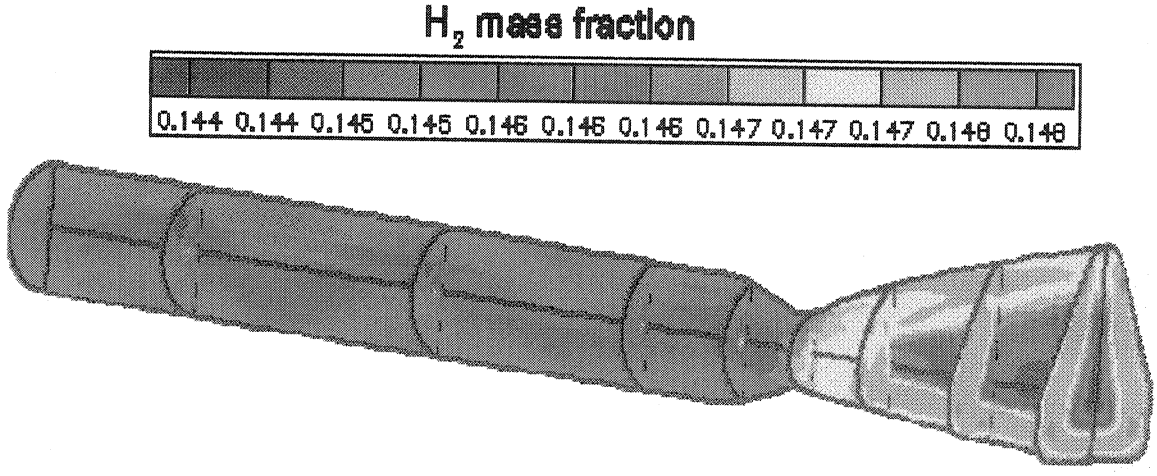

Figure 9e: Combined Cycle 3d analysis, contour plot of H_2 mass fraction.

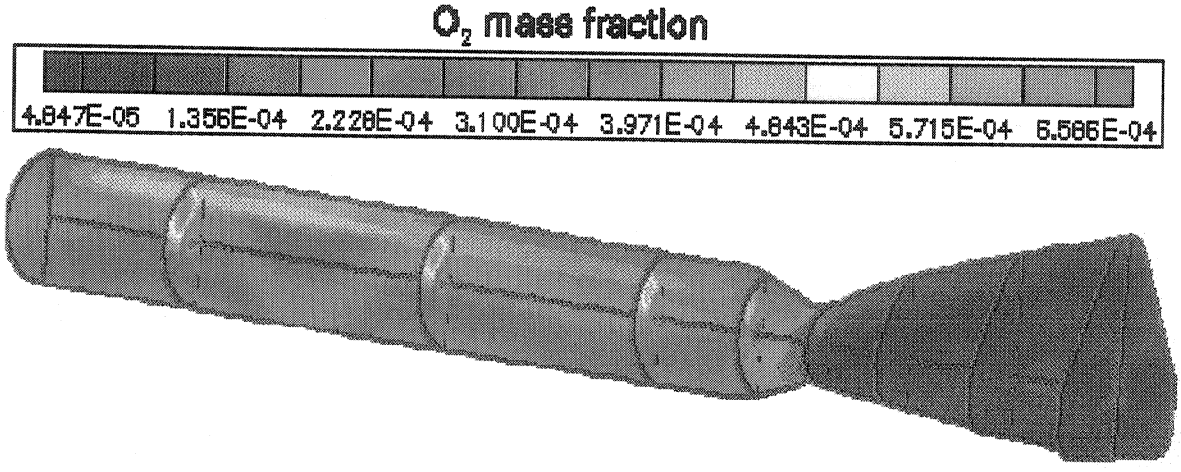

Figure 9f: Combined Cycle 3d analysis, contour plot of H_2 mass fraction.

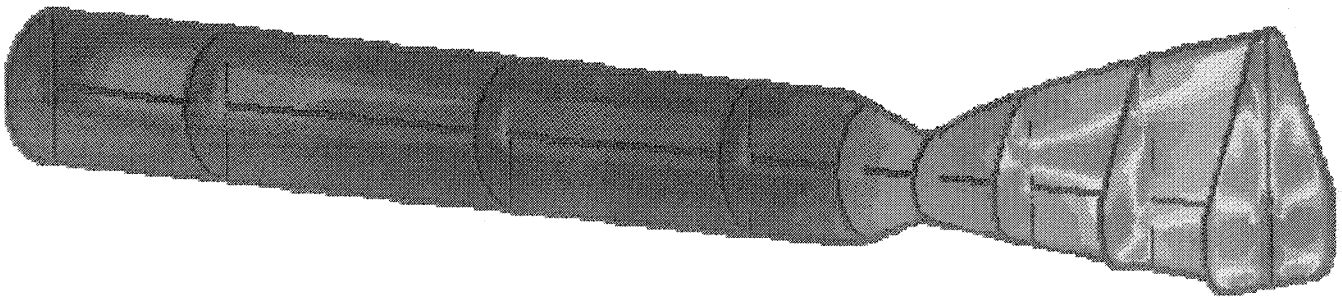

Figure 9a: Combined Cycle 3d analysis, contour plot of mach number.

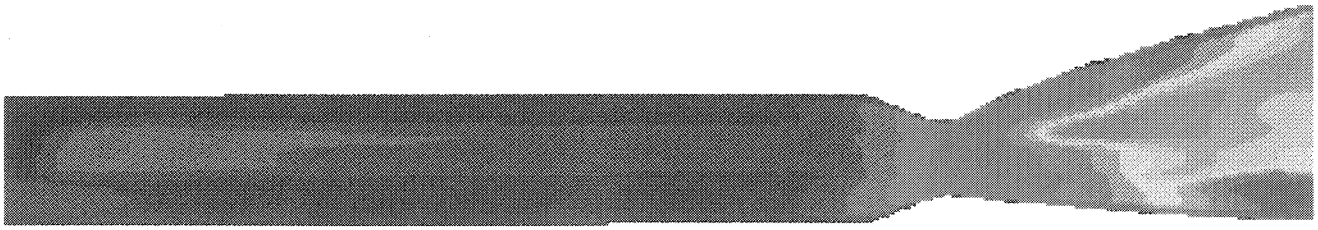

Figure 9b: Combined Cycle 3d analysis, contour plot of mach number along the plane of symmetry.

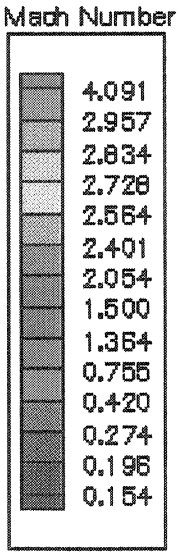

Figure 9c: Combined Cycle 3d analysis, contour plot of mach number along the exit plane

1997
NASA/ASEE SUMMER FACULTY FELLOWSHIP PROGRAM

MARSHALL SPACE FLIGHT CENTER
THE UNIVERSITY OF ALABAMA

PROGRAM RISK PLANNING WITH RISK AS A RESOURCE

Prepared By: Paul S. Ray

Academic Rank: Associate Professor

Institution and Department: The University of Alabama
Industrial Engineering Department
Tuscaloosa, Alabama

NASA/MSFC

Office: System Safety and Reliability Office

Division: Safety and Mission Assurance

MSFC Colleague: Edward H. Kiessling
Deputy Director.
Safety and Mission Assurance Office

1.0 INTRODUCTION

The current focus of NASA on cost effective way of achieving mission objectives has created a demand for a change in the risk management process of a program. At present ,there is no guidelines as to when risk taking is justified due to high cost for a marginal improvement in risk. As a remedial step Dr. Greenfield of NASA, developed a concept of risk management with risk as a resource (6,7)

2.0 RISK MANAGEMENT APPROACH

According to the present rule-based approach, the effort is directed to minimize all identified risks to a program until all resources are exhausted (6,7). In this process , there is no conscious effort to evaluate the cost of a marginal gain in risk level. The whole process is not cost effective .The proposed knowledge -based approach is to trade risk with other resources (e.g. Cost, schedule etc.) for acost effective way.

3.0 PLANNING RISK AND PROGRAM LIFE CYCLE

According to NASA practice, a program has five phases during its life cycle (3,4,5).Program formulation to select the most economic and feasible combination resources will be appropriate during the program formulation phase A and B, while design,development,and operation are implemented during the phases C,D,and E respectively. The risk planning method will be useful for initial planning as well as to review a plan at any time during the program lifetime particularly when some changes occur in program resources

4.0 KEY COMPONENTS OF A TYPICAL PROGRAM

4.1:Typical NASA program areas and resources:

A typical NASA program has the following key functional areas(6,7): technology utilization, system design, parts quality, fabrication, validation/test, and operation. Resources required for a typical functional area are(6,7) are: Cost, schedule, safety/risk, mass, Power, performance,and may include other resources for special program.

4.2 Typical options in a risk trade space:

Usually there are several feasible options any functional area. Each option requires different kind and amount of resources and has different characteristics , limitations, and advantages. Identification of the options available for a functional are is critical to effective planning of a program. Table 1 illustrates the typical options for technology and system design (6,7).

Function	Options
Technology utilization	1. Existing technology, and 2. Advanced technology
System design	1. Single string, 2. Selected redundancy, and 3. Redundancy (blocks and functions)

Table 1 Illustration of Options

4.3 Resource categories ratings, and weights:

Each resource has been classified into five categories based on its impact on a program. The category 1 indicates a low-level resource option ,with rating of 20 while, the category No. 5 indicates a high-level resource option having a rating of 100. The resource categories and their ratings are illustrated in Table 2 below.

Ratings	20	40	60	80	100
Categories	1	2	3	4	5
Resources					
Cost	No impact	Exceeds budget by less than5%	Exceeds budget by 5-9%	Exceeds budget by 10-14%	Exceeds budget by 15% or more
Safety/Risk	Risk score 1-3	Risk score 4-6	Risk score 7-9	Risk score 10-12	Risk score 13-25

Table 2: Illustration of Resource Categories and Ratings

4.4 Safety /risk categories and ratings:

To determine risk resource ratings ,a safety assessment matrix (Table3) has been developed having five levels of severity and five levels of likelihood of a mishap (1,2,8). A risk score is calculated by multiplying the level numbers of the applicable likelihood and severity. Based on this risk scores five risk resource ratings have been assigned as given in Table 3.

		Risk Matrix Score					Risk Score	Risk Trading Score
	5	5	10	15	20	25	1-3	20
	4	4	8	12	16	20	4-6	40
Chance	3	3	6	9	12	15	7-9	60
	2	2	4	6	8	10	10-12	80
	1	1	2	3	4	5	13-25	100
Severity		1	2	3	4	5		

Table 3: Illustration of Risk Assessment and Ratings

4.5 Resource weights:

The resource weights indicate relative importance of the resources depending on the nature and management priorities. For a one-time rare event flight program schedule ios more important , while for a repeated use program like space shuttle program, cost may be more important. The total weight s for a functional option should be equal to the number of resources used for a program.

RISK TRADING METHODOLOGY

5.1 Risk trading process:

The process is program specific and starts with a possible budget, program duration, and management priorities. The first step is to identify the functions and options available for each function in the risk trading space. The step is to identify resources required for each option and assign resource weights according to the nature and priorities of a program. The next step is to compare the feasible options for each functional area and assign resource category appropriate for each option and assign the resource rating as per the Table 1.

5.2 Computational algorithm:

All the computational work is planned to be computerized as a very large number of different option sets are feasible in the risk trade space. The formulae to use are:

$$Rfjk = \frac{1}{n} \sum_{i=1}^{n} (wijk)*(rijk)$$ = Resource score for the jth option in k th functional area.

Where, wi = Weight of the ith resource

ri = score assessed for the resource i

n = number of the resources considered for an option

The computer software will repeat the same process for all feasible option sets and compute the overall program risk trade rating for an option set as follows:

PRTRl = Program resource rating for the l th set of the functional options.

$$= \frac{1}{N} \sum_{K=1}^{N} Rfjk$$

where, N = Number of functions assessed .

Larger value of PRTRl indicates a higher-resource option.

$$PRRl = \text{Program risk Rating} = \frac{1}{N} \sum_{K=1}^{N} rijk(Safety/Risk)$$

6.0 REVIEW AND DECISION PROCESS

6.1 Review process:

The first step in the review process is to examine the computer generated Program resource (PRTR) vs. Program risk (PRR) curve to identify the option sets near the critical zone where the amount of resources required for a marginal improvement in risk increases significantly. The next step is to obtain and review the Resource Trading Summary reports also generated by computer for the selected program risk levels close to the economic boundary determined during the first step of review.

6.2 Decision process:

During the decision step ,the program planning and relevant functional representatives will select the most desired set of options considering residual risk, cost, and other factors relevant to the program. The PRTR vs.PRR curve being nearly flat near the optimal zone, a flexibility of selecting different sets of resources for practically the same level of overall risk will be a great advantage in several cases.

7.0 MERITS OF THE PROPOPSED RISK PLANNING APPROACH

- The knowledge-based approach will improve the risk management process for all future programs.
- The proposed risk planning system will provide a structured guideline for a cost effective way of planning risk for a program.
- Risk planning is based on the overall risk of a program.
- The program characteristics as well as management priorities are taken into account.
- Risk management will be integrated with program planning to ensure efficient overall management.
- The proposed risk planning tool will be useful for adjusting a program in response to change in program resource allocation.
- The potential order-of-magnitude estimate of savings is about 8% of the budget..
- The approach is consistent with the current NASA policy of "better, faster, and cheaper" focus.

8.0 RECOMMENDATIONS

As the proposed knowledge-based system presents definite advantages over the present rule-based approach of risk management of NASA , the following recommendations are made:

- Continue to fine-tune the risk planning methodology developed during the Summer 1997 for computerization. This is needed because a very large number of resource combination sets are feasible for a typical program.

The computation work is heavy and justifies the use of computer.

- Continue developing the proposed computerized risk planning system as continuation of the Summer research program of the University of Alabama.
- Conduct test and /or parallel run of the proposed risk planning system to adjust the sensitivity of the resource rating if needed for better perception of the results.
- Include the use of the proposed risk planning system in the requirements for program planning during the early phase 'B'.
- Implement the computerized system for risk management on trial basis.

9.0 REFERENCES

1. Hazard Prioritization NSTS Hazard Prioritization Working Group. May 1987. Pp.6 to 18.
2. International Space Station Alpha Program. ISSA Risk Summary Card. SSP50134. JSC-NASA, February 1995. pp.1-2.
3. Management of Major System Programs and Projects. NASA NMI 7120.4, November, 1993. pp. 1-4 to 1-6; 2-2 to 2-27.
4. Management of Major System Programs and Projects. NASA NHB 7120.5, November 1993. Pp. 2-2 to 2-26..
5. Management Safety Assessment (MSA). JSC/NASA , NSTS 22973-F, June, 1996.pp. B1 to B17.
6. Risk Management "Risk as a Resource". Presentation at Marshall Space Flight Center. Dr. Michael A. Greenfield on May 22, 1997. pp.31to 32.
7. Risk Management "Risk as a Resource". Presentation at Advanced Project Management, Wallops Flight Facility, Dr. Michael A. Greenfield, June 20,1997.pp. 30 to 38
8. System Engineering "Toolbox" for Design-Oriented Engineers, NASA Reference Publication 1358, December, 1994. Pp. 3-2 to 3-12.

LOW TEMPERATURE PHOTOLUMINESCENCE CHARACTERIZATION OF ORBITALLY GROWN CdZnTe

Timothy M. Ritter
NASA Summer Faculty Fellow
Department of Physical Science, The University of North Carolina at Pembroke, Pembroke, NC 28372

D. J. Larson, Jr.
NASA Summer Faculty Fellow
Department of Material Science, SUNY Stony Brook, Stony Brook, NY 11794

D. Gillies and M. Volz
Space Sciences Laboratory, George C. Marshall Space Flight Center, Huntsville, AL 35816

I. INTRODUCTION

The II-VI ternary alloy CdZnTe is a technologically important material because of its use as a lattice matched substrate for HgCdTe based devices. The increasingly stringent requirements on performance that must be met by such large area infrared detectors also necessitates a higher quality substrate.[Johnson, 1991; Magnea, 1987; Larson, 1993] Such substrate material is typically grown using the Bridgman technique. Due to the nature of bulk semiconductor growth, gravitationally dependent phenomena can adversely affect crystalline quality. The most direct way to alleviate this problem is by crystal growth in a reduced gravity environment. Since it requires hours, even days, to grow a high quality crystal, an orbiting space shuttle or space station provides a superb platform on which to conduct such research. For well over ten years NASA has been studying the effects of microgravity semiconductor crystal growth.[Curreri, 1996] This paper reports the results of photoluminescence characterization performed on an orbitally grown CdZnTe bulk crystal.

II. EXPERIMENT

The bulk $Cd_{1-x}Zn_xTe$ (nominal x = 0.04) material was grown in the Crystal Growth Furnace (CGF) on board the space shuttle Columbia as part of the second United States Microgravity Laboratory (USML-2). The boule, prior to cleaving, was approximately 12 cm in length and 1.5 cm in diameter; see figure 1 for a schematic diagram. The boule was cut along 3 axes to yield wafers with different crystallographic orientations. Those with the prefix S are cross sections of the boule and cut longitudinally down its symmetry axis resulting in rectangular shaped wafers. The samples taken from the middle section of the crystal, OW1-OW13, were cut such that their surfaces are {111} planes. Because they were cut at an angle non-orthogonal to the growth axis the OW samples are oval in shape. The final group of samples were wafered from the "heel" end of the material and are designed W1-W6. The W samples were cut transverse to the growth direction, hence, they are round. The outer surface of the boule contained depressions dispersed around the circumference resulting from bubbles formed prior to solidification. During the cleaving process the cuts often intersected these depressions and appear as a semicircular notch on the circumference of the wafer. (These notches will be referred to as "scallops" throughout the rest of the paper.)

Excitation for the PL measurements was achieved with 5 mW of the 4880 Å line of an Ar^+ ion laser. The collected luminescence was focused onto the entrance slit of a SPEX double spectrometer and detected with a photomultiplier (PMT). The sample was cooled to 5 K in a continuous flow cryostat which was mounted on a mill-bed. The mill-bed provided translation in a plane perpendicular to the surface of the sample and parallel to the optics table. Motion in the third direction was provided by a micrometer mounted to the cryostat insert. The resolution of both positioning devices was at least an order of magnitude less than the smallest step size, 250 μm, employed in the measurements.

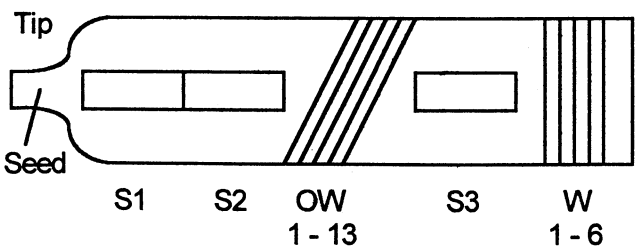

Fig. 1 Schematic diagram of the CdZnTe boule. S, OW, and W designate the three different wafer orientations.

III. Results and Discussion

A representative PL spectra, taken of wafer W4, is shown in figure 2. The dominant feature observed is the acceptor-bound exciton (A^o,X) peak at 1.610 eV. This peak is well resolved having a full width at half maximum (FWHM) of 2 meV. Moving up in energy from the A^o,X a much less intense donor-bound exciton peak is located at 1.614 eV. The origin of these impurities is not certain but typical residual impurities often observed in this material system include Cu, Ag, Na, N, Ca, and Li. [Stadler, 1995] Although it is weak in intensity, the free-exciton peak (1.618 eV) is clearly present

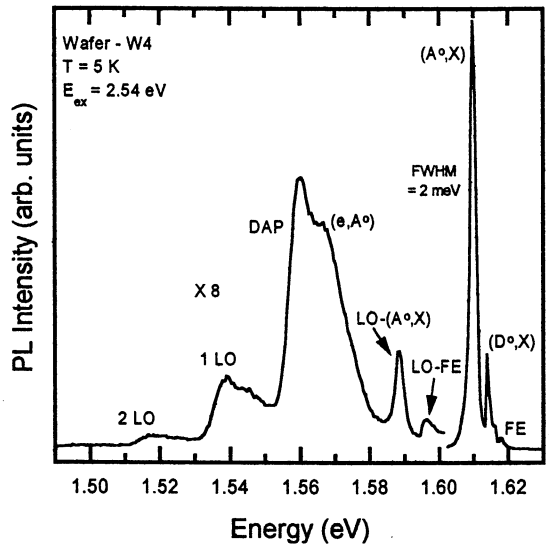

Fig. 2 Typical PL spectra showing all observed features.

The region below A^o,X in energy exhibits several features. The 1-LO phonon replicas ($h\nu_{LO}$ = 21 meV [Magnea, 1987]) of both the free-exciton and A^o,X are distinct at 1.597 eV and 1.589 eV, respectively. In the energy region 1.565 eV it is clear that two peaks are overlapping. In order to determine their origin the excitation energy and temperature dependencies of this broad feature were investigated. The excitation study measured the energy position of the 1.565 eV bands over the incident power range 5 mW - 355 mW. The temperature study was conducted over the span 4.5 K - 120 K. From these two techniques it was determined that the lower energy peak (1.560 eV) is due to donor-to-acceptor (DAP) recombination and the 1.566 eV feature is band-to-acceptor (e,A^o) emission. Three orders of phonon replicas of the DAP and e,A^o are also distinct. In the energy region below 1.5 eV, where broad bands indicative of defects have been observed for this material system,[Stadler, 1995; Johnson, 1991] the spectra of the CdZnTe measured in this study did not exhibit any PL features. The absence of a broad defect band, coupled with the presence of several orders of phonon replicas and the narrow width of the A^o,X peak, indicate that this material is of high quality.

In order to determine the Zn concentration of the material from the PL spectra the energy position of the free exciton peak, along with its known binding energy (10.4 meV)[Magnea, 1987] was utilized. The position of the free exciton peak, rather than A^o,X, was chosen because: i) it was clearly observed in virtually all of the recorded spectra and ii) the acceptor bound peak, while much more intense, can vary in its energy position depending on the species of the dopant atom.[Tobin, 1995] The addition of the binding energy term to the exciton energy position yields an experimental energy bandgap. The Zn concentration is then determined from a comparison of this measured energy gap value with a known expression for the bandgap of $Cd_{1-x}Zn_xTe$ as a function of x. A survey of the literature on CdZnTe revealed that there are many different, though similar, equations which express the relationship between the direct bandgap and the Zn concentration.[Tobin, 1995; Magnea, 1987; Stadler, 1995; Kennedy, 1988; Doty., 1992;

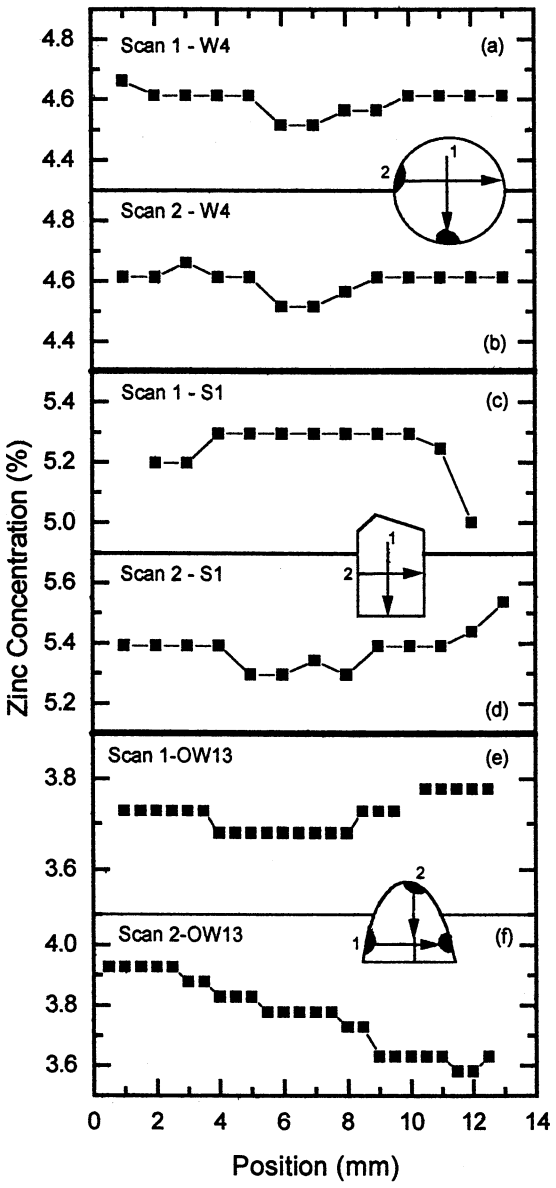

Fig. 3 Transverse Zn concentration across several different wafers. Position coordinate refers to distance from starting point of scan. Inset diagrams are of the wafer showing each scan. Black spots on edges represent the scallops.

Pessa, 1993] In the current work the results of Magnea, al.[Magnea, 1987] and Doty, et. al.[Doty, 1992] were each applied and then averaged to obtain the final concentration value for each data point. The expressions of Magnea and Doty for the bandgap energy of $Cd_{1-x}Zn_xTe$ are

$$E_g(x) = 1.605 + 0.505x + 0.285x^2 \text{ (eV)} \quad (1)$$

and

$$E_g(x) = 1.6068 + 0.455x + 0.33x^2, \text{ (eV)} \quad (2)$$

respectively. The accuracy of this technique for determining the *absolute* Zn mole fraction is limited to ~ ± 0.002, limited by the composition calibration.[Tobin, 1995] On the other hand, the estimated precision of the PL data is < ± 0.001 in concentration x.

Figure 3 shows the Zn concentration as a function of position for three separate wafers, one from each of the three regions of the boule (S, OW, and W) described in the previous section. The position coordinate is the distance from the starting position on the individual wafer for that particular scan. A schematic diagram of each of the 3 wafers has been included to indicate the orientation and direction of the two scans.

The results of the measurements on wafer W4 are shown in Figs. 3 (a) and (b). Scan 1 (fig. 3 (a)) begins 1-2 mm in from the edge of the sample and moves towards one of the scallops along the opposite edge. The last spectra in this scan was taken at the edge of the scallop on the polished surface. Immediately apparent from this data is the decrease in concentration for a 5 mm long portion of the wafer located in its center region. The second scan performed on W4 began at the edge of a scallop and moved approximately along a diameter of the round sample terminating on the opposite edge. An analogous dip in the Zn fraction is apparent for scan 2, displayed in figure 3 (b). This change in concentration measured by scan 2 occurs in the same center region as observed in scan 1, i.e. the center portion of the wafer. Recall that the center of this wafer corresponds to the longitudinal axis of the original boule. The change in concentration, from the edge of the wafer to the center region, is ~ 0.1 %, greater than the point-to-point precision of the measurements stated above.

Figures 3 (c) and (d) display the concentration dependence results for wafer S1. The first scan of this wafer began 4-5 mm in from one side and ended at an edge as shown in the diagram. This path is down the middle of the wafer which coincides with the center region of the boule (see figure 1). For this scan the concentration is seen to remain constant for most of the data, decreasing only at either end. The measurements which comprise scan 2 (fig. 3 (d)) were taken along a path that is approximately a diameter of the original boule. As seen for W4, scan 2 of S1 reveals that the concentration at the outer edges of the wafer is ~ 0.1 % higher than in a 5 mm region located near the center axis.

The concentration variation across sample OW13 is shown in figures 3 (e) and (f). Since this wafer is one from the OW group it is oval shaped. But, the wafer was broken and only one portion of this wafer was measured (see schematic diagram inset). The first scan, which ran in a transverse direction across OW13, began at the edge of a scallop on one side of the wafer and ended on the perimeter of another scallop located at the opposite side. The data (fig. 3 (e)) clearly shows, once again, a region of depressed (~ 0.1 %) concentration around the region of the longitudinal axis of the boule. The concentration dependence measured in scan 2, shown in figure 3 (f), exhibits a continuous decrease along the entire measured region. This occurs because scan 2 terminates at the broken edge of OW13, a point which would be located at the *center* region of the wafer were it whole.

The results from the three samples discussed above (W4, S1, and OW13) are indicative of those observed from all wafers measured in this work. There is an increase in Zn mole fraction when traversing a radius from the center of the cut wafers to their outer perimeter. This includes radii which terminate at one of the scallop shaped defects. There was no apparent anomalous fluctuation in the homogeneity of the CdZnTe in the region of these scallop features in comparison with a non-scallop wafer edge.

A plot of the longitudinal Zn fraction variation along the length of the original boule can be obtained by "reconstructing" the sample from the individual wafer measurements. A single concentration value for each wafer was determined by averaging the results obtained from the center portion of that wafer, i.e. the region in which the ~ 0.1 % concentration decrease was observed. The result of placing these concentration values in the correct sequential order is shown in figure 4. (It must be noted that the horizontal axis is only a list of the wafers and does *not* represent the actual spacing between the wafers.) From the center region of the plot it is apparent that the concentration fluctuation amongst the OW slices is reasonably small at only 0.7 %. Wafers OW2 - OW5 exhibit a progressive decrease in Zn but are within 0.2 % of one

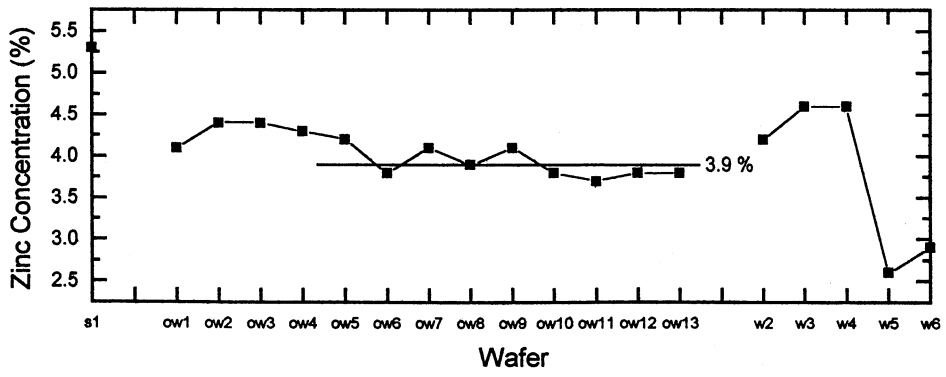

Fig. 4 Zn concentration variation along the boule axis. Solid line is at Zn = 3.9%, the concentration average of the last 8 OW wafers. Horizontal axis is not an accurate spatial depiction of boule length.

another. The individual Zn concentration of each of the last eight wafers in this set is within the experimental error of their average, 3.9 % (solid line in figure). Hence, the region between and including wafers OW6 and OW13 is, within the errors of these measurements, homogeneous. This is not the case for either end of the original boule. The data clearly shows that the "tip" portion of the boule (S1) has the highest ZnTe concentration at 5.3 %. At the "heel" end of the boule the Zn fraction rapidly increases (W2-W4) in comparison to the OW section and then drastically decreases to ~ 2.7 % for the last two wafers measured. These extremes are expected because of the radical growth conditions, e.g. quenching, experienced by the heel section.

IV. Conclusions

We have reported the results of PL characterization of twenty wafers cut from an orbitally processed CdZnTe sample. The sharpness of the near-band-edge features and the lack of any broad defect related bands is indicative of high quality material. The PL spectra also provided an accurate (± 0.2 %) method to determine an absolute spatial variation of the Zn concentration. The PL technique also provides an even more accurate measurement (< ± 0.1 %) of the point-to-point concentration variation within a single wafer. It was found that there is an ~ 0.1 % increase in the ZnTe concentration along the radial direction moving from the central region towards the outer circumference of the boule. This region at the core of the sample is ~ 5 mm in diameter and runs the length of the boule. There was no noticeable difference in concentration, along the outer edge of the boule in the region of the "scallops" which are present in this particular sample. Longitudinally, the Zn fraction decreased from a high of 5.3 % in the "tip" to 2.6 % in the "heel" region. Through the middle region of the boule (OW section), the concentration remains relatively constant at ~ 3.9 %, in good agreement with the nominal concentration of 4.0 %.

References

Curreri, P.A., *Second United States Microgravity Payload: One Year Report*, NASA Tech. Mem. 4737, xvii-xviii (1996).

Doty, F.P., Butler, J.F., Schetzina, J.F., and Bowers, K.A., *Properties of CdZnTe Crystals Grown by a High Pressure Bridgman Method*, J. Vac. Sci. Technol. B **10**, 1418-1422 (1992).

Johnson, S.M., Sen, S., Konkel, W.H., and Kalisher, M.H., *Optical Techniques for Composition Measurement of Bulk and Thin-film $Cd_{1-y}Zn_yTe$*, J. Vac. Sci. Technol. B **9**, 1897-1901 (1991).

Kennedy, J.J., Amirtharaj, P.M., Boyd, P.R., Qadri, S.B., Dobbyn, R.C., and Long, G.G., *Growth and Characterization of $Cd_{1-x}Zn_xTe$ and Hg1-yZnyTe*, J. of Cryst. Growth **86**, 93-99 (1988).

Larson, D.J., Alexander, J.I.D., Gillies, D., Carlson, F.M., Wu, J., and Black, D., *Orbital Processing of High-Quality CdTe Compound Semiconductors*, Joint "L+1" Science Rev. for USML-1 and USMP-1, 129-161 (1993).

Magnea, N., Dal'bo, F., Pautrat, J.L., Million, A., DiCioccio, L., and Feuillet, G., *Molecular Beam Epitaxial Growth of $Cd_{1-x}Zn_xTe$ matched to HgCdTe Alloys*, Mat. Res. Soc. Symp. Proc. **90**, 455-462 (1987).

Pessa, M., and Ahn, D., *ZnSe and its Applications for Blue-Light Laser Diodes*, II-VI Semiconductor Compounds, (World Scientific, 1993), pp.461-484.

Stadler, W., Hofmann, D.M., Alt, H.C., Muschik, T. Meyer, B.K., Weigel, E., Müller-Vogt, G., Salk, M., Rupp, and E., Benz, K.W., *Optical Investigations of Defects in $Cd_{1-x}Zn_xTe$*, Phys. Rev. B **51**, 10619-10630 (1995).

Tobin, S.P., Tower, J.P., and Norton, J.P., *A Comparison of Techniques for Nondestructive Composition Measurements in CdZnTe Substrates*, J. of Elec. Mat. **24**, 697-705 (1995).

1997

NASA/ASEE SUMMER FACULTY FELLOWSHIP PROGRAM

MARSHALL SPACE FLIGHT CENTER
THE UNIVERSITY OF ALABAMA

Friction Stir Welding Development

Prepared By:	Peter L. Romine, Ph.D.
Academic Rank:	Assistant Professor
Institution and Department:	Alabama A&M University Department of Engineering Technology
NASA/MSFC:	
Laboratory:	Materials and Processes
Division:	Metallic Materials and Processes
Branch:	Metals Processes
MSFC Colleagues:	Jeff Ding Chip Jones

Introduction

The research of this summer was a continuation of work started during the previous summer faculty fellowship period. The Friction Stir Welding process (FSW) patented by The Welding Institute (TWI), in Great Britain, has become a popular topic at the Marshall Space Flight Center over the past year. Last year it was considered a novel approach to welding but few people took it very seriously as a near term solution. However, due to continued problems with cracks in the new aluminum-lithium space shuttle external tank (ET), the friction stir process is being mobilized at full speed in an effort to mature this process for the potential manufacture of flight hardware. It is now the goal of NASA and Lockheed-Martin Corporation (LMC) to demonstrate a full-scale friction stir welding system capable of welding ET size barrel sections.

The objectives this summer were:

- Implementation and validation of the rotating dynamometer on the MSFC FSW system.
- Collection of data for FSW process modeling efforts.
- Specification development for FSW implementation on the vertical weld tool.
- Controls and user interface development for the adjustable pin tool.
- Development of an instrumentation system for the planishing process.

Implementation & validation of the rotating dynamometer

The two primary parameters in the friction stir process are rotational speed and plunge force. The rotation speed is set and monitored by the CNC milling machine used to perform the weld. The plunge force is not a typical milling parameter and so it not available on typical mills. The plunge force is a critical parameter in defining design specifications for a friction stir welding system and is likely to the most important parameter in process control of the friction stir welding process.

A major accomplishment of the previous summer was the calibration of motor currents to force on the MSFC FSW system. It is a straight forward process to calculate the plunge force applied from the motor current and the parameters for the motor and mechanical gearing system. Our approach was to monitor the current required to drive the motors controlling each axis of the mill. We then used calibrated load cells to measure the force applied and the corresponding motor currents. From this experiment we obtained scale factors to convert motor currents to pounds of force.

There were many skeptics of the validity of this approach or the quality of the resulting data. A precision rotational dynamometer was investigated and recommended for procurement by NASA. The selected instrument was a multiaxis dynamometer built by the Kistler Corporation. The Kistler dynamometer was designed to measure cutting forces experienced by a milling machine and appeared to be well suited to the MSFC friction stir welding system. The dynamometer is inserted into the spindle of the mill with the FSW tool attached on the

end. The dynamometer can measure the three forces x,y,z and the torque required to turn the tool. These signals are generated in the dynamometer and telemetered magnetically, without the need for slip rings, to a signal conditioning box. A robust +/- 10volt signal is produced by the signal conditioner for connection to a computer data acquisition system. Figure 1. illustrates the FSW system at MSFC in building 4711. The results from the dynamometer verified that the method of calibrated motor currents is a completely valid and economical method for measuring loads.

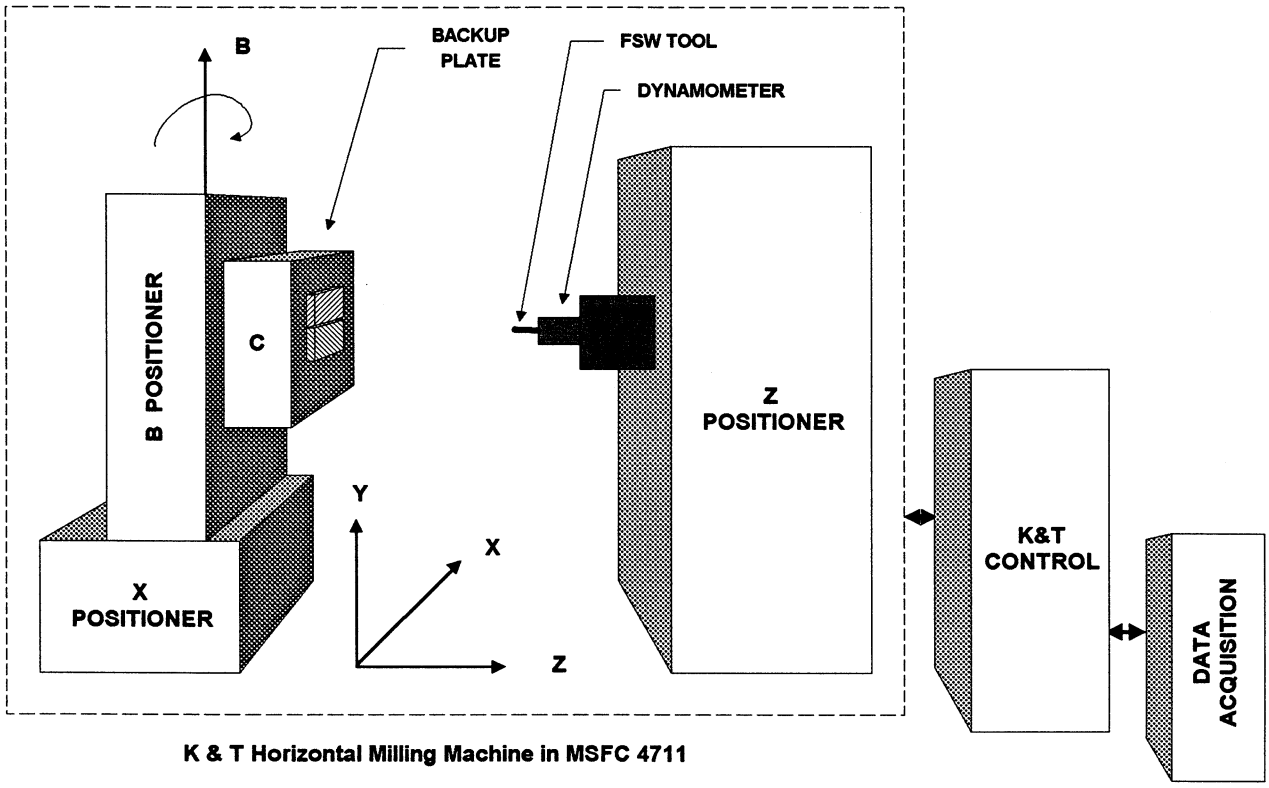

Figure 1. Friction Stir Welding System at MSFC.

Collection of data for FSW process modeling

The dynamometer provides data for the three forces (X,Y,Z) and the torque (Mz) required to turn the tool. The Z force has been the parameter of most concern due to its magnitude and direct effect on weld quality. The primary goal of force measurement has been to determine structural and mechanical design requirements for a friction stir welding system. The Z force and torque establish benchmarks for structural design and horsepower and load requirements for machine design. The X and Y forces have been of less concern due to their smaller values and relatively flat response. However, the X and Y forces were of great interest to those developing a scientific model for the friction stir process.

Typical welds made on the MSFC system last approximately 3 minutes and it was determined that a sampling rate of 2Hz was sufficient to capture the significant information of all loads using calibrated motor currents as well as the Z load from the dynamometer. Due to the X and Y axis being relative to the dynamometer, these axis rotate as the dynamometer rotates so that a continuous X or Y load appears as a sinusoidal output voltage. The frequency of the sinusoid is proportional to the rotational speed of the spindle and it was determined that a sample rate of 50Hz was sufficient to capture this information. Although this was not a technical challenge for a modern data acquisition system, the significantly increased volume of data produced resulted in concerns of storage and data handling.

Specification development for FSW implementation on the vertical weld tool

Due to continued problems with cracks in the super light weight external tank project, NASA and Lockheed-Martin Corporation (builder of the external tank) reached the decision to aggressively investigate the applicability of the friction stir process to the external tank. The plan developed was to design, build and operate a full scale friction stir welding system utilizing the existing vertical weld fixture in building 4705. I was involved in the development of the specification for vertical weld tool system due to my experience with the friction stir process load and torque requirements and the adjustable pin tool under development at MSFC.

Controls and user interface development for the adjustable pin tool

The adjustable pin tool prototype was developed at MSFC during the 1996 summer faculty fellowship period. It was initially developed to address the issues of weld closeout but its application to welding tapered thicknesses was understood. My involvement in the adjustable pin tool has been the design and implementation of the motor and sensor electronics and associated control hardware and software. This included the specification of equipment and software. I expect to have continued involvement in the adjustable pin tool through integration and operation on the new vertical weld tool system.

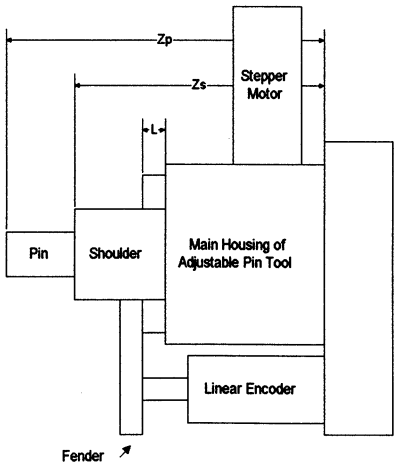

Figure 2. Adjustable Pin Tool (APT)

Development of an instrumentation system for the planishing process

The planishing process has been used to relieve the residual stresses introduced into a plasma welded joint due to the repair process. After the initial weld is performed an extensive inspection process is used to locate weld defects. The defect is then ground out of the weld and a repair weld is inserted. The are of the repair is then planished using a pneumatic hammer and steel bucking bar. Through planishing the distortion from the repair is literally hammered out.

The planishing process has been successfully used to increase weld strength and reduce the occurrence of cracking formerly associated with repair welds. In the past there has been very little science used to specify how the process is to be applied or exactly what is happening during the planishing process. An instrumentation system was developed to measure the planishing forces. The system consists of two quartz load washers and two accelerometers, one each for the planishing gun and bucking bar.

The system will initially be used to collect data to characterize the planishing process. Eventually it could be part of a planishing training system or real-time planishing monitor.

Summary and Conclusion

The Friction Stir Welding process is sure to become a standard joining process for aluminum alloys, especially in the aerospace industry. The projects started this summer will lead to a full scale friction stir welding system that is expected to produce a friction stir welded shuttle external tank type barrel section. The success of this could lead to the implementation of the friction stir process for manufacturing future shuttle external tanks.

Acknowledgment

The accomplishments of this summer would not have been possible without the technical input and direction from my NASA colleague, Jeff Ding of the Metals Processes Branch (EH23). I would also like to thank and commend all of the SFFP administrators and staff for a professionally and smoothly operated program.

1997
NASA/ASEE Summer Faculty Fellowship Program

Marshall Space Flight Center
The University of Alabama in Huntsville

The Effects of Impurities on Protein Crystal Growth and Nucleation: A Preliminary Study

Prepared By:	Constance A. Schall, Ph.D. Assistant Professor
Institution and Department:	University of Tulsa Department of Chemical Engineering
NASA / MSFC:	Biophysics, ES76 Space Sciences Laboratory
MSFC Colleague:	Marcus Pusey, Ph.D.

Introduction

Kubota and Mullin (1995) devised a simple model to account for the effects of impurities on crystal growth of small inorganic and organic molecules in aqueous solutions. Experimentally, the relative step velocity and crystal growth of these molecules asymptotically approach zero or non-zero values with increasing concentrations of impurities. Alternatively, the step velocity and crystal growth can linearly approach zero as the impurity concentration increases. The Kubota-Mullin model assumes that the impurity exhibits Langmuirian adsorption onto the crystal surface. Decreases in step velocities and subsequent growth rates are related to the fractional coverage (θ) of the crystal surface by adsorbed impurities; $\theta = Kx / (1+Kx)$, x=mole fraction of impurity in solution. In the presence of impurities, the relative step velocity, V/Vo, and the relative growth rate of a crystal face, G/Go, are proposed to conform to the following equations (Kubota, N. & Mullin, J.W.).

$$V/Vo \cong G/Go = 1 - \alpha\theta$$

The adsorption of impurity is assumed to be rapid and in quasi-equilibrium with the crystal surface sites available. When the value of α, an effectiveness factor, is one the growth will asymptotically approach zero with increasing concentrations of impurity. At values less than one, growth approaches a non-zero value asymptotically. When α is much greater than one, there will be a linear relationship between impurity concentration and growth rates. Kubota and Mullin expect α to decrease with increasing supersaturation and shrinking size of a two dimensional nucleus.

It is expected that impurity effects on protein crystal growth will exhibit behavior similar to that of impurities in small molecule growth. A number of proteins were added to purified chicken egg white lysozyme the effect on crystal nucleation and growth assessed.

Materials and Methods

Chicken egg-white lysozyme from Sigma (CEWL) was repurified by cation exchange chromatography and recrystallized as previously described (Forsythe, Ewing & Pusey). Turkey egg white lysozyme (TEWL), conalbumin, bovine ribonuclease A and thaumatin from Sigma and bovine serum albumin (BSA) from ICN Biochemicals were used without further purification and were added to CEWL as 'impurities'. All proteins were dialysed against distilled water followed by dialysis against 0.1 M sodium acetate, pH 4.6. CEWL and impurities were mixed in varying proportions. The CEWL solutions were mixed with buffer and 20% NaCl to a final NaCl concentration of 5% (w/v). Twenty microliters of the solution was placed in the well of a 24 well (6 X 4) crystalling plate and placed in an incubator at 20°C. The volume of the crystallizing solution did not change over time (batch crystallization) and CEWL concentration decreased over time as crystals formed. The first column of four wells in the crystallization plate contained no impurity and served as the control. Each column of the crystallizing plate contained four wells and at least one column was used for each initial CEWL concentration and impurity level. The impurity concentration is reported as % of total protein (w/w). Initial CEWL concentration was 15, 21 or 30 mg/ml and saturation concentration at 20°C, 5% NaCl, pH 4.6 is 1.8 mg/ml. Impurity level varied as follows: TEWL 0, 8.8, 14, 18, 22, and 26%, and 0, 4.5, 7, 10, 12.5, and 15%; conalbumin 0, 19, 32, 41, 48 and 54% and 0, 5, 11, 15, 19, and 23%; ribonuclease A 0, 6, 11, 16, 21, and 24%; BSA 0, 18, 31, 40, 47, and 52%; thaumatin 0, 15, 26, 35, 41, and 47% of total protein.

The crystallizing dishes were incubated for two to four weeks. Images of each well were taken and the number of crystals in each well counted. For plates containing TEWL the length of each crystal in the 101 and the 110 was measured only when both lengths were visible for an individual crystal. An aspect ratio was defined as the crystal length in the 101 direction divided by the crystal length in the 110 direction.

The aspect ratios and number of crystals in wells containing added impurity were compared to controls on the same crystallizing plate using a one way analysis of variance (ANOVA) followed by the Tukey multiple comparison test for normally distributed data. For data which was not normally distributed, a Kruskall-Wallis one way ANOVA on ranks followed by Dunn's multiple comparison test was performed. A multiple comparison test was performed only when significant differences were indicated by an ANOVA using SigmaStat software by Jandell.

Results

Turkey egg-white lysozyme (TEWL). There is an apparent change in morphology of CEWL crystals grown in the presence of TEWL. As the relative amount of TEWL increases, CEWL crystals become more elongated in the 101 direction. This effect is more pronounced in samples with an initial concentration of CEWL of 15 or 21 mg/ml than in samples with an initial CEWL concentration of 30 mg/ml (compare slopes of lines in figure 1). The aspect ratio, defined as the ratio of the crystal length in the 101 direction divided by the length in the 110 direction, is plotted as a function of % TEWL of total initial protein in figure 1. The number of CEWL crystals in wells with TEWL did not differ significantly from the number of crystals in control wells containing no TEWL for all initial concentrations of CEWL.

The aspect ratio of crystals in wells with added TEWL is compared to crystals in control wells with no TEWL on the same crystallizing plate using an analysis of variance. The data for each initial concentration of CEWL are from two separate experiments. For one data set with an initial CEWL concentration of 30 mg/ml, only the highest concentration of TEWL (26%) produced significant differences in the aspect ratio when compared to the control wells. A second experiment with lower TEWL concentrations (4.5%, 7.3%, 9.8%, 12.5%, 14.8%) produced crystals with aspect ratios that differed significantly from controls.

At an initial CEWL concentration of 21 mg/ml, all wells with added TEWL resulted in crystals with aspect ratios significantly larger than the control crystals except crystals grown in wells containing 7% TEWL. At an initial concentration of 15 mg/ml crystals grown in 10%, 15%, 18%, and 26% TEWL resulted in crystals with significantly larger aspect ratios compared with control crystals.

Conalbumin. Nucleation was inhibited at an initial concentration of CEWL of 15 mg/ml at very high levels of conalbumin (32% of total protein). At 19% conalbumin the total number of crystals formed did not differ significantly from the controls containing no added conalbumin. At initial CEWL concentration of 21 mg/ml, the results were unclear. In one set of experiments conalbumin concentrations of 11%, 15%, 19% and 23% resulted in formation of significantly more crystals than the controls. In another set of experiments, a greater number of crystals formed when total protein consisted of 48 or 54% conalbumin, but not in wells containing 19 to 41% conalbumin. At the highest initial concentration of CEWL (30 mg/ml), only very high concentrations of conalbumin (greater than 48%) resulted in significantly more crystals when compared with controls.

The morphology of CEWL crystals formed in the presence of conalbumin at any level (from 6% to 54%) was effected at all initial concentrations of CEWL (15, 21 and 31 mg/ml). Crystal edges became less sharp with increasingly greater additions of conalbumin (figure 3). Crystals were submitted for evaluation by X-ray diffraction. It is unclear how the diffraction quality of the crystals is effected by addition of conalbumin.

In further experiments with conalbumin, a 220 microliter quantity of solution with a relative supersaturation of 6 (bulk concentration divided by equilibrium solubility of CEWL at 20°C, 5%NaCl, pH 4.6) was placed in the well of a tissue culture plate. Controls contained no conalbumin. Five replicates each with 5, 10 and 20% conalbumin were either seeded with two microliters of seed solution of relative supersaturation of 35 (incubated for 2 minutes at 20°C) or left unseeded. The plates were incubated at 20°C for approximately two weeks and crystals were counted and measured. There were significantly fewer crystals (no crystals formed) in unseeded wells with 20% added conalbumin in comparison to the controls wells. There were no other

significant differences in the number of crystals in seeded or unseeded wells at any level of conalbumin. Crystals in wells with added conalbumin were significantly smaller than crystals in wells with no added conalbumin.

Figure 1. The effect of TEWL on the aspect ratio of CEWL crystals. Symbols represent the average value of four replicates and one sided error bars represent one standard deviation. The lines are a straight line fit to the data for each initial concentration of CEWL and are drawn only to indicate the general trend of the data with increasing amounts of added TEWL.

Bovine serum albumin (BSA). Addition of BSA to CEWL solutions produced no evident effect on nucleation of CEWL in solutions containing an initial concentration of 15 or 30 mg/ml. At an initial concentration of 21 mg/ml significantly more crystals were produced in wells containing 18% or 40 % conalbumin, but not in wells with 31, 47 or 52% conalbumin.

There was a change in morphology of CEWL crystals grown in the presence of BSA. It appeared that growth of the 101 face was inhibited with increasing proportions of BSA.

Bovine ribonuclease A. Addition of ribonuclease A to CEWL resulted in a significant increase in the number of CEWL crystals compared to controls for all initial concentrations of CEWL tested. At an initial CEWL concentration of 15 mg/ml the number of crystals in a 20 microliter drop of solution was 7.0±2.9. At 6% to 24% ribonuclease the average number of crystals in a 20 microliter drop varied from 114 to 262, with numbers of crystals generally increasing with increasing concentration of ribonuclease A (table 1).

Table 1. Average number of crystals formed in 20 microliter drop with initial CEWL concentration of 15 mg/ml.

% Ribonuclease A (w/w total protein)	Mean number of crystals in 20 microliter drop	Standard deviation of number of crystals
0	7.0	2.9
6	127	12
11	114	19
16	149	28
21	197	17
24	262	57

At initial CEWL concentrations of 21 and 31 mg/ml the average number of crystals in wells containing no ribonuclease was 17±2.4 and 30±1.2 respectively. Crystals in wells containing ribonuclease were too numerous to count, but are estimated to range from 300 to 1000. All crystals exhibited the normal tetragonal morphology of CEWL crystals.

Thaumatin. At an initial CEWL concentration of 15 mg/ml there was no significant difference in the number of crystals formed in wells containing 6 to 11% thaumatin. At higher thaumatin concentration, few (17% thaumatin) or no ((22 to 28% thaumatin) crystals formed. At initial CEWL concentrations of 21 and 30 mg/ml an average of 20 and 44 crystals formed in control wells. In all wells with added thaumatin, an average of 300 to 1,000 crystals formed. All crystals appeared to exhibit the normal CEWL tetragonal morphology.

Discussion and Conclusions

Protein impurity effects on CEWL crystal growth and morphology are specific and show a concentration dependency. TEWL, a protein with high sequence homology to CEWL, inhibits growth of the 110 face. Conalbumin and BSA cause the morphology of CEWL to change. BSA appears to inhibit growth of the 101 face. Conalbumin has been shown to inhibit growth of the 101 face (Judge *et. al.*).

CEWL and TEWL are both composed of 129 amino acids and differ by seven amino acids. Apparent inhibition of growth of the 110 face of CEWL by TEWL results in elongation of the crystals grown in the presence of TEWL. This effect is more pronounced at lower

supersaturation (initial CEWL concentration of 15 mg/ml and 21 mg/ml) than at higher supersaturation (30 mg/ml). This behavior is consistent with the effects predicted by the Kubota and Mullin model and with the behavior of impurities in small molecule growth. The lowest concentration of TEWL used was 5%. Because the crystals are grown in batch wells, the concentration of CEWL will decease as crystals grow. If TEWL is rejected by the crystal the %TEWL (w/w) will increase as the crystallization proceeds and the inhibitory effect on growth may increase over time. Additions of TEWL did not appear to effect nucleation rates.

Conalbumin is a protein which is also present in chicken egg-white and is therefore frequently found in chicken egg-white lysozyme. Conalbumin has a reported PI between 6.1 and a molecular weight of 76 kilodaltons and is structurally dissimilar to CEWL. In studies by Judge *et. al.* conalbumin was found to inhibit growth of the 101 face of CEWL crystals at low supersaturation (14 mg/ml at 18°C where solubility was 1.3 mg/ml) and at high concentration of impurity (30%). At higher concentrations of CEWL, growth rates were not effected by this level of conalbumin. As predicted by the Kubota - Mullin model, supersaturation can modify the inhibitory effect of impurities. Growth was not inhibited with 10% conalbumin at the CEWL concentrations studied by Judge *et. al.*

Addition of large quantities of BSA (18% or greater), did not have a large effect on nucleation of CEWL crystals but appeared to inhibit growth of the 101 face. BSA has a PI of about 4.8 and a molecular weight of 60 kilodaltons.

The effects of impurity additions on nucleation of crystals was not clear. Nucleation was found to both increase and decrease with addition of impurities, depending on supersaturation, % impurity, and the specific protein.

The preliminary studies outlined here indicate that conalbumin effects nucleation of CEWL crystals. This affect appears to be modified by supersaturation. At the lowest concentrations of CEWL examined, 11 mg/ml and 15 mg/ml, nucleation of crystals was completely inhibited with 20% and 32% added conalbumin, respectively. At higher initial concentrations (21 and 31 mg/ml CEWL), nucleation is not inhibited and in some cases a more crystals are formed at high impurity concentration. Edges of CEWL crystals were roughened by addition of any amount of conalbumin at all initial CEWL concentrations examined here.

Bovine ribonuclease A dramatically increased nucleation of CEWL at all initial concentrations of CEWL (15, 21, and 31 mg/ml). Ribonuclease has a PI of 9.3 and a molecular weight of 13.7 kilodaltons. With additions of 6% to 24% ribonuclease, the average number of crystals formed in a 20 microliter drop increased from 7 to 30 to a range of 114 to several hundred. This is in contrast to the results of Abergel *et al.* who demonstrated that nucleation of TEWL was inhibited by addition of ribonuclease.

Addition of thaumatin (PI of 12 and molecular weight of 22 kilodaltons) to solutions inhibited nucleation of CEWL crystals at low initial concentration of CEWL and resulted in increased nucleation at higher initial concentrations of CEWL.

A summary of the effect of impurities on nucleation and growth of CEWL crystals is found in table 2. Only TEWL is homologous with CEWL. Of the proteins which show little sequence homology to CEWL, those with high molecular weight and PI below 7 modified the morphology of CEWL crystals. Dissimilar proteins of relatively high PI and low molecular effected nucleation, but appeared to have little effect on crystal morphology.

Table 2. Summary of effect of protein impurities on nucleation and morphology of CEWL crystals.

Protein	PI (Molecular weight, kd)	Effect nucleation	Effect Growth / Morphology
CEWL	10.7 (14.3)		
TEWL	(14.3)	no	yes
Conalbumin	6.1 (76)	yes (increase & decrease)	yes
BSA	4.8 (60)	no	yes
Ribonuclease A	9.3 (13.7)	yes (increase)	no
Thaumatin	12 (22)	yes (increase & decrease)	no

References

Abergel, C., Nesa, M.P. & Fontecilla-Camps, J.C. Journal of Crystal Growth 110, 11-19 (1991).

Forsythe, E.L., Ewing, F. and Pusey, M.L. (1994) *Acta Cryst.*D**50**, 614-619.

Gilliland, G.L., Tung, M., Blakeslee, D.M. and Ladner, J. (1994) The Biological Macromolecule Crystallization Database, Version 3.0: New Features, Data, and the NASA Archive for Protein Crystal Growth Data. *Acta Cryst.* D**50**, 408-413.

Judge, R.A., Forsythe, E.L., Pusey, M.L., (1997) *The effect of protein impurities on lysozyme growth.* Submitted to *Biotech. & Bioeng.*

Kubota, N. & Mullin, J.W. (1995) *Journal of Crystal Growth*, **152**, 203-208.

1997

NASA/ASEE SUMMER FACULTY FELLOWSHIP PROGRAM

MARSHALL SPACE FLIGHT CENTER
THE UNIVERSITY OF ALABAMA IN HUNTSVILLE

Controller Design for EMA in TVC Incorporating Force Feedback

Prepared By: Dale E. Schinstock, Ph.D.
and Douglas A. Scott, Accompanying Student

Academic Rank: Assistant Professor

Institution and Department: The University of Alabama
Mechanical Engineering Department

NASA/MSFC:

Laboratory: Propulsion Laboratory
Division: Component Development
Branch: Turbomachinery and Control Mechanisms

MSFC Colleague: Rae Ann Weir (EP32)

Introduction

The objective of this research was to develop control schemes and control design procedures for electromechanical actuators (EMA) in thrust vector control (TVC) applications. For a variety of reasons, there is a tendency within the aerospace community to use electromechanical actuators in applications where hydraulics have traditionally been employed. TVC of rocket engines is one such application. However there is considerable research, development, and testing to be done before EMA will be accepted by the community at large for these types of applications. Besides the development of design procedures for the basic position controller, two major concerns are dealt with in this research by incorporating force feedback: 1) the effects of resonance on the performance of EMA-TVC-rocket-engine systems, and 2) the effects of engine start transients on EMA. This report only highlights the major contributions of this research.

Hardware and Modeling

Experimental verification of the control schemes and design techniques were completed using the 1 Hp EMA designed and built by the Component Development Division of the Propulsion Laboratory at NASA MSFC. It was designed to operate with an engine roughly the size of an RL-10 engine (Pratt and Whitney). The actuator was mounted in an inertia simulator, which is basically a large pendulum used to simulate the engine. Fig.1 shows the hardware used in the experiments. The NASA controller originally included and analog position controller, a motor current controller, and a pulse width modulated power converter for the brushless DC motor in the actuator. For this research, the position controller was defeated and a digital controller was implemented. Using a Pentium™ PC, digital feedback of the screw position from a resolver to digital converter in the NASA controller was utilized for position control of the EMA. Several pieces of hardware are not shown in Fig.1: a string potentiometer for the measurement of the pendulum position, a load cell amplifier, an interface card for the PC, and a large impulse hammer with a piezoelectric load cell and amplifier (PCB GK291B50).

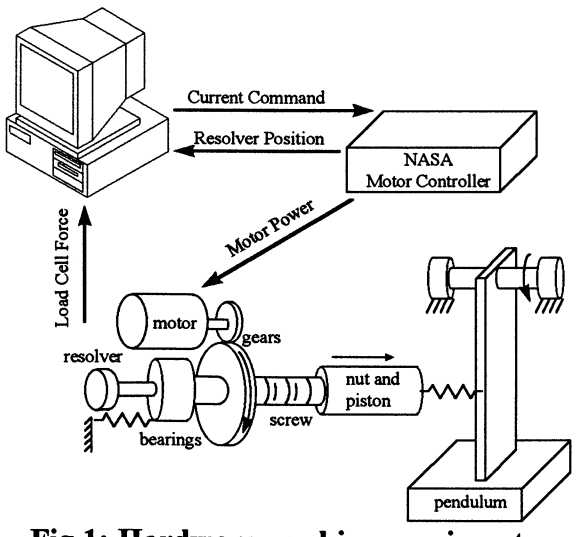

Fig.1: Hardware used in experiments

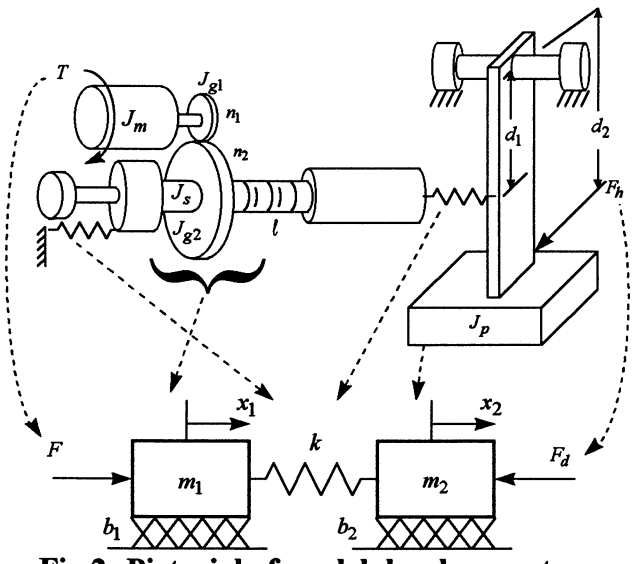

Fig.2: Pictorial of model development

A pictorial representation of the model development is shown in Fig.2. Equations (1) through (5) are necessary for the calculation of some of the model parameters. A linear model of the mechanical system is given in equations (6) through (9).

$$N = n_1 \ell / (2\pi n_2) \tag{1}$$

$$m_1 = (J_m + J_{g1}) / N^2 + (J_s + J_{g2})(2\pi / \ell)^2 \tag{2}$$

$$m_2 = J_p / d_1{}^2 \tag{3}$$

$$F = T / N \tag{4}$$

$$F_d = F_h d_2 / d_1 \tag{5}$$

$$F(s) = (m_1 s^2 + b_1 s + k) X_1(s) - k X_2(s) \tag{6}$$

$$F_d(s) = (m_2 s^2 + b_2 s + k) X_2(s) - k X_1(s) \tag{7}$$

$$\frac{X_1(s)}{F(s)} = \frac{m_2 s^2 + b_2 s + k}{s(m_1 m_2 s^3 + (m_1 b_2 + m_2 b_1) s^2 + (m_1 k + m_2 k + b_1 b_2) s + k(b_1 + b_2))} \tag{8}$$

$$\frac{X_2(s)}{X_1(s)} = \frac{k}{m_2 s^2 + b_2 s + k} \tag{9}$$

Fig. 3 is a block diagram representation of a more complete linear model of the system including the final control architecture chosen after evaluation of several different architectures. The proportional-integral-derivative (PID) position controller and the dynamic force feedback (DFF) compensation filter are implemented digitally in the PC. The force transmitted, $F_t(s)$, through the actuator is measured by the load cell. The DFF filter is similar to the dynamic pressure feedback (DPF) compensation currently used in the controllers for the hydraulic actuators used on the Space Shuttle Main Engines (SSME) (Davis 1973a, Davis 1973b).

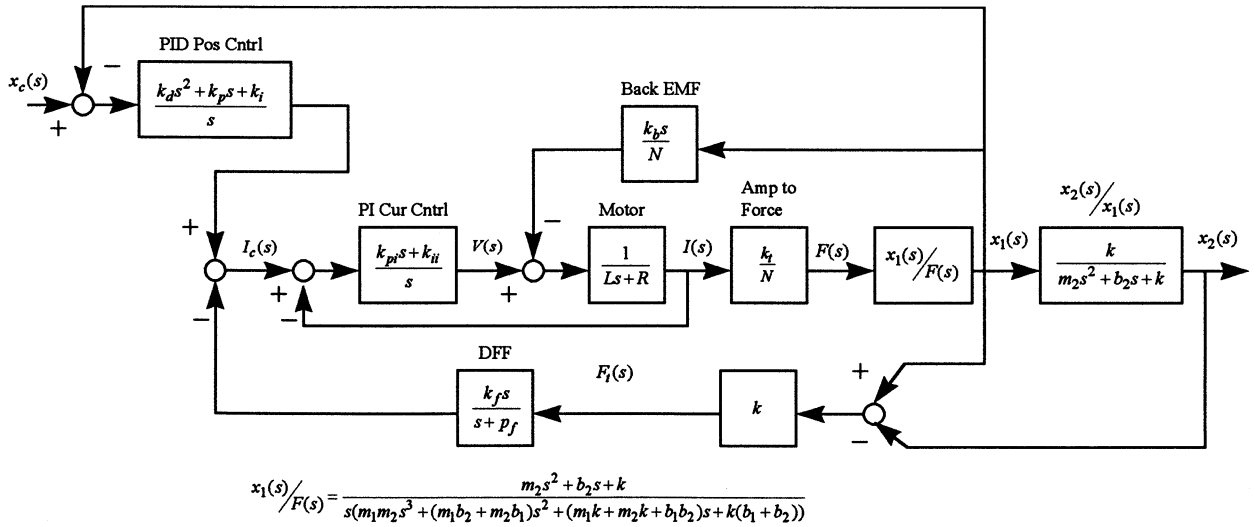

Fig.3: Linear model

Controller Design

A position controller and transmitted force controller have contradictory goals. Therefore, an attempt to simultaneously use two separate compensation loops like the PID controller and the DFF filter in Fig.3 will result in ineffective control of the force and/or the position unless they operate at different frequencies. However, it is advantageous to reduce the undesirable effects of position feedback at resonance. Furthermore, the engine start transient forces occur mainly at the resonant frequency of the system. Therefore, the basic concept of the controller design is to design the position and the force loops separately, with the position loop having good performance at low frequencies and the DFF loop having good performance around the resonance. This is depicted in Fig.4.

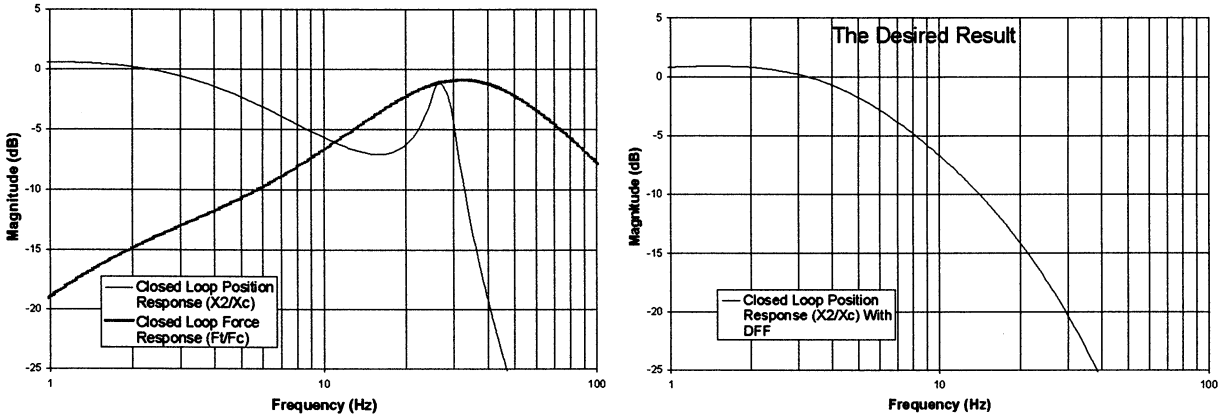

Fig.4: Concept of the control design

The linear model in Fig.3 is reduced slightly for controller design. A simpler model is shown in Fig.5. The electrical dynamics of the current controller and the back emf feedback have been removed. As will be seen in the results, this simplification did not significantly affect the response. Equations (10) through (15) and (16) through (19) are design equations developed for the PID position controller and the DFF filter respectively. These equations should be applied with discretion since every situation will be slightly different. However, they should be a good starting point for any similar design.

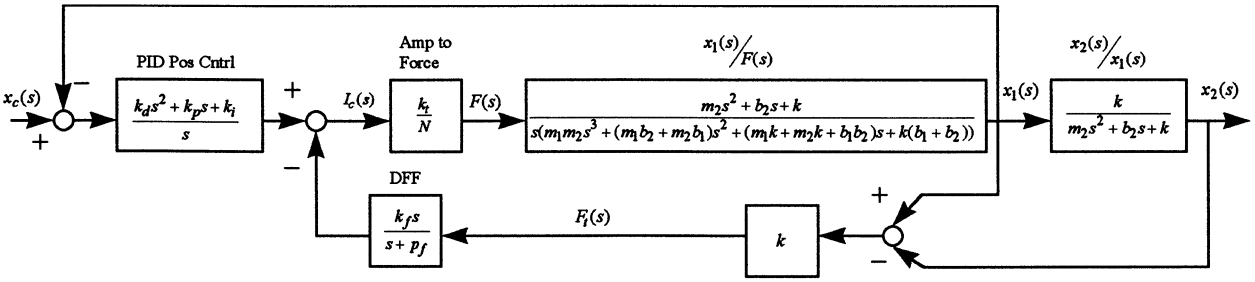

Fig.5: Linear model used in compensation design

$$\omega_{BWp} = 2\pi(\text{Target Position BandWidth in Hz}) \tag{10}$$

$$z_1 = \frac{(b_1 + b_2)}{(m_1 + m_2)} \tag{11}$$

$$z_2 = \frac{\omega_{BWp}}{10} \tag{12}$$

$$k_d = \frac{1}{\left|G_1(j\omega_{BWp})\right|} = \sqrt{\frac{{\omega_{BWp}}^4\left((m_1+m_2)N/k_t\right)^2}{{\omega_{BWp}}^2+\left(\omega_{BWp}/10\right)^2}}, \text{ where } G_1(s) = \frac{k_t(s+z_2)}{N(m_1+m_2)s^2} \tag{13}$$

$$k_p = k_d(z_1+z_2) \tag{14}$$

$$k_i = k_d z_1 z_2 \tag{15}$$

$$\omega_{res} = 2\pi(\text{Position Resonance in Hz}) \tag{16}$$

$$p_f = 10\omega_{res} \tag{17}$$

$$\omega_{BWf} = 2\omega_{res} \tag{18}$$

$$k_f = \frac{1}{\left|G_2(j\omega_{BWf})\right|} \text{ where } G_2(s) = \frac{k_t k(m_2 s+b_2)s}{N(s+p_f)(m_1m_2s^3+(m_1b_2+m_2b_1)s^2+(m_1k+m_2k+b_1b_2)s+k(b_1+b_2))} \tag{19}$$

Results

The design equations, (10) through (19), were applied to the system used in the experiments. Data for the frequency response of the closed loop position system and for the time response of the transmitted force resulting from hammer impulses was taken. Fig.6 shows the experimentally developed frequency response of the system with and without the DFF compensation. The data points are indicated with dots. The frequency response obtained from the linear model in Fig.5 is also shown. The results are quite encouraging. The DFF reduced the resonant peak by a factor of 10 (20 dB). Furthermore, the models match the actual data fairly well. Similar results were obtained for a 10 Hz position bandwidth design. This reduction in the resonance is a very important result not only because it drastically decreases the magnitude of the forces in the actuator but also because it will result in a more stable subsystem to be used in the control of the dynamic vehicle system.

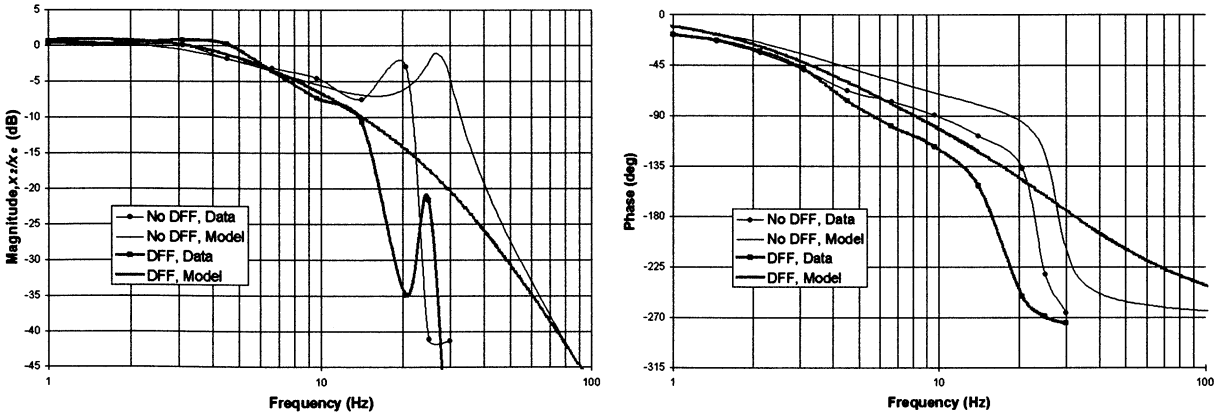

Fig.6: Frequency response of the closed loop position systems w/ 5Hz bandwidth design (0.1 inch amplitude sinusoidal command except at resonance)

Fig.7 illustrates a typical hammer impulse response of the transmitted force. This response is shown along with a simulated response from a nonlinear simulation model constructed in

Simulink™ from Math Works Inc. This model includes all of the dynamics in the linear model shown in Fig.3 and several nonlinear effects such as backlash, static friction, motor current saturation, and voltage saturation. Fig.8 shows some of the experimental data obtained from the many impulse hammer tests conducted. It plots the peak magnitude of the transmitted force versus the area of the hammer impulse. It shows results obtained from several systems: a 10 Hz bandwidth position controller and no DFF, the system with no power applied to the motor controller, a 10 Hz bandwidth position controller with DFF, and a 5 Hz bandwidth position controller with DFF. The DFF significantly reduced the transmitted force. It should therefore reduce the effects of engine start transients on an EMA.

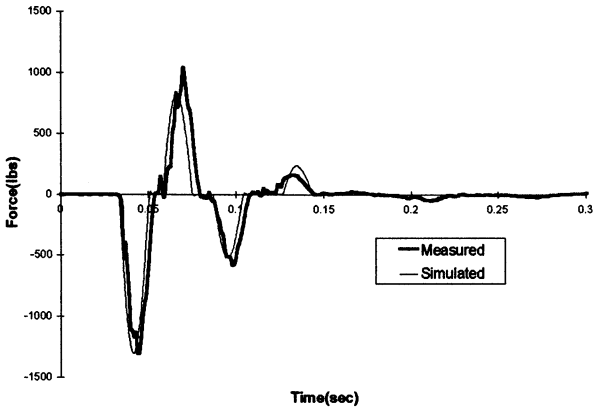

Fig.7: Transmitted force due to a hammer impulse area impulse of 5.8 lb*s; position control only

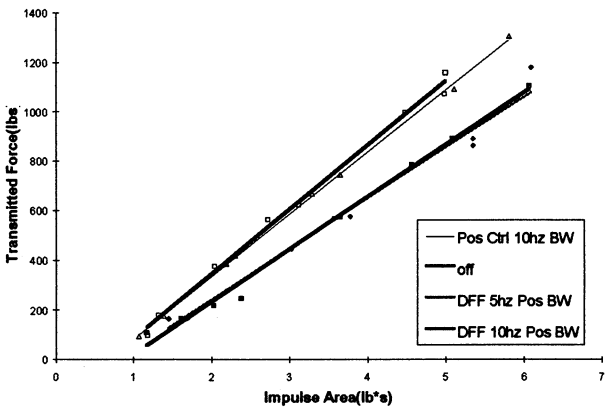

Fig.8: Peak transmitted force vs. hammer

It is reasonable to expect the DFF to reduce the peak force due engine start transients even more than the results in Fig.8. This is because the engine transient forces usually take a few force oscillation cycles to build before they start to decay, unlike the impulse response shown in Fig.7. The forcing function for the transient forces is probably somewhere "in between" an impulse input and driving the position controller at the resonance. At resonance the forces build with time to a large steady state oscillation. By driving the 5 Hz bandwidth position controller without the DFF with a 0.05 in. amplitude sinusoid at resonance, the load cell output is saturated at 2500 lb by the oscillation peaks. However, with the DFF the same input results in a peak amplitude of approximately 600 lb.

References

Davis, M. E. (1973a), *Optimum Gains Determination.* Unpublished report to Mr. C. S. Cornelius, Report No. SP-261-0805 NASA MSFC, October 9,1973.

Davis, M. E. (1973b), *Bulk Modulus and Valve Dynamics Effect on Linear SSME-TVC.* Unpublished report to Mr. C. S. Cornelius, Report No. SP-261-0805-1 NASA MSFC, October 10,1973.

1997

NASA/ASEE SUMMER FACULTY FELLOWSHIP PROGRAM

MARSHALL SPACE FLIGHT CENTER
THE UNIVERSITY OF ALABAMA IN HUNTSVILLE

MODELING OF A TWO-PHASE JET PUMP WITH PHASE CHANGE, SHOCKS AND TEMPERATURE-DEPENDENT PROPERTIES

Prepared By: S.A. Sherif, Ph.D.

Academic Rank: Associate Professor

Institution and Department: University of Florida
Department of Mechanical Engineering

NASA/MSFC

Office: Thermal Engineering and Design Branch
Division: Thermal and Life Support Division

MSFC Colleague: Patrick L. Hunt

Introduction

One of the primary motivations behind this work is the attempt to understand the physics of a two-phase jet pump which constitutes part of a flow boiling test facility at NASA-Marshall. The flow boiling apparatus is intended to provide data necessary to design highly efficient two-phase thermal control systems for aerospace applications. The facility will also be capable of testing alternative refrigerants and evaluate their performance using various heat exchangers with enhanced surfaces. The test facility is also intended for use in evaluating single-phase performance of systems currently using CFC refrigerants.

Literature dealing with jet pumps is abundant and covers a very wide array of application areas. Example application areas includes vacuum pumps which are used in the food industry, power station work, and the chemical industry; ejector systems which have applications in the aircraft industry as cabin ventilators and for purposes of jet thrust augmentation; jet pumps which are used in the oil industry for oil well pumping; and steam-jet ejector refrigeration, to just name a few. Examples of work relevant to this investigation includes those of Fairuzov and Bredikhin (1995).

While past researchers have been able to model the two-phase flow jet pump using the one-dimensional assumption with no shock waves and no phase change, there is no research known to the author apart from that of Anand (1992) who was able to account for condensation shocks. Thus, one of the objectives of this work is to model the dynamics of fluid interaction between a two-phase primary fluid and a subcooled liquid secondary fluid which is being injected employing atomizing spray injectors. The model developed accounts for phase transformations due to expansion, compression, and mixing. It aslo accounts for shock waves developing in the different parts of the jet pump as well as temperature and pressure dependencies of the fluid properties for both the primary two-phase mixture and the secondary subcooled liquid.

Analysis

The objective of this research effort is to develop an analytical model capable of predicting the performance of a two-phase jet pump. The model developed will account for phase transformations which are likely to take place in the nozzle, mixing chamber and diffuser (see Figure 1). Complete details of this model can be obtained from the NASA colleague.

Primary Nozzle. The approach employed in the analysis described in this report is an extension of the isentropic homogeneous expansion (IHE) model described in the literature. In addition to the primary nozzle, the extension to the model covers the rest of the jet pump components and is thus labled as an isentropic homogeneous expansion/ compression (IHE/C) method. This method assumes that the velocities of the two phases are equal and that thermal equilibrium between the phases exists. It further assumes that both the expansion in the nozzle and compression in the diffuser are isentropic and that the working fluid property data correspond to those of a static, equilibrium, two-phase system with plane interfaces.

In order to be able to deal with the flow in the jet pump as a homogeneous two-phase mixture, equivalent properties are derived for the mixture in terms of corresponding properties for its vapor and liquid phases. In the nozzle part of the jet pump, the two-phase primary fluid will be treated as predominantly gaseous with liquid particles suspended in it. It is hypothesized that the presence of the liquid particles in the mixture is such that the latter can still behave as a gas, but with modified properties.

The mass flow rate of the two-phase fluid flowing through the primary nozzle can be expressed according to the following equation (Shapiro, 1953):

$$m_n = \frac{A_n p_{ni}}{\sqrt{T_{ni}}} \sqrt{\frac{\gamma_n}{R_n}} \frac{M_n}{\left[1+\frac{(\gamma_n-1)}{2} M_n^2\right]^{(\gamma_n+1)/[2(\gamma_n-1)]}} \tag{1}$$

where the quantities with the subscript "n" are those of the two-phase primary fluid while flowing through the nozzle. To obtain an expression for the specific heat ratio of the primary fluid, γ_n, the mixture quality in the primary nozzle, x_n, is used in conjunction with the definition of γ_n:

$$\gamma_n = \frac{C_{p,n}}{C_{v,n}} = \frac{x_n C_{p,g,n} + (1-x_n) C_{L,n}}{x_n C_{v,g,n} + (1-x_n) C_{L,n}} \tag{2}$$

Utilizing the following relationships

$$R_{g,n} = C_{p,g,n} - C_{v,g,n} \tag{3}$$

$$C_{p,g,n} = \gamma_{g,n} C_{v,g,n} \tag{4}$$

Equation (2) can be rewritten as

$$\gamma_n = \frac{x_n \gamma_{g,n} R_{g,n} + (1-x_n)(\gamma_{g,n}-1) C_{L,n}}{x_n R_{g,n} + (1-x_n)(\gamma_{g,n}-1) C_{L,n}} \tag{5}$$

To obtain an expression for the two-phase gas constant of the primary fluid, R_n, we utilize the expressions for $C_{p,n}$, $C_{v,n}$ and the definition of R_n to get

$$R_n = x_n R_{g,n} \tag{6}$$

With the exception of the specific heat at constant-pressure of the vapor phase, the properties of interest are fairly independent of temperature and pressure. For the two-phase primary fluid, the properties $C_{p,n}$, $C_{v,n}$, γ_n, and R_n are therefore going to be predominantly functions of the primary fluid vapor-liquid composition or the quality, x_n, and will be functions of temperature to the extent that $C_{p,g,n}$ depends on the temperature. Having established this fact, we can now proceed to perform two-phase calculations

throughout the nozzle to establish the conditions of the two-phase primary fluid at the nozzle exit. This will be done by first computing the mixture specific entropy at nozzle inlet, s_{ni}, as follows:

$$s_{ni} = s_{ni,L} + x_{ni}\,(s_{ni,g} - s_{ni,L}) \tag{7}$$

where $s_{ni,g}$ and $s_{ni,L}$ represent the saturated vapor and saturated liquid specific entropies evaluated at the nozzle inlet pressure, p_{ni}.

Next, the nozzle exit pressure is assumed and the saturated vapor and saturated liquid specific entropies, $s_{ne,g}$ and $s_{ne,L}$, respectively, are computed. Since the flow is assumed isentropic throughout the nozzle, the specific entropy at the nozzle exit will be equal to that at the nozzle inlet. This allows the quality of the primary fluid at the exit, x_{ne}, to be computed

$$x_{ne} = \frac{(s_{ne} - s_{ne,L})}{(s_{ne,g} - s_{ne,L})} \tag{8}$$

Since the exit pressure has been assumed, the exit temperature will have also been specified (since the fluid is in the mixture region). This allows computing the vapor specific heat at constant pressure, $C_{p,g,ne}$, the gas constant of the vapor phase, $R_{g,ne}$, and the vapor phase ratio of specific heats, $\gamma_{g,ne}$ all evaluated at the nozzle exit. These, in addition to the primary fluid quality computed from Equation (8), can then be used to compute the primary fluid specific heat ratio from Equation (5).

Now that the exit pressure and mixture specific heat ratio are known, the exit Mach number can be computed employing the following equation (Shapiro, 1953):

$$M_{ne} = \left\{ \frac{2}{(\gamma_{ne} - 1)} \left[\left(\frac{p_{ni}}{p_{ne}} \right)^{(\gamma_{ne}-1)/\gamma_{ne}} - 1 \right] \right\}^{1/2} \tag{9}$$

Using the exit Mach number, M_{ne}, along with the value of the primary fluid specific heat ratio, γ_{ne}, the area ratio between the exit and throat can be computed using the following equation (Shapiro, 1953):

$$\frac{A_{ne}}{A_{nt}} = \frac{1}{M_{ne}} \left[\frac{2}{(\gamma_{ne} + 1)} \left\{ 1 + \frac{(\gamma_{ne} - 1)}{2} M_{ne}^2 \right\} \right]^{(\gamma_{ne}+1)/[2(\gamma_{ne}-1)]} \tag{10}$$

Since A_{ne}/A_{nt} is a known quantity for a specified nozzle geometry, the area ratio computed from Equation (10) can now be compared to that assigned by the nozzle configuration. If the two values did not agree, then Equation (10) can be used to compute the Mach number at the nozzle exit corresponding to the actual area ratio, but employing the computed value of γ_{ne} from the previous calculation step. The new value of the Mach number can now be used to compute a new value for the nozzle exit pressure, p_{ne}, using the following equation (Shapiro, 1953):

$$\frac{p_{ni}}{p_{ne}} = \left[1 + \frac{(\gamma_{ne} - 1)}{2} M_{ne}^2\right]^{\gamma_{ne}/(\gamma_{ne}-1)} \tag{11}$$

Again, the value of γ_{ne} used in Equation (11) is the same as the one employed in the previous calculation step. Once the nozzle exit pressure has been found, the exit temperature, T_{ne} can also be found since the primary fluid is a two-phase mixture. The new exit temperature is then used to correct the value of the vapor phase specific heat at constant pressure, $C_{p,g,ne}$, and the vapor phase gas constant, $R_{g,ne}$, both evaluated at the nozzle exit. As mentioned earlier, variations in the gas phase ratio of specific heats as well as the specific heat of the liquid phase are relatively insensitive to temperature variations in the temperature range of interest to this study. While updating the values of these parameters to account for the newly calculated temperature value at the nozzle exit is relatively straightforward, it will not be performed here since its effect on the accuracy of the results should be fairly minimal.

With the newly calculated exit pressure, the specific entropies of the saturated vapor and saturated liquid evaluated at the nozzle exit pressure can be found and used to calculate the updated value of the primary fluid quality at the nozzle exit using Equation (8) and the isentropic flow assumption. This quality can, in turn, be used to calculate the primary fluid ratio of specific heats at the exit, γ_{ne}, employing Equation (5). Knowing, γ_{ne}, a new value for the Mach number at the exit can be calculated using Equation (9) and subsequently a new area ratio can be calculated using Equation (10). The calculated area ratio should then be compared to the actual area ratio, and in case they do not agree, the whole procedure is repeated until convergence.

After convergence has been reached, the values of all the relevant parameters of the primary fluid at the nozzle exit should be updated. This should include the ratio of specific heats γ_{ne}, gas constant R_{ne}, specific heats $C_{p,ne}$ and $C_{v,ne}$, temperature T_{ne}, pressure p_{ne}, quality x_{ne}, entropy s_{ne}, enthalpy h_{ne}, density ρ_{ne}, and Mach number M_{ne}. The enthalpy can be computed using the following equation:

$$h_{ne} = h_{ne,L} + x_{ne}\,(h_{ne,g} - h_{ne,L}) \tag{12}$$

where $h_{ne,L}$ and $h_{ne,g}$ represent the saturated liquid and saturated vapor enthalpies evaluated at the exit pressure, p_{ne}. The density, ρ_{ne}, on the other hand, can be computed from the following equation (Shapiro, 1953):

$$\frac{\rho_{ni}}{\rho_{ne}} = \left[1 + \frac{(\gamma_{ne} - 1)}{2} M_{ne}^2\right]^{1/(\gamma_{ne}-1)} \tag{13}$$

Of course the specific volume at the nozzle exit, v_{ne}, is the reciprocal of the density and can easily be determined. The mass flow rate of the primary fluid can now be computed from Equation (1). The area employed in the equation should correspond to the exit section since the Mach number and fluid properties used correspond to the exit.

With the knowledge of the mass flow rate, as well as the exit area and density, the nozzle exit velocity can be computed using the continuity equation

$$V_{ne} = \dot{m}_n / (\rho_{ne}\, A_{ne}) \tag{14}$$

where the quantities $v_{ni,g}$ and $v_{ni,L}$ represent the specific volume of the saturated vapor and saturated liquid of the primary fluid evaluated at the nozzle inlet pressure, p_{ni}.

Liquid Sprayers. As was reported earlier, atomizing sprayers are used to inject subcooled liquid into the mixing chamber of the jet pump. In order to relate the pressure and velocity of the secondary liquid at the inlet of the mixing chamber to those at the inlet of the sprayers, Bernoulli's equation is used

$$\left(p_{si} - p_{mi}\right) = \frac{1}{2}\rho_s\left(V_{s,mi}^2 - V_{si}^2\right) \tag{15}$$

Additional details can be found with the NASA colleague.

Mixing Chamber. The governing conservation equations for a control volume representing the mixing chamber are those of the continuity, momentum, and energy (in integrated forms):

$$\dot{m}_m = \dot{m}_n + \dot{m}_s \tag{17}$$

$$A_{ne}\, p_{ne} + A_s\, p_{mi}\cos\alpha - A_{me}\, p_{me} = \dot{m}_m V_{me} - \dot{m}_n V_{p,mi} - \dot{m}_s V_{s,mi}\cos\alpha \tag{18}$$

$$\dot{m}_m\left(h_{me} + \frac{V_{me}^2}{2}\right) = \dot{m}_n\left(h_{ni} + \frac{V_{ni}^2}{2}\right) + \dot{m}_s\left(h_{si} + \frac{V_{si}^2}{2}\right) \tag{19}$$

Additional details about the mixing chamber analysis can be found with the NASA colleague.

Throat and Diffuser. Because it is highly likely that a condensation shock would take place some where in either the throat or the diffuser, the latter will be divided into three segments; the part of the diffuser upstream of the shock, the shock layer itself, and the part of the diffuser downstream of the shock. For both parts upstream and downstream of the shock, control volume analyses will be performed. For the shock layer, the standard normal shock relations for a two-phase substance will be implemented.

The problem on hand can proceed in two different but equivalent routes. The first route is to assume the location of the condensation shock and let the solution predict the diffuser exit conditions. This route leads to predicting the jet pump compression ratio with a prescribed shock location. The other route is one in which the exit pressure of the diffuser is controlled (such as the work of Fairuzov and Bredikhin, 1995) and the location of the shock is determined as part of the solution. In this report, the latter approach is chosen. Complete details on the governing equations of the throat and diffuser can be found with the NASA colleague.

Conclusions

The research effort on which this document partly reports described a relatively simple model capable of describing the performance of a two-phase flow jet pump. The model is based on the isentropic homogeneous expansion/compression hypothesis and is capable of fully incorporating the effects of shocks in both the mixing chamber and the throat/diffuser parts of the pump. The physical system chosen is identical to that experimentally tested by Fairuzov and Bredikhin (1995) and should therefore relatively easy to validate.

References

Anand, G., 1992, "Phenomenological and Mathematical Modeling of a High Pressure Steam Driven Jet Injector," Ph.D. Dissertation, The Ohio State University, Columbus, Ohio.

Fairuzov, Y.V. and Bredikhin, V.V., 1995, "Two-Phase Cooling System with a Jet Pump for Spacecraft," AIAA *Journal of Thermophysics and Heat Transfer*, Vol. 9, No. 2, April-June, pp. 285-291.

Shapiro, A.H., 1953, *The Dynamics and Thermodynamics of Compressible Fluid Flow*, The Ronald Press Company, New York, New York.

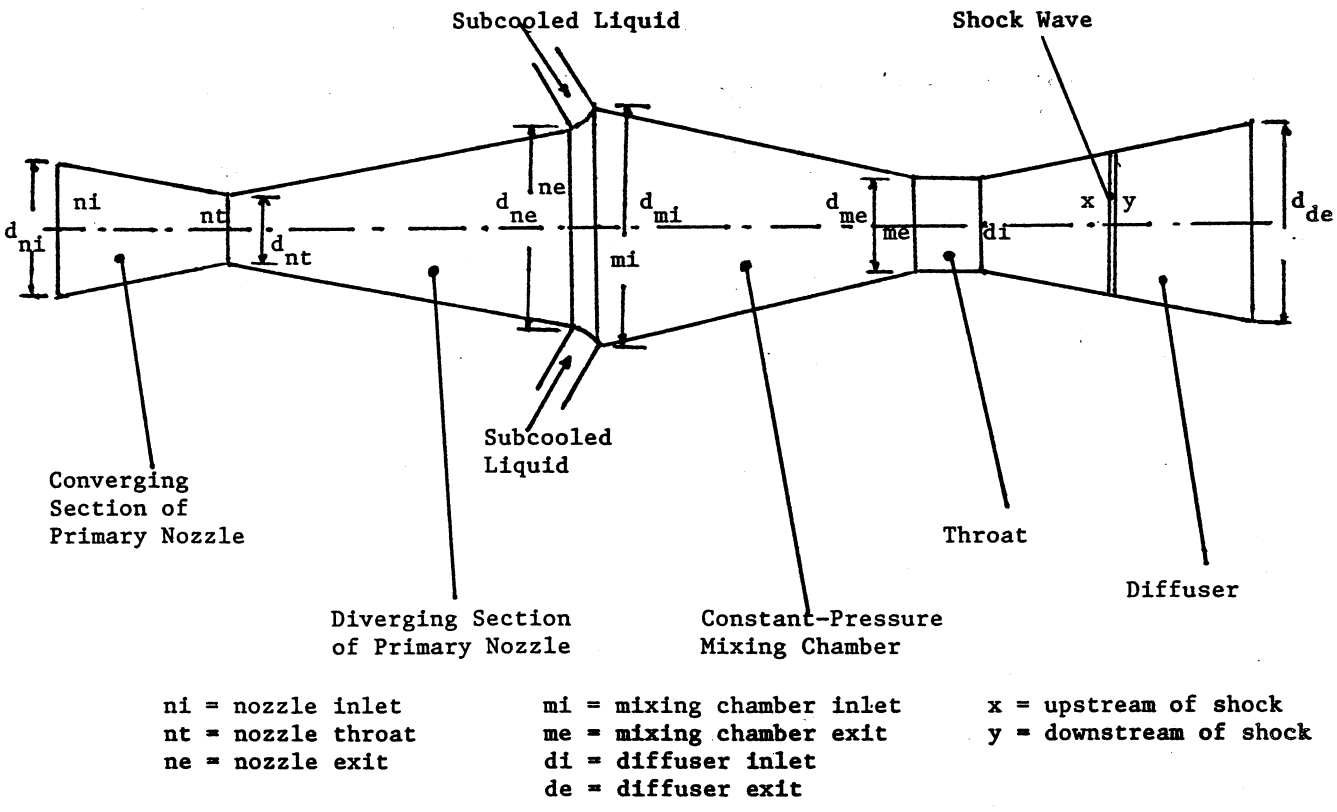

Figure 1. Physical model of the jet pump

1997

NASA/ASEE SUMMER FACULTY FELLOWSHIP PROGRAM

MARSHALL SPACE FLIGHT CENTER
THE UNIVERSITY OF ALABAMA IN HUNTSVILLE

SOFTWARE PRODUCTS FOR TEMPERATURE DATA REDUCTION OF PLATINUM RESISTANCE THERMOMETERS (PRT)

Prepared By:	Jerry K. Sherrod, Ph.D.
Institution and Department:	Pellissippi State Technical Community College Business and Computer Technology
NASA/MSFC:	Instrumentation Branch Astrionics Laboratory
MSFC Colleague:	William B. White

Introduction

The main objective of this project is to create user-friendly personal computer (PC) software for reduction/analysis of platinum resistance thermometer (PRT) data.

The Callendar-Van Dusen Equation

The Callendar-Van Dusen equation is the accepted method (International Temperature Scale - 1927, ITS-27, and International Practical Temperature Scale - 1948, IPTS-48) for calculating resistance, *R*, given a temperature, *t*, for PRTs.

The general expression for the Callendar-Van Dusen equation is: (Rosemount Report 68023F)

$$R_t = R_0\left\{1+\alpha\left[t-\delta\left(\frac{t}{100}\right)\left(\frac{t}{100}-1\right)-\beta\left(\frac{t}{100}-1\right)\left(\frac{t}{100}\right)^3\right]\right\} \qquad (1)$$

where: Rt = resistance at temperature t (ohms)
R0 = resistance at 0°C
t = temperature, °C
α, δ, and β are calibration constants

For temperatures above 0°C, $\beta = 0$, and equation (1) becomes

$$R_t = R_0\left\{1+\alpha\left[t-\delta\left(\frac{t}{100}\right)\left(\frac{t}{100}-1\right)\right]\right\} \qquad (2)$$

and this equation is known as the **Callendar Equation**.

When $t_1 = 100°C$ then, from equation (2)

$$\alpha = \frac{R_{100}-R_0}{100R_0} \qquad (3)$$

where α is the temperature coefficient over the range 0°C to 100°C.

Knowing the value of α, δ can be calculated from a third calibration point, t_2 as follows:

$$\delta = \frac{t_2 - \left(R_{t_2} / R_0 - 1 \right) / \alpha}{\left(t_2 - 100 \right)\left(t_2 / 100 - 1 \right)} \tag{4}$$

Finally, knowing the value of α and δ, β can be calculated from a fourth calibration point, t_2, (below 0°C) as follows:

$$\beta = \frac{R_0\left(1 + \alpha t_3 \right) - R_{t_3}}{R_0 \alpha \left(t_3 / 100 - 1 \right)\left(t_3 / 100 \right)^3} - \frac{\delta}{\left(t_3 / 100 \right)^2} \tag{5}$$

For efficient computation, however, a method that relates α, β, and δ is desirable. For this reason, constants **A**, **B**, and **C** can be computed as follows:

$$A = \alpha(1 + \delta/100) \tag{6}$$

$$B = -\alpha\delta/10^4 \tag{7}$$

$$C = -\alpha\beta/10^8 \tag{8}$$

or

$$\alpha = A + 100B \tag{9}$$

$$\delta = -10^4 B/(A + 100B) = 10^4 B/\alpha \tag{10}$$

$$\beta = -10^8 C/(A + 100B) = -10^8 C/\alpha \tag{11}$$

With these constants, equation (1) may be computed with

$$W = 1 + At + Bt^2 + Ct^3(t-100) \tag{12}$$

where W is the resistance ratio R_t/R_0 and C = 0 when t > 0°C

This approach allows the calibration to use three temperature points in addition to 0°C. One is a low temperature < 150°C, another is a high temperature > 250°C, and a third temperature ≅ 100°C. The constants A, B, and C may be computed by solution of the simultaneous equations:

$$W_1 = 1 + At_1 + Bt_1^2 \quad \text{for } (T_1 > 0°C) \tag{13}$$

$$W_2 = 1 + At_2 + Bt_2^2 \quad \text{for } (T_2 > 0°C) \tag{14}$$

$$W_3 = 1 + At_3 + Bt_3^2 + Ct_3^3(t_3 - 100) \quad \text{for } (t_3 < 0°C) \tag{15}$$

The solution set is as follows:

$$A = \frac{\left(W_2 - 1\right)t_1 / t_2 - \left(W_1 - 1\right)t_2 / t_1}{t_1 - t_2} \tag{16}$$

$$B = \frac{\left(W_2 - 1\right) / t_2 - \left(W_1 - 1\right) / t_1}{t_2 - t_1} \tag{17}$$

$$C = \frac{W_3 - 1 - At_3 - Bt_3^2}{t_3^3\left(t_3 - 100\right)} \tag{18}$$

Solving for Temperature

Equation (12) must be solved for temperature, *t*, to easily compute the temperature represented by a measured resistance. For temperatures above 0°C only, the solution is as follows:

$$t = \frac{\sqrt{A^2 - 4B(1 - W)}}{2B} - A \tag{19}$$

For temperatures < 0°C, another method must be used. The first derivative of equation (12) is used to successively approximate *t*. This equation is

$$\frac{dW}{dt} = A + 2Bt + 4Ct^{2}(t - 75) \qquad (20)$$

where C = 0 for t > 0°C

Software Products for Using these Methods

Software products were designed and created to help users of PRT data with the tasks of using the Callendar-Van Dusen method. Sample runs are illustrated in this report. The products are available from Mr. Bill White, Bldg. 4487, EB-22, Marshall Space Flight Center, Alabama 35812.; telephone (205) 544-6417; email: William.B.White@msfc.nasa.gov.

Sample Output

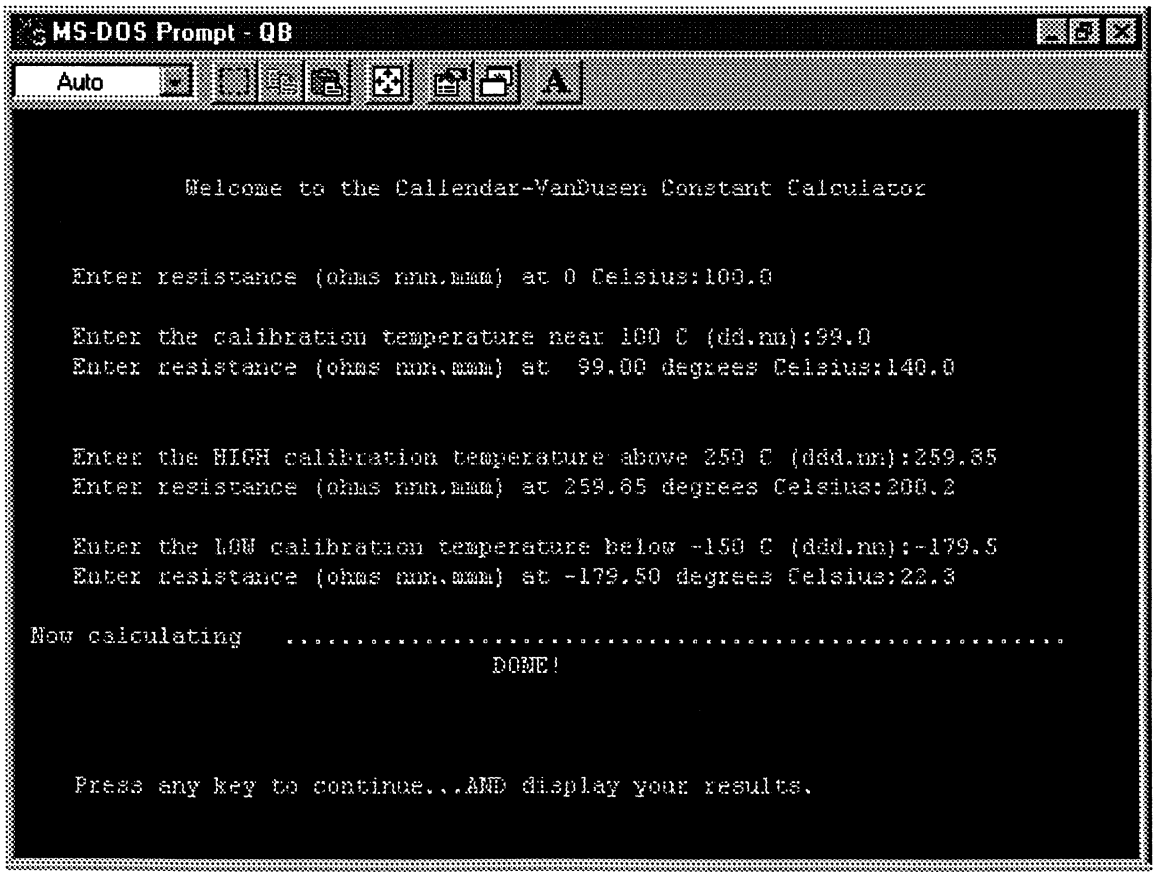

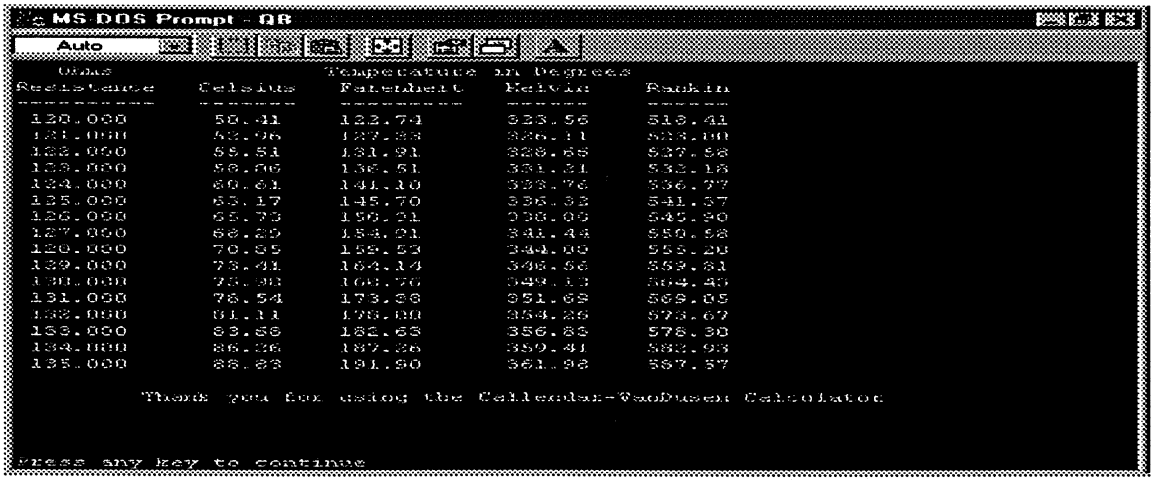

Acknowledgments

The author would like to acknowledge the assistance and guidance of NASA colleague William B. (Willie) White in this research. In addition, the entire team members of EB-22 (B Wing), especially Bobby Money, James Currie, Clint Patrick, and Branch Chief Joe Zimmerman helped acquaint me with the facilities and procedures of the laboratory and branch.

References

Temperature Calibration and Interpolation Methods for Platinum Resistance Thermometers, Rosemount Report 68023F, Rosemount Inc.

1997
NASA/ASEE SUMMER FACULTY FELLOWSHIP PROGRAM

MARSHALL SPACE FLIGHT CENTER
THE UNIVERSITY OF ALABAMA IN HUNTSVILLE

X33 REUSABLE LAUNCH VEHICLE CONTROL ON SLIDING MODES: CONCEPTS FOR A CONTROL SYSTEM DEVELOPMENT

Prepared By:	Yuri B. Shtessel, Ph.D.
Academic Rank:	Associate Professor
Institution and Department:	University of Alabama in Huntsville Department of Electrical and Computer Engineering
NASA/MSFC:	
Office:	Structures and Dynamics Laboratory
Division:	Guidance and Control Systems
MSFC Colleagues:	Neal D. Hendrix Charles Hall Mark Jackson Don Krupp

Introduction

Control of the X33 reusable launch vehicle is considered. The launch control problem consists of automatic tracking the launch trajectory which as assumed to be optimally precalculated. It requires development of reliable, robust control algorithm that can automatically adjust to some changes in mission specifications (mass of payload, target orbit) and the operating environment (atmospheric perturbations, interconnection perturbations from the other subsystems of the vehicle, thrust deficiencies, failure scenarios). One of the effective control strategies successfully applied in nonlinear systems is the *Sliding Mode Control.* The main advantage of the Sliding Mode Control is that the system's state response in the sliding surface remains insensitive to certain parameter variations, nonlinearities and disturbances.

Concepts for a Control System Development

The three-time-scale controller is designed for the X33 vehicle launch (ascending) mode. The outer loop (guidance) controller is designed using dynamic inversion or sliding mode control technique. The vector of angular rates command is formed in the outer loop to provide an asymptotic tracking of the Euler angles' reference profiles. This vector is tracked in the inner loop via the smoothed sliding mode controllers. Roll, pitch and yaw torque signals are considered as control inputs. The inner loop transient response must be much faster then the outer loop one. A control allocation algorithm is employed to allocate torque commands into end-effector deflection commands, which are executed by actuators. The desired transient response of execution of end-effector deflection commands can be achieved via the "very-inner loop" controller. A structure of the X33 vehicle control system is developed and shown in fig.1.

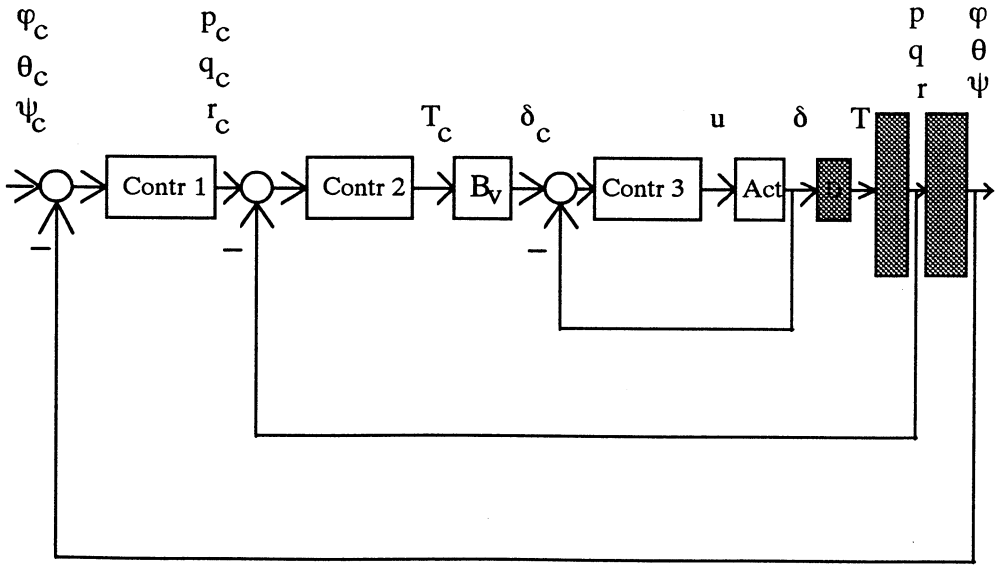

Fig. 1 A structure of the X-33 vehicle control system

Mathematical Model

Orientation equations are given in terms of Euler angles ψ, θ, φ and body rates p, q, r.

$$\begin{bmatrix} \dot{\varphi} \\ \dot{\theta} \\ \dot{\psi} \end{bmatrix} = R(\varphi,\theta,\psi)\begin{bmatrix} p \\ q \\ r \end{bmatrix}, \qquad R(\varphi,\theta,\psi) = \begin{bmatrix} 1 & \tan\theta\sin\varphi & \tan\theta\cos\varphi \\ 0 & \cos\varphi & -\sin\varphi \\ 0 & \dfrac{\sin\varphi}{\cos\theta} & \dfrac{\cos\varphi}{\cos\theta} \end{bmatrix} \tag{1}$$

The equations of the X33 vehicle rotational motion are

$$\begin{bmatrix} \dot{p} \\ \dot{q} \\ \dot{r} \end{bmatrix} = \begin{bmatrix} f_1(p,q,r,t,J) \\ f_2(p,q,r,t,J) \\ f_3(p,q,r,t,J) \end{bmatrix} + B_1(J)\begin{bmatrix} L \\ M \\ N \end{bmatrix} \tag{2}$$

$$\begin{cases} f_1(p,q,r,t,J) = \dfrac{1}{J_{xx}}\left[J_{xy}\dot{r} - qr\left(J_{zz} - J_{yy}\right) + J_{xz}pq\right] + M_{1d}(t) \\ f_2(p,q,r,t,J) = \dfrac{1}{J_{yy}}\left[-pr\left(J_{xx} - J_{zz}\right) - J_{xz}\left(p^2 - r^2\right)\right] + M_{2d}(t), \\ f_3(p,q,r,t,J) = \dfrac{1}{J_{zz}}\left[J_{xz}\dot{p} - pq\left(J_{yy} - J_{xx}\right) - J_{xz}qr\right] + M_{3d}(t) \end{cases} \quad \mathrm{B_1(J)} = \begin{bmatrix} \dfrac{1}{J_{xx}} & 0 & 0 \\ 0 & \dfrac{1}{J_{yy}} & 0 \\ 0 & 0 & \dfrac{1}{J_{zz}} \end{bmatrix}$$

The vector of control moments $T = \left[L, M, N\right]^T$ is generated by five aerodynamic surfaces and an engine, and is related to the deflection vector $\delta \in \Re^8$ as follows: $T = D(.)\delta$, where $D(.) \in \Re^{3\times 8}$ is a nonlinear matrix calculated on the basis of a table-look-up data. The mathematical models of actuators are taken as follows:

$$\begin{cases} \dot{x}_{i,1} = x_{i,2} \\ \dot{x}_{i,2} = -\omega_i^2 x_{i,1} - 2\xi\omega_i x_{i,2} + \omega_i^2 u_i \\ \delta_i = x_{i,1} \end{cases} \tag{3}$$

where u_i is a control input, $\omega_i = 26.4\, rad/s$, and $\xi_i = 0.7 \quad \forall i = \overline{1,3}$.

The problem is to design the control laws $u_i \quad \forall i = \overline{1,8}$ to provide the robust de-coupled tracking of Euler angle reference profiles to the X33 vehicle in a launch mode.

The Outer Loop (Guidance) Smoothed Sliding Mode Controller Design

The sliding surfaces are introduced as follows:

$$\begin{bmatrix}\sigma_1\\ \sigma_2\\ \sigma_3\end{bmatrix}=\begin{bmatrix}\tilde{\varphi}\\ \tilde{\theta}\\ \tilde{\psi}\end{bmatrix}+K\begin{bmatrix}\int\tilde{\varphi}dt\\ \int\tilde{\theta}dt\\ \int\tilde{\psi}dt\end{bmatrix},\ K=\begin{bmatrix}k_1 & 0 & 0\\ 0 & k_2 & 0\\ 0 & 0 & k_3\end{bmatrix} \tag{4}$$

where $\tilde{\varphi}=\varphi_c-\varphi,\ \tilde{\theta}=\theta_c-\theta,\ \tilde{\psi}=\psi_c-\psi$ are Euler angles' tracking errors. A smoothed sliding mode controller is designed to provide attractivity of the ε_i - vicinities of the sliding surfaces

$$\begin{bmatrix}p_c\\ q_c\\ r_c\end{bmatrix}=R^{-1}(\varphi,\theta,\psi)\left\{\begin{bmatrix}\dot{\varphi}_c\\ \dot{\theta}_c\\ \dot{\psi}_c\end{bmatrix}+K\begin{bmatrix}\tilde{\varphi}\\ \tilde{\theta}\\ \tilde{\psi}\end{bmatrix}+\begin{bmatrix}\rho_1 & 0 & 0\\ 0 & \rho_2 & 0\\ 0 & 0 & \rho_3\end{bmatrix}\begin{bmatrix}sat\dfrac{\sigma_1}{\varepsilon_1}\\ sat\dfrac{\sigma_2}{\varepsilon_2}\\ sat\dfrac{\sigma_3}{\varepsilon_3}\end{bmatrix}\right\},\ \varepsilon_i>0,\rho_i>0\ \ \forall i=\overline{1,3} \tag{5}$$

Inner Loop Smoothed Sliding Mode Controller Design

The corresponding sliding surfaces are designed as follows:

$$\begin{bmatrix}\tilde{\sigma}_1\\ \tilde{\sigma}_2\\ \tilde{\sigma}_3\end{bmatrix}=\begin{bmatrix}e_1\\ e_2\\ e_3\end{bmatrix}+C^1\begin{bmatrix}\int e_1d\tau\\ \int e_2d\tau\\ \int e_3d\tau\end{bmatrix},\quad C^1=\begin{bmatrix}c_1^1 & 0 & 0\\ 0 & c_2^1 & 0\\ 0 & 0 & c_3^1\end{bmatrix}, \tag{6}$$

where $e_1=p_c-p,\ e_2=q_c-q,\ e_3=r_c-r$ are the angular rates tracking errors. The inner loop smoothed sliding mode controller is designed to provide attractivity of the ε_i - vicinities of the sliding surfaces

$$T_c=\begin{bmatrix}L_c\\ M_c\\ N_c\end{bmatrix}=\begin{bmatrix}\hat{L}_{eq}\\ \hat{M}_{eq}\\ \hat{N}_{eq}\end{bmatrix}+\begin{bmatrix}\tilde{\rho}_1 & 0 & 0\\ 0 & \tilde{\rho}_2 & 0\\ 0 & 0 & \tilde{\rho}_3\end{bmatrix}\begin{bmatrix}sat\dfrac{\tilde{\sigma}_1}{\varepsilon_1}\\ sat\dfrac{\tilde{\sigma}_2}{\varepsilon_2}\\ sat\dfrac{\tilde{\sigma}_3}{\varepsilon_3}\end{bmatrix},\ \tilde{\rho}_i>a_i\ \forall i=\overline{1,3}. \tag{7}$$

$$\left|\Delta_{1eq}\right|=\left|L_{eq}-\hat{L}_{eq}\right|\le a_1,\ \left|\Delta_{2eq}\right|=\left|M_{eq}-\hat{M}_{eq}\right|\le a_2,\ \left|\Delta_{3eq}\right|=\left|N_{eq}-\hat{N}_{eq}\right|\le a_3. \tag{8}$$

$$\begin{bmatrix} L_{eq} \\ M_{eq} \\ N_{eq} \end{bmatrix} = B_1^{-1}\left\{\begin{bmatrix} \dot{p}_c \\ \dot{q}_c \\ \dot{r}_c \end{bmatrix} + C^1\begin{bmatrix} e_1 \\ e_2 \\ e_3 \end{bmatrix} - \begin{bmatrix} f_1(p,q,r,t,J) \\ f_2(p,q,r,t,J) \\ f_3(p,q,r,t,J) \end{bmatrix} + \frac{1}{2}B_1^{-1}\frac{dB_1}{dt}\tilde{\sigma}\right\} \tag{9}$$

Control Allocation

The command vector of control moments T_c is executed by corresponding actuators through deflections of five aerodynamic surfaces and an orientation of the thrust vector of the rocket engine. An optimal allocation matrix $B_v(.)$ must be identified such that $\delta_c = B_v(.)T_c$.

"Very" Inner Loop Controller Design

The control inputs $u_i \ \forall i = \overline{1,8}$ of the actuators must be designed to make the compensated dynamics of the actuators much faster then the inner loop sliding mode dynamics.

X33 Launch Vehicle Smoothed Sliding Mode Controller Design in Launch Mode

The elements of the inertia matrix of the X33 vehicle in the launch mode are given

$$\begin{cases} J_{xx} = 806555.0 - 1261.0t & J_{yy} = 2371654.0 - 6175.0t \\ J_{zz} = 2781705.0 - 7026.0t & J_{xz} = 16494 - 198.0t \qquad J_{xy} = J_{yz} = 0 \end{cases} \tag{10}$$

The outer loop smoothed sliding mode controller is designed for the X33 vehicle as follows:

$$\begin{cases} p_c = a - b\sin\varphi \\ q_c = b\cos\varphi + c\sin\varphi\cos\theta \\ r_c = -b\sin\varphi + c\cos\varphi\cos\theta \end{cases}, \quad \begin{cases} a = \dot{\varphi}_c + 0.4\tilde{\varphi} + \rho_1(\tilde{\varphi} + 0.4\int\tilde{\varphi}dt) \\ b = \dot{\theta}_c + 0.4\tilde{\theta} + \rho_2(\tilde{\theta} + 0.4\int\tilde{\theta}dt) \\ c = \dot{\psi}_c + 0.4\tilde{\psi} + \rho_3(\tilde{\psi} + 0.4\int\tilde{\psi}dt) \end{cases} \tag{11}$$

The values of parameters $\rho_1 = 4.0, \ \rho_2 = 3.5, \ \rho_3 = 4.0$ are chosen experimentally. The inner loop smoothed sliding mode controller for the X33 vehicle is designed as well. This is

$$\begin{cases} L_c = \hat{L}_{eq} + \tilde{\rho}_1(e_1 + 1.884\int e_1 dt) \\ M_c = \tilde{M}_{eq} + \tilde{\rho}_2(e_2 + 1.884\int e_2 dt) \\ N_c = \tilde{N}_{eq} + \tilde{\rho}_3(e_3 + 1.884\int e_3 dt) \end{cases} \qquad \begin{cases} \tilde{L}_{eq} = J_{xx}(-f_1(.) + 1.884e_1) \\ \tilde{M}_{eq} = J_{yy}(-f_2(.) + 1.884e_2) \\ \tilde{N}_{eq} = J_{zz}(-f_3(.) + 1.884e_3) \end{cases} \tag{12}$$

$$\begin{cases} f_1(.) = \dfrac{1}{J_{xx}}\left[-qr\left(J_{zz}-J_{yy}\right)+J_{xz}pq\right] \\ f_2(.) = \dfrac{1}{J_{yy}}\left[-pr\left(J_{xx}-J_{zz}\right)-J_{xz}\left(p^2-r^2\right)\right] \\ f_3(.) = \dfrac{1}{J_{zz}}\left[J_{xz}\dot{p}-pq\left(J_{yy}-J_{xx}\right)-J_{xz}qr\right] \end{cases} \tag{13}$$

The values of parameters $\tilde{\rho}_1 = 1.0\cdot 10^7$, $\tilde{\rho}_2 = 1.5\cdot 10^7$, $\tilde{\rho}_3 = 1.5\cdot 10^7$ are chosen experimentally. Smoothed sliding mode controllers (11) - (13) are implemented as follows:

$$\begin{aligned} L_c = {} & \tilde{\rho}_1[\rho_1\tilde{\varphi} - \rho_2\tilde{\theta}\sin\varphi + 0.4\rho_1\int\tilde{\varphi}d\tau - 0.4\rho_2\sin\varphi\int\tilde{\theta}d\tau - p] + 1.884\tilde{\rho}_1[\rho_1\int\tilde{\varphi}d\tau \\ & - \rho_2\int\tilde{\theta}\sin\varphi d\tau + 0.4\rho_1\iint\tilde{\varphi}d\tau dt - 0.4\rho_2\int\sin\varphi\int\tilde{\theta}d\tau dt - \int pdt] \end{aligned} \tag{14}$$

$$\begin{aligned} M_c = {} & \tilde{\rho}_2[\rho_2\tilde{\theta}\cos\varphi + \rho_3\tilde{\psi}\sin\varphi\cos\theta + 0.4\rho_2\cos\varphi\int\tilde{\theta}d\tau + 0.4\rho_3\sin\varphi\cos\theta\int\tilde{\psi}d\tau - q] \\ & + 1.884\tilde{\rho}_2[\rho_2\int\tilde{\theta}\cos\varphi dt + \rho_3\int\tilde{\psi}\sin\varphi\cos\theta dt + 0.4\rho_2\int\cos\varphi\int\tilde{\theta}d\tau dt \\ & + 0.4\rho_3\int\sin\varphi\cos\theta\int\tilde{\psi}d\tau dt - \int qdt] \end{aligned} \tag{15}$$

$$\begin{aligned} N_c = {} & \tilde{\rho}_3[-\rho_2\tilde{\theta}\sin\varphi + \rho_3\tilde{\psi}\cos\varphi\cos\theta - 0.4\rho_2\sin\varphi\int\tilde{\theta}d\tau + 0.4\rho_3\cos\varphi\cos\theta\int\tilde{\psi}d\tau - r] \\ & + 1.884\rho_3[-\rho_2\int\tilde{\theta}\sin\varphi dt + \rho_3\int\tilde{\psi}\cos\varphi sos\theta dt - 0.4\rho_2\int\sin\varphi\int\tilde{\theta}d\tau dt \\ & + 0.4\rho_3\int\cos\varphi\cos\theta\int\tilde{\psi}d\tau dt - \int rdt] \end{aligned} \tag{16}$$

Simulations showed that the designed smoothed sliding mode controllers provide a very accurate, highly robust tracking of Euler angle profiles during the X33 vehicle launch mode.

Conclusions

Employing time scaling concept a new two (three)-loop structure of the control system for the X33 launch vehicle was developed. Smoothed sliding mode controllers were designed to robustly enforce the given close-loop dynamics. Simulations of the 3-DOF model of the X33 launch vehicle with the table-look-up models for Euler angle reference profiles and disturbance torque profiles showed a very accurate, robust tracking performance.

Acknowledgment

I would like to express my gratitude to N. D. Hendrix, C. Hall, M. Jackson and D. Krupp for the excellent management of the Summer Faculty Program and engineering support of my research.

1997

NASA/ASEE SUMMER FACULTY FELLOWSHIP PROGRAM

MARSHALL SPACE FLIGHT CENTER

THE UNIVERSITY OF ALABAMA IN HUNTSVILLE

APPLICATION OF PARAMETRIZED POST-NEWTONIAN METHODS TO THE GRAVITATIONAL IS OF SATELLITE ENERGY EXCHANGE DATA

Prepared by: Larry L. Smalley, Ph.D.

Academic Rank: Professor

Institution and Department: University of Alabama in Huntsville
Department of Physics

NASA/MSFC:

Office: Advanced Projects Branch
Division: Program Development

MSFC Colleague: Jonathan Campbell, Ph.D.

Introduction

Project Satellite Energy Exchange (SEE) is a free-flying, high altitude satellite that utilizes space to construct a passive, low-temperature, nano-g environment in order to accurately measure the poorly known gravitational constant G plus other gravitational parameters that are difficult to measure in an earth-based laboratory Eventually data received from SEE must be analyzed using a model of the gravitational interaction including parameters that describe deviations from general relativity and experiment. One model that can be used to *fit* the data is the Parametrized post-Newtonian (PPN) approximation [4] of general relativity (GR) which introduces ten parameters which have specified values in (GR). It is the lowest-order, consistent approximation that contains non linear terms. General relativity predicts that the Robertson parameters, γ (light deflection), and β (advance of the perihelion), are both 1 in GR. Another eight parameters, α_k , j=1,2,3, and ζ_k, k=1,2,3,4 and ξ, are all zero in GR. Non zero values for α_k parameters predict preferred frame effects; for ζ_k , violations of globally conserved quantities such as mass, momentum and angular momentum; and for ξ, a contribution from the Whitehead theory of gravitation, once thought to be equivalent to GR. In addition, there is the possibility that there may be a preferred frame for the universe. If such a frame exists, then all observers must measure the velocity w of their motion with respect to this universal rest frame. Such a frame is somewhat reminiscent of the concept of the *ether* which was supposedly the frame in which the velocity of light took the value *c* predicted by special relativity. The SEE mission can also look for deviations from the r^{-2} law of Newtonian gravity, adding parameters α and λ for non Newtonian behavior that describe the magnitude and range of the r^{-2} deviations respectively. The foundations of the GR supposedly agree with Newtonian gravity to first order so that the parameters α and λ are zero in GR. More important, however, GR subsequently depends on this Newtonian approximation to build up the non linear higher-order terms which forms the basis of the PPN frame work.

The SEE Encounter and Post-Newtonian Approximation

Other than establishing the physical design of the SEE platform, it is also necessary to determined how the data taken can be analyzed. Ostensibly the major experiment that occurs is called Satellite Energy Exchange which occurs when a small mass satellite in a slightly lower lying orbit overtakes a very much larger mass satellite, called a shepherd, in a slightly higher orbit. As the small mass nears the shepherd, the mutual attraction increases the total energy of the smaller satellite which subsequently moves to a *higher* orbit and *slows* down. The effect on the much more massive shepherd is nearly negligible. In the frame of the shepherd, the smaller mass satellite approaches in a slightly lower orbit, moves to a slightly higher orbit and then appears to recede in the direction from which it came subsequently meeting the shepherd again 360° away where another SEE encounter occurs again. Such *orbits*, as seen in the rotating frame of the shepherd, are called *horseshoe* orbits. Experimentally, the closest point of approach of the small satellite to the shepherd is a direct measurement of the *local* gravitational constant G_L. In the somewhat similar Cavendish experiment, which measures the relative acceleration of two masses, the equivalent local gravitation constant depends on *seven* PPN parameters plus the relative motion of the of the laboratory with respect to the universal rest frame. This analysis must be completed for the SEE encounter itself. Several more experiments can be conducted in the SEE capsule such as a long term measurement of the constancy of the gravitational "constant" itself. This introduces another parameter which relates any deviation to the Hubble constant. The motion of the shepherd with

respect to the sun and the moon (as well as the Earth which is the primary gravitational source for the shepherd) allows the possibility of polarization of orbits and the measurement of the difference between active and passive gravitational mass, or equivalently the direct measurement of the possible violation of the weak equivalence principle. These effects can be described in terms of the Nordtvedt effect which itself depends on nine PPN parameters.

Experiments and PPN Additional Parameters

A short list of (possible) additional experiments that can be accomplished in the SEE platform is given by:

- The possibility of non r^{-2} behavior (two additional parameters).
- New experiments such as the behavior of an initially symmetric, gravitationally bound Particle Cloud in a zero-g, drag-free orbit (at least two PPN parameters).
- Perihelion shift of the shepherd (at least six PPN parameters).
- Orbital resonances with the Earth's ordinary geopotential field for harmonic components of the rotation period of the Earth (resonance for α_2).
- Scalar—Vector—Tensor theories (etc.) (additional parameter(s)).
- The effect of the spin of specifically prepared test particles(polarized and shielded from the magnetic field) can be measured (five PPN parameters).

Status of PPN analysis for SEE

In most cases the actual contributions of the PPN parameters have not been completely analyzed for experiments proposed for the SEE mission. Will has complied a list of the applications of the PPN formalism for the classical test of relativity, such as the perihelion advance and light deflection plus more modern tests such as time delay of radar signals and lunar laser ranging. Thus without a basic foundation in the PPN formalism, it will be impossible to extract meaningful consequences of the SEE data.

Introduction to and Consequences of PPN Analysis

The design of the SEE experimental package beyond measurement of G is in the formative stages. It is estimated In order to understand the PPN formalism, a program was initiated this summer to familiarize members of the SEE team on the fundamentals of the PPN framework. This review consisted of a basic introduction to the essentials of gravitational theory plus an introduction to the post-Newtonian approximation and subsequently the extension of general relativity to a general framework called the *Parametrized* Post-Newtonian approximation from which likely deviation of GR can be tested. The importance of this familiarization will become evident below.

From the design characteristics of the SEE satellite that the absolute value of G can be measured to at least one part in 10^6 for each event; and the temporal behavior, to one part in $10^{12\text{-}13}$ depending on the duration of the tracking of the shepherd, i.e. the total path length of the shepherd. It turns out that the limits on the temporal behavior of G is close to the value necessary to test speculations concerning unified theories such as string or

supergravity theories. However the actual dependence on parameters (PPN or otherwise) has not been calculated for most of the proposed experiments. This means, for example, that the actual SEE encounter (or any other experiment proposed for the SEE satellite) must be recalculated in terms of the PPN metric in order to investigate the actual dependence on the PPN parameters. These calculations were not attempted during the period of this research effort but are now well within the capability of the team.

An important aspect of the above calculations allows the establishment of the connection between the various proposed experiments that will be conducted during a SEE Mission. It is obvious from the discussions above, that a single experiment will not, for the most part, be able to set the value of the any single PPN parameter by itself. In general, each experiment will yield data that is a complicated function of PPN parameters that must be compared with every other experiment in the reduction of data to experimental limits on the PPN parameters. **In general, nothing should be assumed *a priori* concerning the value of these parameters.** If the set of experiments is not sufficient to determine **all** the individual parameters, then experimental limits can only be placed upon functional relationships among the parameters.

A second aspect, once these parametric functions for each experiment have been analyzed, is the crucial input in the necessary error analysis of the SEE mission itself. **This is an essential task necessary for the detailed design of the mission itself.**

Modified Malin Theory

A new experimental configuration for SEE was developed as a test case for extending the types of experiments that could give an independent relationships amongst the PPN parameters. Such an example is a configuration of particles that could be observed in the SEE capsule. The thrust of this work is in a slight modification of Malin's theory which is a non viable, alternate theory of gravity. As it stands, Malin's theory does not satisfy most of the requirements for a viable theory of gravity such as the correct Newtonian limit and globally conserved quantities such as total momentum and angular momentum. The field equation for Malin's theory is given by [3]

$$R_{k\ell} = \kappa T_{k\ell} \qquad (1)$$

where $\kappa = 4\pi G$, G is the gravitational constant, $R_{k\ell}$ is the Ricci tensor, and $T_{k\ell}$ is the matter energy-momentum tensor. If the left hand side of the above equation consisted of the Einstein tensor $\frac{1}{2}G_{k\ell} = \frac{1}{2}\left(R_{k\ell} - \frac{1}{2}g_{k\ell}R\right)$, where $G_{k\ell}$ is the Einstein Tensor, $g_{k\ell}$ is the metric tensor and R is the Riemann scalar, then all the limits and conservation laws described above would be satisfied provided that $\nabla_i T_j^{\,i} = 0$. In general, $\nabla_i R_j^{\,i} \neq 0$ which implies that the divergence of the energy-momentum is also not zero. However it turns out that if the divergence of the energy-momentum satisfies the condition $\nabla_i T_j^{\,i} = \lambda R_j$ where λ is a function of O(2) in the gravitational potentials, then it is possible to slightly modify Eq.(1) so that the effective energy-momentum tensor T_{eff}^{jk}

$$G^{jk} = \kappa T_{eff}^{jk} = \kappa\{T_{PF}^{jk} + \frac{1}{2} g^{jk}[\zeta_3 \rho\Pi + 3\zeta_4 p]\} \qquad (2)$$

which does not satisfy global conservation laws,. The ζ_3 and ζ_4 PPN parameters then represent fourth order corrections to Euler's equations of motion and represents a theoretical framework for testing the magnitude of these corrections. A possible experimental test bed is discussed below for their measurement.

Experimental Configuration

Consider a collection of N small, spherically symmetric, electrically neutral particles of uniform density. Let the particles be collected into a spherical shape of Radius R. In zero g, this could be a *bag* that that positively holds that particles in a spherical until the experiment begins. If the bag could be remove, and the spherical shape were initially maintained, the particles would have the effective low temperatures of about 80 K of the SEE environment. The gravitational force on individual particles of mass m at radius $r < R$ is approximately given by

$$\mathbf{F}(r) \approx -G\rho(r)V(r)\frac{\hat{\mathbf{r}}}{r} \approx -G\left(\frac{Nm^2}{R^3}\right)\hat{\mathbf{r}} \qquad (6)$$

for a spherically symmetric system with uniform density. Then for $R=20\ r_0$, where r_0 is the radius of a *20-g* ball of density about *5 g/cm*^{3}, $N \approx 8000$ and $r_0 \approx 1$ cm. The approximate binding force on a particle at the surface of the spherical aggregation is $F(R) \approx 5 \times 10^{-2}$ *dynes*. At a temperature of about *80 K*, the mean motion of the particles in the aggregation will be about *40 nm/s*. This velocity should be compared with the escape velocity of a single ball from the surface of the spherical aggregate $v_{exc} \approx 3.3 \times 10^{-3}\, cm/s$ which shows that the thermal velocity is negligible in comparison with the kinetic energy necessary for escape from the spherical aggregate. Thus the spherical aggregate appears to be a bound system with regard to thermal perturbations. Over a long period of time, these tiny perturbations will alter both the shape and density distributions $\mathbf{F}(r) \rightarrow \mathbf{F}(\mathbf{r})$, $\rho(r) \rightarrow \rho(\mathbf{r})$ which will bring in multipole moments of the mass distribution. In orbit about the Earth, the gravity gradient forces will also perturb the spherical shape. This perturbation will eventually lead to collisions between the balls. The difference in orbital velocity from a small ball at the top of spherical aggregate and one at the bottom (*bt*) along the radius of the satellite to the Earth is given by $\Delta v_{bt} \approx 1.9 \times 10^{-2}\, cm/s$ and the relative motion of *nearest neighbor(nn)* particles is given $\Delta v_{nn} \approx 9.5 \times 10^{-4}\, cm/s$ where R_E is the orbital radius. The nearest neighbor velocity is an indication of stability; however, it is the ratio:: $\Delta \upsilon_{esc}$ :: $\Delta \upsilon_{nn} \approx 3$ which will determine whether a particle will acquire escape velocities. Thus the system appears to be marginally stable. There are several methods that could be used to obtain useful data for this system.

- Test for anomalous (heat) energy dissipation. This would be directly related to the internal energy and pressure of the system and therefore to ζ_3 and ζ_4.
- Use the evolution of the morphology of the aggregate over a long period of time to study the microstructure of the aggregate[Gokhale, 1996].
- Analyze the fractal dimension of the aggregate which is a direct measure of the force law between the small balls [Slobodrian, 1996].

Post-Newtonian Approximations Data Base

One of the first goals in this ongoing study was to collect a comprehensive data base to facilitate the study of the post-Newtonian approximation and its application to Project SEE. This has resulted in a collection of papers and references, collected by Kelly Smith (Accompanying Student) comprising over 400 entries dedicated to research in the area of the post-Newtonian approximation and the PPN theory. This data base, compiled using Microsoft Access, is now available on disc from Larry Smalley, Department of Physics, University of Alabama in Huntsville, Huntsville AL 35899 or by email: smalley@pluto.cs.uah.edu.

References

1. Gokhale, A., "Effect of gravity on the evolution of spatial arrangements of features in microstructures: A quantitative approach," Microgravity Material Science Conference, June 10-11, 1996, Huntsville, AL.

2. Slobodrian, R., "Fractal Aggregates in Microgravity," Microgravity Material Science Conference, June 10-11, 1996, Huntsville, AL.

3. Smalley, L.L., "Rastall's and related theories are conservative gravitational theories although physically inequivalent to general relativity," J. Phys. A: Math. Gen. **16**, 217 (1983).

4. Will, Clifford M., "Theory and Experiment in Gravitational Physics," (Cambridge University Press, New York, First Paper Back Edition 1985).

1997

NASA/ASEE SUMMER FACULTY FELLOWSHIP PROGRAM

MARSHALL SPACE FLIGHT CENTER
THE UNIVERSITY OF ALABAMA IN HUNSTVILLE

DESIGN OF THE EXPERIMENTAL EXPOSURE CONDITIONS TO SIMULATE IONIZING RADIATION EFFECTS ON CANDIDATE REPLACEMENT MATERIALS FOR THE HUBBLE SPACE TELESCOPE

Prepared By:	L. Montgomery Smith
Academic Rank:	Associate Professor
Institution:	University of Tennessee Space Institute
Department:	Department of Electrical Engineering

NASA/MSFC:

Office:	Electromagnetics and Aerospace Environments
Division:	Systems Engineering
MSFC Colleagues:	K. Stuart Clifton
	James W. Howard, Jr.
	Richard Altstatt

Introduction

Component stuctures consisting of 5- and 10-mil thickness Teflon (FEP) backed by plated layers of Aluminum or Silver and Inconel have been identified as candidate replacement materials for external components of the Hubble Space Telescope (HST). However, the effects of exposure to the space ionizing radiation environment (primarily trapped electrons and protons) is not known. Therefore, it was desired to ground-test these materials for degradation due to radiation exposure to trapped electrons and protons in the region of the HST orbit for the time period of Launch to SM2 (2490 days). This report describes the design of the ground-based experiment to simulate the space radiation effects using existing and available laboratory particle accelerators.

A major consideration in the experiment design was the limited energy ranges for the laboratory electron and proton accelerators (Edwards, 1997). Two electron accelerators were available with energy ranges from 1 keV to 50 keV and 220 keV to 2500 keV. A proton accelerator was available with an energy range of 70 keV to 700 keV. All accelerators operated at a flux of 1 nA/cm^2 (6.25×10^9 particles/cm^2· sec). The spectral distributions for the space environment electron and proton fluxes were known and are shown in Fig. 1 (Barth, 1997). As can be seen, the laboratory accelerators were not capable of duplicating these spectra exactly. Therefore, special effort was required to determine the appropriate exposure times to the available particle energies that would approximate in some sense of optimality the HST space radiation environment effects on these materials.

The approach taken was to determine computationally the dose to each material structure as a function of depth for both the full HST spectrum and for a limited number of discrete energies attainable by the available particle accelerators. Then, the optimum exposures for the monoenergetic particle fluxes were calculated by determining a least-squares approximation of their combined dose-versus-depth profiles in the material structures to the full spectrum profile. Dose-versus-depth for the electron fluence was calculated using the Integrated TIGER Series (ITS) Monte Carlo radiation transport code (Halbleib, et al, 1992), while the dose-versus-depth for the proton fluence was found by use of the Space Radiation prediction code (Letaw, 1990-1997). Special-purpose programs were written to perform the minimum-least-squares approximation.

Despite a "notch" in the available electron energies extending from 50 to 220 keV, exposure times for 50-keV, 220-keV and 500-keV monoenergetic fluxes were found that approximated the space electron fluence effects over 4-, 5- and 10-mil depths in Teflon. Ranging from 1000 to 3400 seconds, these times were realizable with the laboratory accelerators. The results for the proton exposures were severely limited by the 700 keV maximum machine energy with the HST full spectrum extending to over 500 MeV. The experimental dose profile could only approximate the full spectrum exposure profile for a small fraction of the material depth. Optimal exposure times for 200-keV, 500-keV and 700-keV monoenergetic fluxes on the order of milliseconds were determined, however, they were not realizable to any degree of accuracy with the available laboratory accelerators.

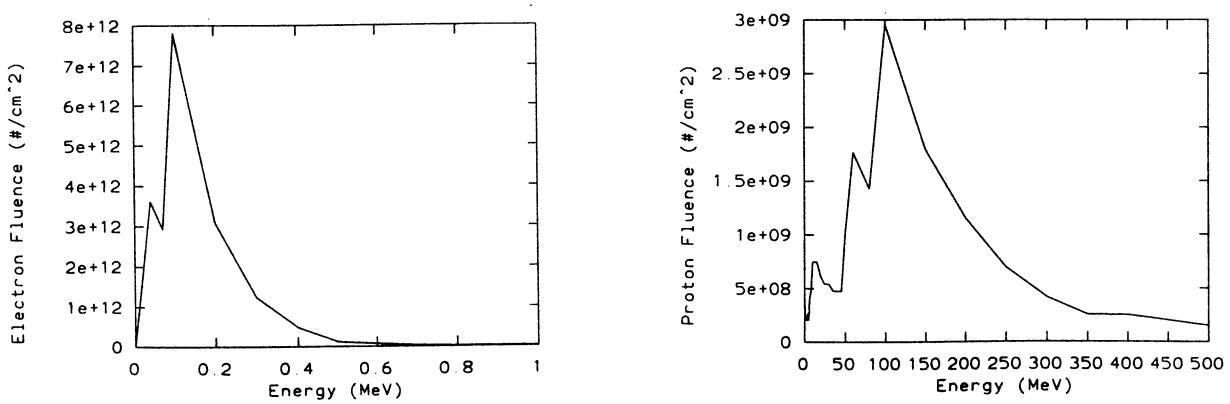

Fig. 1. Spectral distributions for the HST trapped electron and trapped proton fluences.

Calculation of the Dose-Versus-Depth Profiles

The first phase in the experiment design was to determine the dose as a function of depth in the candidate material structures. Six candidate material structures were initially considered, all of which consisted of a slab geometrical configuration:

1. 10-mil Teflon (FEP)/backed by 150-nm Silver (Ag)/backed by 27.5-nm Inconel
2. 5-mil FEP/150-nm Ag/27.5-nm Inconel/2-mil Kapton
3. 10-mil FEP/backed by 100-nm Aluminum (Al)
4. 5-mil FEP/100-nm Al/2-mil Kapton
5. 5-mil FEP/150-nm Ag/27.5-nm Inconel
6. 5-mil FEP/100-nm Al

The slab geometry simplified the analysis in terms of input files for the dose calculations and execution times for the Monte Carlo analysis. Although it was felt that the back surface platings would have negligible effects, they were initially included in the electron dose-versus-depth study for completeness.

The electron exposure calculations employed the TIGER 1-D slab geometry Monte Carlo radiation transport member code of the Integrated TIGER Series (Halbleib, et al, 1992). Files for the component materials were written for the XGEN scattering cross-section generation code, and input files for each structure were written for the TIGER code. Data for the HST trapped electron spectral fluence was used to model the spectral distribution of incident electrons on the front surface of each structure. The Teflon layer was divided into 25 subzones (for the 5-mil cases) or 50 subzones (for the 10-mil cases) so that the energy deposition in each subzone calculated by TIGER gave a direct measure of the dose as a function of depth.

The results are shown in Fig. 2, which shows the energy deposition in MeV (normalized to one particle per cm^2) as a function of depth into the Teflon layers for the six cases considered. As expected, the different back platings had negligible effect on the doses in the Teflon, and any discrepancies in the curves are felt to be the result of statistical uncertainties in the Monte Carlo process.

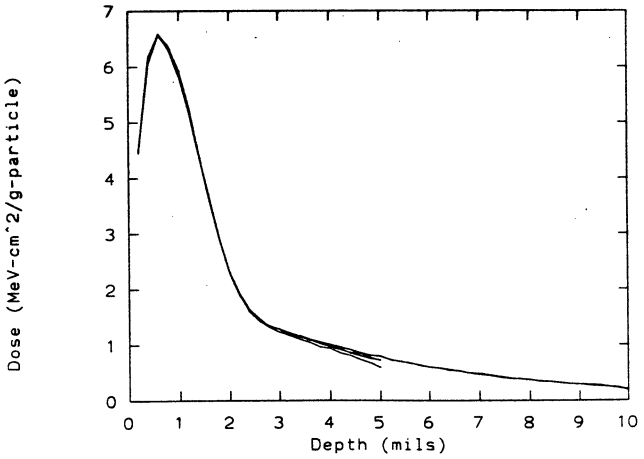

Fig. 2. Energy deposition as a function of depth in Teflon for the full HST electron spectrum.

Based upon experience with the dose-versus-depth calculations for electrons, the corresponding calculations for the proton flux were restricted to the simple case of a single layer of 10-mil thick Teflon. Although several computer codes were considered for usage, the Space Radiation prediction code (Letaw, 1990-1997) was chosen primarily because of availability and familiarity. Bcause this code is limited in the materials that can be input, Lexan was chosen as the medium for the dose-versus depth code calculations, being that which is closest to Teflon in its material properties.

Calculation of the dose as a function of depth was something of a tedious process even with the spectral distribution of protons well-tabulated. Different thicknesses of the Lexan were treated as shielding material and the dose rate behind each thickness calculated for the full spectrum proton fluence. In this way, the dose-versus-depth profile was constructed for the input "shielding thicknesses."

The results are shown in Fig. 3, which shows the dose in rads (normalized to one particle per cm^2) as a function of depth into the Lexan layers over the 10 mil depth considered. Worth noting are the extremely low dose values and the penetration of the protons into the material. These effects result from the large amount of high-energy protons in the original incident spectrum.

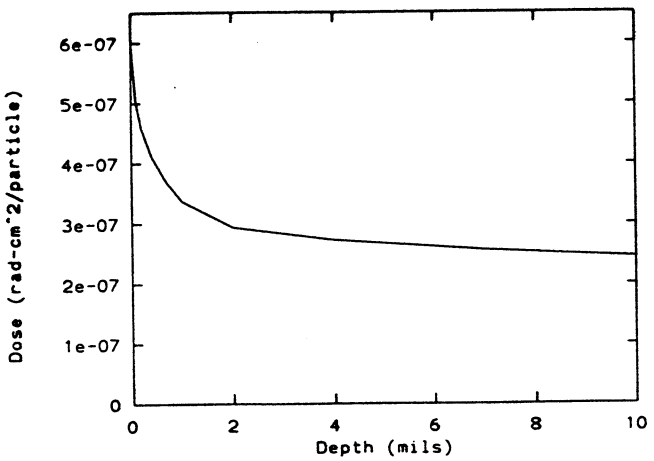

Fig. 3. Dose as a function of depth in Lexan for the full HST proton spectrum.

Determination of the Experimental Exposures

To determine the optimal exposure conditions, discrete particle energies were selected that were available with the laboratory accelerators, and dose-versus-depth profiles for the corresponding monoenergetic particle fluxes were computed. Using the data from these curves, optimal weightings and an overall scale factor were determined that minimized the mean-square-error between the linear combination of the monoenergetic profiles and the dose-versus-depth profile as calculated for the full HST spectrum. These optimal weightings allowed for a direct conversion to accelerator exposure times for the particle energies selected.

For the electron exposure conditions, four discrete energies were selected: 50 keV, 220 keV, 350 keV, and 500 keV. Energy deposition as a function of depth into a 10-mil slab of Teflon was calculated for each of these energies. A special-purpose C program was then written to take the data from these profiles and perform a five-parameter (four weightings and an overall scale factor) exhaustive search to minimize the mean square error between the composite curve and the full spectrum curve for the first case considered (10-mil Teflon thickness.) Optimization was performed for depths of 4, 5 and 10 mils, and weighting factors were calculated to within $\pm 0.5\%$ uncertainty.

Figure 4 shows the results for optimization of the discrete energy weightings over the full 10-mil depth. While the profiles appear quite dissimilar, it should be noted that energies in the range 50 keV to 220 keV encompass the peak in the space environment electron fluence spectrum and yet are exactly those unavailable in the laboratory accelerators. Without that range of energies, extremely accurate duplication is not to be expected.

Based upon the preceding analysis, the following experimental procedures were recommended for simulation of the space electron radiation environment on candidate components of the Hubble Space Telescope:

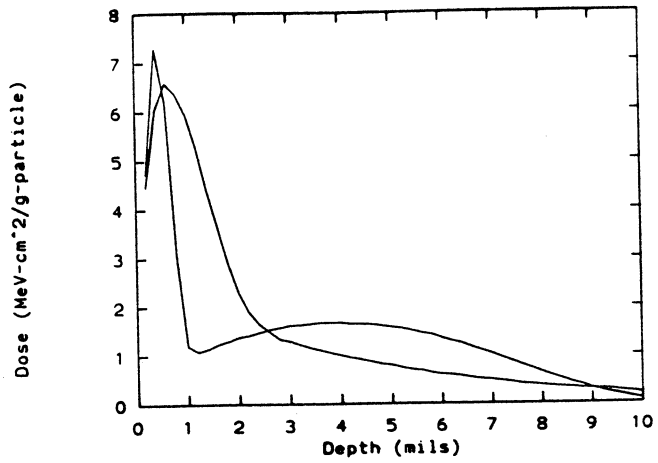

Fig. 4. Comparison of electron flux dose-versus-depth full spectrum profile with composite profile for discrete energies with weightings optimized over full 10-mil thickness of Teflon.

To simulate dose for 4-mil depth:

- Expose to 50-keV electron flux for 1005 ± 5 seconds
- Expose to 500-keV electron flux for 3363 ± 16 seconds

To simulate dose for 5-mil depth:

- Expose to 50-keV electron flux for 1104 ± 5 seconds
- Expose to 500-keV electron flux for 2703 ± 13 seconds

To simulate dose for 10-mil depth:

- Expose to 50-keV electron flux for 1289 ± 6 seconds
- Expose to 220-keV electron flux for 895 ± 4 seconds

These exposure times are within the normal operating parameters for the available laboratory accelerators. Thus, realizable experimental procedures were found that simulated the space radiation trapped electron environment to an acceptable degree of fidelity.

For the proton exposure conditions, three discrete energies were selected: 200 keV, 500 keV, and 700 keV. Dose as a function of depth into the first 0.5 mil of the 10-mil slab of Lexan was calculated for each of these energies. A special-purpose C program was then written to take the data from these profiles and perform a four-parameter (three weightings and an overall scale factor) exhaustive search to minimize the mean square error between the composite curve and the full spectrum curve. Optimization was performed only over this limited depth of 0.5 mils since protons at these low energies were found not to penetrate the Lexan any further.

Figure 5 shows the results for optimization of the discrete energy weightings over this 0.5-mil depth. The profiles agree reasonably well, but beyond this depth, doses from the monoenergetic protons are virtually zero. Without a much higher range of energies, accurate simulation of the space environment effects for any larger depth is not possible

From the optimal weightings and scale factor, the exposure times for the given laboratory electron accelerators were determined and are given by: 0.0085 sec exposure time for 200 keV protons, 0.0092 sec exposure time for 500 keV protons, and 0.016 sec exposure time for 700 keV protons. The available laboratory accelerators are not capable of being controlled to within the timing accuracy required to perform these exposures. Thus, while optimal values were determined to simulate at least the surface exposure effects of the space radiation trapped proton environment, the results were not realizable with the existing equipment.

Based upon the brevity of optimal exposure times and limited depth of effectiveness, it was recommended that no exposure to protons be performed. However, if proton exposure was essential to the simulation effort, it was recommended to use only the highest energy avaliable (700 keV) and expose components to that proton flux for the shortest time realizable with the existing laboratory accelerator.

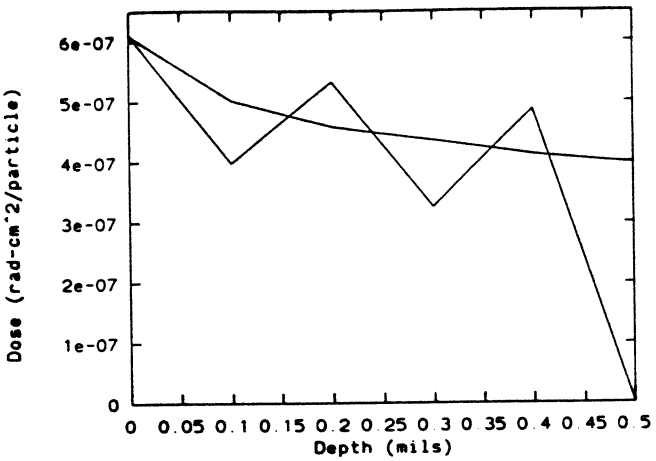

Fig. 5. Comparison of proton flux dose-versus-depth full spectrum profile with composite profile for discrete energies with weightings optimized over first 0.5-mil thickness of Lexan.

Summary and Conclusions

In this effort, experimental exposure times for monoenergetic electrons and protons were determined to simulate the space radiation environment effects on Teflon components of the Hubble Space Telescope. Although the energy range of the available laboratory particle accelerators was limited, optimal exposure times for 50 keV, 220 keV, 350 keV, and 500 KeV electrons were calculated that produced a dose-versus-depth profile that approximated the full spectrum profile, and were realizable with existing equipment. For the case of proton exposure, the limited energy range of the laboratory accelerator restricted simulation of the dose to a depth of 0.5 mil. Also, while optimal exposure times were found for 200 keV, 500 keV and 700 keV protons that simulated the full spectrum dose-versus-depth profile to this depth, they were of such short duration that existing laboratory could not be controlled to within the required accuracy.

In addition to the obvious experimental equipment issues, other areas exist in which the analytical work could be advanced. Improved computer codes for the dose prediction – along with improved methodology for data input and output – would accelerate and make more accurate the calculational aspects. This is particularly true in the case of proton fluxes where a paucity of available predictive software appears to exist. The dated nature of many of the existing Monte Carlo particle/radiation transport codes raises the issue as to whether existing codes are sufficient for this type of analysis. Other areas that would result in greater fidelity of laboratory exposure effects to the space environment is the use of a larger number of mononergetic particle fluxes and improved optimization algorithms to determine the weighting values.

References

Barth, J., Internal Memorandum: HST Radiation Environment/MLI Degradation, Marshall Space Flight Center, May 1997.

Edwards, D., Private communication, Marshall Space Flight Center, July 1997.

Halbleib, J. A., Kensek, R. P., Mehlhorn, T. A., and Valdez, G. D., *ITS Version 3.0: The Integrated TIGER Sries of Coupled Electron/Photon Monte Carlo Transport Codes*, SAND91-1634, March 1992.

Letaw, J. R., *Space Radiation SoftCopy Manual*, Space Radiation Associates, 1990-1997.

1997

NASA/ASEE SUMMER FACULTY FELLOWSHIP PROGRAM

MARSHALL SPACE FLIGHT CENTER
THE UNIVERSITY OF ALABAMA IN HUNTSVILLE

Mechanistic Models of Friction Stir Welding

Prepared By:	Michael B. Stewart
Academic Rank:	Assistant Professor
Institution and Department:	University of Arkansa - Mechanical Engineering Department
NASA/MSFC:	
Laboratory:	Materials and Processes
MSFC Colleague:	Dr. Arthur C. Nunes

Mechanistic Models of Friction Stir Welding
Short Report

Michael B. Stewart
University of Arkansas
with
Arthur C. Nunes
NASA Marshal Space Flight Center

Purpose:

This report is submitted in partial fulfillment of the requirements of NASA's Summer Faculty Fellowship program. Due to the length restrictions, it should be considered only an extended abstract. The full report was submitted to my NASA colleague, Arthur C. Nunes, EH23.

Background:

Friction stir welding is a welding process developed at The Welding Institute (TWI) in England. The method uses very large strain plastic deformation of the material to join two pieces of metal together. The material is deformed using a tool which is forced between the two pieces which rotates causing a bond. Beyond this, very little is actually known although many people working in the field are willing to speculate on the detailed mechanisms involved. Some measurements made using sacrificial thermocouples at the weld joint indicate that the maximum temperature during the weld process is on the order of 370C - well below the melting temperature of the material. However, at this temperature, the material properties are highly temperature dependent, and the yield stress is approximately an order of magnitude less at this temperature than it is at room temperature.

As expected, there are many interpretations of the physical mechanisms occurring during the weld process. Although there is very little published concerned with FSW, some of the anecdotal theories will be described. One describes the primary mechanism as frictional heating at the front of the tool caused by slip between the tool and the material (Boeing). At elevated temperatures, the weld material becomes soft and deforms around the tool but not essentially altered by the tool rotation, similar to an extrusion. As the material meets again at the rear of the tool, the temperatures and pressures are sufficient to cause the material to bond. All other structures seen are secondary and unimportant.

Another theory examined last summer at NASA's Marshall Space Flight Center (MSFC) was that there was no slip between the tool and the material resulting in a rotating mass of plastic weld material traveling at a variety of angular velocities - the greatest at to tool surface diminishing to zero at the outer edge of the plastic mass surrounding the tool. This conceptual model was followed by simplified calculations which showed that the balance of moments through the weld plug was not possible under steady state conditions and realistic temperature profiles. This led to some consideration of a quasi-steady oscillating process. Later when force measurements became available some models were modified and new ones were proposed.

Mixed Zone Model (MZ):
The difficult job of proposing and evaluating models is made much easier by the experimental work currently being done at MSFC. An earlier model assumed that the weld material surrounding the pin tool was a continuously deforming 'pool' of material. An analysis of the required force balance is provided by Nunes, 1996. The first step is to assume a shear stress - temperature relationship,

$$\tau = a(T - T_m)^n$$

where $\tau\left[\frac{F}{L^2}\right]$ is the flow stress, T is the local temperature, T_m [C] is the melting temperature, and $a\left[\frac{F}{T^n L^2}\right]$ is an empirical constant, and n is a positive integer chosen to fit the available data. Next, a force balance requires that the moment be in equilibrium Thus, $r^2\tau$=const. Combining these, we can write,

$$\frac{T - T_m}{T_R - T_m} = \left(\frac{R}{r}\right)^{n/2}, r \geq R$$

FSW joins two pieces at temperatures less than the melting temperature which makes $T_R \leq T_m$. As long as n is positive (a reasonable assumption) this requires that the temperature gradient causes heat to be conducted back towards the tool. There is no reasonable mechanism which allows the tool to be a heat sink of sufficient magnitude for this to

occur. The possibility that transients were causing temperature pulses moving through the material was proposed. However, even an oscillatory heat generation pattern at the pin tool surface will still experience the maximum temperature at the tool surface and simply oscillates over time. The other possibility is that heat generation occurs preferentially away from the tool surface in a time dependent manner. The thermal pulse cannot migrate, only decay but the maximum temperature location could move with the position of maximum heat generation.

It can be shown that the heat generation and slip planes must be away from the tool surface and the energy equation would require transient thermal behavior. This behavior would be observed in the experimental data but none is apparent. When this contradiction with the MZ model was discovered, the added effect of strain rate was considered. This mechanism is commonly found in the literature describing constitutive relations in plastic deformation. Examples of these models can be found in Miller (1987), Besseling and van der Giessen (1994), and Gilman (1969). These constitutive models have form the basis for finite element (FE) predictions of plastic deformation such as the MatMod equations developed by Miller (1987).

Start by determining a simplified functional relationship between temperature, strain and strain rate in the range of conditions found in FSW. Data is scarce but in Miller (1987) some data is available. We require that the total moment exerted at any radial position be constant The data in Miller was collected at two strain rates, $\dot{\varepsilon}$=.02s^{-1} and $\dot{\varepsilon}$=2.0s^{-1}. Although it is reasonable to expect that the effect for much larger strain rates will increase, the effects are close to linear except when crossing boundaries on the map between diffusional flow, creep, and "dislocation glide" regimes where the values change abruptly. We have a relationship between temperature difference, strain rate difference, and the change in radius. We pick the temperature and strain rate difference and calculate the change in radius. The results showed that the trends were correct but that the effect of strain rate was too small to fully account for the observed weld region.
In conclusion, the MZ model appears to have questionable validity

Single Slip Surface Model (S^3):

This model uses the concept weld plug surrounding the pin tool as a rigid body rotating with the tool. In this case, the weld plug rotates as a solid body at the same angular velocity as the tool. There is a single slip plane where all of the work input from the tool is converted to heat in the weld material. The weld plug is uniform in temperature and the heat is conducted only away from the weld plug with a negative temperature gradient outside the plug. This type of plastic strain is insensitive to the strain rate. In order for the tool to move through the weld material, the plug must entrain new material on the front edge of the weld plug, rotate it around to the rear and deposit it. By definition, there is no material convected into the weld plug which means that the plug, once established, has very slow exchange with the weld material. Diffusion is the primary mechanism. Thermal Model:

Temperature measurements taken during the FSW process show a maximum temperature of approximately 380C. Measurements were made using a sacrificial thermocouple which limits it to the undeformed portion of the weld material. For the MZ model, this limitation is important because heat generation through friction is volumetrically distributed through the weld plug. For this model the limitation is unimportant because the heat generation is concentrated at the single slip plane and the weld plug is a uniform temperature with heat removal only by conduction outside the slip plane.

An estimate of the maximum temperature can be made and compared to the measured value. We start with the simplified form of first law of thermodynamics,

$$\dot{W}_{in} = \dot{Q}_{out}.$$

The work in is the work supplied by the tool and the heat out is removed by conduction. In practice these numbers are not quite that simple to supply. The dynamometer measures all forces. However, only those forces involved in dissipative material motion add to the work input. Heat removal will not be simply by conduction to an infinite plate of weld material. At hot locations, radiation and convection will transfer heat directly to the environment and the plate is finite. The work input will be estimated by,

$$\dot{W}_{in} = \int \left(\tau_{ij} V_j \right) \cdot dA$$

F[N] is the force, V[m/s] is the velocity of the material motion, τ_{ij}[Pa] is the stress tensor, A[m^2] is the area, Ω[rad/s] is the angular velocity, and T[N m] is the torque. The dynamometer measurements allow us to estimate several work inputs. Fortunately all are mutually orthogonal and can be used directly. The work input due to torque is approximately 2.11kW, work from tool translation is approximately .008kW, and work from forces into the plane of the material is approximately 2.2kW.

From the energy balance, this work input is converted to heat and must be conducted away. Several estimates were made of the heat transfer and temperature field but only the most realistic estimate will be described here. In Carslaw and Jaeger (1957) several solutions are developed which may approximate the FSW process. The one used here is a moving strip along a semi-infinite medium where the strip generates heat at a finite rate. To use this solution the top and bottom surface of the weld material is assumed to be insulated to approximate the infinite extent in the z direction. The motion is assumed to take place in the -x direction also infinite and the y values of the domain are assumed to extend from 0 to infinity. Thus the finite extent of the weld material will need to be ignored. The solution is written as,

$$T(x,y) = \frac{\kappa Q}{\pi k V} \int_{X-B}^{X+B} \exp[u] K_0\left\{u^2 + Y^2\right]^{1/2}\right\} du$$

X=Vx/2κ, Y=Vy/2κ, B=Vb/2κ

Q is the heat generated per unit depth, k is the thermal conductivity, V is the velocity, κ is the thermal diffusivity, b is the half width of the strip, and K_0 is the modified Bessel function of the second kind of order zero. The integral is evaluated by using a set of four polynomial approximations to I_0 and K_0 which are accurate over the entire real axis (Ambromowitz and Stegun, NBS), and numerically integrating the integral using a simple trapezoidal rule. Numerical purists will disagree on the use of the trapezoidal rule but the function is relatively well behaved if plotted, the accuracy requirements are modest as this is a rough estimate, and a sensitivity study on the number of subdivisions showed that it converged very easily. The resulting profile had a maximum temperature of approximately 400C which agrees reasonably well with measurements. The value for b was set as the weld plug radius. This choice does not reflect the actual heat transfer area (a semi-circle) but does not distort the width of the initial disturbance. The relatively good agreement between predicted temperatures and measured maximum temperature simply indicates that the overall balance between measured power input and the measured temperature appears to be reasonable. It also indicates that the models and assumptions used also appear to be reasonable. It does not represent a real predictive capability.

Mechanical Model:

Theoretical Calculation:

The simplicity of this model makes it possible to calculate the required forces. The assumptions needed to make this calculation are that both the temperature and geometry of the plug are known beforehand. Using the geometry seen in photographs of the weld cross section, the geometry is approximated as a tapered cylinder. The required properties are the yield stress as a function of temperature. In the previous model (MZ), the yield stress was a function of both temperature and strain rate. The assumption was that the mechanisms were creep and diffusion. In this model the single slip plane requires a very high strain rate mechanism which is essentially strain rate independent. The uniform temperature weld plug will be assumed to be at 370C which is approximately the measured value. At this temperature the yield stress for aluminum alloy 2219 is 26MPa. The moment is written as,

$$M = \int dM = \int_{z=0}^{z=.6} \tau 2\pi r^2(z) dz$$

The equation for r as a function of z is linear, or r(z) = a + bz

$$M = 2\pi\tau \int_{z=0}^{z=.6} (a + bz)^2 dz = 109\ \mathrm{N \cdot m}$$

Experimental Calculation:

From the experiments, the measured torque is

$$M_{torque} = 35 ft \cdot lbf = 47 N \cdot m.$$

The contribution from material moved by the threads is added in a complex pattern of material motion which, in a reference plane moving with the tool would appear as a toroidal movement.

$$M_{threads} \cong 50 N \cdot m$$

Combining both contributions, the total moment from experimental measurements is

$$M_{total} = M_{torque+} M_{threads} \cong 98N \cdot m$$

This is within 10% of the calculated value which is better agreement than we should get given the assumptions which were made. Again, this analysis is not a predictive tool because it requires the temperature and weld plug shape known in advance. It does support the validity of the S^3 model by showing that the forces required match the forces supplied (at least to the accuracy available).

Weld Plug Shape Prediction using the S^3 model:

During the FSW process, the actual shape and temperature at the slip surface is not a random event. Instead, these variables are selected on the basis of physical principles which, if determined correctly, provides a true predictive capability not yet developed. In mechanics, both solid and fluid, a common principle which has been successfully used to model observed phenomena is a minimum energy concept. The FSW process is not static so we modify the concept to be a minimum power requirement. The shape of the weld plug will change to minimize the required power input subject to boundary conditions imposed by the tool shape and motion. The power requirement will strongly depend on the plug temperature which also depends on the power input which dissipates to increase the internal energy. The coupled processes of energy and mechanical power must be satisfied simultaneously to determine either the temperature or the shape of the weld plug. A crude algorithm based on hand calculations was developed which would help determine weld plug shape. Three candidate shapes were evaluated. The first shape simply follows the tool profile (pin and shoulder) which has the minimum weld plug volume. The second shape, called a modified mushroom shape, represents a simplification of the shapes observed in photographs. The final shape is a simple cylinder with a radius of the tool shoulder.

Case 1: Tool shape - total Power Required $\tilde{P}_{tot} = \tilde{P}_T + \tilde{P}_S \cong 2\pi\sigma\Omega\left(7.37x10^{-7}\right)$

Case 2: Modified Mushroom Shape - $\tilde{P} = \sigma\Omega 2\pi\left(8.55x10^{-7}\right)$

Case 3: Cylinder Shape - $P \cong 2\pi\sigma\Omega\left(1.024x10^{-6}\right)$

By comparing the coefficient of all three shapes, the ranking suggests that the cylinder is the least likely. Because the tool shape is extreme, the likely shape of weld plug would be probably lie between the modified mushroom and the tool shape. The calculation should be continued with shapes lying between these two shapes to finally converge on the most likely shape. Although this is tedious to calculate by hand, it may be possible to write a simple computer code which can find the minimum power shape using a search algorithm.

Computer Optimization of Shape:

Start by using an approximate equation for the required power,

$$\tilde{P} = (\sigma\Omega\pi / 2)(r_{i+1} + r_i)^2 \sqrt{(r_{i+1} + r_i)^2 + (z_{i+1} + z_i)^2}$$

We can minimize this by ignoring the constants (σ, Ω, and π)

$$Min(\tilde{P}) = Min\{(r_{i+1} + r_i)^2 \sqrt{(r_{i+1} + r_i)^2 + (z_{i+1} + z_i)^2}\}$$

The computer code used a very simple search algorithm. Like most search algorithms, this one will converge on a local minimum which may or may not be the global minimum. In fact, the actual physical shape of the weld may not be a global minimum or any particular local minimum. However, nature is often kind and the calculated minimum usually corresponds to the most realistic value. If there is doubt, different initial conditions will often find other extrema, should they exist. This algorithm was used to calculate the shape of the weld plug for two conditions. The first is that the bottom is free to move and the second closed the bottom of the weld plug with a radius equal to zero. Both calculated shapes were independent of the initial conditions and were quite similar except for the bottom several points.

Material Motion:

MZ Model:

One of the striking differences between the two models discussed here, (the MZ and S^3 models) is the behavior of the moving material surrounding the pin tool. The area surrounding the pin tool in the MZ model acts as a reservoir which exchanges material freely with its surroundings. If we assume that the material in front of the pin tool is simply

ingested into the mixed zone and that the material in the mixed zone is completely mixed before it exits at the rear, the composition of any solutes of the alloy is easy to predict using a simple rate equation. With these assumptions, the equation is,

$$\frac{C - C_0}{C_0} = -\exp\left(-\frac{4Vt}{\pi d}\right)$$

V is the forward velocity of the tool, C_0 is the concentration of an solute in the weld material at the current position, C is the concentration of the solute in the weld plug, d is the diameter of the weld plug and t is time. As expected, the concentration of any solute relaxes towards the local value in the form of a decaying exponential function. Large velocity in the x direction and small plug diameter reduces the transition time. The effect of diameter may seem surprising at first but it simply represents the ratio of storage volume to the boundary area.

S^3 Model:
With a single slip surface, the weld plug behaves like a solid body rotating with the pin tool. Material is transported around the weld plug in a thin layer. Exchange of material with the surrounding weld material is slow. Of interest is the maximum thickness of the thin layer transporting the transporting material around the weld plug, which occurs at $\theta = \pi$,

$$T_{\max}(\pi) = \frac{2V}{\Omega} \cong 7.6x10^{-5} m.$$

This estimate is useful to evaluate some previous measurements using tracers, in particular Boeing's experiment using small spheres for tracers. Here we see a very thin layer, much thinner than the diameter of the tracer spheres. In theory, tracers should not influence the behavior of the process being studied but these spheres are larger than the predicted width of the layer. This makes detailed conclusions from that experiment suspect. While the tracer spheres were much too large to provide information on the S^3 model is does provide a test of the MZ model. For a process like that of the MZ model there is no thin layer which would be disturbed by these spheres. The spheres should be ingested into the large area of plastically deforming material surrounding the pin tool similar to any solute found in the surrounding material. Like the previous argument concerning the solute concentration for the MZ model, the spheres should be released randomly from the mixed zone in both time and location. The pictures actually show that the spheres were left primarily in a line behind the weld plug. The actual dynamics of the interaction between hard spheres and any type of plastically deforming material is a complex issue. The behavior of a spheres with dimensions larger than a layer of deforming material (S^3)cannot be predicted. Similarly the behavior of hard spheres in a deforming material with continuously variable strain rates (MZ) currently defies prediction. With that caveat, we can argue that it does suggest the material surrounding the pin tool is not a well mixed mass of continuously deforming material such as proposed by the MZ model.

Conclusions:

Given the S^3 and the MZ model and the estimates made above, how can we choose between the two models? One fairly strong test is to run an experiment with the tool going from one material into another. If the materials have detectably different alloys, the composition of the weld plug should not change from the initial material if the S^3 model is correct. The composition of the weld plug should gradually change from the composition of the first material to the composition of the second material if the MZ model is correct. The test ends by removing the tool from the second material, making a cross section of the weld plug, and measuring profiles of solute composition in the cross section of the weld plug. This is planned and may be completed before the end of this phase of the project. A word of caution is that either model will be an idealization of the actual process. There will be some exchange of material even if the S^3 model is the best description. To discriminate between the two models we should consider zero exchange as one extreme S^3, and the composition previously predicted from the MZ model as the other extreme. The actual results should lie somewhere between those two extremes and a clear choice emerges if the results were very near one prediction or the other. The final possibility is that the composition of the weld plug is completely of the second material which would not confirm either of the two models discussed here. In that case another model is needed. Perhaps the one proposed by Boeing where there is no weld plug and the softened material is simply pushed around the tool.

Beyond the question of simply identifying the mechanisms which are important in the FSW process we can use this type of modeling to provide guidance in using this process for different materials and different geometrys. For example, it is now possible to predict the tool forces and operating temperatures for material of a different thickness. We do this by using both the energy balance and the force balance and require that they be in equilibrium. The basic technique was described previously in the report. Similarly, the forces and temperatures for different materials can be predicted using the same techniques with data relating the yield stress to the temperature of that material.

More interestingly we are now able to study some of the details of the process. Photographs of the weld cross section shows a vortex like structure oriented along the weld joint. This structure may or may not have any importance in the weld properties. This rolled up structure appears to be caused by the downward motion of material caused by the rotation of the threads. Recent data and the opinion of the people studying this process indicates that the z forces on the tool are caused by this motion and that it represents important work input into the weld. The models support this argument by requiring that the z forces and predicted material motion due to the thread rotation are needed to maintain the balance between the thermal outputs and the mechanical inputs. If the primary importance of the motion of the threads is simply to increase the work input, we can eliminate the threads and add additional mechanical energy in other ways such as by increasing the diameter of the weld plug (tool shoulder diameter) or by increasing the tool rotational speed of the tool or both and measure the weld properties with and without the vortex structures.

Some potential optimizations of the process can be identified using the model. Tool forces can be reduced by increasing the weld temperature. The temperature can be increased by increasing the mechanical work input or reducing the translational (x) speed of the tool. Mechanical work input comes primarily from either the rotation of the tool and the motion caused by the pin tool threads (z forces). The translation of the tool (x forces) represents a very small input of mechanical energy. Of the important inputs, the z forces are the most difficult to support during the welding process which again argues that the rotational work input is the easiest to increase. An increase in the rotational speed should then be accompanied by an increase in thread pitch to alter the relative effects of rotation with z forces.

If weld temperatures strongly influence the resulting tensile strength of the weld, it is possible to increase translational speed and maintain weld strength by adjusting the work input (probably the rotational work input alone) to maintain a constant weld temperature. Similarly, if the weld temperature is not (by itself) an important factor in weld strength, mechanical work input can be increased at constant translational speed to reduce the needed tool forces.

The last comment is that the tool shoulder currently has two purposes. The first is to add rotational energy and the second is to prevent the material from deforming plastically in the z direction. Potentially some of the disadvantages of operating at higher temperatures (the tendency to soften the material to such an extent that it is not effectively constrained by the tool shoulder) could be eliminated by adding an annular extension of the shoulder that does not rotate or add mechanical work. The relative size of the rotating portion of the shoulder relative to the size of the non-rotating portion could be changed to improve weld characteristics. Possibly the entire shoulder should be stationary.

As we can see, the result of modeling is to add more questions than it answers and the primary objective is not to understand FSW but to help direct the research to improve it.

Acknowledgments:

This report is the result of the efforts of many people. First and foremost, I would like to thank Arthur C. Nunes for his patient discussions and understanding during this 10 week period. As he well knows, it was not a linear effort from conception to this point. Many of the models and ideas were originally his and were only expanded by me. Even after he proposed some of these ideas, he was probably dismayed and most certainly restrained as he watched where I went with them. The final report certainly reflects his strong input but not necessarily the conclusions. To anyone interested in the results of this report I would strongly suggest discussing it with Dr. Nunes to get his interpretation.

Experimental data was supplied by a group headed by Jeff Ding, (NASA) and his team which included Glynn Adams (University of Arkansas), Peter Romine (Alabama A&M University), and Peter Oleogotz (Boeing Aircraft). The Summer Faculty Fellowship Program was very capably managed by Gerald Karr and his staff. The support staff at MSFC was very accommodating and were able to provide computer and communications support which made my time here very productive. My thanks to them all.

References:

1) The Aluminum Association, "Aluminum standards and data 1997", (1997)
2) Ambromowitz and Stegun, (19??), Handbook of Mathematical Functions, National Bureau of Standards, Department of Commerce.
3) Argon, A.S., (1975), Constitutive Equations in Plasticity, The MIT Press, Cambridge, MA.
4) Besseling, J.F., and van der Giessen, E., (1994), Mathematical Modeling of Inelastic Deformation, Chapman and Hall, London.

5) Carslaw and Jaeger, (1957), Heat Conduction, Oxford University Press, Oxford.
6) Gilman, J.J., (1969), Micromechanics of Flow in Solids, McGraw-Hill, Inc. New York.
7) Miller, A.K., (1987), Unified Constitutive Equations for Creep and Plasticity, Elsevier Applied Science, London.
8) Nunes, A.C., (1997), personal communication.

1997

NASA/ASEE SUMMER FACULTY FELLOWSHIP PROGRAM

MARSHALL SPACE FLIGHT CENTER
THE UNIVERSITY OF ALABAMA IN HUNTSVILLE

IMAGING EXTRA-SOLAR PLANETS WITH AN ULTRA-LARGE SPACE TELESCOPE

Prepared By: Charles R. Taylor, Ph.D.

Academic Rank: Assistant Professor

Institution and Department: Western Oregon University
Division of Natural Sciences and Mathematics

NASA/MSFC:

Office: Program Development
Division: Advanced Systems and Payloads
Branch: Space Science & Applications Office

MSFC Colleague: Jonathan W. Campbell, Ph.D.

Introduction

NASA's Origins Program is directed toward two main goals: Imaging of galactic evolution in the early universe, and searching for planets orbiting nearby stars.1 The Next-Generation Space Telescope (NGST), operating at low temperature with an 8-m aperture, is well designed to meet the first goal. The goal of imaging planets orbiting nearby stars is more problematic. One line of investigation has been the ULTIMA concept (Ultra-Large Telescope, Integrated Missions in Astronomy).

In this report, I will lay out the resolution requirements for telescopes to achieve the imaging of extrasolar planets, and describe a modeling tool created to investigate the requirements for imaging a planet when it is very near a much brighter star.

Resolution requirements for extrasolar planet imaging

Figure 1 shows the resolution requirements for three tasks related to imaging extrasolar planets. It would appear the HST already has the resolution needed to begin to image the faint blue galaxies, which indeed it has. The HST would also appear to have the capability to separate the images of nearby extrasolar planets from the stars they orbit, which is not the case. The stars are so much brighter than the planets that the diffraction haloes in the images overwhelm the images of the planets. Of the four telescope concepts, none approaches the requirement for imaging details on faces of extrasolar planets. Only the 100-m telescope is capable of imaging a Sun-like star at 10 pc, although a star is bright enough that a filled aperture is not needed for this task.

Imaging a planet orbiting a nearby star

A spreadsheet tool to calculate the signal in a large space telescope from a planet orbiting a nearby star, and compare it with photon noise in the diffraction halo of the star, has been constructed and made available on the Internet (http://www.wou.edu/research/physics/taylorc/taylorc.html).

The distribution of energy with wavelength for a blackbody at temperature T_B is

$$f(\lambda)=\frac{15}{\lambda}\left(\frac{hc}{\pi\lambda k\,T_B}\right)^4\left[e^{\frac{hc}{\lambda kT_B}}-1\right]^{-1}=\frac{2\pi hc^2}{\sigma\,{T_B}^4\lambda^5}\left[e^{\frac{hc}{\lambda kT_B}}-1\right]^{-1} \qquad (1.)$$

where

$$\sigma=\frac{2\pi^5k^4}{15h^3c^2} \qquad (2.)$$

is the Stefan-Boltzmann constant. The distribution is normalized such that

$$\int_0^\infty d\lambda \; f(\lambda) = 1. \tag{3.}$$

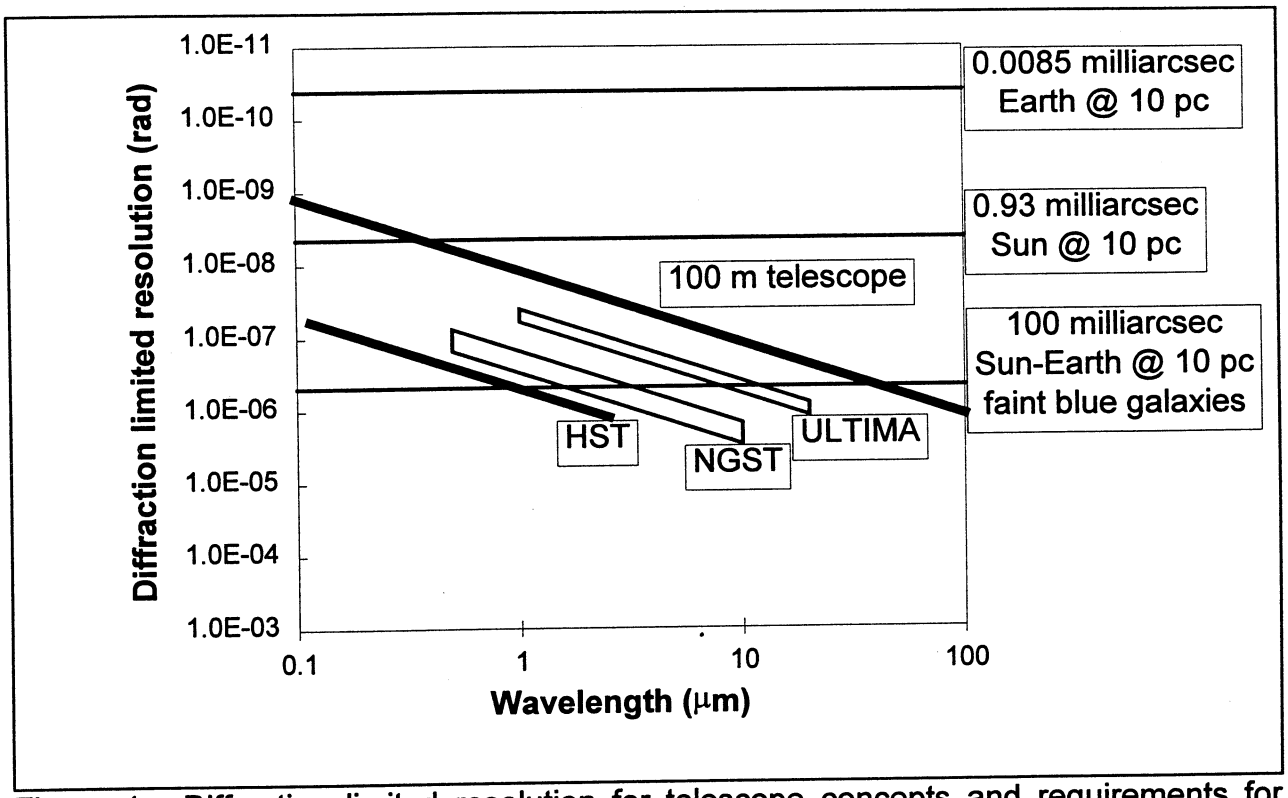

Figure 1. Diffraction limited resolution for telescope concepts and requirements for extrasolar planet imaging. The horizontal lines, starting from the lowest, are the requirements for separating the image of an Earth-like planet from a Sun-like star at 10 pc (which is about the same as the requirement for imaging faint blue galaxies in the early universe), imaging details on the face of the star itself, and imaging details on the face of the planet. The diffraction limited resolution decreases with increasing wavelength, but long wavelengths (near 10 μm) are needed to achieve the goals of the Origins Project.

The distribution of energy in the image of a monochromatic point source in an unobstructed circular aperture of diameter D is given in the Fraunhofer limit by

$$g(u) = \frac{1}{\pi u^2} J_1^2\left(\frac{\pi D u}{\lambda f}\right) \tag{4.}$$

where u is a radial coordinate centered on the image in the focal plane and f is the focal length.

The energy of a photon of wavelength λ is given by

$$E = \frac{hc}{\lambda} \tag{5.}$$

From equations 1, 4, and 5 it follows that the number of photons from a blackbody point source reaching a pixel is

$$N_B = \phi \tau \int dA \int_0^\infty d\lambda \eta(\lambda) \frac{1}{\pi u^2} J_1{}^2\left(\frac{\pi D u}{\lambda f}\right) \times \frac{2\pi hc^2}{\sigma T_B{}^4 \lambda^5} \frac{1}{e^{\frac{hc}{\lambda k T_B}} - 1} \times \frac{\lambda}{hc} \qquad (6.)$$

where ϕ is the energy flux on the aperture, τ is the integration time, and η is the throughput of the instrument as a function of wavelength. If we assume a blackbody source of radius R_B at a distance R, the flux is

$$\phi = \frac{\pi}{4} \frac{R_B{}^2 D^2}{R^2} \sigma T_B{}^4 \qquad (7.)$$

Equation 7 can be rewritten to express the emitted signals of a star and a planet at essentially the same distance.

$$N_S = \frac{\pi}{4} \frac{R_S{}^2 D^2}{R^2} \tau \int dA \int_0^\infty d\lambda \eta(\lambda) \frac{1}{\pi u^2} J_1{}^2\left(\frac{\pi D u}{\lambda f}\right) \frac{2\pi c}{\lambda^4} \frac{1}{e^{\frac{hc}{\lambda k T_S}} - 1} \qquad (8.)$$

$$N_{PE} = \frac{\pi}{4} \frac{R_P{}^2 D^2}{R^2} \tau \int dA \int_0^\infty d\lambda \eta(\lambda) \frac{1}{\pi u^2} J_1{}^2\left(\frac{\pi D u}{\lambda f}\right) \frac{2\pi c}{\lambda^4} \frac{1}{e^{\frac{hc}{\lambda k T_P}} - 1} \qquad (9.)$$

The temperature of a planet with no internal energy source can be estimated as

$$T_p = T_s \left[(1-a) \frac{R_s{}^2}{4r^2} \right]^{\frac{1}{4}} \qquad (10.)$$

where a is the albedo and r is its distance from the star.

An equation similar to Equation 9 holds for the light reflected by a planet,

$$N_{PR} = \frac{a R_p{}^2}{8r^2} \frac{\pi}{4} \frac{R_S{}^2 D^2}{R^2} \tau \int dA \int_0^\infty d\lambda \eta(\lambda) \frac{1}{\pi u^2} J_1{}^2\left(\frac{\pi D u}{\lambda f}\right) \frac{2\pi c}{\lambda^4} \frac{1}{e^{\frac{hc}{\lambda k T_S}} - 1} \qquad (11.)$$

where r_p is the radius of the planet. Note that the temperature in the wavelength integral is that of the star.

We are interested in the signal from the star at points well removed from the central diffraction peak. The Airy pattern varies greatly across the diffraction rings, but when averaged over a pixel or a wavelength band the variations will be suppressed. The Bessel function at large values of the argument can be approximated by

$$J_1(z) \approx \sqrt{\frac{2}{\pi z}} \cos\left(z - \frac{3\pi}{4}\right). \tag{12.}$$

Averaging over the oscillations of the cosine function, and setting the distribution to a constant near the peak, we have a decent approximation of the entire distribution in the following equation.

$$g(u) \approx \begin{cases} \frac{\pi^3}{27}\left(\frac{D}{\lambda f}\right)^2 & u < \frac{3}{\pi^2}\left(\frac{\lambda f}{D}\right) \\ \frac{\left(\frac{D}{\lambda f}\right)^2}{\left(\frac{\pi Du}{\lambda f}\right)^3} & u > \frac{3}{\pi^2}\left(\frac{\lambda f}{D}\right) \end{cases} . \tag{13.}$$

This approximation is used only for the star signal away from the central peak,

$$N_{S\,halo} \approx \frac{\pi}{4}\frac{{R_S}^2 D^2}{R^2}\tau\frac{2cfw^2}{\pi^2 Du^3}\int_0^\infty d\lambda\eta(\lambda)\frac{1}{\lambda^3}\frac{1}{e^{\frac{hc}{\lambda kT_S}}-1}. \tag{14.}$$

The original variable u has been integrated away; the variable u in equation 14 is the distance of the pixel from the center of the bright star image.

For the planet signal, the central peak is calculated. I approximate the square pixel as a circle of the same area, and take the average of two cases: the center of the image in the center of the pixel, and the center of the image at the corner of four pixels. This yields

$$\begin{aligned} &\int dA \frac{1}{\pi u^2} {J_1}^2\left(\frac{\pi Du}{\lambda f}\right) \approx \\ &\approx \frac{5}{8} - \frac{1}{2}{J_0}^2\left(\frac{\sqrt{\pi}Dw}{\lambda f}\right) - \frac{1}{2}{J_1}^2\left(\frac{\sqrt{\pi}Dw}{\lambda f}\right) - \frac{1}{8}{J_0}^2\left(\frac{2\sqrt{\pi}Dw}{\lambda f}\right) - \frac{1}{8}{J_1}^2\left(\frac{2\sqrt{\pi}Dw}{\lambda f}\right) \end{aligned} . \tag{15.}$$

The pixel width w is taken to be half of the Airy disk diameter,

$$w = \frac{1.22 f \lambda_o}{D} \qquad (16.)$$

for the wavelength λ_0 for which the focal plane is optimized for Nyquist sampling. Practically, this equation will fix the focal length of the instrument based on the chosen aperture and available pixel width.

Note also that the angular separation of the planet and star, on average, is

$$\alpha = \frac{r}{\sqrt{2}R} \qquad (17.)$$

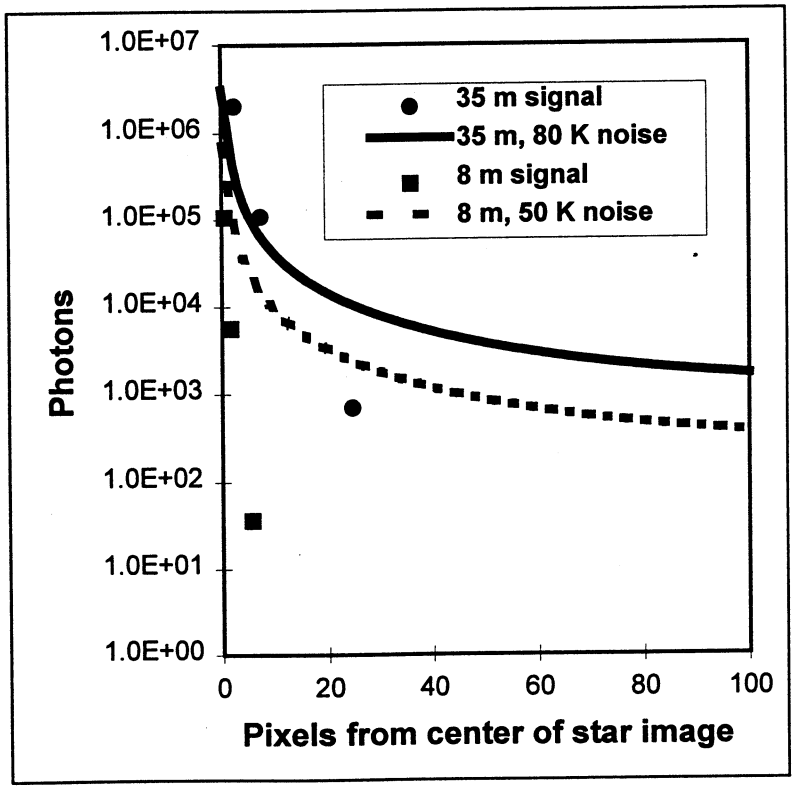

Figure 2. Earth-like extrasolar planet signals and photon noise from nearby Sun-like star, in 35 m and 8 m telescopes. The distance of the star is 5 pc, and the planets are 1,3, and 10 AU from the star.

An example of the results of the calculation is shown in Figure 2. A planet is considered Earth-like if its radius and albedo are equal to those of the Earth. A Sun-like star is one with the same radius and temperature as the Sun. I take the distance to be 5 pc, a distance within which there are about 60 stars. I assume a pixel size of 25 μm optimized for a wavelength of 8 μm, and a band-pass filter to exclude light outside of the range from 10 μm to 20 μm. The likely signal levels from Earth-like planets at 1, 3, and 10 AU are shown for two apertures: 8 m and 35 m. The planet signals are well below the noise at 8 m but above noise levels in the 35 m diameter aperture for the 1 and 3 AU orbits.

Reference

1 A. Dressler, ed., Exploration and the Search for Origins: A Vision for Ultraviolet—Optical-Infrared Space Astronomy, Report of the "HST and Beyond" Committee, Association of Universities for Research in Astronomy, Washington, DC, 1996, http://ngst.gsfc.nasa.gov/project/bin/HST_Beyond.PDF.

1997

NASA / ASEE SUMMER FACULTY FELLOWSHIP PROGRAM

MARSHALL SPACE FLIGHT CENTER
THE UNIVERSITY OF ALABAMA IN HUNTSVILLE

DEVELOPMENT OF A SUNSPOT TRACKING SYSTEM

Prepared By:	Jaime R. Taylor, Ph.D.
Academic Rank:	Assistant Professor
Institution and Department:	Austin Peay State University Department of Physics
NASA/MSFC:	
Laboratory:	Astrionics Laboratory
Division:	Instrumentation & Control
Branch:	Instrumentation
MSFC Colleague:	Ron McIntosh

1. Introduction

Large solar flares produce a significant amount of energetic particles which pose a hazard for human activity in space (Moore et. al. 1990). In the hope of understanding flare mechanisms and thus better predicting solar flares, NASA's Marshall Space Flight Center (MSFC) developed an experimental vector magnetograph (EXVM) polarimeter to measure the Sun's magnetic field (West and Smith 1994). The EXVM will be used to perform ground-based solar observations and will provide a proof of concept for the design of a similar instrument for the Japanese Solar-B space mission.

The EXVM typically operates for a period of several minutes. During this time there is image motion due to atmospheric fluctuation and telescope wind loading. To optimize the EXVM performance an image motion compensation device (sunspot tracker) is needed. The sunspot tracker consists of two parts, an image motion determination system and an image deflection system. For image motion determination a CCD or CID camera is used to digitize an image, than an algorithm is applied to determine the motion. This motion or error signal is sent to the image deflection system which moves the image back to its original location. Both of these systems are underdevelopment.

2. Tracking Algorithms

Two algorithms will be tested for use with the sunspot tracking system. The centroid algorithm works by calculating the centroid of each successive image then determining the shift in the centroid from one image to the next (Mansfield 1996). A modification of the centroid algorithm is presented here where the motion in each direction is calculated using only one row and one column respectively,

$$X_{cen} = \frac{\sum_{i=1}^{N} x \cdot f(i, M_x)}{\sum_{i=1}^{N} f(i, M_x)}, \qquad Y_{cen} = \frac{\sum_{j=1}^{N} y \cdot f(M_y, j)}{\sum_{j=1}^{N} f(M_y, j)}, \tag{1}$$

where $f(i,M_x)$ and $f(M_y,j)$ are the image intensity for a pixel in a particular row and column respectively, and M_x and M_y are the row and column number. The row and column are chosen to overlap the true centroid of the sunspot of interest.

A simplified correlation algorithm (SCA) has been developed specifically for sunspot tracking. The SCA works by first determining error parameters from the initial image. This is done using,

$$E_r = \sum_{i=1}^{N} sign(x_{ref} - i)[f_{ref}(i) - f(i)], \tag{2}$$

where $f_{ref}(i)$ and $f(i)$ are the image pixel intensity for a given row or column of the reference image and the currently acquired image respectively, and i is a pixel index. The variable x_{ref} is an arbitrary reference point such as the centroid of the reference image and has units of pixel width (e.g., if the reference point is in the center of the fifth pixel, x_{ref} would be equal to 5.5). The function sign($x_{ref} - i$) is +1 if $x_{ref} - i > 0$ or -1 if $x_{ref} - i < 0$. The error scaling parameter α is determined by shifting the reference image one pixel and then applying Equation 2 with the shifted image used as $f(i)$. x_o, the image motion, is defined as

$$x_o = \alpha E_{r1} + x_{ref}, \tag{3}$$

where E_{r1} is the value obtained from Equation 2 with $f(i)$ being the reference image shifted by one pixel. The reference image being shifted by one pixel yields α is equal to $1/E_{r1}$. As the reference image is not symmetric, the error scaling parameter α is calculated separately for movements in the positive and the negative direction (α_+ and α_-) for both the X and the Y axes. An appropriate α is selected based on the direction of sunspot movement which is determined from the sign of E_r (Chmielowski and Taylor 1997, and Chmielowski and Klien 1993).

There are obviously advantages and disadvantages to each algorithm. The centroid algorithm is easy to understand and to implement once the image has been preprocessed. The difficulty is with preprocessing the image. In order for the centroid algorithm to work any linear trends in the data must be removed (i.e. the linear trend in intensity near the limb of the sun), and any extraneous features, like a portion of a second sunspot, must be masked out. The disadvantage of the SCA algorithm is that it requires the initial calculation of error parameters, and a scheme might be necessary for updating the error parameters if the intensity of the image changes over time. The advantage of the SCA algorithm is that it will track on whatever is in the field of view, provided there is a sufficiently large object, a sunspot, somewhere in the image. The linear trend of the image near the limb of the sun is not an issue, nor are extraneous features.

3. Sunspot Tracking System

Testing of the preceding sunspot tracking algorithms on simulated sunspots suggested that only one row and one column of pixels were necessary for tracking, providing a factor of N savings in calculation time and image acquisition time over algorithms requiring an entire image. Furthermore determination of movement in each direction is independent implying two identical independent systems for tracking can be developed. Figure 1 shows a diagram of the sunspot tracking system for one axis.

I. Image Motion Determination System.

To acquire the image a CID camera was chosen. The CID camera has the capability of reading out selected rows or a selected row of pixel information at higher rates than the entire image, 700Hz for one row. Two CID cameras will be used, one rotated 90° with respect to the other with a beam splitter used to send the image to each camera. The system will start by reading the entire image and locating a sunspot. Once a sunspot is located a row from each CID

camera will be chosen, for one camera this will correspond to a column of data. The row and column will be chosen to include either the centroid of the sunspot or the minimum value of the sunspot, note these are not necessarily the same location.

The CID camera operates at a significantly lower rate than CCD linear arrays. CCD linear arrays are available that operate near 10kHz as opposed to operating at 700Hz. The primary advantage of using the CID cameras is that a row of pixels exist at the location of the sunspot and must simply be chosen. If two linear CCD arrays were used they would have to be mechanically moved to the location of the sunspot. The scientific camera would have to be used to locate the sunspot to give a location for the CCDs to be moved to.

The locating algorithm will be implemented in the controller digital signal processing (DSP) board, Figure 1. Once the image motion is determined a control algorithm will determine a signal to send from the DSP through an amplifier to the image deflection system.

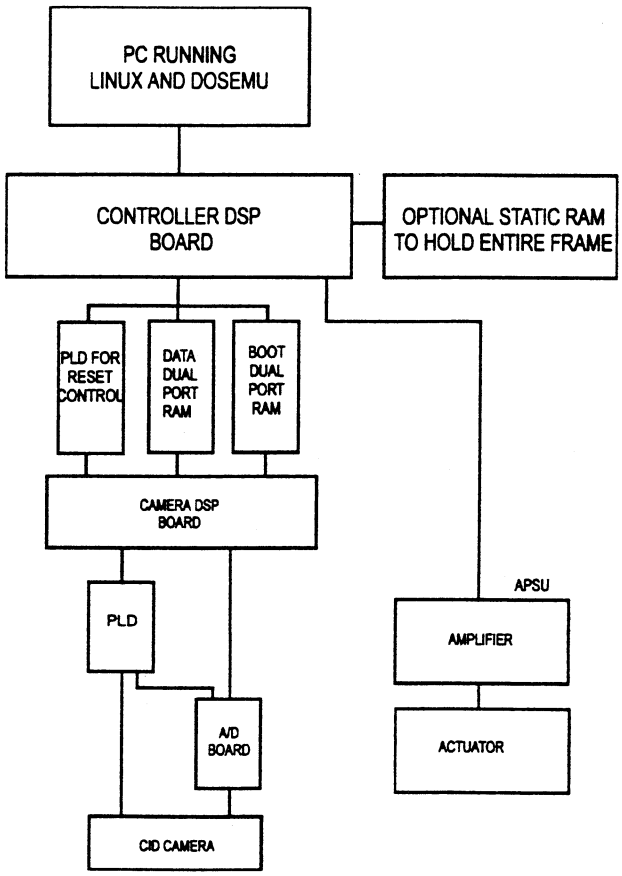

Figure 1.

II. Image Deflection System.

A one mirror image deflection system will be used for each independent tracking system. A magnetostrictive actuator has been chosen to move each mirror about the given axis. A magnetostrictive actuator was chosen over piezoelectrics due to their larger range of motion and larger driving force. The design issues to consider are how to mount the actuator, how to mount the mirror, and what to use to allow the mirror to rotate about one axis only.

The EXVM has already been built and a limited amount of space is available for the entire tracking system. In order to conserve space an attempt was made to mount the actuator vertically. In this configuration the actuator produced significant transverse vibrations in the optical table it was mounted on. Note that the optical table is similar in size and design to the bottom of the EXVM where delicate instrumentation will be mounted. Mounted vertically the actuator "beats" the optical table like a drum. It was determined the actuator must be mounted horizontal to the table surface. In this configuration it "stretches" the table top, like stretching

the head of a drum. In order for the image deflection system with the horizontal mounted magnetostrictive actuators to be used with the EXVM, the EXVM "box" with have to be redesigned.

It is desired that the horizontal actuator mount have resonant frequencies above the operating frequencies of the system. This is a desire for optimal performance, but is not a requirement; the control algorithm could compensate by reducing the gain at the resonant frequency. A combination of structural modeling using MatLab and experiment are being used to design the actuator mount. Testing the first design showed a resonant frequency at 160Hz. MatLab modeling showed that the resonant frequency was at 130Hz. The usefulness of modeling in this case is not its ability to predict; its usefulness is in its ability to give insight into what is causing the resonance. From the understanding gained from MatLab modeling, the actuator mount has been redesigned and should have a resonant frequency over 800Hz.

The remaining design issues are with mounting the mirror and designing something that allows the mirror to rotate about one axis with a high angular resolution. These issues are being addressed through a combination of testing and modeling.

4. Summary

Two algorithms are available for sunspot tracking which require the use of only one row and one column of image data. To implement these algorithms two identical independent systems are being developed, one system for each axis of motion. Two CID cameras have been purchased; the data from each camera will be used to determine image motion for each direction. The error signal generated by the tracking algorithm will be sent to an image deflection system consisting of an actuator and a mirror constrained to move about one axis. Magnetostrictive actuators were chosen to move the mirror over piezoelectrics due to their larger driving force and larger range of motion. The actuator and mirror mounts are currently under development.

Acknowledgments

The author would like to thank Ron McIntosh for his suggestions and support of this work, and Ed West and Don Hediger for their involvement. The author would also like to thank Patrick Bunton for his work on the image deflection system, and Charles Oliver for the design of the image motion determination system. This work was supported by NASA/ASEE SFFT.

References

Chmielowski, M. and Klien, L., "A High-Precision, Real-Time Position Locating Algorithm for CCD-based Sun and Star Trackers," PASP, vol. 105, pp. 114-116, January 1993.

Chmielowski, M. and Taylor, J. "A Real-Time Sunspot Tracking Algorithm," PASP, vol. 109, pp. 837-842, July 1997.

Mansfield, P., "Machine Vision Tackles Star Tracking," Laser Focus World, pp. S21-S24, May 1996.

Moore, P., Hunt, G., Nicholson, I., and Cattermole, P., The Atlas of the Solar System, Crescent Books, New York, 1990.

West, E. A., and Smith, M. H., "Polarization Characteristics of the MSFC Experimental Vector Magnetograph," SPIE, vol. 2265, pp. 272-283, July 1994.

1997
NASA/ASEE SUMMER FACULTY FELLOWSHIP PROGRAM

MARSHALL SPACE FLIGHT CENTER
THE UNIVERSITY OF ALABAMA IN HUNTSVILLE

TECHNOLOGY TRANSFER ACTIVITIES OF NASA/MSFC: ENHANCING THE SOUTHEAST REGION'S PRODUCTION CAPABLIITIES

Prepared By:	George W. Trivoli, Ph.D.
Academic Rank:	Professor of Finance/Eminent Scholar
Institution and Department:	Jacksonville State University Department of Finance and Statistics
NASA/MSFC:	
Office:	Technology Transfer
Branch:	Program Control and Management Support Office
MSFC Colleague:	David Cockrell

Introduction

Although this researcher is not an engineer or science faculty, invaluable knowledge and experience have been gained from this NASA/ASEE Summer Faculty Fellowship. This year's research and activities was related to the previous summer's research; but the experience presented new and varied challenges. This researcher was fortunate to have maximum interaction with NASA colleague, David Cockrell and fellow Summer Faculty Fellow, Christina M. Mastrangelo. It would be both a privilege and honor to continue a relationship with the Technology Transfer Office.

During the past year a Cooperative Agreement between NASA/MSFC and The College of Commerce and Business Administration, Jacksonville State University was instituted. Dean William Fielding of the College of Commerce and Business Administration is anxious to aid the efforts of NASA/MSFC in its technology transfer activities.

The principal benefits gained by this researcher include the opportunity to conduct research in a non-academic, real world environment. In addition, this researcher was able to interact with the excellent professional staff of the Technology Transfer Office. This researcher has gained enhanced respect and understanding of the staff and facilities of Marshall Space Flight Center.

Preparation of a Simple Model of Production Possibility Frontier

This researcher was charged with the task of developing a simplified model to illustrate the impact of how NASA/MSFC technology transfer activities contribute to shifting outward the Southeast region's and the nation's productive capacity. What follows is a background report of the impact of technological growth on the nation's production possibility frontier (ppf).[1]

The production possibility frontier (ppf) illustrates scarcity and choice in an economy by using a simple model of an economy in which only two goods can be produced. The ppf is called a frontier since it represent the limits of output possibilities given the current level of resources and technology. The frontiers of knowledge and capability are able to expand and the ppf is no exception. Over time, as resources are accumulated and new technologies are applied, the ppf will expand outward.

Recent developments in growth theory have made rates of technology change and/or population growth an intregal part of the model of growth.[3] Technology change includes changes in technological knowledge (*eg.* ways to employ robots in the production process), as well as new knowledge (*eg.*

Managerial strategies). According to estimates of Edward F. Denison, during the period 1920 - 82, technology change accounted for 28 percent of the growth in the U.S., and is the most important influence on labor productivity.[2]

Simple Model of Two-Product Economy

Suppose a two-product economy located on a remote island inhabited only by Joe Six-pack. The island provides for all his material needs, but he must spent time to feed himself. His options are to catch fish or harvest coconuts. He values both of these foods in his diet and can spend up to eight hours a day to obtain them. This can be illustrated by means of a simple ppf for Joe's economy.

The relationship between Joe's options are shown in Figure 1. For instance, the basic message of the ppf is that as more fish are caught, fewer coconuts can be collected. The inverse relationship between fish and coconuts illustrates the opportunity cost to Joe using his limited resource, time.

Figure 1

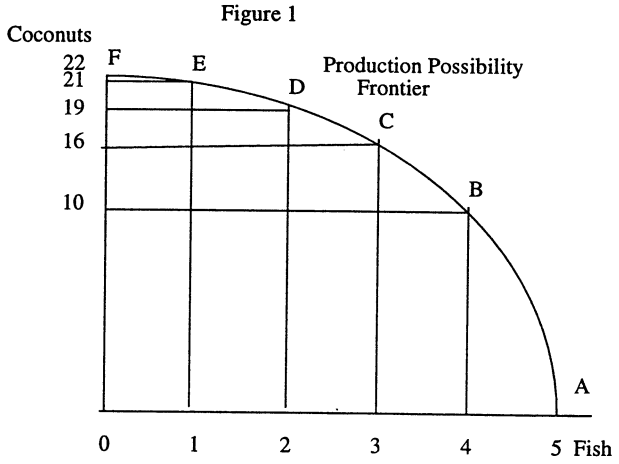

As Joe increases his catch from zero to a maximum of five, we see the number of coconuts he collects drops off at a nonlinear rate. In other words, the opportunity cost of the first fish is only one coconut, but as he spends more time fishing, he gathers less coconuts. This illustrates the concept of the *theory of increasing costs*, which states that as an economy adds to its production of any one good, the marginal (extra) opportunity cost of that good will tend to rise. This explains why the ppf appears bowed outward.

Returning to Joe's island, each working hour of the day he must choose between fishing or gathering coconuts. The most productive fishing occurs at certain hours of the day when fish are biting; while all hours are equally well suited to gathering coconuts. Joe knows that the number of coconuts gathered per hour declines as he spends more hours fishing, thus he gathers the most accessible

coconuts first. In the beginning he can reduce hours of coconut gathering allowing more time to catch fish at a cost of relatively few coconuts. However, adding more hours to his fishing time leads to less incremental productivity in fishing while taking away productive hours gathering coconuts. This illustrates the law of increasing costs.

Technological Improvements

Technological improvements can increase productivity in an economy generally, as has been the case with better information flows made possible by modern computers and telecommunications. Often however, technological improvements are specific to an industry. For instance, a biotechnological advance might improve crop yields for agriculture but have no effect on, say, the steel industry. Figure 2 illustrates the difference between general growth in an economy and specialized growth, when the economy starts from the original ppf. In the case of general growth shown in Figure 2A, productivity of all goods and services are increased, as in the case with improved computers and telecommunications. In the case of specialized growth shown in Figure 2B, productivity increases in a particular sector, say, agriculture.

Figure 2

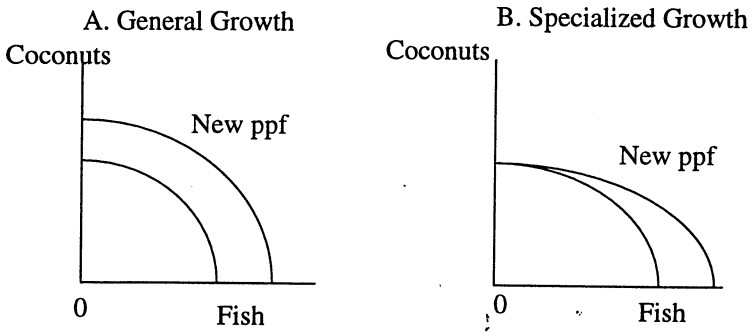

Production possibilities depend upon how much of each resource the economy has, as well as the technology that is available to make use of those resources. As resources increase or technology improves, production possibilities grow. On the other hand, a natural disaster or exhaustion of a natural resource tends to cause the economy's resource base to shrink, thus causing the production possibility frontier to shrink (*eg.* shift the ppf curve inward).

Let's return to Joe Six-pack's island. Suppose Joe were to take some time to construct some netting to use in catching fish and some additional netting to collect the coconuts as they fall from the trees. The nets are capital goods that

embody technological improvements, allowing Joe to catch more fish and collect more coconuts per hour. These improvements shift Joe's ppf outward (Figure 2A) allowing Joe to have both more fish and coconuts than before.

Transferring NASA/MSFC technology to private industry contributes to improvements in both industrial production techniques and improved products and services for the entire economy. In the case of NASA/MSFC technology transfer activities, the outward shift in the production possibility frontier may be either specialized (*eg*, improved healthcare) or more generalized (*eg*, improvements in computers). In either case, the productive capacity of the Southeast region and the U.S. is enhanced as NASA/MSFC technology is adapted to the private sector.

Technology Transfer Activities of NASA/MSFC

Let's turn to some specifics regarding the technology transfer activities of NASA at Marshall Space Flight Center (MSFC). The activities involve a broad cross section of businesses, both large and small, throughout the United States. For instance, a small clothing manufacturer, Apparel Manufacturing Company, is using computer simulation developed by NASA/MSFC and the University of Alabama. The Modular Manufacturing and Simulation Data Package allows multiple clothing items to be made simultaneously with a rapid turn-around time for orders. The company indicates that it cut operating costs up to 20 percent, increased sales by $1.5 million; and added over 30 employees.

NASA/MSFC technology transfer aids small, medium and large firms alike. For instance, various divisions of Pratt & Whitney (United Technologies) that have served as prime contractors on the Space Shuttle Program have successfully commercialized several adapted NASA technologies. These include the application of water jet stripping technology as an environmentally friendly way of cleaning vital jet engine parts on major airline planes, as well as for use on ships, boats, barges and floating dry docks.

Medical science and meteorology have also benefited from NASA/MSFC technology transfer activities. A vision screening system developed at NASA/MSFC is helping the Vision Research Corporation of Birmingham, AL detect vision abnormalities and diseases in hundreds of thousands of children across the United States. The system involves photographing the children's eyes and analyzing the patterns reflected from them. Different eye abnormalities and diseases cause the eyes to reflect light in different ways. Each abnormality has a reflection "signature," thus permitting immediate diagnosis.

Meteorology has also benefited from NASA/MSFC technology transfer activities. The system provides a storm projection system that allows electric utilities and emergency management officials to plot dangerous storm's projected movements. Baron Services developed a means of changing the computer generated data into audio data for transmission by radio station sub-carriers for reception by clients through an antenna, and decoded by computer display. Surely, all of these instances of transferring NASA/MSFC technologies to the private industry helped to push outward our nation's production possibility frontier.

This researcher worked closely with fellow researcher, Christina Mastrangelo in developing a methodology for analyzing technology assistance data for evidence of economic impact on the SE region. Actual survey results from leading SIC codes in manufacturing and service industries in the SE region are compared to the U.S. Department of Commerce values. These data, although tentative, do lend support to our contention that technology assistance of NASA/MSFC contributes to shifting outward the ppf; at least in the eleven major industries studied.

Conclusions and Recommendations

This researcher has gained a great deal of insight into the operations of the Technology Transfer activities of NASA/MSFC over the three summers spent as a Summer Faculty Fellow. It is the desire of this researcher to continue as a consultant to the Technology Transfer Office in the future.

Based upon the experiences and background gained over the past three years, several recommendations are listed briefly below.
(1) Continue integration of technology assistance data of NASA/MSFC with comparative data from the U.S. Department of Commerce to demonstrate the impact of NASA/MSFC technology spin-offs on the primary industries assisted.
(2) Add several questions to the TTA questionnaire instrument sent out by TecMasters, Inc., and continue collecting and refining data from the Southeast Alliance technology assistance surveys.
(3) Continue to develop success stories in cooperation with business partners, but concentrate on stories illustrating human interest factors, as well as jobs and productivity improvements.

References

[1] Collinge and Ayers, Economics by Design, (Prentice Hall, 1997), pp. 42 - 47.
[2] Dennision, E.F., Trends in American Growth 1929 - 82, (Washington, D.C., The Brookings Institution, 1985), p. 15ff.
[3] Romer, Paul "Capital Accumulation and Long-Run Growth", in R. J. Barro, Modern Business Cycle Theory, (Cambridge, Mass., Harvard University Press, 1989).

1997

NASA/ASEE SUMMER FACULTY FELLOWSHIP PROGRAM

MARSHALL SPACE FLIGHT CENTER
THE UNIVERSITY OF ALABAMA IN HUNTSVILLE

CHARACTERIZATION OF PVT GROWN ZnSe BY LOW TEMPERATURE PHOTOLUMINESCENCE

Prepared by: Ling Jun Wang, Ph.D.

Academic Rank: Associate Professor

Institution and Department: University of Tennessee at Chattanooga
Department of Physics, Geology and Astronomy

NASA/MSFC:

Lab: Space Sciences Laboratory
Division: Microgravity Science and Applications

MSFC Colleagues: Ching-Hua Su and S. L. Lehoczky

Introduction

ZnSe, a II-VI semiconductor with a large direct band gap of 2.7 eV at room temperature and 2.82 eV at 10 K, is considered a promising material for optoelectric applications in the blue-green region of the spectrum. Photoemitting devices and diode laser action has been demonstrated as a result of decades long research. [1-6]. A key issue in the development of II-VI semiconductors is the control of the concentration of the various impurities. The II-VI semiconductors seem to defy the effort of high level doping due to the well known self compensation of the donors and the acceptors. A good understanding of roles of the impurities and the behavior of the various intrinsic defects such as vacancies, interstitials and their complexes with impurities is necessary in the development and application of these materials [7]. Persistent impurities such as Li and Cu have long played a central role in the photoelectronic properties of many II-VI compounds, particularly ZnSe. The shallow centers which may promote useful electrical conductivity are of particular interest. They contribute the richly structured near gap edge luminescence, containing weak to moderate phonon coupling and therefor very accessible information about the energy states of the different centers. Significance of those residual impurities which may contribute such centers in II-VI semiconductors must be fully appreciated before improved control of their electrical properties may be possible.

Low temperature photoluminescence spectroscopy is an important source of information and useful tool of characterization of II-VI semiconductors such as ZnSe. The low temperature photoluminescence spectrum of a ZnSe single crystal typically consists of a broad band emission peaking at 2.34 eV, known as the Cu-green band, and some very sharp lines near the band gap. These bands and lines are used to identify the impurity ingredients and the defects. The assessment of the quality of the crystal based on the photoluminescence analysis is then possible. In this report we present the characterization of a ZnSe single crystal as grown by physical vapor transport method, with special intention paid to the possible effects of the gravitational field to the growth of the crystal.

Experimental

The low temperature photoluminescence measurements were performed on a as grown ZnSe single crystal cooled to below 10 °K by a CRYO Industries of America, Inc. system. The single crystal is usually cooled to below 10 kelvin with helium vapor. The ultraviolet 364 nm line of an Coherent Innova 300 argon laser is selected for excitation. The energy of this UV line is 3.4 eV, well above the 2.82 eV band gap of ZnSe at 6 kelvin. The photoluminescence spectra were recorded using a Spex 1877D spectrometer which is interfaced to an IBM desktop computer. The position of the sample can be translated by two micrometers with an accuracy of 0.05 mm. The movable sample stage enables us to study the morphology of the sample surface. The sample is translated

vertically by a step of 0.5 mm and horizontally by a step of 0.254 mm (10 mil). The two dimensional scan is carried out in the spectral range between 22430 cm^{-1} to 22650 cm^{-1} (2.78 eV to 2.81 eV) that cover the three major peaks (EX, I_2 and I_1^{deep}). The broad spectrum is taken from 15000 cm^{-1} to 22650 cm^{-1} (1.86 eV to 2.81 eV) to study the general features of the luminescence.

Results

The low temperature luminescence spectra show the typical features seen in the pure ZnSe crystals. The well known Cu-green emission band that peaks at 2.34 eV is clearly seen. This band is believed to be associated with residual copper impurity in ZnSe, resulting from the recombination of an electron in the conduction band with a hole captured at a Cu_{Zn}^{x} center, located 0.35 eV above the valance band. [8-12].

One of the important peaks observed is the broad peak at 2.803 eV, which is the intrinsic free exciton (EX) emission of ZnSe [13,14]. The most dominant peak of the spectra is the I_2 peak at 2.796 eV. This broad peak is actually the superposition of a few narrower peaks associated with neutral and ionic donor-bound excitons (DBE) or with native defects [13-23]. The second most prominent peak is the I_1^{deep} line at 2.783 eV. The origin of the I_1^{deep} line is thought to be exciton annihilation at Cu acceptors made by Cu atoms occupying Zn lattice sites (CuZn) or at Zn vacancies (VZn). [13,14,17, 22, 24,26-28].

Although the intensity of these prominent peaks reflect the concentration of the impurity and the defects, it depends heavily on the surface condition of the crystal that necessarily affects the efficiency of signal collection. Since the EX peak is related to the recombination of the intrinsic free exciton which has nothing to do with any impurity or defects, we then take the intensity ratios of the I_2 peak and the I_1^{deep} peak over the EX peak as indications of the relative strength of these peaks. The sample crystal is scanned along the direction of the gravitational field in the spectrum range of 22400 cm^{-1} to 22650 cm^{-1} (2.779 eV to 2.810 eV). The plots of the intensity ratios show a nearly linear dependence on the gravity. The I_2 line, decreases monotonicaly in the direction of the gravitational field, while the I_1^{deep} line stays pretty much plat. This gives a hit that the gravity might play a role in the growing process of the semiconductor crystals.

Conclusions

Low temperature photoluminescence offers an effective tool and an important source of information for characterization of II-VI semiconductors such as ZnSe. The sharp near band edge spectrum lines, especially the neutral donor bond exciton line I_2 at 2.799 eV, the neutral acceptor bond exciton line I_1^{deep} at 2.783 eV, and the intrinsic free exciton line at 2.802 eV can prove the most useful lines for such characterization. These lines are very prominent and persistent. They stay within 20 meV, a pretty short range for practical scan of the samples within reasonable time constrain. These peaks are heavily investigated experimentally and theoretically, and therefore are the best candidates for more credible

quality assessment of the crystal. No conclusive identification, however, has been ventured in the literature. This is partially due to the fact that the photoluminescence spectra are sensitive to the growing method, the post treatment and the sample preparation. The reliability of photoluminescence characterization is crucially dependent upon the identification of the spectrum lines and bands. The spectrum lines have to be carefully studied and a database prepared before one can have a handy and confident scheme of crystal characterization.

The most reliable but expensive and time consuming way of line identification is of course the doping experiments. The correlation experiments offer the less expensive alternatives. For example, one can study the correlation of the spectrum lines with respect to annealing and aging, or with the change of the excitation energy and the sample temperature. The lifetime studies of the individual peaks can prove to be very fruitful tool to identify these peaks.

Our investigation show that the gravitational field might play a role in the crystal growth. Since the growing ampoule usually has a typical diameter in the order of one centimeter, it seemss hardly conceivable that the difference in gravitational field over such small distance can affect the growing process in any significant way. However, it is well known that the physical properties of the semiconductors are extremely sensitive to the concentration of the impurities and the defects, which are usually a few orders of magnitude smaller than the lattice concentration. A very slight change in the partial pressure of the ingredients in the physical vapor can cause changes in the relative concentration of the impurities and the defects.

References

1. R.J. Seymour, B.J. Fitzpatrick, and R.N. Bhargava, IEEE J. Quantum electron. QE-14, 462 (1978).
2. S. Colak, B.J. Fitzpatrick, and R.N. Bhargava, J.Cryst. Growth 72, 504 (1985).
3. J.E.Potts, T.L. Smith, H.Cheng, B. Yang, and B.W. Wessels, J. Cryst. Growth 86, 935 (1988).
4. C.A. Zmudinski, Y.Guan, and P.S. Zory, IEEE Photon. Technol. Lett. 2, 94 (1990).
5. M.A. Haase, J. Qiu, J.M. Depuydt, and H. Cheng, Appl. Phys. Lett. 59, 1272 (1991).
6. J.M. Depuydt, M.A. Haase, J.Qiu, and H. Cheng, J. Cryst. Growth 117, 1078(1992).
7. Henry C.H., Nassau K., Shiever J.W., Phys. Rev. B4 2453, (1971).
8. Gerald B. Stringfellow an Richard H. Bube, Phys. Rev. 171, 903 (1968).
9. J. L. Patel, J.J. Davies an J. E. Nicholls, J. Phys. C: Solid State Phys., 14, 5545-5557, (1981).
10. M. Yamaguchi and T Shigematso , Jap J. App. Phys. **17**, 335-40 (1978).
11. M. Aven, R.E. Halsted, Phys. Rev. 137, A228 (1965).
12. S. Iida, J. Phys. Soc. Japan 26, 1140 (1969).
13. P.J. Dean, D.C. Herbert, C.J. Werkhoven, B.J. Fitzpatrick and R.N. Bhargava, Phys. Rev. B23, 4888 (1981).
14. J.L. Merz, H. Kukimoto, K. Nassau, and J.W. Shiever, Phys. Rev. B 6, 545 (1972).

15. P.J. Dean, A.D. Pitt, P.J. Wright, M.L. Young and P.Cockayne, Physica 116B, 508 (1983).
16. T. Yao, J. Crystal Growth 72, 31 (1985).
17. B.Hu, A. Yin, G. Karczewski, H.Luo, S.W. Short, N.Samarth, M. Dobrowolska and J.K. Furdyna, J. Appl. Phys. 74(6), 4153 (1993).
18. T. Yodo, T. Koyama, and K. Yamashita, J.Appl. Phs. 64(5), 2403 (1988).
19. K. P. Giapis, Da-Cheng Lu, and K. F. Jenson, Appl Phy. Lett 54(4), 353 (1989).
20 T.Yao, Y. Makita, and S. Maekawa. Jpn J Appl Phy 20, L 741 (1981).
21. H. Cheng, S.K. Mohapatra, J.E. Potts and T.L. Smith, Journal of Crystal Growth 81, 512-517 (1987).
22. V.Yu. Ivanov, Yu.G. Semenov, M. Surma and M. Godlewski, Phys. Rev. B54, 4696, (1996).
23. Z. Zhu, H. Mori, and T. Yao, J. Appl. Phys. 73(3), 1146 (1993).
24. S.M. Huang, Y. Nozue, and K. Igaki, Jpn J. Appl.Phys. 22, L420 (1983).
25. E. Tournie, C. Morhain, G. Neu, M. Laugt, C. Ongaretto, and J.P. Faurie, J. Appl Phy.,Vol 80, N0.5, 2984 (1996).
26. Y. Hishida, T. Toda, T. Yoshie, K. Yagi, T. Yamaguchi, and T. Niina, Appl. Phy. Lett., l64(25), 20, 3420 (1994).
27. J.L. Merz, K. Nassau, and J.W. Shiever, Phys.Rev. B8, 1444 (1973).
28. C.H. Henry, K. Nassau, and J.W. Shiever, Phys. Rev. B4, 2453 (1971).

1997
NASA/ASEE SUMMER FACULTY FELLOWSHIP PROGRAM

MARSHALL SPACE FLIGHT CENTER
UNIVERSITY OF ALABAMA IN HUNTSVILLE

INCLUDING AEROELASTIC EFFECTS IN THE CALCULATION OF X-33 LOADS AND CONTROL CHARACTERISTICS

Prepared By: Thomas A. Zeiler, Ph. D

Academic Rank: Assistant Professor

Institution and Department: University of Alabama, Tuscaloosa
Dept. of Aerospace Engineering and Mechanics

NASA/MSFC:

Lab: Structures and Dynamics Laboratory
Division: Structural Analysis Division
Branch: Structural Dynamics and Loads Branch

MSFC Colleague: Samuel B. Fowler

Introduction

Up until now, loads analyses of the X-33 RLV have been done at Marshall Space Flight Center (MSFC) using aerodynamic loads derived from CFD and wind tunnel models of a rigid vehicle. Control forces and moments are determined using a rigid vehicle trajectory analysis and the detailed control load distributions for achieving the desired control forces and moments, again on the rigid vehicle, are determined by Lockheed Martin Skunk Works. However, static aeroelastic effects upon the load distributions are not known. The static aeroelastic effects will generally redistribute external loads thereby affecting both the internal structural loads as well as the forces and moments generated by aerodynamic control surfaces. Therefor, predicted structural sizes as well as maneuvering requirements can be altered by consideration of static aeroelastic effects.

Objective

The objective of the present work is the development of models and solutions for including static aeroelasticity in the calculation of X-33 loads and in the determination of stability and control derivatives. Since structural analysis of the X-33 vehicle is being done in NASTRAN, it was decided that the models and analyses would be done using NASTRAN Aeroelastic Supplement's Static Aeroelasticity solution sequence (SOL 144) (Ref. 1). Essentially, NASTRAN's trim solutions are considered incremental changes to those represented by the rigid loads and control force solutions. Load distributions determined by these rigid analyses are applied to the model as "external" loads during the aeroelastic solution. Alone, the aeroelastic load redistributions would bring the vehicle out of the desired flight condition. However, the aeroelastic trim solution can determine changes in the trim variables (e.g. angle of attack, sideslip, control deflections) that will maintain the desired trim condition. Values of stability and control derivatives for the rigid and flexible vehicle are also produced by the SOL 144. A second result of the static aeroelastic solution is internal loads/stress recovery. This latter part of SOL 144 is essentially identical to the regular static solution in NASTRAN (SOL 101).

Mathematical Foundation

Following is a mathematical description of the problem to be solved. While the form of the equations presented herein is not identical to that presented in the NATRAN Aeroelastic Supplement User's Guide, it is mathematically equivalent and more readily followed.

The case of an unrestrained vehicle is a good bit more complicated than that of the restrained structure for several reasons. One is the fact that the load-deflection relation involves the "free body flexibility" matrix. The deflection under load of an unrestrained structure can't be found simply by inverting the stiffness matrix because the stiffness matrix is singular. A second complication arises from the need to consider such details of the flight condition as trim conditions.

The unrestrained nature of the structure is handled by the so-called inertia relief formulation, which will be discussed briefly. The structure is assumed restrained at a support point against rigid body motion, and corresponding load-deflection relation of the restrained structure is expressed in the usual way but with certain differences in detail,

$$\mathbf{P}_{net} = \mathbf{K}\delta_{res} \tag{1}$$

$\mathbf{P}_{net}$ is the vector of *net* loads being the combination of externally applied loads (aerodynamic, propulsive, etc.) and mass-intensive loads, such as gravity and inertial loads. These loads are self-equilibrating for a free body. If we expand equation (1) ,

$$\begin{Bmatrix} \mathbf{P}_{0net} \\ \mathbf{P}_{sup\,port} \end{Bmatrix} = \begin{bmatrix} \mathbf{K}_{\ell\ell} & \mathbf{K}_{\ell r} \\ \mathbf{K}_{r\ell} & \mathbf{K}_{rr} \end{bmatrix} \begin{Bmatrix} \delta_{0\ell} \\ \mathbf{0} \end{Bmatrix} \tag{2}$$

$\mathbf{K}_{\ell\ell}$ is the restrained structure stiffness matrix. $\mathbf{P}_{support}$ is the load vector at the "support" which, for a free body *should* be zero, again because the net loads are self-equilibrating. The deflections of the unrestrained points are related to the net loads by

$$\delta_{0\ell} = \mathbf{K}_{\ell\ell}^{-1}\mathbf{P}_{0net} \tag{3}$$

The important steps are to relate the net loads to the externally applied loads, and the restrained structure deflections to the unrestrained structure deflections.

The global deflections δ of the unrestrained vehicle are the sum of the eff ects of the actual displacements of the support (including rotations), and the deflections $\delta_{0\ell}$ of the unrestrained points relative to the support. This is expressed by

$$\delta = \Phi_r\delta_r + \delta_{res} \tag{4}$$

where Φ_r is the rigid body modeshape matrix that distributes rigid body motions at the support to all the nodes and δ_r is the vector of rigid body motions at the support points. The crucial step is to stipulate that the body axes that the rigid body displacements describe are *mean axes*. The condition that has to be met in this case is that the vector of total nodal displacements and the rigid body modes are mass orthogonal. This "mean axis contraint" is enforced by

$$\Phi_r^T\mathbf{M}\delta = \Phi_r^T\mathbf{M}\Phi_r\delta_r + \Phi_r^T\mathbf{M}\delta_{res} = \mathbf{M}_r\delta_r + \Phi_r^T\mathbf{M}\delta_{res} = \mathbf{0} \tag{5}$$

where $\mathbf{M}_r$ is the rigid body mass matrix (generally a 6x6, positive definite matrix). From eqn. (5) we obtain,

$$\delta_r = -\mathbf{M}_r^{-1}\Phi_r^T\mathbf{M}\delta_{res}$$

When the above is substituted back into (4), we obtain,

$$\delta = \left[\mathbf{I} - \Phi_r\mathbf{M}_r^{-1}\Phi_r^T\mathbf{M}\right]\delta_{res} = \mathbf{R}\delta_{res} \tag{6}$$

The matrix $\mathbf{R}$ is the inertia relief matrix, although the reason for this name becomes clearer when the relation of the net loads to the externally applied loads is determined as follows.

The resultant overall external loads at the support are given by

$$\mathbf{F}_r = \Phi_r^T\mathbf{P}$$

The vector $\mathbf{F}_r$ is typically comprised of the three aerodynamic forces, the three aerodynamic moments, and propulsive forces and moments. The accelerations produced by these loads are found by premultiplying $\mathbf{F}_r$ by the inverse of the rigid body mass matrix,

$$\mathbf{a}_r = \mathbf{M}_r^{-1}\mathbf{F}_r = \mathbf{M}_r^{-1}\Phi_r^T\mathbf{P}$$

Note that $\mathbf{a}_r$ includes the effect of gravity. This is true by the equivalence principle that states that

we cannot distinguish between the inertial load resulting from an acceleration and the load resulting from gravitation. Now the rigid accelerations at all of the node points can be found from

$$\ddot{\boldsymbol{\delta}} = \boldsymbol{\Phi}_r \mathbf{a}_r = \boldsymbol{\Phi}_r \mathbf{M}_r^{-1} \boldsymbol{\Phi}_r^T \mathbf{P}$$

The inertial loads, or more correctly the "mass-intensive" or "body" loads (including gravity), at each node point are then

$$\mathbf{P}_{inertial} = -\mathbf{M}\ddot{\boldsymbol{\delta}} = -\mathbf{M}\boldsymbol{\Phi}_r \mathbf{M}_r^{-1} \boldsymbol{\Phi}_r^T \mathbf{P}$$

Finally the net loads are the combination of the externally applied loads and the body loads,

$$\mathbf{P}_{net} = \mathbf{P} + \mathbf{P}_{inertial} = \left[\mathbf{I} - \mathbf{M}\boldsymbol{\Phi}_r \mathbf{M}_r^{-1} \boldsymbol{\Phi}_r^T\right]\mathbf{P} = \mathbf{R}^T \mathbf{P} \tag{7}$$

We may find the restrained structure deflections resulting from the net loads as

$$\begin{Bmatrix} \boldsymbol{\delta}_{0\ell} \\ \mathbf{0} \end{Bmatrix} = \begin{bmatrix} \mathbf{K}_{\ell\ell}^{-1} & \mathbf{0} \\ \mathbf{0} & \mathbf{0} \end{bmatrix} \begin{Bmatrix} \mathbf{P}_{0net} \\ \mathbf{P}_{supports} = \mathbf{0} \end{Bmatrix} \qquad \text{or} \qquad \boldsymbol{\delta}_{res} = \mathbf{a}_{res} \mathbf{P}_{net} \tag{8}$$

Substituting for the net load vector and premultiplying by $\mathbf{R}$

$$\boldsymbol{\delta} = \mathbf{R}\mathbf{a}_{res}\mathbf{R}^T\mathbf{P} = \mathbf{a}_f \mathbf{P} \tag{9}$$

The matrix $\mathbf{a}_f$ is the so-called "free body flexibility" matrix which is singular.

Thus far, there is nothing especially aeroelastic in the development for the unrestrained vehicle. We will begin the aeroelastic formulation by first considering the various components of the externally applied load vector, $\mathbf{P}$. $\mathbf{P}$ is composed of initial aerodynamic and propulsive loads as determined for the rigid vehicle, with incremental loads resulting from deformation of the structure, incremental changes in control surfaces and vehicle attitude. The initial loads can also account for initial vehicle camber, attitude, angular velocity, estimated control deflections, etc. Preferably, these initial loads are determined through means more sophisticated and comprehensive than the lifting surface theories used in aeroelastic modeling. We may then write the load vector as

$$\mathbf{P} = \mathbf{P}_0 + \Delta\mathbf{P}^{prop} + \bar{q}\mathbf{Q}\boldsymbol{\delta} + \bar{q}\mathbf{Q}_t \Delta\mathbf{v}_t + \bar{q}\mathbf{Q}_\omega \Delta\boldsymbol{\omega} \tag{10}$$

$\mathbf{P}_0$ is the initial aerodynamic and propulsive load vector, $\Delta\mathbf{P}^{prop}$ is the incremental propulsive load vector (if applicable), $\Delta\mathbf{v}_t$ is increments in the aerodynamic trim variables (angles of attack and sideslip, and control deflections), $\mathbf{Q}_t$ is a matrix of GAF's for these trim variables, $\Delta\boldsymbol{\omega}$ is increments in the vehicle's angular rates, and $\mathbf{Q}_\omega$ is the corresponding matrix of GAF's. $\bar{q}\mathbf{Q}\boldsymbol{\delta}$ is the vector of aerodynamic loads resulting from deformation.

Using equation (10) in equation (9), we may obtain the deformation vector,

$$\boldsymbol{\delta} = \mathbf{A}^{-1}\mathbf{a}_f\mathbf{P}_0 + \mathbf{A}^{-1}\mathbf{a}_f\Delta\mathbf{P}^{prop} + \bar{q}\mathbf{A}^{-1}\mathbf{a}_f\mathbf{Q}_t\Delta\mathbf{v}_t + \bar{q}\mathbf{A}^{-1}\mathbf{a}_f\mathbf{Q}_\omega\Delta\boldsymbol{\omega} \tag{11}$$

where $\mathbf{A}^{-1} = \left[\mathbf{I} - \bar{q}\mathbf{a}_f\mathbf{Q}\right]^{-1}$ is the aeroelastic deflection amplification matrix.

Substituting equation (11) into equation (10),

$$\mathbf{P} = \mathbf{B}\mathbf{P}_0 + \mathbf{B}\Delta\mathbf{P}^{prop} + \bar{q}\mathbf{B}\mathbf{Q}_t\Delta\mathbf{v}_t + \bar{q}\mathbf{B}\mathbf{Q}_\omega\Delta\omega \tag{12}$$

where $\mathbf{B} = \left[\mathbf{I} + \bar{q}\mathbf{Q}\mathbf{A}^{-1}\mathbf{a}_f\right] = \left[\mathbf{I} - \bar{q}\mathbf{Q}\mathbf{a}_f\right]^{-1}$ is the aeroelastic load amplification matrix. Equation (12) gives the external loads acting on the vehicle including aeroelastic effects. Now we consider trim.

Six Degree-of-Freedom Equations of Motion

The six DOF EOM of the vehicle may be written,

$$\mathbf{F} = \mathbf{M}_r g\Theta + \mathbf{M}_r\dot{\mathbf{v}} + \tilde{\Omega}\mathbf{M}_r\mathbf{v} \tag{13}$$

$\mathbf{F}$ is comprised of the three external force componets and three external moment. As such, it can be expressed in terms of the external nodal forces of equation (12) as

$$\mathbf{F} = \Phi_r^T\mathbf{P} \tag{14}$$

$\mathbf{M}_r$ is the rigid body mass matrix, seen earlier. g is the magnitude of the acceleration of gravity, and the vector Θ is defined, for the support point at (or at least near) the vehicle's c.g., by

$$\Theta = \lfloor sin\theta \quad -cos\theta sin\phi \quad -cos\theta cos\phi \quad \mathbf{0}_{1X3} \rfloor^T$$

which arises from the vector transformation of the gravity vector from the local vertical frame to the body frame. Hence, θ and ϕ are two of the Euler angles for this transformation. If the support point were not at the c.g., then the zero vector in the lower partition would contain offset components between the c.g. and the support point. Note that a traditional flight mechanics body frame is assumed here: $+x$ - axis forward; $+y$ - axis right; $+z$ - axis out the underside. The matrix $\tilde{\Omega}$ is defined by

$$\tilde{\Omega} = \begin{bmatrix} \tilde{\omega} & \mathbf{0} \\ \mathbf{0} & \tilde{\omega} \end{bmatrix} \qquad \text{where} \qquad \tilde{\omega} = \begin{bmatrix} 0 & -r & p \\ r & 0 & -q \\ -p & q & 0 \end{bmatrix}$$

and p, q, and r are the body axis components of the angular velocity vector. The effect of $\tilde{\omega}$ is to accomplish the vector product of the angular velocity vector with another vector. Finally, $\mathbf{v}$ is comprised of the body axis components of the translational and angular velocities of the vehicle,

$$\mathbf{v} = \lfloor u \quad v \quad w \quad p \quad q \quad r \rfloor^T = \lfloor V cos\alpha cos\beta \quad V sin\beta \quad V sin\alpha cos\beta \quad p \quad q \quad r \rfloor^T$$

For relatively mild maneuvers and small aerodynamic angles we may make the approximations,

$$\tilde{\Omega}\mathbf{M}_r\mathbf{v} \approx m\lfloor 0 \quad Vr \quad -Vq \quad \mathbf{0}_{1X3} \rfloor^T = m\mathbf{a}_c \qquad \text{and} \qquad \mathbf{v} \approx \lfloor V \quad V\beta \quad V\alpha \quad p \quad q \quad r \rfloor^T$$

recognizing the first three entries in $\mathbf{a}_c$ as centripital acceleration components. Combining equations (12), (13), and (14),

$$\mathbf{F} = \Phi_r^T \mathbf{B} \mathbf{P}_0 + \Phi_r^T \mathbf{B} \Delta \mathbf{P}^{prop} + \bar{q} \Phi_r^T \mathbf{B} \mathbf{Q}_t \Delta \mathbf{v}_t + \bar{q} \Phi_r^T \mathbf{B} \mathbf{Q}_\omega \Delta \omega = \mathbf{M}_r g \Theta + \mathbf{M}_r \dot{\mathbf{v}} + m \mathbf{a}_c \qquad (15)$$

The motions and orientations in the rightmost side of equation (15) can be expressed as the sum of initial values plus perturbations. The initial values would be those consistent with the initial load distribution $\mathbf{P}_0$. The perturbations are those consistent with the perturbations in the center part of equation (15) combined with the aeroelastic increments produced by multiplication by $\mathbf{B}$. Note also that the traditional stability and control derivatives (derivatives of aerodynamic force and moment coefficients with respect to aerodynamic angles, control surface deflections, and angular velocity components) are contained within the terms $\Phi_r^T \mathbf{B} \mathbf{Q}_t$ and $\Phi_r^T \mathbf{B} \mathbf{Q}_\omega$. The presence of the matrix $\mathbf{B}$ makes these "flex" values. Note that if dynamic pressure is set to zero the stability and control derivatives become "rigid" values. We may replace the rightmost term in equation (15) by

$$\mathbf{M}_r g \Theta + \mathbf{M}_r \dot{\mathbf{v}} + m \mathbf{a}_c = -mg \tilde{\mathbf{M}}_r \mathbf{N} \qquad (16)$$

The matrix $\tilde{\mathbf{M}}_r$ is simply $\mathbf{M}_r$ divided by m, the mass of the vehicle. The vector $\mathbf{N}$ is

$$\mathbf{N} = \begin{bmatrix} n_x & n_y & n_z & \mathbf{N}_\omega^T \end{bmatrix}^T$$

The top three entries are load factors, and the vector in the bottom partition is essentially angular accelerations divided by g. It is these six acceleration quantities that NASTRAN's aeroelastic supplement actually includes as potential specified input or as responses to be determined. So then,

$$-mg \tilde{\mathbf{M}}_r \mathbf{N} = \Phi_r^T \mathbf{B} \mathbf{P}_0 + \Phi_r^T \mathbf{B} \Delta \mathbf{P}^{prop} + \bar{q} \Phi_r^T \mathbf{B} \mathbf{Q}_t \Delta \mathbf{v}_t + \bar{q} \Phi_r^T \mathbf{B} \mathbf{Q}_\omega \Delta \omega \qquad (17)$$

Equations (16) and (17) form the core of the aeroelastic trim problem. Let us suppose that the vector $\mathbf{N}$ is specified, as are the angular velocities. From equation (17) we may obtain trim variable perturbations as

$$\Delta \mathbf{v}_t = -\frac{1}{\bar{q}} \left[\Phi_r^T \mathbf{B} \mathbf{Q}_t \right]^{-1} \left[mg \tilde{\mathbf{M}}_r \mathbf{N} + \Phi_r^T \mathbf{B} \mathbf{P}_0 + \Phi_r^T \mathbf{B} \Delta \mathbf{P}^{prop} + \bar{q} \Phi_r^T \mathbf{B} \mathbf{Q}_\omega \Delta \omega \right] \qquad (18)$$

Within a computer program, logic may be written to partition the matrix equations according to what is specified or unknown. The potential trim solution variables are: 3 load factors; 3 angular accelerations; 3 angular velocities; 2 aerodynamic trim angles (angles of attack and sideslip); and control surface deflections. Strictly speaking, we may only have six unknown variables because we only have six equations of equilibrium. NASTRAN can deal directly with all of the above mentioned variables.

Conclusions

The aeroelastic model was developed and implemented and results have been obtained showing flexibility effects on stability and control derivatives and internal loads. The proprietariness of the results could not be determined in time to include them in this report. Flight simulations need to include aeroelastic effects. Dynamic aeroelasticity needs to be considered.

Reference

1. Rodden, William P., and Johnson, Erwin H., "MSC/NASTRAN Aeroelastic Analysis," *User's Guide, Version 68*, The Macneal-Schwendler Corporation, 1994.

REPORT DOCUMENTATION PAGE

Form Approved
OMB No. 0704-0188

Public reporting burden for this collection of information is estimated to average 1 hour per response, including the time for reviewing instructions, searching existing data sources, gathering and maintaining the data needed, and completing and reviewing the collection of information. Send comments regarding this burden estimate or any other aspect of this collection of information, including suggestions for reducing this burden, to Washington Headquarters Services, Directorate for Information Operation and Reports, 1215 Jefferson Davis Highway, Suite 1204, Arlington, VA 22202-4302, and to the Office of Management and Budget, Paperwork Reduction Project (0704-0188), Washington, DC 20503

1. AGENCY USE ONLY *(Leave Blank)*	2. REPORT DATE	3. REPORT TYPE AND DATES COVERED
	September 1998	Contractor Report (Final Report)

4. TITLE AND SUBTITLE
Research Reports—1997 NASA/ASEE Summer Faculty Fellowship Program

5. FUNDING NUMBERS
NGT8–52836

6. AUTHORS
G.R. Karr*, J. Dowdy, L.M. Freeman**, Editors

7. PERFORMING ORGANIZATION NAMES(S) AND ADDRESS(ES)
*The University of Alabama in Huntsville and
**The University of Alabama, Tuscaloosa, Alabama

8. PERFORMING ORGANIZATION REPORT NUMBER
M–897

9. SPONSORING/MONITORING AGENCY NAME(S) AND ADDRESS(ES)
National Aeronautics and Space Administration
Washington, D.C. 20546–0001

10. SPONSORING/MONITORING AGENCY REPORT NUMBER
NASA/CR—1998–208803

11. SUPPLEMENTARY NOTES

12a. DISTRIBUTION/AVAILABILITY STATEMENT
Unclassified–Unlimited
Subject Category 99
Nonstandard Distribution

12b. DISTRIBUTION CODE

13. ABSTRACT *(Maximum 200 words)*

For the 33rd consecutive year, a NASA/ASEE Summer Faculty Fellowship Progam was conducted at the Marshall Space Flight Center (MSFC). The program was conducted by the University of Alabama in Huntsville and MSFC during the period June 2, 1997 through August 8, 1997. Operated under the auspices of the American Society for Engineering Education, the MSFC program was sponsored by the Higher Education Branch, Education Division, NASA Headquarters, Washington, D.C. The basic objectives of the program, which are in the 34th year of operation nationally, are (1) to further the professional knowledge of qualified engineering and science faculty members, (2) to stimulate an exchange of ideas between participants and NASA, (3) to enrich and refresh the research and teaching activities of the participants' institutions, and (4) to contribute to the research objectives of the NASA centers.

The Faculty Fellows spent 10 weeks at MSFC engaged in a research project compatible with their interests and background and worked in collaboration with a NASA/MSFC colleague. This document is a compilation of Fellows' reports on their research during the summer of 1997. The University of Alabama in Huntsville presents the Co-Directors' report on the administrative operations of the program. Further information can be obtained by contacting any of the editors.

14. SUBJECT TERMS	15. NUMBER OF PAGES
Astrionics, Structure and Dynamics, Materials and Processes, Systems Analysis and Integration, Propulsion, Space Sciences, Mission Operations, Information Systems, Advanced Spacecraft and Payload Systems, Preliminary Design, Technology Transfer	446
	16. PRICE CODE A19

17. SECURITY CLASSIFICATION OF REPORT	18. SECURITY CLASSIFICATION OF THIS PAGE	19. SECURITY CLASSIFICATION OF ABSTRACT	20. LIMITATION OF ABSTRACT
Unclassified	Unclassified	Unclassified	Unlimited

National Aeronautics and
Space Administration
AT01S
George C. Marshall Space Flight Center
Marshall Space Flight Center, Alabama
35812